Numerical Study of Innovative Scramjet Inlets Coupled to Combustors Using Hydrocarbon-Air Mixture

A Dissertation

Presented to

The Academic Faculty

by

Faure Joel Malo-Molina

In Partial Fulfillment

of the Requirements for the Degree

Doctor of Philosophy in the

School of Aerospace Engineering

Georgia Institute of Technology

May 2010

Numerical Study of Innovative Scramjet Inlets Coupled to Combustors Using Hydrocarbon-Air Mixture

Approved by:

Dr. Stephen M. Ruffin, Advisor
School of Aerospace Engineering
Georgia Institute of Technology

Dr. Marilyn Smith
School of Aerospace Engineering
Georgia Institute of Technology

Dr. Suresh Menon
School of Aerospace Engineering
Georgia Institute of Technology

Dr. Houshang Ebrahimi
Senior Engineer
Software Engineering Associates, Inc.

Dr. José A. Camberos
Senior Aerospace Engineer
USAF-AFRL/RBAC
Wright-Patterson Air Force Base

Date Approved:

ACKNOWLEDGMENTS

The author is grateful to Dr. Paul H. Kutschenreuter at Air Force Research Lab (AFRL)/ Aerospace Vehicles Integration and Demonstration Branch (RBAI) for providing the initial inviscid design for Jaws. Likewise, to Prof. Graham Candler at the University of Minnesota for providing the basis for the Sugar Scoop geometry employed. Assistance was received from Dr. Stephen M. Ruffin at Georgia Institute of Technology, Dr. Datta V. Gaitonde and Dr. José Camberos at the AFRL-RBAC (Air Vehicles Computational Branch, Computational Science Center of Excellence, Wright-Patterson Air Force Base, Ohio) and Dr. Houshang B. Ebrahimi at Software Engineering Associates, Inc., Carson City, Nevada. This work has been supported from 2006 through 2009 by the Air Force Office of Scientific Research, monitored by Dr. John Schmisseur and Dr. Fariba Fahroo. Computational resources were made available by the Major Shared Resource Centers of the Department of Defense through continuously awarded challenge awards. This work is dedicated to my three children (Danilo, Mateo and Gabriela) and my wife Dr. Diane M. Just for all their support and patience.

TABLE OF CONTENTS

ACKNOWLEDGMENTS ..... **III**

LIST OF TABLES ..... **VIII**

LIST OF FIGURES ..... **IX**

LIST OF EQUATIONS ..... **XIV**

LIST OF SYMBOLS ..... **XVIII**

SUMMARY ..... **XXI**

CHAPTER 1: INTRODUCTION **1**

1.1 SCRAMJET OVERVIEW 1

1.2 CONVENTIONAL INLETS AND THEIR ISSUES 2

1.3 JAWS INLET CONCEPT 6

1.4 SCOOP INLET CONCEPT 9

1.5 RESEARCH OBJECTIVES 10

CHAPTER 2: NUMERICAL APPROACH **16**

2.1 OVERVIEW OF CFD IN SCRAMJETS 16

2.2 SUMMARY OF GPACT CODE 17

2.3 CHEMICAL MECHANISM 18

2.3.1 Species Screening 20

2.3.2 Finite Rate Chemistry Model 23

2.4 TURBULENT MODELS 27

2.4.1 RANS Model 28

2.4.2 LES Model 30

2.5 CODE VALIDATION & VERIFICATION 34

2.5.1 Analysis of Double Fin Turbulent Interaction at Mach 4 37

2.5.2 Cavity-Based Flame Holders 42

2.5.3 Supersonic Flow over an Open Ramp Cavity 45

2.5.4 Stepped Combustor with Double Jet Interaction 49

CHAPTER 3: INLET ANALYSIS 52

3.1 INLET ANALYSIS OVERVIEW 52

3.1.1 Baseline Inlet Analysis 52

3.1.2 Innovative (Circular) Inlets Analysis 54

3.2 ON-DESIGN ANALYSIS 57

3.2.1 Baseline (On-Design) 57

3.2.2 Jaws Inlet (On-Design) 63

3.2.3 Scoop Inlet (On-Design) 73

3.2.4 Discussion of Results (On-Design Inlets) 79

3.3 OFF-DESIGN ANALYSIS 81

3.3.1 Baseline Inlet (Off-Design) 81

3.3.2 Jaws Inlet (Off-Design) 88

3.3.3 Scoop Inlet (Off-Design) 97

3.3.4 Discussion of Results (Off-Design Inlets) 104

3.4 CONCLUSIONS REGARDING THE ISOLATED INLETS, ON-/OFF-DESIGN 106

CHAPTER 4: DEVELOPMENT OF A SUPERSONIC COMBUSTOR CONFIGURATION 108

4.1 SUPERSONIC COMBUSTOR'S CAVITY 108

4.2 INJECTION STRATEGY 111

4.3 RECTANGULAR COMBUSTOR DEVELOPMENT 115

4.3.1 Analysis 115

Top Single Injection: 117

Top and Bottom Injection: 120

Top, Bottom and interlaced Injection: 123

4.3.2 Discussion of Results (Previous Rectangular Combustors) 126

4.4 COMBUSTOR PARAMETRIC STUDY 127

4.4.1 Overview 128

4.4.2 Computational Domain 129

4.4.3 Parametric Analysis, Averaging Strategy 129

Frozen Chemistry Assumption: 133

Finite-Rate Chemistry Assumption: 139

4.4.4 Discussion of Results (Parametric Study) 142

CHAPTER 5: CIRCULAR COMBUSTOR ANALYSIS 144

5.1 ANNULAR CONFIGURATION DEVELOPMENT 144

5.2 CIRCULAR SCRAMJET COMBUSTOR: FROZEN CHEMISTRY 149

5.2.1 Uniform Inflow, Frozen Chemistry 149

5.2.2 Jaws Inflow, Frozen Chemistry 160

5.2.3 Scoop Inflow, Frozen Chemistry 166

5.2.4 Uniform, Jaws vs. Scoop inflow, Frozen Assumptions 173

5.2.5 Rectangular vs. Circular Combustors 176

5.2.5 Discussion of Results (Circular Combustor, Frozen Chemistry) 179

5.3 CIRCULAR COMBUSTOR SELECTION: INFLOW ASSUMPTIONS AND FINITE-RATE CHEMISTRY 180

5.3.1 Uniform Inflow (Finite-Rate Chemistry) 182

5.3.2 Jaws Inflow (Finite-Rate Chemistry) 186

5.4.2 Scoop Inflow (Finite-Rate Chemistry) 189

5.3.5 Uniform, Jaws vs. Scoop inflow, Finite Rate Assumptions 191

5.3.6 Discussion of Results (Circular Combustor, Finite-Rate Chemistry) 196

5.4 UNSTEADY ANALYSIS: URANS VS. LES 197

5.4.1 Computational Modeling 200

5.4.2 URANS with Finite-Rate Chemistry 203

5.4.3 LES with Finite-Rate Chemistry 204

5.4.4 URANS vs. LES 208

5.4.5 Discussion of Results (URANS vs. LES, Finite-Rate Chemistry) 211

CHAPTER 6: CONCLUSIONS 216

6.1 OVERVIEW: 216

6.2 HYPERSONIC INLETS (ON-/OFF-DESIGN) 217

Isolated Hypersonic Inlet Analysis: 217

Inlet and Combustor Integration: 218

6.3 SUPERSONIC COMBUSTORS 219

Inflow and Chemical Assumptions (Rectangular vs. Circular Configurations): 219

Unsteady Assumptions (URANS vs. LES): 222

6.4 SUMMARY 223

APPENDIX A 226

APPENDIX B 229

REACTION RATES IN A LINEAR FORM (ETHYLENE-AIR MIXTURE): 229

REFERENCES 242

LIST OF TABLES

Table 1: Ethylene information and properties. 19

Table 2: Reaction types and their chemical sources. 24

Table 3: Chemical reactions of the reduced mechanism (Ethylene-Air mixture) 27

Table 4: Normalized inlet results (On-Design). 79

Table 5: Normalized inlet results (Off-Design). 105

Table 6: Circular cross-section scramjet combustor Cases 149

Table 7: Integration analysis for frozen Cases 1a-c 159

Table 8: Integration analysis for frozen Cases 2a-c. 166

Table 9: Integration analysis for frozen Cases 3a-c. 172

Table 10: Integrated pressure and temperature averaged for Cases 1-3c. 175

Table 11: Circular combustor cases with finite-rate chemistry 182

Table 12: Pressure and temperature inside cavity (Cases 1-3cr). 194

Table 13: Integrated scramjet performance results. 195

Table 14: ER=0.5, $X(C_2H_4)=0.007$ and $X(O_2)=0.042$. 226

Table 15: ER=0.75, $X(C_2H_4)=0.007$ and $X(O_2)=0.028$. 227

Table 16: ER=1.0, $X(C_2H_4)=0.007$ and $X(O_2)=0.021$. 227

Table 17: ER=1.0, $X(C_2H_4)=0.00145$ and $X(O_2)=0.021$. 228

LIST OF FIGURES

Figure 1: Baseline inlet configuration. 3

Figure 2: Inviscid Mach number contours and shock structure. 3

Figure 3: Typical cowl-lip interaction at Mach 8. 5

Figure 4: Jaws inlet configuration. 7

Figure 5: Inviscid Mach number contours and shock structure for Jaws inlet configuration. 8

Figure 6: Busemann circular inlet configuration (Scoop) 10

Figure 7: Normalized Pressure flowfiled inside a Busemann inlet. 10

Figure 8: Scheme of CFD models in GPACT 17

Figure 9: Temperature and CO molar fraction versus time. 21

Figure 10: Double fin configuration mesh and velocity profile comparison. 39

Figure 11: Genesis of characteristic low total pressure pattern through swept viscous/inviscid interactions. 40

Figure 12: Double fin interaction: iso-surface, surface oil, streamlines and contours. 42

Figure 13: The closed and open cavity grids. 44

Figure 14: GPACT validations for two different cavity based flame-holders. 45

Figure 15: Numerical grid of a 20^{o} ramped cavity validation case (1^{st} mesh). 46

Figure 16: 20^{o} ramped cavity validation case. 47

Figure 17: Experimental comparison to GPACT. 48

Figure 18: Mach number contours, z-plane. 50

Figure 19: Normalized Pressure and U-velocity ratio profiles. 50

Figure 20: Grid structure for the Baseline inlet design. 53

Figure 21: Innovative inlets' structured meshes. 56

Figure 22: Shock structure, Mach number contours and center line profiles for the Baseline inlet. 58

Figure 23: Baseline inlet results at symmetry plane and x-stations. 60

Figure 24: Viscous results for the on-design Baseline, Temperature (K) contours and streamlines. 61

Figure 25: Turbulent Baseline solutions, on-design. 62

Figure 26: Inviscid shock structure and Mach number for Jaws. 64

Figure 27: Turbulent solutions for Jaws, on-design. 66

Figure 28: Turbulent surface oil flow for the Jaws, on-design. 68

Figure 29: Bottom symmetry section of Jaws, with non-slip oil flow at the walls and streamlines depicted at the vortex separation (a-c) and (d) validation of a supersonic double 15° fin interaction. 70

Figure 30: Mach number contours for on-design Jaws. 71

Figure 31: Normalized Pitot pressure for on-design Jaws. 72

Figure 32: Turbulent Scoop contours, on-design. 75

Figure 33: Surface oil flow for the Scoop. 77

Figure 34: Scoop inlet exit profiles at on-design conditions. 78

Figure 35: Off-design (3° pitch) Baseline results. 83

Figure 36: Off-design (3° pitch) results at the exit plane of Baseline inlet. 84

Figure 37: Off-design (3^{o} yaw) Baseline results. 86

Figure 38: Off-design (3° yaw) results at the exit plane of the Baseline inlet. 87

Figure 39: Mach number contours for off-design (3° pitch) Jaws. 89

Figure 40: Pitot pressure ratio contours for off-design (3° pitch) Jaws.....90

Figure 41: Off-design (3° pitch) Jaws. 92

Figure 42: Mach number contours for off-design (3° yaw) Jaws. 94

Figure 43: Pitot pressure ratio contours for off-design (3° yaw) Jaws.....95

Figure 44: Off-design (3° yaw) Jaws results: x-planes contours, oil-flow and separated streamlines. 96

Figure 45: Off-design Scoop inlet results for 3° pitch.....98

Figure 46: Off-design (3° pitch) Scoop inlet oil-flow in a normalized shear wall scalar..99

Figure 47: Scoop inlet results at off-design (3° yaw).....102

Figure 48: Upper iso-view Mach number contours at x-planes.....103

Figure 49: Scoop inlet results at off-design (3° yaw).....104

Figure 50: Schematic of key combustor physics.....109

Figure 51: Typical cavity combustor designs 111

Figure 52: Schematic of the under-expanded transverse fuel injection flow field structures.....114

Figure 53: Grid structure for a combustor configuration.....116

Figure 54: Contours at center z-plane, single perpendicular injection. 118

Figure 55: Fuel (JP8), Oxygen, Water and Carbon Dioxide mole fractions (from top to bottom) at the center plane for a single perpendicular injection configuration combustor. 119

Figure 56: Contours at *z*-planes, upper/lower dual injection. 121

Figure 57: Reactants at symmetry *z*-plane, upper/lower dual injection 122

Figure 58: Products at symmetry *z*-plane, upper/lower dual injection. 123

Figure 59: Dual row and interlaced injection strategy configuration. 124

Figure 60: Temperature (K) at walls and iso-surface of $Y(CO_2)$. 124

Figure 61: Rectangular scramjet combustor configurations. 132

Figure 62: Fuel mass fraction at *z*- and several *x*- planes. 134

Figure 63: Mixing factor comparison; rectangular configurations. 138

Figure 64: Rectangular combustor Case 1, finite-rate chemistry. 141

Figure 65: Previous rectangular combustors (left side, Cases 1, 4 and 9) converted into circular combustors (right side, Configurations A-C). 145

Figure 66: Circular combustor prototypes. 147

Figure 67: Configuration C, dimensions and structured mesh. 148

Figure 68: Configuration A results, uniform flow (Case 1a). 151

Figure 69: Y_{fuel} contours and injection streamline traces (Case 1a). 152

Figure 70: Configuration B results, uniform flow (Case 1b). 153

Figure 71: Configuration C results, uniform flow (Case 1c). 155

Figure 72: Case 1c, frozen chemistry and uniform inflow. 156

Figure 73: Mach number contours for Cases 1-3c, a-c respectively. 158

Figure 74: Configuration A results; Jaws inflow and frozen chemistry (Case 2a). 161

Figure 75: Configuration B results, Jaws inflow and frozen chemistry (Case 2b). 162

Figure 76: Case 2c results, $1/4^{th}$ view. 164

Figure 77: Case 2c results at symmetry planes, full view. 165

Figure 78: Configuration A results, Scoop profile and frozen chemistry. 168

Figure 79: Configuration B results, Scoop profile and frozen chemistry. 170

Figure 80: Case 3c results, Scoop profile with frozen chemistry. 172

Figure 81: Fuel mass fraction at 8 x-planes at the cavity region.....173

Figure 82: Results comparison for Cases 1-3c.....175

Figure 83: Mixing factor comparison for rectangular and circular combustors Configurations A-C, with/out chemistry and inflow profiles. 177

Figure 84: Fuel penetration depth comparison of configurations. 178

Figure 85: Cross sectional area relationships to the fuel penetration: Rectangular versus Circular combustor. 179

Figure 86: Case 1cr results, uniform flow and chemically reactive. 184

Figure 87: Case 1cr results, uniform chemical reactive.....185

Figure 88: Case 2cr results, Jaws inflow with chemistry. 187

Figure 89: Case 2cr solutions at symmetry planes. 189

Figure 90: Case 3cr solutions at the vertical symmetry plane. 190

Figure 91: Mass fraction CO contours at symmetry planes for Cases 1-3cr. 192

Figure 92: Results comparison for Cases 1-3cr. 193

Figure 93: Computational grid for a $1/8^{th}$ section with symmetrical boundary conditions, circular combustor. 202

Figure 94: URANS results with finite-rate assumption, Configuration C: Mach Number, Pressure (Pa) and Temperature (K) from left to right columns. 204

Figure 95: LES with finite-rate assumption, Configuration C.....205

Figure 96: Asymptotic behavior of LES after t=1.4 msec. 207

Figure 97: URANS (left side) versus LES (right side).....210

LIST OF EQUATIONS

Equation 1: Arrhenius 25

Equation 2: Generalized chemical reaction 25

Equation 3: Forward reaction rate 26

Equation 4: Reverse reaction rate 26

Equation 5: Net specie reaction rate of production/destruction 26

Equation 6: Mass fraction transport. 28

Equation 7: Mean passive scalar turbulent transport. 29

Equation 8: Favre variance. 29

Equation 9: Mean scalar dissipation rate term. 30

Equation 10: LES flow variables decomposition. 32

Equation 11: Subgrid-scale kinetic energy. 33

Equation 12: Subgrid-scale stress. 33

Equation 13: Subgrid-scale transport. 33

Equation 14: Subgrid-scale eddy viscosity. 33

Equation 15: Favre filtering mass fraction transport. 34

Equation 16: Transport of subgrid fluctuations of mass fraction. 34

Equation 17: Turbulent diffusion due to transport of subgrid fluctuations. 34

Equation 18: Swirl 88

Equation 19: Frozen fuel/air mixing factor. 136

Equation 20: Reactive fuel/air mixing factor. 137

Equation 21: Thrust per unit area ratio. 194

Equation 22: Production of $C_2H_{4(g)}$ mass fraction. 229

Equation 23: Production of $C_2H_{2(g)}$ mass fraction. 229
Equation 24: Production of $O_{2(g)}$ mass fraction. 229
Equation 25: Production of $O_{(g)}$ mass fraction. 229
Equation 26: Production of $H_{2\,(g)}$ mass fraction. 230
Equation 27: Production of $H_{(g)}$ mass fraction. 230
Equation 28: Production of $OH_{(g)}$ mass fraction. 230
Equation 29: Production of $H_2O_{(g)}$ mass fraction. 230
Equation 30: Production of $N_{2\,(g)}$ mass fraction. 230
Equation 31: Production of $N_{(g)}$ mass fraction. 230
Equation 32: Production of $NO_{(g)}$ mass fraction. 231
Equation 33: Production of $CO_{2(g)}$ mass fraction. 231
Equation 34: Production of $CO_{(g)}$ mass fraction. 231
Equation 35: Linear form for the produced mass fraction. 231
Equation 36: Two-Body reaction 231
Equation 37: Three-Body reaction. 231
Equation 38: $C_2H_{4(g)}$ mass production. 232
Equation 39: $C_2H_{2(g)}$ mass production. 232
Equation 40: $O_{2(g)}$ mass production. 232
Equation 41: $O_{(g)}$ mass production. 233
Equation 42: $H_{2(g)}$ mass production. 233
Equation 43: $H_{(g)}$ mass production. 233
Equation 44: $OH_{(g)}$ mass production. 234
Equation 45: $H_2O_{(g)}$ mass production. 234

Equation 46: $N_{2(g)}$ mass production. 234
Equation 47: $N_{(g)}$ mass production. 234
Equation 48: $NO_{(g)}$ mass production. 235
Equation 49: $CO_{2(g)}$ mass production. 235
Equation 50: $CO_{(g)}$ mass production. 235
Equation 51: Linearization of $C_2H_{4(g)}$ mass production. 235
Equation 52: Linearization of $C_2H_{2(g)}$ mass production. 236
Equation 53: Linearization of $O_{2(g)}$ mass production. 236
Equation 54: Linearization of $O_{(g)}$ mass production. 236
Equation 55: Linearization of $H_{2(g)}$ mass production. 237
Equation 56: Linearization of $H_{(g)}$ mass production. 237
Equation 57: Linearization of $OH_{(g)}$ mass production. 238
Equation 58: Linearization of $H_2O_{(g)}$ mass production. 238
Equation 59: Linearization of $N_{2(g)}$ mass production. 238
Equation 60: Linearization of $N_{(g)}$ mass production. 238
Equation 61: Linearization of $NO_{(g)}$ mass production. 239
Equation 62: Linearization of $CO_{2(g)}$ mass production. 239
Equation 63: Linearization of $CO_{(g)}$ mass production. 239
Equation 64: Linearization of species into Matrix form. 240
Equation 65: Chemical source. 240
Equation 66: 3D Unsteady Navier-Stokes. 241

LIST OF SYMBOLS

Alphanumeric:

a	Speed of sound
A	Area, Arrhenius constant
b	Arrhenius temperature constant
C	Chemical concentration, molar and/or mass terms
D	Geometrical depth (cavity), molecular diffusion
e	Energy
E	Energy of production
ER	Equivalent ratio
f	Fuel fraction, LES flow variable holder
F	Thrust/force; N
i	$Species=1... 13$
Jj	Transport of subgrid fluctuation of the mass fraction
k	Chemical, turbulent kinetic energy/dissipation rate coefficients
L	Geometrical length (cavity); m
mf	Mixing factor for frozen and/or finite-rate cases
M	Mach number, arbitrary third body reactant
MW	Molecular weight
N	Number of moles, molecular number
P,p	Pressure; Pa
q	Heat flux; $Watts$
Q	Heat; J

r	Radius; *m*
R	Gas constant
Re	Reynolds number
S	Entropy, swirl
t	Time variable; *sec*
T	Temperature; *K*
u	Downstream or horizontal component of the velocity (x-direction); *m/s*
U	Velocity magnitude; *m/s*
v	Vertical component of the velocity; *m/s*
w	Velocity component of the velocity (z-direction); m/s
W	Chemical source; *kg/sec*
X	Molar fraction
Y	Mass fraction
Z	Mean passive turbulent scalar, Favre's (average/variance)

Greek

α	Angle of attack (pitch)
β	Angle of attack (yaw)
γ	Ratio of specific heat
Δ,δ	Rate of change
ε	Entropy
θ	Radial direction or angle of curvature
κ	Thermal conductivity

λ	Eigen-value
v	Kinematic viscosity
π	*Pi=3.14159265358979323846…*
ρ	Density; kg/m^3
τ	Trust ratio, stress
μ_t	Eddy viscosity
υ	Molar value
φ	Stoichiometric coefficient
χ	Molar concentration

Superscript

$\cdot$	Rate of change
‘	Molar number for the reactant/s
“	Molar number for the product/s, variance value
*	Non-dimensional quantity
~	Roe averaged value
n	Known value
$n+1$	Unknown value (future step)
°	Degrees/angle of curvature
¯	Averaged value
sgs	Sub-grid scale

Subscript

1	Free stream/inlet conditions (*i.e.* pressure or temperature)
a	Arrhenius, activation (Energy)
b	Backward or reverse reaction
e	Exit plane
d	Drag
f	Hydrocarbon fuel, forward reaction
f_mix	Chemically frozen mixture (see mixing factor)
g	Gaseous phase
i	Inlet or entrance plane, tensor notation or numbering to numerical stencil
j	Jet conditions (fuel injection), tensor notation or numbering to numerical stencil
k	Subgrid kinetic energy term, tensor notation or numbering to numerical stencil
r_mix	Chemically reactive mixture (see mixing factor)
s	Stagnation or total values
sgs	*LES* Subgrid model notation
u	Universal
o	Pitot conditions
x,y,z	Position in the direction or component of

SUMMARY

The research objective is to use high-fidelity multi-physics Computational Fluid Dynamics (CFD) analysis to characterize 3-D scramjet flowfields in two novel streamline traced circular configurations without axisymmetric profiles. This work builds on a body of research conducted over the past several years. In addition, this research provides the modeling and simulation support, prior to ground (wind tunnel) and flight experiment programs. Two innovative inlets, Jaws and Scoop, are analyzed and compared to a Baseline inlet, a current state of the art rectangular inlet used as a baseline for on/off-design conditions. The flight trajectory conditions selected were Mach 6 and a dynamic pressure of 1,500 psf (*71.82 kPa*), corresponding to a static pressure of 43.7 psf (*2.09 kPa*) and temperature of 400.8 R◦ (*222.67 C°*). All inlets are designed for equal flight conditions, equal contraction ratios and exit cross-sectional areas, thus facilitating their comparison and integration to a common combustor design.

Analysis of these hypersonic inlets was performed to investigate distortion effects downstream in common generic combustors. These combustors include a single cavity acting as flame holder and strategically positioned fuel injection ports. This research not only seeks to identify the most successful integrated scramjet inlet/combustor design, but also investigates the flow physics and quantifies the integrated performance impact of the two novel scramjet inlet designs. It contributes to the hypersonic air-breathing community by providing analysis and predictions on directly-coupled combustor numerical experiments for developing pioneering inlets or nozzles for scramjets.

Several validations and verifications of General Propulsion Analysis Chemical-kinetic and Two-phase (GPACT), the CFD tool, were conducted throughout the research. In addition, this study uses 13 gaseous species and 20 reactions for an Ethylene/air finite-rate chemical model. The key conclusions of this research are:

1. *Flow distortion in the innovative inlets is similar to some of the distortion in the Baseline inlet, despite design differences*. In both innovative inlets, the resulting flowfield distortions were due to shock boundary layer interactions similar to those found in the Baseline. The Baseline and Jaws performance attributes are stronger than Scoop, but Jaws accomplishes this while eradicating the cowl lip interaction, and lessening the total drag and spillage penalties.

2. *The innovative inlets work best on-design, whereas for off-design, the traditional inlet yields a higher performance*. Although the innovative inlets' designs mitigated some of the issues encountered in traditional configurations, they underperform at off-design conditions. The strategy used in Jaws was less prone to interaction with the near wall flow, and yields lesser pressure losses and higher efficiency at on-design conditions compared to the others. In general, the overall values for Scoop seem lowest of all due to lesser entrainment. Its drag coefficient and thrust to mass capture ratios are higher than the Baseline configuration.

3. *Early pressure losses and flow distortions actually aid downstream combustion in all cases*. Although interactions captured by the viscous simulations for the on-design conditions increase losses in the inlets, they enhance turbulence in the isolator, favoring the mixing of air and fuel, and improving the overall factor of the

system. Jaws inlet demonstrates the most valuable design with higher performance, but its factor later in the combustor drops relative to its rectangular counterpart.

4. *A parametric study of the location and direction of injection is conducted to select the configuration for fuel penetration, mixing factor (factor) and other combustion qualities.* Although the trends observed with and without chemical reactions are the same, the former yields roughly 10% higher mixing factor. Unlike at frozen conditions, when chemical reactions are considered, a high compression area was observed upstream of the cavity, not present when modeling Jaws. The upstream reactions from the cavity have a significant impact on the development of the shear layers and downstream development of the entire combustion.

5. *Steady and unsteady simulations are conducted to characterize the ignition process, flame anchoring and flashback effects*. This unsteadiness enlarges the circulation region in and around the cavity, allowing the reactions to propagate forward through the shear layer, and increases the mixing factor. In Scoop, these effects are exacerbated due to the thicker low energy profile surrounding the walls and most of the lower section of the combustor. In the steady assumptions, the forward reactions and their effects are positioned farthest upstream, closest to the combustor entrance.

6. *Unsteady Reynolds Average Navier-Stokes (URANS) and Large Eddy Simulation (LES) modeling are compared to explore overall flow structure and for comparison of individual numerical methods.* In URANS, the flashback effects are midway between the entrance and the step, whereas in LES, this effect is near the edge of the step in addition to yielding a higher combustion factor. Thus, the turbulence model and inflow assumptions can critically affect the total outcome of such devices.

CHAPTER 1: INTRODUCTION

1.1 SCRAMJET OVERVIEW

Development of combustion systems to facilitate hypersonic flight have been ongoing since the late 1950s.[1 and 2] In order to achieve such hyper velocities, combustors must be able to produce substantial thrust at supersonic speeds.[3] Despite advances in scramjet analysis, many uncertainties persist about three-dimensional, supersonic chemically reacting flows, and significant challenges need to be overcome. These challenges include the high heat loads and low combustion factor arising from inefficient mixing at high-speeds.[4] Simulation methods can complement difficult to perform experiments and thus play a major role in developing a comprehensive understanding of the key phenomena that determine performance.

The finite rate at which chemical reactions occur limits scramjet operations to those with supersonic flow in the combustor. Such physical limitations occur when the chemical time scales are at the limit or less than the kinetic time of the flow. Because of this, some scramjet designs are incapable of reaching their minimum required power.[5] In addition, large pressure losses across the shocks and throughout the entire propulsion system hinder its output. These effects prevent current scramjet combustion technology from achieving a desirable performance with a combustor entry Mach number higher than 2 and pressure of around 3 *atm*, even when using high energetic density fuels such as Hydrogen. For conventional designs, this translates to a flight Mach number of

around 10. The current research aims to increase the speed range attainable with scramjets. By safely operating hypersonic vehicles at much higher flight Mach, we could deliver fast travel across continents while expanding access to space.

1.2 CONVENTIONAL INLETS AND THEIR ISSUES

Figure 1 depicts the Baseline scramjet configuration considered in this work.[6] This configuration is selected due to its traditional design, and it has an equal flight trajectory as the two innovative circular inlets. Rectangular configurations have been widely used since the 1950s, and they represent the current state of the art.

The Baseline inlet design follows to some extent that described by Gaitonde,[7] but with some key differences. First, the ramp angles of the inlet are equally increased so that the nominal Mach number, from inviscid estimates, is roughly 2 at the entrance of the combustor. Second, since the inlet and combustor were the main focus, the nozzle flow was not of particular interest and was therefore truncated. The design is comprised of a dual-plane compression inlet system followed by a constant-area combustor. The design is easily created from an inviscid streamline traced methodology where the flow turns through a series of four shocks. Two ramps with equal turning angles are determined for conditioning the upstream airflow to the desirable combustor inlet conditions (i.e., pressure, temperature and velocity). Figure 1 shows the Baseline inward turning inlet prototype design for comparison.

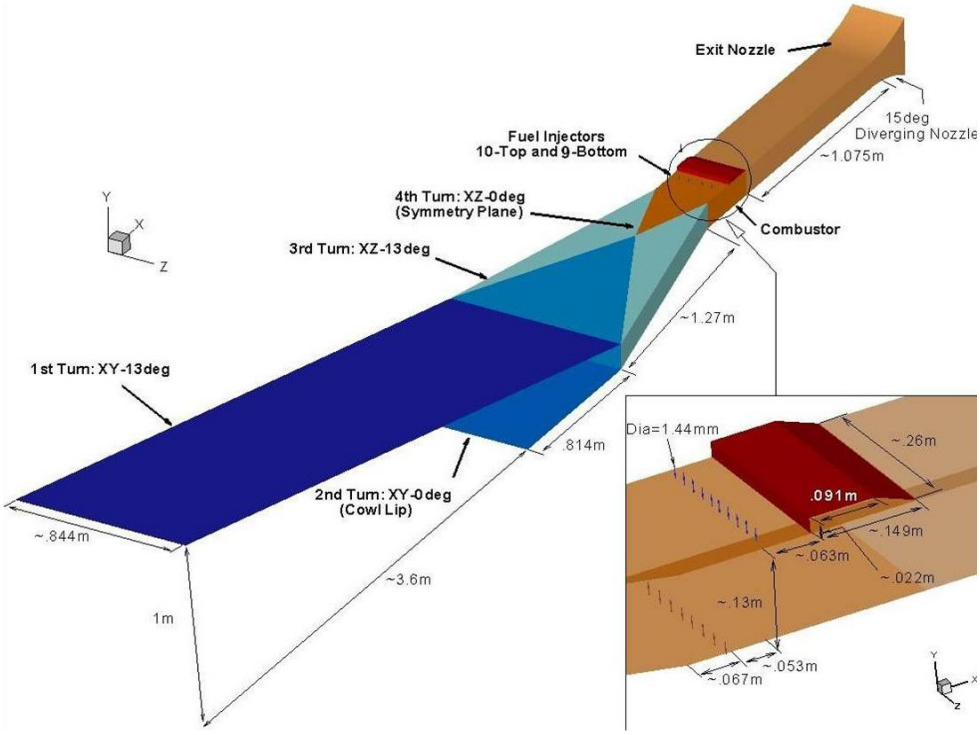

Figure 1: Baseline inlet configuration.

The following figure depicts the basic four planar shock structure and Mach number contours at the vertical *xy*-symmetry and most horizontal plane for the half-symmetry Baseline configuration as computed for its on-design conditions and assuming non-viscous effects.

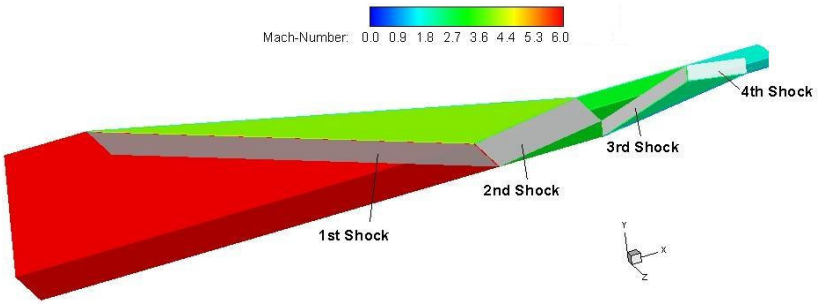

Figure 2: Inviscid Mach number contours and shock structure.

Multiple air vehicle integrations and design simplicity drives most examined scramjet inlet configurations to be rectangular, yet this yields some non-desirable structures along several cross-flow planes.[8, 9] The evolution of low total pressure regions associated with vertical structures is shown in Section 1.2.1 for a validation case (see Figure 11). In the constant-area duct, these regions effectively merge, leading to a peculiar situation in which the center of the configuration exhibits lower velocity than the off-center region.

The existing coherent structures may be explained in terms of viscous/inviscid interactions which give rise to fully three-dimensional separation. As noted by Dallman,[10] separation is a fundamentally different phenomenon in 3-D than in 2-D. Whereas topological considerations mandate a recirculation pattern in the latter, with a closed bubble and the presence of reversed flow (i.e., with a negative u component), three-dimensional separation generally yields open structures (i.e., that do not reattach to the walls) and often no reversed flow. This is the case in the present situation as well.

In addition, the sharp cowl lip design as in the Baseline inlet (see Figure 1) results in large moments and heating loads, and markedly reduces the performance and life cycle of the scramjets (Ref. 7). This is caused by a close impinging shock to bow shock interaction of type-one (TP1) and -two (TP2), as shown in Figure 3a-c.[11 and 12] These shock-to-shock interaction types are in blunt bodies such as cowl lips and/or double cone configurations.[13]

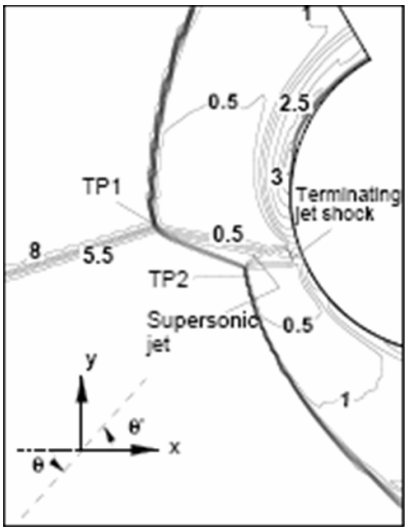

(a) Mach number

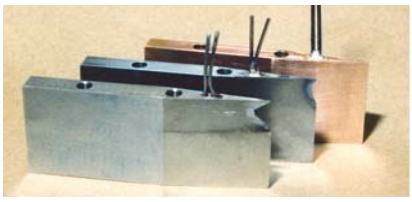

(b) Test articles (Cowl-lips)

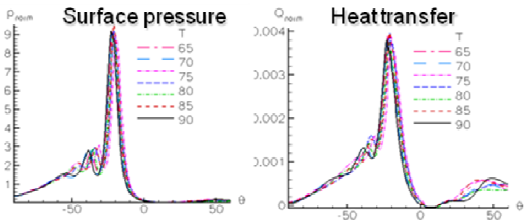

(c) Pressure ratio and heat loads

Figure 3: Typical cowl-lip interaction at Mach 8.

Two new hypersonic turning inlets, denoted Jaws and Scoop because of their general appearance, are investigated and compared to a Baseline counterpart which represents a state of the art configuration. These inlets may improve the properties of the internal flow path by modifying shock-boundary layer and shock-shock interactions that affect the overall factor of the engine (Ref. 5). Their designs promise to mitigate some of the conventional inlet issues such as the large parasite drag, cowl-lip interactions, corner flows, reduced mass capture, etc. This work compares the two prototypes with a Baseline inlet similar to one previously analyzed, with emphasis on drag forces and flow characteristics. All three designs are well-suited to exploring the generic three dimensional fluid dynamic features likely to be encountered in a scramjet. These geometries are designed to consider their internal viscous effects and shock interactions, and their geometrical modification details are not shown here.

1.3 JAWS INLET CONCEPT

Figure 4 shows the innovative Jaws inlet used in this study. This design, like the Baseline, is comprised of a dual-plane compression inlet system followed by a constant- axisymmetric area combustor. The inlet profile is inviscidly designed using a streamline traced methodology where the flow turns through a series of four shocks. Just as in the Baseline inlet, two ramps with equal angles and contraction ratios are determined for conditioning the upstream airflow to the desirable combustor inlet conditions. This prototype inlet was initially proposed by Paul H. Kutschenreuter and numerically analyzed in this body of work with his collaboration (see Ref. 6). Further studies of geometrical modifications to lessen viscous-inviscid interaction have been pursued to improve the surface contours. In addition, vehicle integration and start up conditions of such geometries is starting to be explored in conjunction with wind tunnel testing by the USAF Air Vehicle Division and NASA.

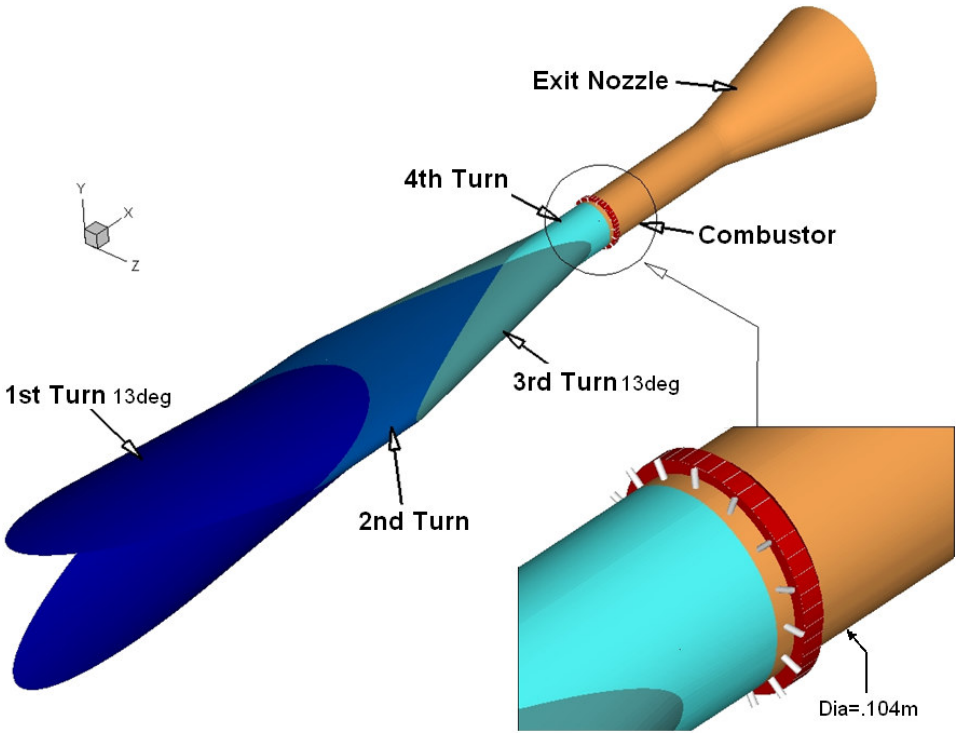

Figure 4: Jaws inlet configuration.

Again, Figure 5 depicts the basic shock structure and Mach number contours at the vertical and horizontal symmetry planes for a quarter-symmetry Jaws configuration as computed for its on-design conditions and assuming non-viscous effects. Note the striking similarity to its counterpart, half-symmetry Baseline configuration (i.e., compare Figure 5 to Figure 2). Although Jaws has a circular non-axisymmetric configuration, the inviscid shock formation is planar on the *xy*- and *xz*-planes.

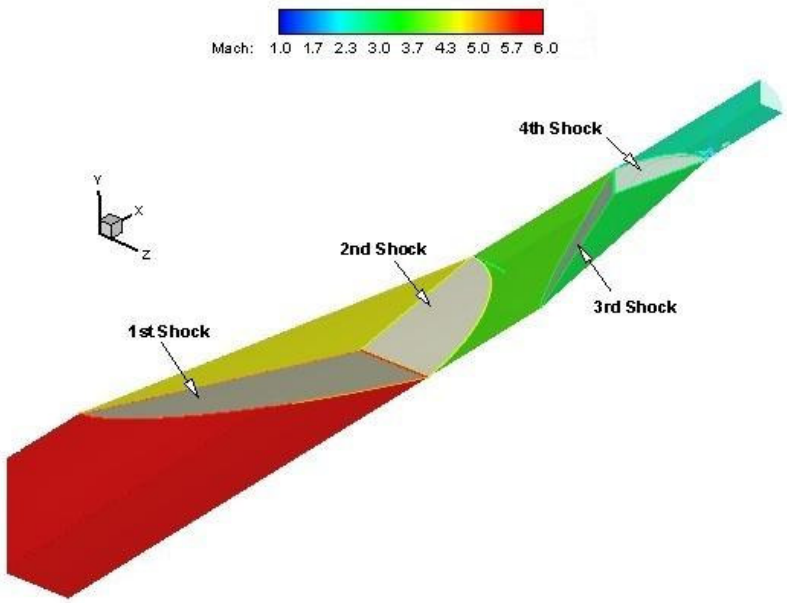

Figure 5: Inviscid Mach number contours and shock structure for Jaws inlet configuration.

This innovative design promises better performance due to three main differences. First, the inlet is designed to generate a set of planar shocks to follow along the leading edges of its outer lips, further reducing the parasite drag and spillage observed in the Baseline. Second, two shocks initially formed from this first encounter turn and interact with each other right upstream of the second turn. This eliminates the cowl lip effects present in the Baseline counterpart. And third, the vertical structures present near the rectangular corners of the inlet floor and near the isolator (the region between the inlet and combustor segment) walls are eradicated by the straightforward cylindrical profile.

1.4 SCOOP INLET CONCEPT

Figure 6 shows the Scoop inlet, a design very different from the others. The compression is designed to occur as a single plane axisymmetric compression. Many earlier designs of streamline traced inlets have been under development since the 1940s, offering useful advantages similar to the Jaws inlet design.[14 and 15] For scramjet engines, Scoop has demonstrated a very high inviscid factor when compared to conventional (rectangular and axisymmetric) inlets.[16] Although the Scoop is a very efficient type of Busemann inlet at its designed conditions, it can perform poorly for self-starting characteristics or transitioning from a ramjet to scramjet.[17] This inviscid Busemann inlet is designed by streamlines using well-known oblique shock relations. According to Tam and Baurle, "The traced streamlines are envisioned as solid surfaces, allowing the generation of inlets with swept walls. These swept surfaces provide a mechanism for flow spillage, which enlarges the self-starting envelope of the inlet. The streamline tracing technique has the added benefit of allowing the designer to alter the overall inlet shape to meet any required vehicle packaging constraints."[18] Scoop is thus a streamtraced Busemann inlet of a circular design (see Figure 6).

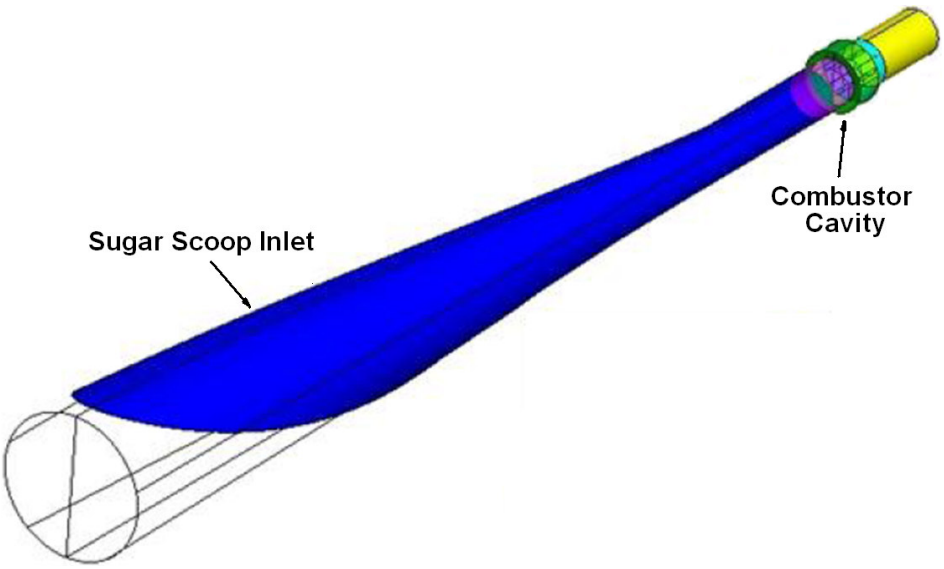

Figure 6: Busemann circular inlet configuration (Scoop).

Figure 7 illustrates a typical Busemann flowfield. As in the previous configuration, a planar 3D conical shock is formed on the leading edges of the inlet. Past this shockwave, a series of isentropic compression waves are conically symmetric and coalesce at the apex of the terminating conical shock (Ref. 16).

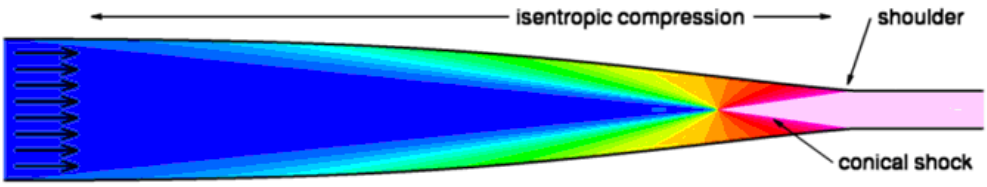

Figure 7: Normalized Pressure flowfiled inside a Busemann inlet.

1.5 RESEARCH OBJECTIVES

The main objective of this research is to conduct a high-fidelity multi-physics CFD analysis of two innovative hypersonic inlets, Jaws and Scoop, and

compare them to a traditional rectangular inlet used as a Baseline. The internal flow paths and overall coupled effects of these non-rectangular, non-axisymmetric scramjet engines are detailed for preliminary on-design and off-design conditions of their tip-to-tail configurations. This modeling and simulation work was conducted in support of the integration development and the internal experimental work conducted on these inward turning inlets. Later work will follow ground and flight test experiments in the *Hifire-II* (Hypersonic International Flight Research Experimentation-II) program, a collaboration of the United States and the Australian Departments of Defense (see Ref. 19). The Hifire series of up to 10 planned hypersonic flight experiments is part of a joint research program between the Australian Defence Science and Technology Organisation and the United States Air Force at AFRL. This collaborative research involves the Air Vehicle and Propulsion Directorate at AFRL (AFRL-RB and -RZ) and The School of Aerospace Engineering at Georgia Institute of Technology.

The novel designs seek to mitigate issues encountered in current state of the art or more traditional hypersonic inlets such as cowl lip interactions, large flow separation and interactions due to sharp corners, high temperature and pressure loads at the leading/cowl edges, strong vortices passing corners (e.g., Ref. 64), flow separation at the core and spillage (internal flow not captured by the inlet), inviscid-viscous interactions, etc. These problems contribute to larger drag and pressure losses through the system and might make them inefficient or inoperable.

The examination of these inlets also focuses on the distortion effects felt downstream in a circular combustor during its preliminary development. Understanding their flow paths will greatly aid future combustor designs like these novel configurations as well as exploring ways to control the encounter distortions (via magneto-hydro dynamics, micro-ramps or others). Insights from this study drove the development and design modifications to a geometry tested in NASA Langley during the Fall of 2008, in the 20 inch (0.508 m) Mach 6 facility (Refs. 20 and 21). Hypersonic inlets must be designed to condition the air flow from flight trajectory to best fit their supersonic combustor requirements (e.g., lean burning, high combustion factor, reduced ignition delay and length, etc.), while avoiding un-start and/or thermal choking. Supersonic combustors face other related issues such as: combustion instability, flashback/blow-off effects, ignition, flame anchoring, rapid transition from ramjet to scramjet (subsonic to supersonic flow path), and others. These many issues are caused by the short residence time in supersonic combustors (i.e., the time that it takes to transfer chemical to kinetic energy is of equal scale as the time to travel across the combustor), thus they require rapid mixing and ignition. Although the combustion might not be stabilized, one solution to this problem is the use of cavities on the peripheral walls, which act as flame holders to reduced the ignition time and increase mixing in the near region. In this research, all combustor designs include a single cavity and strategically positioned and/or directed fuel injection ports. The work demonstrates the importance of evaluating and

comparing entire hypersonic air-breathing engines to determine their performances.

This research investigates the flow physics and the integrated performance impact of two novel scramjet inlet designs. Simulation-guided analysis is used to understand basic phenomena, derive design guidance principles and help evolve these configurations for future hypersonic vehicles. This work provided analysis and predictions on coupled combustor experiments when developing pioneering inlets or nozzles for scramjets. In addition, several validations and/or verifications of the CFD tool (GPACT) are conducted throughout the entire research. It also proposes and applies a much needed reduction mechanism for an Ethylene/air finite-rate chemical model. The following steps detail how the research was accomplished.

1. The on/off-design Baseline inlet configuration is calculated for use as a point of comparison. The internal 3D flowfield is analyzed using inviscid and viscous calculations.

2. On/off-design numerical solutions are conducted for two innovative inlets, including the so-called "Jaws" concept, designed with streamline tracing techniques, and a contoured "Scoop" framework. Both inlet designs follow the same prescribed principles and assumptions when conditioning the freestream flow further into the combustor.

3. The phenomenological models of these inlets' performances are compared to determine the best isolated inlet segment.

4. These are further analyzed and compared when integrated to common combustors.

5. A secondary parametric analysis of ten different combustor prototypes is used to moderate the complexity and feasibility of comparing circular configurations to earlier research done on rectangular configurations.

6. From the previous step, the three rectangular configurations are selected and modified into an axisymmetric combustor. The circular configurations are then computed for uniform (averaged), Jaws and Scoop inflow profiles assuming frozen chemistry.

7. The combustor yielding the highest fuel-air mixing factor and flammability conditions near the cavity is then selected and reanalyzed for the same inflow profiles and with finite-rate chemistry.

8. Additional work on the average inflow condition is conducted on the most promising combustor. The most efficient injection strategy is analyzed using finite-rate assumptions and two unsteady approaches: URANS and LES, to better understand the starting characteristics and thermal shocking effects.

CHAPTER 2: NUMERICAL APPROACH

2.1 OVERVIEW OF CFD IN SCRAMJETS

In the design of advanced propulsion systems in supersonic combustors, computational modeling plays a major role in defining the required performance over the flight envelope, as well as in testing the sensitivity of the design to the various modes of scramjet operation (e.g., afterburner, rocket, ramjet, and scramjet). Computational modeling techniques, complemented with select ground and flight testing, are expected to be the engineering approach of choice in the development of new Air Force and NASA air and space propulsion programs. Therefore, an increased emphasis is placed on developing and applying CFD models to simulate the flowfield environments and performance of advanced propulsion systems. This places a premium on the development of the next generation of computational tools that can be used effectively and reliably in a design environment by non-CFD specialists. Experience gained from the use of current research-oriented CFD models is essential to guide the successful development of engineering application tools. Since the new approaches will rely less on testing and more on CFD results, a careful strategy is needed to ensure that the models are appropriate, and that the right assumptions are made for each circumstance.

2.2 SUMMARY OF GPACT CODE

Simulations were conducted with the GPACT numerical code (see Ref. 25 and 46). Physical models for propulsion applications must include turbulence, chemistry, and boundary-layer transition. Among these, turbulence is the pacing item and has the most bearing on the fidelity of the calculations. The current workhorse turbulence models used in engineering are of the one- and two-equation types. As shown in the following figure, multiple chemistry, phase flow, numeric and turbulence models are available in GPACT (Figure 8).

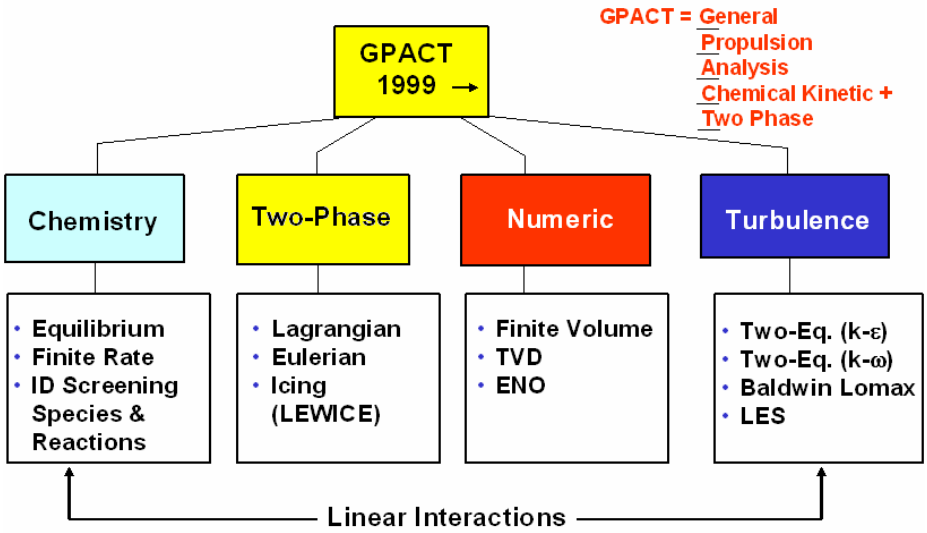

Figure 8: Scheme of CFD models in GPACT

A Reynolds-averaged Navier-Stokes (RANS) numerical approach is utilized for all computations, assuming steady state conditions and a two-equation *kw* turbulence model. Although RANS approaches are not as sufficiently accurate as LES or DNS for predicting many important reacting flows, they are less costly for some practical applications. In this research, the RANS approach becomes

very effective when identifying trends along several configurations and/or conducting parametric studies. Previous work on this very geometry has demonstrated the advantages of using LES.[22] A finite volume RANS is assumed with a Roe flux vector splitting, a 3rd-order in space and 2nd-order in time, upwind-bias. Solid boundaries are resolved by the y^+ wall function, with small dissipation values and no turbulence viscosity limits. The RANS CFD model includes a finite rate chemical kinetic mechanism as described in the following section, which is loosely coupled to the turbulence model.

To design a proper injector strategy and combustor chamber, fuel penetration, mixing, wall temperatures and heat loads must be predicted. Overall performance must also be computed to facilitate parametric design studies, as described herein. The complexity of the combustion process occurring in a fluid medium is attributable to two factors. First, the so-called "combustion process" actually encompasses many physical processes, with dissimilar temporal and spatial scales, that can be distinctively described or modeled. Secondly, all of these processes are usually strongly coupled together, making it difficult to simplify the problem. For these reasons, *GPACT* is an ideal tool for this research.

2.3 CHEMICAL MECHANISM

Most non-/premixed experiments conducted in supersonic combustors using hydrocarbon-air mixtures have considered Ethylene (or Ethene), due to its physical properties and experimental qualities. Thus, the fuel of choice for this study was narrowed down by the experimental component of these configurations

through collaboration with AFRL/RZ (Propulsion Directorate) to gaseous Ethylene. Its chemical compound has the formula C_2H_4, and it is the simplest alkene. Because it contains a carbon-carbon double bond, Ethylene is called an *Unsaturated-Hydrocarbon* or an *Olefin*.[23]

Ethylene is extremely important in industry, and is the most produced organic compound in the world. Used primarily as an intermediate in the manufacture of other chemicals, this particular hydrocarbon has a low operating temperature and pressure, making it super flammable. Since it is widely produced, its cost is lower than other, higher "Jet Propellant" (*JP*) type hydrocarbon fuels used in air-breathing engines, making it widely used in testing operations.[24] For additional information on Ethylene fuel please refer to Table 1.

Table 1: Ethylene information and properties.

Molecular formula	C_2H_4
Molar mass	28.05 g/mol
Density and phase	1.178 kg/m³ at 15 °C, gas
Solubility in water	3.5 mg/100 ml (17 °C)
Melting point/Boiling point	−169.2 °C/−103.7 °C
Critical point	282.4 K (9.2 °C) at 5.04 MPa (50 atm)
Std. enthalpy of formation $\Delta_f H°_{gas}$	+52.47 kJ/mol
Molar entropy $S°_{gas}$	219.32 $J \cdot K^{-1} \cdot mol^{-1}$

2.3.1 Species Screening

Detailed chemical kinetic descriptions of hydrocarbon-air mixture combustion may require the tracking of hundreds of chemical species and thousands of reaction steps. For the foreseeable future, CPU time and computer memory limitations will prohibit implementation of fully detailed descriptions of combustion chemistry into 3-D CFD simulations of practical devices. Issues such as ignition, flame stabilization, combustion factor, and pollutant formation are extremely important in the design of the next generation of air-breathing engines. Accurate simulation of these phenomena requires that significant chemical kinetic detail be retained in computer models. Within CFD simulations, the number of species tracked impacts the memory usage and CPU time. As a result, any available methods must be used to minimize this number while retaining essential features of the detailed chemistry. The number of species required for simulation of combustion processes depends on the nature of the phenomenon, and the type of information desired from the simulation. The chemical model selected for the research herein was validated and verified from a series of four reduced mechanisms. Each mechanism used the same 13 species. The first used 20 reactions, the second used a different 20, the third used 15, and the fourth used another 10 reactions. These reduced chemical models were compared to a much more detailed model (made up of 56 species and 168 step reactions) and experimental data at Arnold Engineering Developing Center (AEDC), Arnold – AFB, TN. [25, 26, 27] For this C_2H_4-air premixed case, the ignition delay (temperature

versus time) and X_{CO} (production/destruction of CO molar fraction over time) decay histogram are shown in Figure 9a,b.

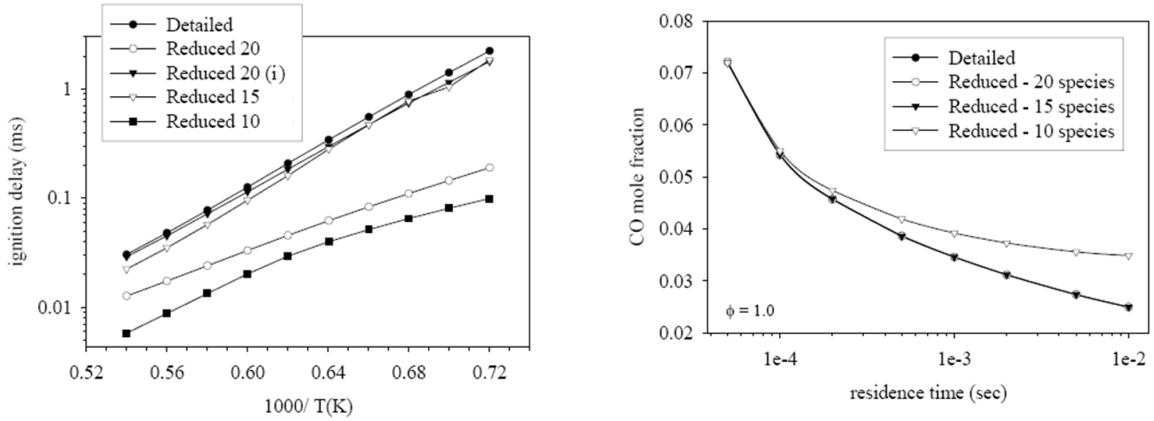

(a) Temperature ratio (b) X(CO)

Figure 9: Temperature and CO molar fraction versus time.

As concluded from this previous work, the reduced 13 species and 20 reaction mechanisms yield a very good agreement with a detailed model; see Figure 9a,b. This reduced model is then compared against two others found in the literature. The first model was created at Purdue University, and consists of 70 species and 463 elementary steps provided by Qin, et al. [28] It has hierarchical structures with H_2 and CO chemistry at the base, supplemented as needed by reaction channels of larger chemical species. While the development of this mechanism focused on propane (C_3H_8) combustion, the parameter optimization targets included experiments with additional fuels. Model predictions were eventually tested against CH_4, C_2H_4, C_2H_6, C_3H_4, C_3H_6, and C_3H_8 laminar flame speed and shock tube ignition delay data. The second chemical model is much

simpler than all the other models while providing a more quasi-equilibrium chemistry than a single global reaction, composed of 7 species with 3 step mechanisms.[29]

Two other competitive mechanisms were previously verified and evaluated against experimental data involving ignition delay, species profiles in shock-tube oxidation, laminar flame speeds, and burner stabilized flames: a mechanism developed at the University of Delaware which contains 75 species and 529 elementary reactions,[30] and another developed at The University of Southern California, featuring 111 species and 784 reactions.[31] These two extensive mechanisms were not considered herein, due to their costly computer demands. Further work is forthcoming on all of these mechanisms with additional experimental tests. Additional combustion data is required in order to provide more information on their validity for combustion of C_2H_4 mixtures of non-premixed cases.

Additional calculations were completed by an in-house code, an established Parabolized Navier-Stokes (PNS) that can compute 2 dimensional chemically reactive flowfields relatively fast of premixed mixtures. This PNS code with general finite-rate chemistry had previously been validated and verified for combustors and nozzle analyses and is being utilized as a nozzle design code for NASP applications.[32] A simple 2D grid was created (20x1,000 points) to obtain comparisons of temperature rise and species concentration. A generic two-dimensional constant area duct premixed C_2H_4-air test case was used as a baseline test case (see APPENDIX A).[33]

The uniform premixed C_2H_4-air mixture inflow conditions were: ER (equivalent ratio) = 1.0, static pressure, P = 101,325 Pa velocity, and initial static temperature of T = 1,000 K. The second (Mawid) mechanism cannot describe ignition delay properly due to a lack of initial radical production and thus did not compare well to the other two reaction models, given its 15-20% error. It appears that the intermediate species are crucial for a reasonable combustor simulation in this low-temperature range (~1,000 K). The results using the multiple-reaction model of PU with the PNS solutions and the AEDC calculations are quite a bit more accurate in this comparative numerical study, within 2% error. This leads to an important conclusion that the simpler, less computer resource-intensive one-dimensional kinetic model could be used for reaction screening and ignition delay studies, as opposed to the more complex 3D CFD coupled with such detailed chemical models. Although the PU model can be valid for a much wider range of temperature, pressure and stoichiometric values, the shorter AEDC mechanism showed a good agreement within 5% of the experimental data limited for temperature variations from 1,000 K to ~3,000 K and ER from 0.5 to 1.0 (close to the average values obtained from the preliminary research on the Baseline inlet configuration).

2.3.2 Finite Rate Chemistry Model

All combustion models can be divided into two main groups according to the assumptions on the reaction kinetics: equilibrium or finite rate. In equilibrium, one assumes the reactions to be infinitely fast or comparable to the

time scale of the species mixing process. This simple approach is not the one taken in this study. Historically, mixing of the species is the older approach, and it is still widely used today. It is simpler to solve than finite rate chemistry models, but often introduces errors into the solution since it assumes quasi-equilibrium.

In finite rate models, chemical kinetics solvers are based on the source term. This is the approach used in this study. The linearization procedure formulation is shown for this section. The research herein contains only five possible reaction types as expressed in Table 2. The specie denoted by M is an arbitrary third body reaction; all species are assumed to have equal third body efficiencies here.

Table 2: Reaction types and their chemical sources.

	Reactions	**Chemical source**
1	$A + B \Leftrightarrow C + D$	$\dot{W}_1 = K_F c_A c_B - K_b c_C c_D$
2	$A + B + M \Leftrightarrow C + M$	$\dot{W}_2 = K_F c_A c_B c_M - K_b c_C c_M$
3	$A + B \Leftrightarrow C + D + E$	$\dot{W}_3 = K_F c_A c_B - K_b c_C c_D c_E$
4	$A + B \Leftrightarrow C$	$\dot{W}_4 = K_F c_A c_B - K_b c_C / K_p$
5	$A + M \Leftrightarrow C + D + M$	$\dot{W}_5 = K_F c_A c_M - K_b c_C c_D c_M$

The variables k_f and k_b are the forward and backward chemical coefficients respectively and they are determined from the Gibbs free energy curve fits in

GPACT's data bank. These rate coefficient types are calculated by Equation 1. E_a is the activation energy or the amount of energy required to make the reaction start and carry on spontaneously. Higher activation energy implies that the reactants need more energy to start than a reaction with lower activation energy. The variables A and b are empirical constants.[34]

Equation 1: Arrhenius

$$k_{f,b} = AT^b \exp\left(E_a / R_u T\right)$$

From a general chemical reaction for n different species (where i = 1…n)

Equation 2: Generalized chemical reaction

$$\sum_{i=1}^{n} \nu_i' x_i \Leftrightarrow \sum_{i=1}^{n} \nu_i'' x_i$$

The stoichiometric mole number of the reactants and products are ν_i' and ν_i'' respectively. From the Law of Mass Action, the rate of change of species by the forward and backward or reverse reactions is given in Equation 3 and Equation 4, respectively. Consequently, Equation 5 shows the net reaction rate for each of the species involved.

Equation 3: Forward reaction rate

$$\frac{\partial[x_i]}{\partial t} = (\nu_i'' - \nu_i')k_f \prod_{i=1}^{n} [x_i]^{\nu_i'}$$

Equation 4: Reverse reaction rate

$$\frac{\partial[x_i]}{\partial t} = -(\nu_i'' - \nu_i')k_b \prod_{i=1}^{n} [x_i]^{\nu_i''}$$

Equation 5: Net specie reaction rate of production/destruction

$$\frac{\partial[x_i]}{\partial t} = (\nu_i'' - \nu_i')\left(k_f \prod_{i=1}^{n} [x_i]^{\nu_i'} - k_b \prod_{i=1}^{n} [x_i]^{\nu_i''} \right)$$

All chemically reacting computations are modeled using a two-step reversible finite-rate, 13 gaseous species (C_2H_4, C_2H_2, CO_2, CO, OH, O_2, O, H_2, H, H_2O, NO, N and N_2), Ethylene chemistry model (with 20 reactions pertinent to Ethylene-Oxygen and Nitrogen based combustion products) and Gordon/McBride thermodynamic curve fits.[35 and 36] The chemical mechanism parameters for the rate coefficient were taken from Ref. 37 (for Reactions: 14-16) and 38 (for Reactions: 1-13 and 17-20). Please refer to Appendix B for the full 3-D Unsteady Navier-Stokes equation derivation, which includes a 13 species transport equation (Equation 66). Table 3 shows the 20 reaction set for the 13 species.

Table 3: Chemical reactions of the reduced mechanism (Ethylene-Air mixture)

React. 1	$C_2H_4 \leftrightarrow C_2H_2 + H_2$	React. 11	$H + OH + M \leftrightarrow H_2O + M$
React. 2	$C_2H_2 + O_2 \leftrightarrow 2CO + H_2$	React. 12	$H + O + M \leftrightarrow OH + M$
React. 3	$CO + O + M \leftrightarrow CO_2 + M$	React. 13	$2O + M \leftrightarrow O_2 + M$
React. 4	$CO + O_2 \leftrightarrow CO_2 + O$	React. 14	$N + NO \leftrightarrow N_2 + O$
React. 5	$CO + OH \leftrightarrow CO_2 + H$	React. 15	$N + O_2 \leftrightarrow NO + O$
React. 6	$OH + H_2 \leftrightarrow H_2O + H$	React. 16	$N + OH \leftrightarrow NO + H$
React. 7	$O + OH \leftrightarrow O_2 + H$	React. 17	$H_2 + O_2 \leftrightarrow 2OH$
React. 8	$O + H_2 \leftrightarrow OH + H$	React. 18	$2H + H_2 \leftrightarrow 2H_2$
React. 9	$2OH \leftrightarrow O + H_2O$	React. 19	$2H + H_2O \leftrightarrow H_2 + H_2O$
React. 10	$2H + M \leftrightarrow H_2 + M$	React. 20	$2H + CO_2 \leftrightarrow H_2 + CO_2$

2.4 TURBULENT MODELS

In a scramjet combustor, a major consideration is the use of sufficient grid resolution to capture the three-dimensional viscous regions and jet interactions (e.g., mixing layers and wakes) near the wall and in the core flow. This issue of grid resolution works in concert with the important turbulence modeling issues: determining the rate of mixing in flows with strong swirl; matching the reduced spreading rate seen in supersonic mixing layers such as those used for film cooling; and modeling the injector base pressurization process. The effect of turbulence on the chemical kinetic source term may be a consideration primarily at low scramjet Mach numbers, where lower inlet exit static temperatures and

higher turbulence intensities exist. Higher-order phenomenological models such as algebraic stress and full Reynolds stress models are yet to be demonstrated conclusively on realistic 3D reacting flow problems. Thus, additional analysis on hypersonic air-breathing engines is needed. Additional work herein explores the unsteadiness and other key physical elements of the most promising combustor prototype via URANS and LES.

2.4.1 RANS Model

This body of research will generally limit such assumptions with a *kw*-Wilcox (see Ref. 60) model to follow trend analysis and to identify the top scramjet system design from the study of inlets and combustors. This is the second most widely used two-equation model that has been developed for over two decades. Previous work in supersonic combustors showed a greater agreement when using this turbulent model (see Ref. 22, 26 and 62). Although the treatment of non-turbulent free-stream boundaries is problematic, this turbulent model is superior both in its treatment of the viscous near-wall region, and its accounting for the effects of stream-wise pressure gradients.[39]

In turbulent flows, Favre averaging is often used, to reduce the scales, and the mass fraction transport equation is transformed to:

Equation 6: Mass fraction transport.

$$\frac{\partial \overline{\rho}\tilde{Y}_k}{\partial t} + \frac{\partial \overline{\rho u}_j \tilde{Y}_k}{\partial x_j} = \frac{\partial}{\partial x_j}\left(\overline{\rho D_k \frac{\partial Y_k}{\partial x_j}} - \overline{\rho}\left(\widetilde{u_i'' Y_k''} \right) \right) + \overline{\dot{w}}_k$$

$$where: \quad \widetilde{u_i'' Y_k''} = turbulent - fluxes \quad and \quad \overline{\dot{w}_k} = reaction - terms$$

The mean passive scalar turbulent transport equation is,

Equation 7: Mean passive scalar turbulent transport.

$$\frac{\partial \overline{\rho}\tilde{Z}}{\partial t} + \frac{\partial \overline{\rho u}_j \tilde{Z}}{\partial x_j} = \frac{\partial}{\partial x_j}\left(\overline{\rho D_k \frac{\partial Z}{\partial x_j}} - \overline{\rho}\, \widetilde{u_i'' Z''} \right)$$

In addition to the mean passive scalar equation, an equation for the Favre variance is often employed.

Equation 8: Favre variance.

$$\frac{\partial \overline{\rho}\, \widetilde{Z''^2}}{\partial t} + \frac{\partial \overline{\rho}\tilde{u}_j\, \widetilde{Z''^2}}{\partial x_j} = \frac{\partial}{\partial x_j}\left(\overline{\rho}\, \widetilde{u_i'' Z''} \right) - 2\overline{\rho}\, \widetilde{u_i'' Z''} - \overline{\rho}\tilde{\chi}$$

$$where, \quad \widetilde{Z''^2} = Favre's$$

The mean scalar dissipation rate term and the variance diffusion fluxes need to be modeled as follows.

Equation 9: Mean scalar dissipation rate term.

$$\tilde{\chi} = 2D\left|\frac{\partial \tilde{Z}''}{\partial x_j}\right|^2$$

Note that all the validation cases were predicated upon a *k-w* turbulence model. Although the results suggest that such models are capable of reproducing the larger structures observed in the mean flow, there remain significant uncertainties in fine scale features including unsteadiness and heat transfer rates. For cases in which finite-rate chemistry was invoked, the species interactions are treated as laminar, thus the key performance of combustion is not realistically captured. The ignition process under these steady state assumptions cannot be compared since the chemical time scales must be directly coupled to the turbulent effects, with the exception of the unsteady cases that use URANS and LES.

2.4.2 LES Model

LES and other modeling approaches capture large scale dynamic motions essential to predicting emissions and combustion instabilities. This approach shows promise for accurately capturing the large-scale unsteady structures in the combustor flow field region. This method can potentially provide accurate unsteady statistics as well as time-averaged quantities critical to simulation of the transport processes important for predicting flame anchoring and blowout limits. Because of their reduced CPU requirements, CFD tools using Reynolds Averaged Navier-Stokes (RANS) equations are increasingly relied upon for use in detailed

engine component design, and will likely remain the workhorse design method for years to come. In contrast, LES modeling requires large computational resources, which limits practical parametric studies and applications of large, more realistic configurations. Further development of the LES model, however, is needed to provide a higher computational factor while maintaining its desired accuracy. Their high-fidelity models can be utilized for simulation of reacting and two-phase flow environments, where the coupled turbulence is imperative in non-premixed situations. LES can capture the effects of small scale turbulence on droplet dispersion, and turbulence modulation in the presence of both vaporizing and non-vaporizing droplets. Some researchers are already capable of predicting the flow in some practical engine components, including all the primary and secondary flows, chemically reactive flow conditions ranging from low-speed subsonic, to transonic and supersonic in complex geometry.[40, 41, 42]

The LES general conservation equations for mass, momentum, energy, and chemical species are filtered to obtain equations for the large-scale (energy containing) variables needed for LES. The filtered equations contain unknown terms such as a subgrid turbulence stress tensor and a subgrid reaction rate that must be modeled. Unlike typical steady-state turbulence models, the subgrid models for LES are a function of the local grid (or filter) size.[43] The subgrid turbulence utilized herein was approximated with the Localized Dynamic Subgrid Kinetic energy Model (LDKM).[44, 45] This kinetic energy subgrid-scale model has recently been integrated into GPACT to closure the kinetic chemistry to the turbulence. Within the LDKM, the eddy viscosity is computed as a function of

the local grid size (Δ) and the subgrid turbulent kinetic energy (k_{sgs}): $v_t = C_t \Delta k_{sgs}^{0.5}$. A transport equation for the k_{sgs} is solved and requires terms obtained from velocity gradients at a test filter level. The test filter width is around twice the grid filter width. The subgrid chemistry is described with an assumed probability density function (PDF) method. The PDF is a 2-dimensional function of the mixture fraction and progress variable (fuel fraction), where these variables are assumed to be independent of each other. Filtered transport equations for the mean and variance of the mixture fraction and reaction progress are solved. The subgrid reaction rate is obtained by integrating the instantaneous fuel reaction rate over the 2-D PDF. Source terms in the transport equations for the mixture fraction and progress variable variance are obtained from the subgrid turbulent kinetic energy and dissipation rate. In contrast to the RANS assumption, where the species interactions are treated as laminar, the LES assumes the species and turbulent interactions.

In the LES, the flow variables are decomposed into the resolved (super-grid scale) and unresolved (sub-grid scale) components by a spatial filtering operation, such as:

Equation 10: LES flow variables decomposition.

$$f = \bar{f} + f'' \quad where: \quad \bar{f} = resolved \quad and \quad f'' = unresolved$$

Equation 11: Subgrid-scale kinetic energy.

$$k_{sgs} = \frac{1}{2}\left(\bar{u_k}^2 - \bar{u}_k^{\,2} \right)$$

The subgrid-scale stress and transport equations for the subgrid-scale kinetic energy are then:

Equation 12: Subgrid-scale stress.

$$\tau_{ij} - \frac{2}{3} k_{sgs} \delta_{ij} = -2 C_k {k_{sgs}}^{1/2} \Delta \bar{S}_{ij}$$

Equation 13: Subgrid-scale transport.

$$\frac{\partial \bar{k}_{sgs}}{\partial t} + \frac{\partial \bar{u}_j \bar{k}_{sgs}}{\partial x_j} = -\tau_{ij} \frac{\partial \bar{u}_i}{\partial x_j} - C_\varepsilon \frac{{k_{sgs}}^{3/2}}{\Delta} + \frac{\partial}{\partial x_j}\left(\frac{\mu_t}{\sigma_k} \frac{\partial \bar{k}_{sgs}}{\partial x_j} \right)$$

The subgrid-scale eddy viscosity is computed using k_{sgs} as shown in Equation 14.

Equation 14: Subgrid-scale eddy viscosity.

$$\mu_t = C_k {k_{sgs}}^{1/2} \Delta$$

The LES approach for reactive flows introduces equations for the filtered species mass fractions within the compressible flow field. Similar to RANS (Equation 6), but using Favre filtering instead of Favre averaging, the filtered mass fraction transport equation is:

Equation 15: Favre filtering mass fraction transport.

$$\frac{\partial \overline{\rho} \tilde{Y}_k}{\partial t} + \frac{\partial \overline{\rho u}_j \tilde{Y}_k}{\partial x_j} = \frac{\partial}{\partial x_j}\left(\overline{\rho D_k \frac{\partial Y_k}{\partial x_j}} - J_j \right) + \overline{\dot{w}}_k$$

J_j is the transport of subgrid fluctuations of mass fraction to be modeled.

Equation 16: Transport of subgrid fluctuations of mass fraction.

$$J_j = \tilde{u_j Y_k} - \tilde{u}_j \tilde{Y}_k$$

Fluctuations of diffusion coefficients are often ignored and their contributions are assumed to be much smaller than the apparent turbulent diffusion due to the transport of subgrid fluctuations. The first term on the right hand side is then:

Equation 17: Turbulent diffusion due to transport of subgrid fluctuations.

$$\frac{\partial}{\partial x_j}\left(\overline{\rho D_k \frac{\partial Y_k}{\partial x_j}} \right) \approx \frac{\partial}{\partial x_j}\left(\overline{\rho} D_k \frac{\partial \tilde{Y}_k}{\partial x_j} \right)$$

2.5 CODE VALIDATION & VERIFICATION

Before using any CFD model in a design or analysis environment, confidence in the results obtained from the models above must be established. This is accomplished by performing a series of validation exercises, where the results of the calculations are compared with well-characterized experimental

data. The objective is to determine the accuracy of the physical and numerical approximations included in the models and to determine whether model modifications are needed to improve the reliability of the calculated results or to improve the numerical factor of the calculation method. Validation not only guards against source coding errors but also provides estimates of the effect of numerical parameters on the computed solution. Several steps have been identified to assist validation and verification of complex CFD models found in GPACT. These steps can be described as follows (see Ref. 25 and 46):

1. Define the critical performance parameter information and primary physical phenomenologies affecting these parameters and establish the corresponding CFD modeling requirements.
2. Establish the appropriate governing equations and the corresponding physical modeling requirements.
3. Identify and acquire appropriate, well-characterized benchmark data to establish a standardized database to validate computer models.
4. Perform computations for the exact experimental conditions and determine the model sensitivity to the numerical and modeling assumptions
5. Document the validation effort results to the extent necessary to provide other CFD model users with knowledge of the model's capabilities, including the overall accuracy of the calculated results

and the sensitivity of the solution to internal parameters such as numerical damping and computational grid refinement.

Some validation cases are selected to conduct a grid analysis and comparison of related canonical geometries in this research for the Inlets and Combustors section analysis. For additional validations and verifications of the CFD tool utilized herein, an extensive database on GPACT has been extended during the last two decades by Ebrahimi et al. [46, 47, 48, 49] In addition, previous validation of GPACT has been done on fully-coupled, three-dimensional flows with finite-rate chemistry (Ref. 25). The work herein was completed with the utilization of HPC (High Performance Computing) computer resources awarded under a 3-year challenge award in collaboration with the research and development branch of the propulsion directorate of AFRL.[50, 51, 52] The computational resources were the Hawk system at the AFRL-DSRC (a Department of Defense shared resource center). Hawk is a SGI-Altix 4700, dual core system that has a total of 9,216 cores divided into 18 nodes with 512 cores each.

Subsequent subsections in this chapter detail four different validation cases. All of the cases that solve for RANS use the Roe's fluxes scheme with a *kw*-Wilcox turbulence model. The wall functions were not invoked in this approach. The turbulent Prandlt and Schmidt numbers were set at 0.75 and 0.5 for all simulations respectively. All the steady-state assumption cases, like these validation solutions, were advanced until the L2 norm of the residual was reduced

by at least six orders of magnitude from its initial values. To minimize truncating errors, the MUSCL parameter k was chosen to be 0.3333, together with a min-mod limiter to ensure total variation diminishing. The laminar transport properties for the viscosity and conductivity use the Sutherland model. The CFL stability constrained was ramped from 1-5 in most cases for every time the solution was saved ~1k iterations.

2.5.1 Analysis of Double Fin Turbulent Interaction at Mach 4

This research investigates two innovative hypersonic inlet prototypes prior to their experimental analysis. A canonical configuration of the baseline configuration is chosen to validate the CFD tool, as well as help select the appropriate grid and turbulence model to analyze the properties of the internal flow path and distortion effects caused by shock-boundary layer and shock-shock interactions. To further understand their interaction near the wall throughout a supersonic channel, a case is explored as explained by Gaitonde et al. (Ref. 53 and 54).

This generic configuration is selected because it involves shock-shock interaction flow phenomena similar to that occurring in conventional rectangular inlets. Figure 11 shows a canonical swept interaction problem comprised of two sharp fins mounted at an angle of attack on a plate. The flow parameters are chosen to duplicate experimental data.[55 and 56] The freestream air conditions are Mach number of 4, Re=80×10^6/m, Ps =1.5 MPa, and Ts=295 K. For this case the simulation was conducted with a perfect gas assumption, utilizing three different meshes. These grids, as all others herein, were created using Gridgen V5

software. The points on the lines/connectors use a *Tanh* function for their distributions of $1x10^{-4}$ towards the walls and edges of the fins. The first grid was coarse and was created with 2.6 M points; the second medium size grid was made with 3.5 M points; and the third much finer grid has around 4.4 M points. All the grids are set to be structured with a high density towards the solid boundaries to yield a y^+~0.8. Unlike the rest of the validation cases, the CFL number for this particular case was ramped up from 0.1 to 1.0. The desired L2 norm of $1x10^{-6}$ was achieved for the three meshes within 2.1, 3.2 and 4.76 hours, respectively, using a total of 64 processors. The frontal/inflow *x*-plane is plotted in for the three meshes (from left to right, respectively) and the entire fine grid configuration (Figure 10a and b, respectively). In addition, Figure 10c shows the normalized velocity profile from the wall to the boundary layer edge between the three grids. This height is approximately about 0.5 mm from the floor and within ~31 points for the fine mesh. The comparison is made at a center surface point right flush with the leading edge of the double fin configuration, prior to the separation shown later in this section. Although the grids differed from each other by 20% fewer points (between fine, medium and coarse), the results have very small differences in their profiles.

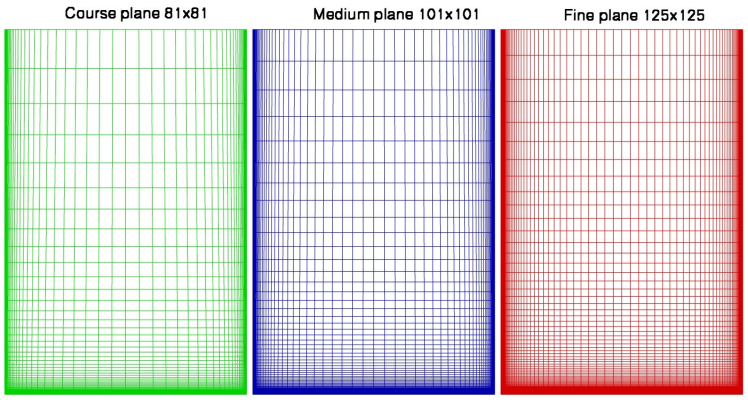

(a) Coarse, medium and fine grid comparison at inflow/x-plane

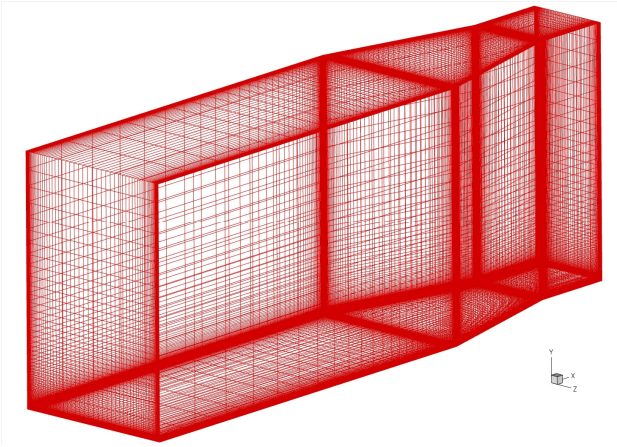

(b) Full grid configuration

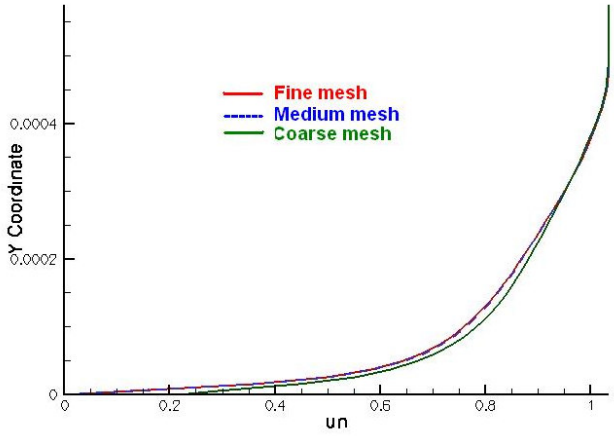

(c) Normalized velocity near the wall at center/leading edge of fins

Figure 10: Double fin configuration mesh and velocity profile comparison.

Figure 11 shows the double fin configuration with its presumed shock structure, cross flow interactions from the center streamlines and normalized Pitot pressure contours comparing the experiment to CFD results, respectively.

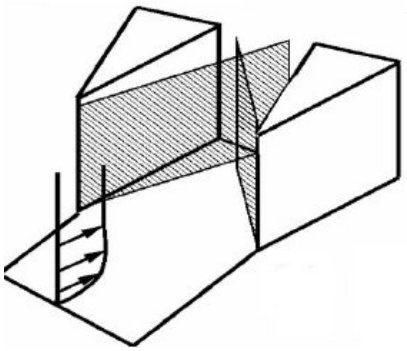

(a) Geometrical setup

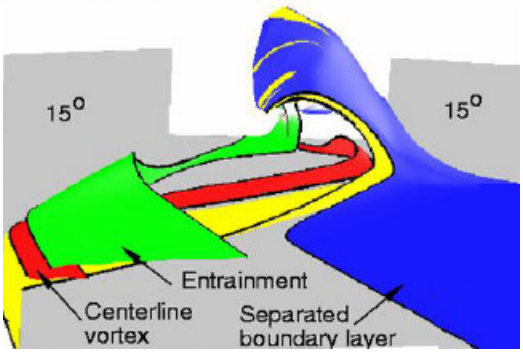

(b) Cross flow patterns

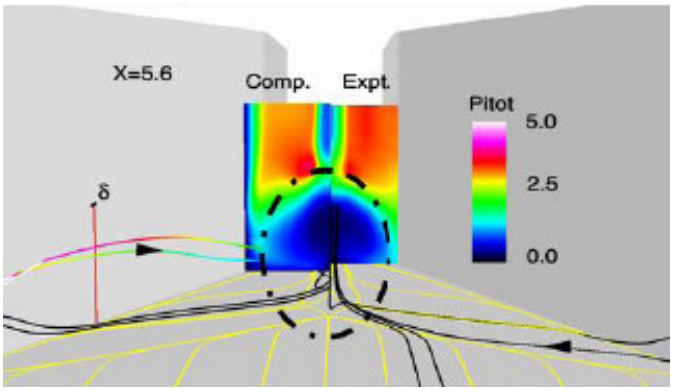

(c) Pitot pressure comparison

Figure 11: Genesis of characteristic low total pressure pattern through swept viscous/inviscid interactions.

As pointed out in Section 1.2, these viscous/inviscid interactions yield large flow separation in conventional hypersonic inlet designs, and a similar dynamic is established in the inlets under study. As explained by Gaitonde et al.,

the main feature is the central low energy region at the bottom (see Ref. 53). Comparing the experimental data to the simulation demonstrates that this essentially inviscid rotational feature is captured accurately. Although the CFD solution is not a mirror image of the experimental data, this is largely due to the fact that the experimental data do not extend to the surface, whereas the CFD solution does (see Figure 12c). The associated flowfield structure in Figure 12b shows that the shock-induced adverse pressure rise separates the incoming boundary layer (shown in blue) from the surface. The entrained fluid from the sides attaches near the swept interaction generator and occupies the region underneath the center line vortex. The separated boundary layer does not reattach, but rather warps and the limiting ribbon becomes arch-like. As a result, the ejected low-speed fluid near the surface yields a low total pressure region bounded by the entrained fluid from the sidewalls.

Figure 12a shows an iso-surface of low velocity that depicts the flow starting to lift from the sidewalls toward the center bottom of the channel, separating and shaping into a horseshoe vortex pattern downstream. Similarly, Figure 12b-c shows side and upper views of the shock interaction and pressure surface as the streamlines intermingle at the core, respectively. Note that the incoming boundary layer from the bottom of the surface (shown in blue) and the entrained fluid from the sidewalls (shown in red) are kept color coded throughout Chapter 3.

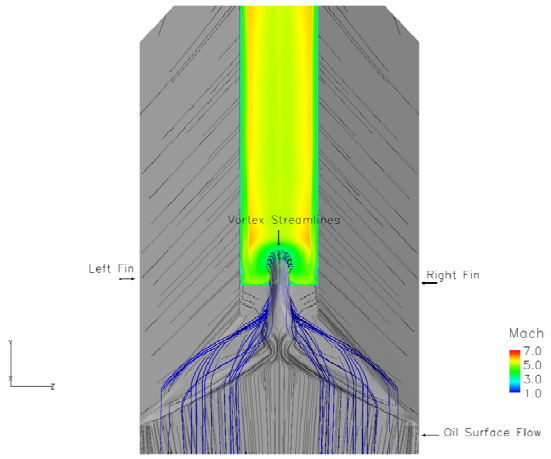

(a) Downstream view at exit plane

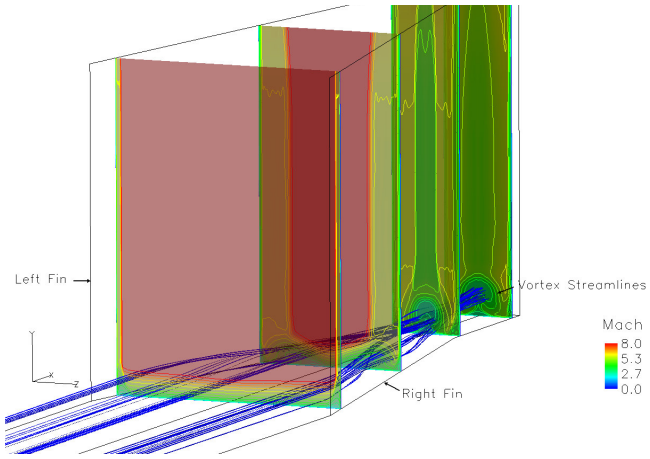

(b) Iso-view of Mach Number *x*-planes

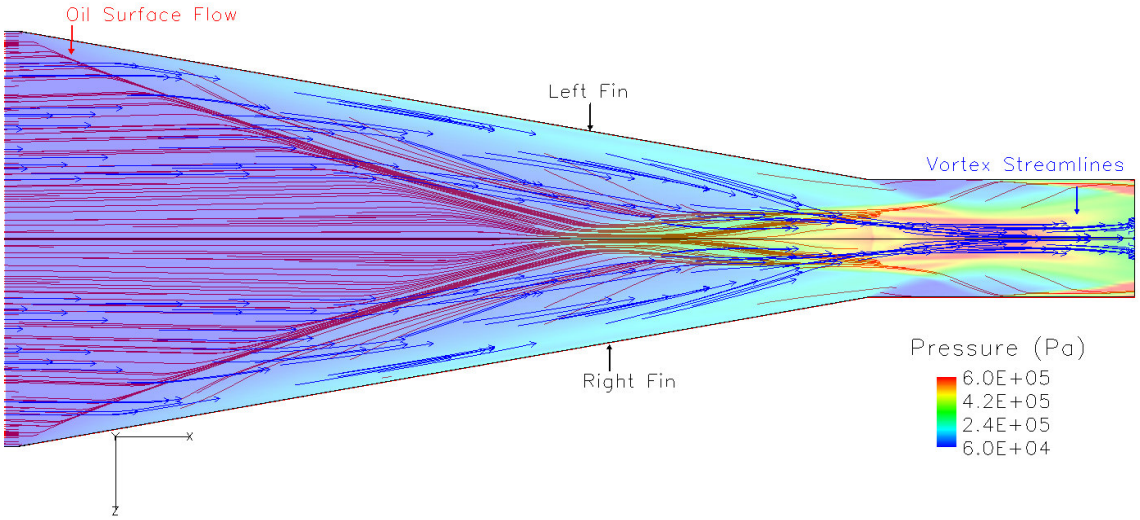

(c) Top view near the surface *y*-plane, Pressure (Pa) and streamlines

Figure 12: Double fin interaction: iso-surface, surface oil, streamlines and contours.

2.5.2 Cavity-Based Flame Holders

For validation of this work, two cavity configurations were selected from available experiments, each with an *L/D* ratio equal to 3.[57] These experiments were conducted with a Mach 3 facility nozzle operated at a stagnation pressure of

0.69 MPa and a stagnation temperature of 300 K for both experiments and computations discussed in the following sections. Both of the flame-holder models feature similar geometry: depth (D=9 mm) and length (L=27 mm). The first case shows a closed cavity and the second is an open, 30º ramped cavity configuration. A 2-D structured grid with about 50k points clustered near the walls was implemented on both configurations. The achieved y^+ on these cases was near 1. Again, GPACT solver was used with the same setting as before and the computational domain is divided into two 2-D structure grids. The walls are simulated with adiabatic assumption and the exit/farfield plane uses a first order extrapolation. The first and second meshes have around 54k points equally packed towards the walls, exactly as in the previous finer grid, which also yields a y^+ of ~1.0. Figure 13 shows the structure meshes for both cavity cases. The grid is made of two structure blocks: 1) the first zone of the channel has 121x321 points, and 2) second zone represents cavity with 111x141 points. The first zone is partitioned in 41 points before the step, 141 points between the two edges of the cavity and 141 points downstream from the cavity. The spacing variation values were set at $1x10^{-5}$, with a selected *Tanh* distribution function for all the connectors. This grid selection clustered the points near the walls as they are angled downstream from the edges of the cavity (leading and trailing) to best follow the compression/expansion waves found from the experimental Shadowgraphs and Schlierent photographs (see Fig. 5 in Ref. 57). For both cases (open and closed cavities), the flow condition at the 1st domain (channel) was initialized by the freestream values, while the 2nd domain (cavity) is assumed to

have the same properties as of the freestream except that the velocity is initialized at 0.1m/s. The solutions for these cases were attained within ~1.1 hours using 32 processors.

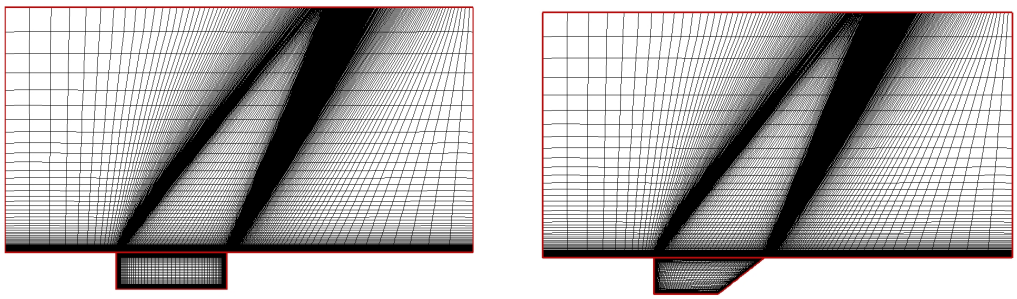

(a) Closed cavity (b) Open (30^o) cavity

Figure 13: The closed and open cavity grids.

Figure 14a,b shows Mach number contours (top) and the normalized surface pressure comparison between the measured and computational calculated configuration (bottom), respectively. The normalized pressure at the wall is represented versus the distance from the leading edge to the floor and to the trailing edge of the cavity as in terms of D, thus the total wall distance is 5D. Although, the model was two-dimensionally simplified and an imposed laminar boundary layer at the inflow plane was described, the trends were modeled reasonably well within 5% difference from the experiment. These results suggested that the rectangular cavity geometries were properly characterized by GPACT. The calculations, however, did not show any signs of large-scale unsteadiness. This phenomenon is not uncommon when standard eddy-viscosity-based turbulence models are employed for flows over a cavity. Although a

steady-state assumption was predicted for the surface pressure in these rectangular geometries, the cavity flow structure is not steady in nature.

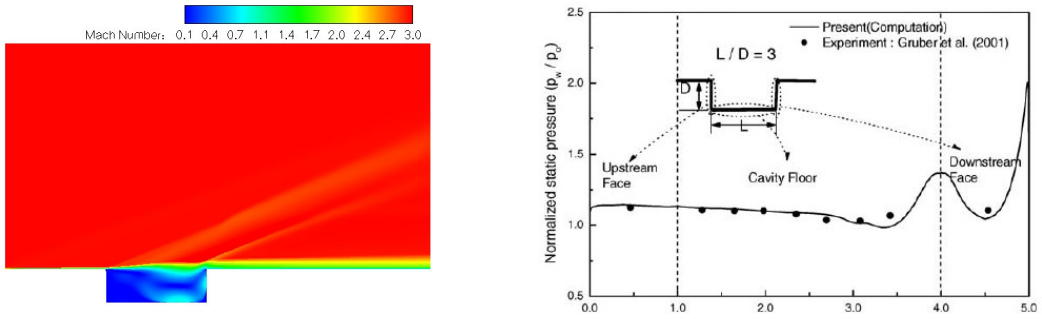

(a) Closed cavity

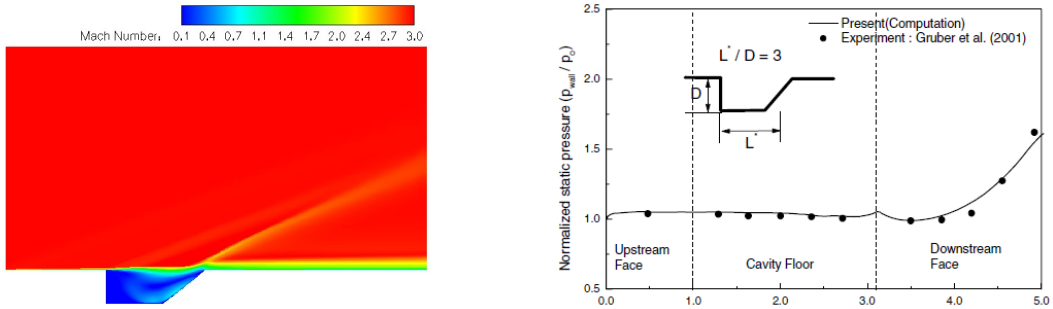

(b) Open (30^{o}) cavity

Figure 14: GPACT validations for two different cavity based flame-holders.

2.5.3 Supersonic Flow over an Open Ramp Cavity

A similar case with a supersonic flow over a ramped cavity was conducted to evaluate the effective reattachment of a free shear layer in a supersonic turbulent flow.[58] The GPACT code is validated against data collected from a ramped cavity experiment involving a perfect-gas working fluid. The ramped cavity experiment provides a combination test case to evaluate the numerical tool in a similar flowpath of supersonic flame holders as those studied in this research

(see Ref. 98). The geometry consists of a rearward-facing step in combination with a downstream compression corner. The freestream Mach number is 2.92 and the velocity boundary profile is forced to the inflow plane (i_{min}). The step height is 1.0 in (25.4 mm). The velocity profile is developed over a 9-in (228.6 mm) straight section, and the compression corner is 2.4263 in (61.628 mm) downstream of the step at an angle of 19.9687 degrees.

For this case, two 2-D structure grids were implemented and initialized by the freestream values. The walls are simulated with adiabatic assumption and the exit/farfield plane uses a first order extrapolation. The first and second meshes have around 50k points and different density near the solid walls, yielding a y^+ of 1.0 and 1.5 respectively. Figure 15 shows the 1st structure mesh as an example. The grid is made of two structure blocks: 1) the first is upstream of the step with 61x91 pts, and 2) second block includes from the step floor the farfield with 231x201 pts, of which 111x111 pts were positioned inside the cavity.

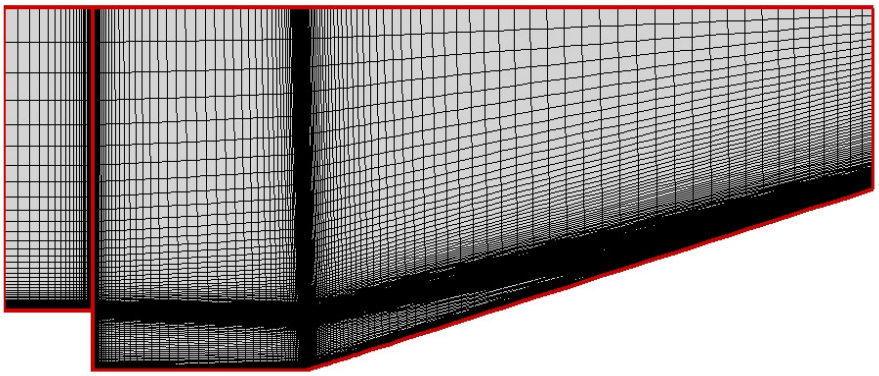

Figure 15: Numerical grid of a 20° ramped cavity validation case (1st mesh).

The computed Mach number for the first mesh and streamline flow field is presented in Figure 16a. The figure gives evidence of the free shear layer that detaches across the cavity and towards the ramp downstream, resulting in an oblique shock. The streamlines captured inside the cavity show a sturdy recirculation region that collapses by the incline. The normalized surface static-pressure distribution predicted by GPACT using two different meshes is compared to the experimental pressure data in Figure 16b. Both meshes yield a convergence L2 norm around ~1.4 hours using 32 processors.

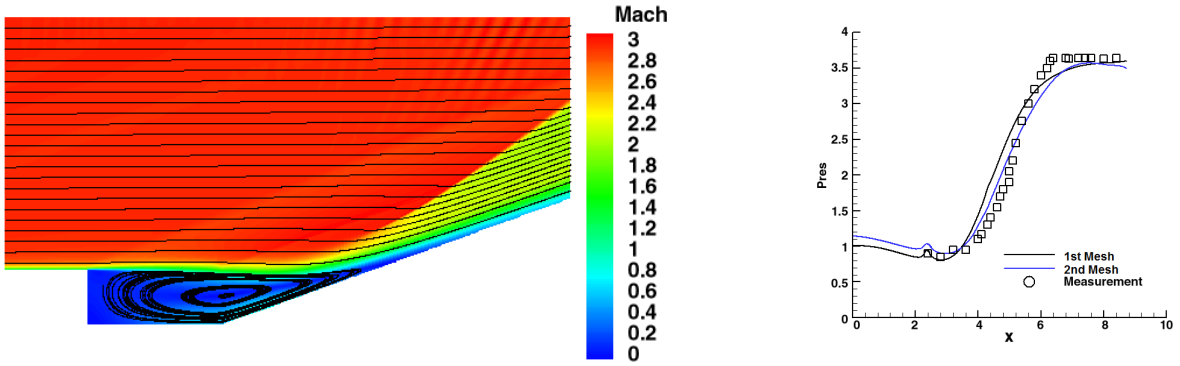

(a) Mach number and streamlines

(b) Normalized wall pressure

Figure 16: 20° ramped cavity validation case.

Profiles of the horizontal component of the velocity (normalized) versus the vertical distance from the edge of the step (mm) are presented in Figure 17. The numerical results are compared with the experimental measurements at three stations downstream from the cavity step. Results from both grids exhibit a reasonable agreement, within 5% of the experimental data of the boundary layer interaction over the cavity and downstream on the ramp. Although the grids are

clustered differently (the first results in a higher number of points within the step region than the second), the trends are similarly captured by both meshes. For most of the compared stations, the first mesh seems to over predict the velocity profile, while the second mesh underestimates such results compared to the measurements. This effect is an uncertainty that slightly displaces the shock and the shear layer separation. The separation interacts downstream from the step onto the ramp, resulting in a very dynamic system.

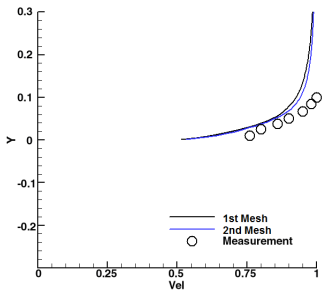

(a) x-station=25.4 mm

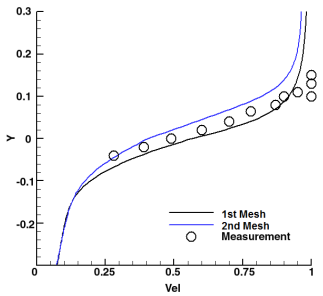

(b) x-station=38.1 mm

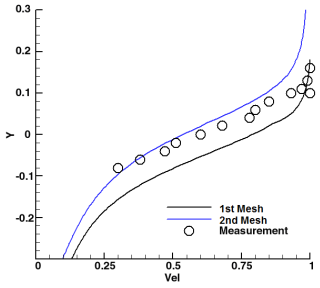

(c) x-station=63.5 mm

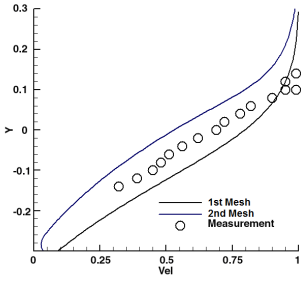

(d) x-station=88.9 mm

Figure 17: Experimental comparison to GPACT.

2.5.4 Stepped Combustor with Double Jet Interaction

A literature survey was performed to identify experimental measurement programs with sufficient documentation of the geometry and flow conditions required for CFD code validation. Detailed measurements were extracted from the documents and archived to establish a standard validation database. The selected experiments include a range from simple flow simulations to more complex conditions representative of subsonic to hypersonic combustor flow fields.

The staged normal injection of two N_2 jets located behind a rearward-facing step into a Mach number of 2 freestream airflow was validated as well; this was experimentally investigated by McDaniel.[59] The geometry consists of a channel with a 3.18-mm step height and two 1.93-mm injectors positioned on the channel centerline at 3 and 7 step-heights, respectively, downstream of the step. A stagnation temperature of 300 K and pressure of 274 KPa specifies the main freestream flow conditions used to initialize the entire computational domain. Two 2-D structure grids with 0.08 M and 0.16 M points were computed and compared to the experiment. The CFL used on both of these cases was reduced and set to increase from 0.1 to 1.0. The coarse and fine grids reach their L2 norm convergence with similar results around 1.7 and 2.1 hours using 64 processors, respectively.

Figure 18: Mach number contours, z-plane.

Comparisons of the experimental data with computed normalized static pressure and streamwise velocity profiles at stations *X/D* = 0, 3.0, 6.0 and 6.6 are shown in Figure 19a-e, respectively. As shown below, GPACT matches quite well to the measured data at every station for both meshes. As seen in the previous case, the trends are similar for both meshes. In all of the selected stations, the coarser mesh over predicts the normalized velocity profile compared to the finer mesh.

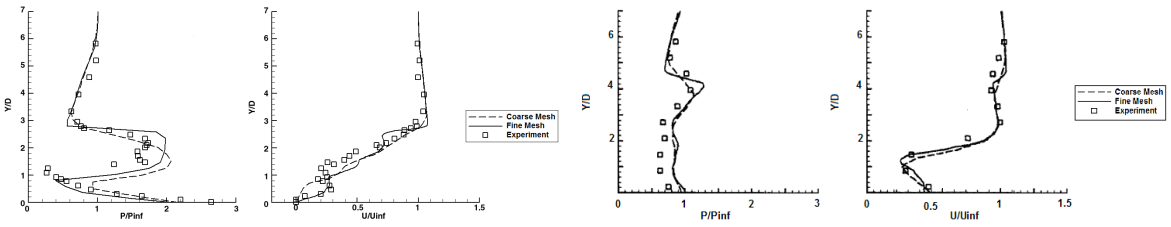

(a) *x/D*=0.0 (b) *x/D*=3.0

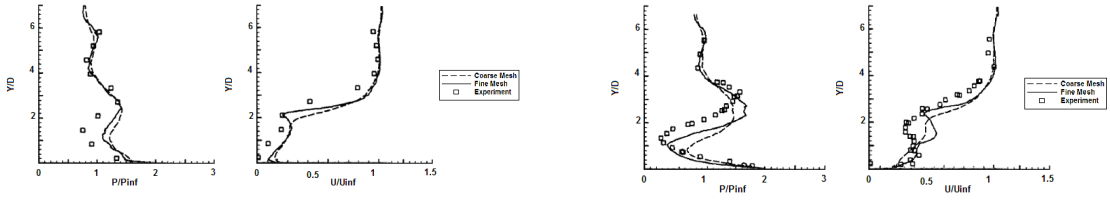

(c) *x/D*=6.0 (d) *x/D*=6.6

Figure 19: Normalized Pressure and U-velocity ratio profiles.

In conclusion, from the different validations conducted in this chapter, the finer grid demonstrated a better agreement with the experimental measurements. Thus, all other grids in this research are generated with the finer grid to yield a higher fidelity and agreement to future ground and flight tests.

CHAPTER 3: INLET ANALYSIS

3.1 INLET ANALYSIS OVERVIEW

The free-stream conditions chosen for this study are Mach 6, $Re=3.75\times10^6/m$, $P_1=1{,}978N/m^2$ and $T_1=222.2K$. These flow conditions represent a typical flight trajectory of interest for the inlets investigated herein. Since the temperature is relatively low in the nozzle (less than *1,000K*), chemical reactions of air were not considered when analyzing the inlets. Two different cases are examined for each of the three inlet configurations. The first case provides an understanding of the internal flow without viscous effects and describes the planar shocks and shock-shock interactions in the designs. The second case includes viscous effects calculated using a Roe flux-difference scheme. Although both sets of cases utilized the same Roe scheme, the viscous cases were employed together with the Mid-Mod limiter, and the fine-scale effects of turbulence were simulated with a *k-w (Wilcox)* model.[60] After these inlets were computed, their profiles at the exit plane were then used downstream at the entrance to the combustor.

3.1.1 Baseline Inlet Analysis

Figure 20 shows the computational domain; a structured mesh is employed to analyze the region of interest (for more details, please see Figure 1). The Baseline scramjet is symmetric about the *xz*-plane, and thus only half of the scramjet is computed using a structured mesh. The grid indices (i, j and k) are

generally oriented in the streamwise (x), vertical (y) and spanwise (z) axes respectively.

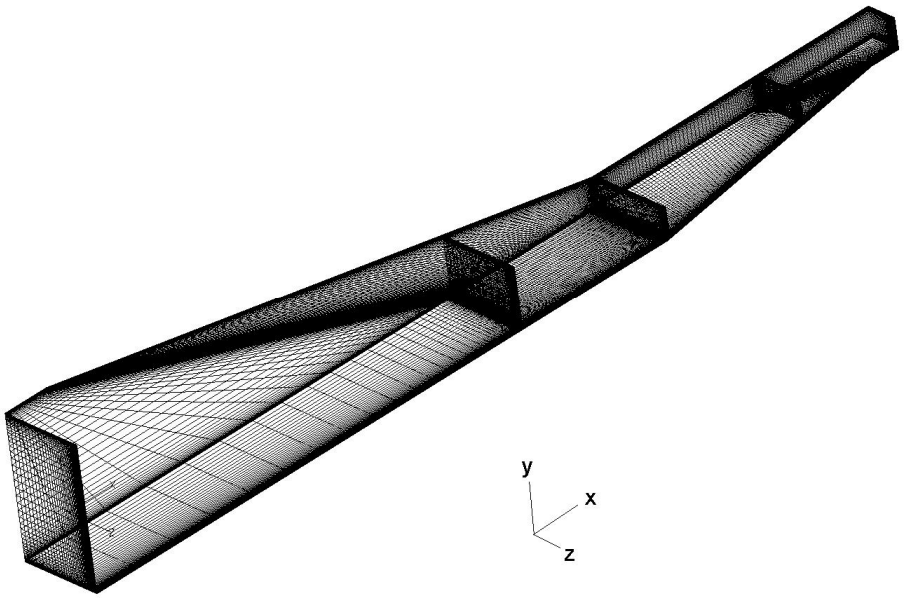

Figure 20: Grid structure for the Baseline inlet design.

As noted earlier, this configuration is operated through successive pitch and yaw compressions. Ramps are inclined to the freestream, yielding similar planar shocks initially from the upper and lower surfaces, and subsequently from the sidewall compressions. The boundary conditions are: freestream at the front and sides of the entrance/exterior of the inlets, adiabatic/non-slip at the walls, a 1st order extrapolation at the back exit plane, and slip wall for the exterior sides of the entrance as well as the symmetry planes. Note that using a slip wall condition at the exterior sides of the Baseline inlet is somewhat inaccurate since the flow spillage would not be correctly accounted for. Previous work on this configuration demonstrated that creating a larger zone upstream of the inlet might

affect less than 2% of the captured mass and spillage, not enough to justify a larger grid which adds to the computational time (Ref. 6). Thus, this condition can only be exploited when this section of the inlet is grouped into a series of the same inlets next to each other (side-to-side). Otherwise, air leaks behind and around the first shock (cowl) interaction due to the static pressure differential between the outside (freestream) and the flow captured in the inlet. For the Baseline inlet configuration, this makes the first set of shocks interact differently. The first set of shocks becomes non-planar (rounded boundaries), exposing the cowl lip and lower sections of the second ramp to a greater stagnation area and higher heating loads.

The throat area of the Baseline inlet has a width equal to twice the throat height, and an area contraction ratio of 6. For the Baseline inlet, the fuselage ramp has an initial height that terminates at the point where the pitch-plane shock from the ramp reflects off the cowl-lip, and sidewalls are assumed to start. The sidewalls of the inlet are inclined at equal angle to the free-stream. The resulting span-wise shockwaves facilitate the evolution of a highly three-dimensional flow at the entrance of a constant-area duct representing the isolator/combustor segment,[61] which starts where the crossing shocks (from inviscid estimates) reach the opposite walls.

3.1.2 Innovative (Circular) Inlets Analysis

Figure 21a,b exhibits the mesh structure for Jaws and Scoop, but is not shown at scale. The upstream plane is again chosen to be perpendicular to the

axis. The leading edge again forms a coordinate surface and mesh planes assume a fold at the axis. Note also that the mesh has an axisymmetric topology and thus has a singularity along the axis, which is treated as a boundary condition. For the Jaws inlet, its length is 1.7m and contains about 4.3×10^6 mesh points. By design, the cross-section areas at the trailing edge of each of the two inlets are the same, and their contraction ratios are close to the Baseline plan. This permits a common combustor component design, described in Chapter 5. Only turbulent cases are simulated to include the losses associated with shock effects from those produced by viscous/inviscid interactions. The turbulence fine-scale effects are simulated with the two-equation *kw-Wilcox* model and an efficient point implicit method for time integration.

In each case, structured body conforming meshes are employed with emphasis on ease of generation. Figure 21 shows several ξ constant planes along the length of the device. The leading edge of the configuration forms a coordinate surface, and the inclination of these planes to the vertical plane varies along the configuration but assumes a vertical orientation at the entrance of the combustor. From a mesh topology standpoint, singularities appear on the boundaries (marked *S*). These structural H-types of grids, however, do not pose any difficulty for the finite-volume solution procedure. Since no angle of attack or sideslip is considered, only one side of the plane of symmetry is simulated. The overall length of the Scoop inlet segment is 2.3m and 2×10^6 mesh points are employed.

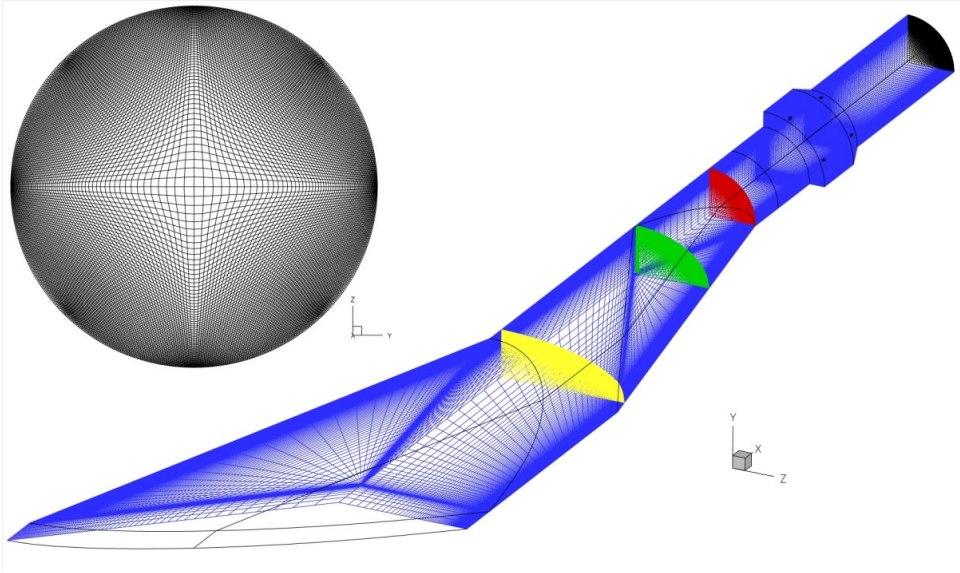

(a) Jaws, ¼ geometry

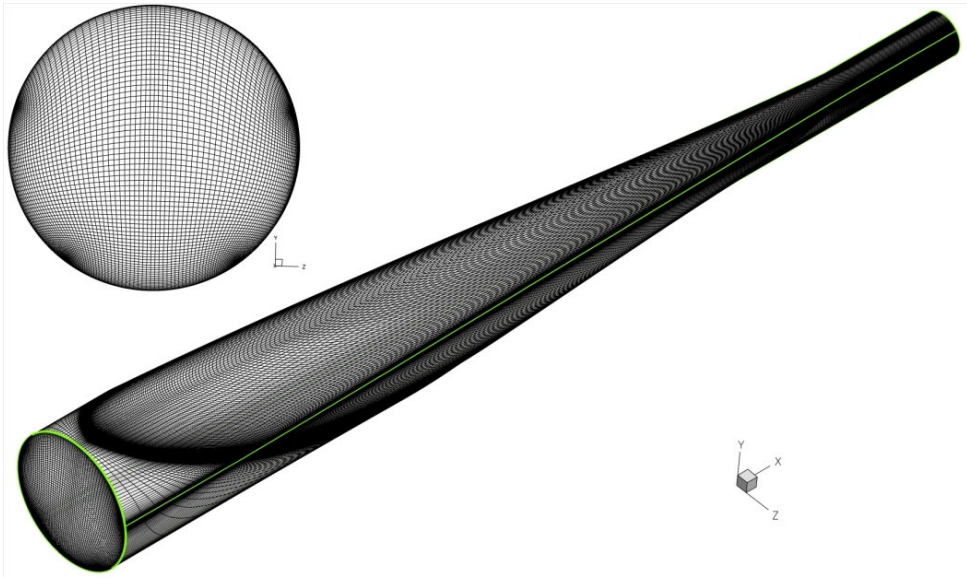

(b) Scoop, full geometry

Figure 21: Innovative inlets' structured meshes.

All geometries were initially simulated without viscous effects to match basic design characteristics; for this the Euler equations were employed. A standard central second-order scheme is employed for the viscous fluxes. After

finalizing the design, subsequent cases were analyzed with the full 3-D steady Navier-Stokes equations together with a *k-w* model (see Ref. 60) without body forces or external heat addition. The spatial accuracy used for all calculations was 2^{nd} order, with a Gauss-Seidel iterative matrix solution scheme. These three inlets' structure grids resulted in a y^+ of around *~0.85*, indicating sufficient number of points near the wall to properly capture the boundary layer.

3.2 ON-DESIGN ANALYSIS

The three following subsections on inward turning inlet analysis only describe the on-design solutions at 0-degrees of pitch and yaw (Section 3.2.1-3). The Jaws case, as opposed to the Scoop, and similar to the Baseline configuration, produced planar shocks by design. Due to the pronounced sensitivity within the viscous and inviscid interactions, both innovative prototypes should be carefully considered and compared to their counterpart with a turbulent analysis to further understand the distortion profile formed at the combustor entrance.

3.2.1 Baseline (On-Design)

In Figure 22 as in Figure 2, the structures are clearly planar as designed. Aspects of the solution along the centerline for the Baseline inward turning inlet are also shown in Figure 22. The traces of various shocks are clearly evident in the jumps observed. The Mach number drops from about 6 to slightly above 4.4 after the first shock pair (since this reflects the point of reflection on the symmetry plane). A further reduction is observed after the second reflection towards the

isolator to about 2. The contraction pressure ratio, pressure recovery, temperature and Mach numbers are designed to be equivalent across the three geometries. In this configuration, the forward sidewalls of the inlet set the shock on its lips, similar to the other two novel designs, and increase the mass captured with a reasonable penalty of additional skin friction drag (see the 1st shock position, Figure 22). Previous work on similar designs with different integration showed about 20% less mass captured.[62] In this inviscid analysis, the inlet was initialized entirely as the freestream. The CFL was set to increase from 1.0 to 5.0, and L2 norm convergence was reached around 0.18 hours using 64 processors.

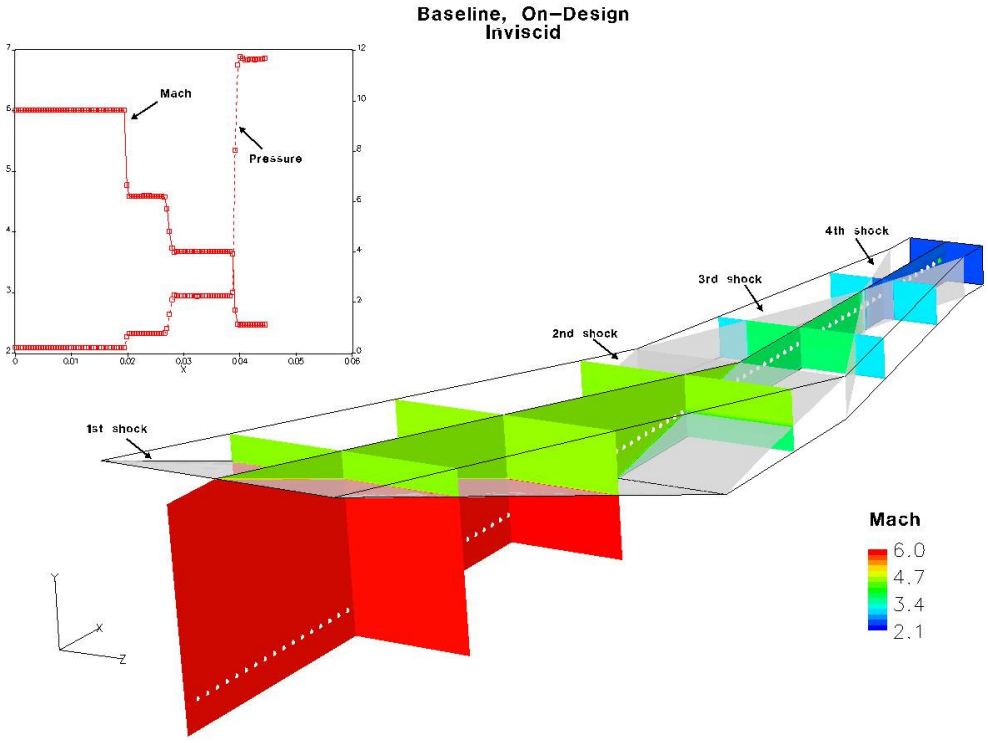

Figure 22: Shock structure, Mach number contours and center line profiles for the Baseline inlet.

For the viscous turbulent analysis, the inlet was initialized from its previous inviscid results. The CFL was set to vary from 0.5 to 3.0, and the L2 norm convergence was reached around 3.7 hours later using 64 processors.

Figure 23 depicts the turbulent flow structure for the Baseline inlet configuration through several Mach number and normalized Pitot pressure contours at the symmetry plane (k_{min}), a y-plane (horizontal) located 3mm away from the boundary layer at the bottom surface of the inlet and six other x-planes of interest. The oblique shockwave caused by the first compression ramp follows the expected path. This shock bounces off the cowl lip (Station II) and impinges on the top boundary where the boundary layer exhibits a significant thickening as a result. At this location, the sidewalls converge to produce a swept shock system to yield a highly three-dimensional flow (Station III). Further into the inlet two shocks (3^{rd} and 4^{th}) cross in a non planar manner at the symmetry z-plane (see Station IV) causing the 4^{th} shock to shift position considerably from the initially predicted calculation (Euler solution); the inset in Figure 23 shows the result of this complex interaction. Finally, the 4^{th} shock impacts the side walls at 0.025m (see Station V) upstream from the inviscid design at the straight section into the combustor. This effect adversely impacts performance of the inlet through pressure distortion and drag caused by the premature contraction. As shown in Figure 23, the flow turns and expands around the 4^{th} corner producing a recirculation flow. From this inlet calculation at the i_{max} plane (see Station VI), the boundary layer profiles and all other variables may employed to provide an initial condition for the flow entering the combustor.

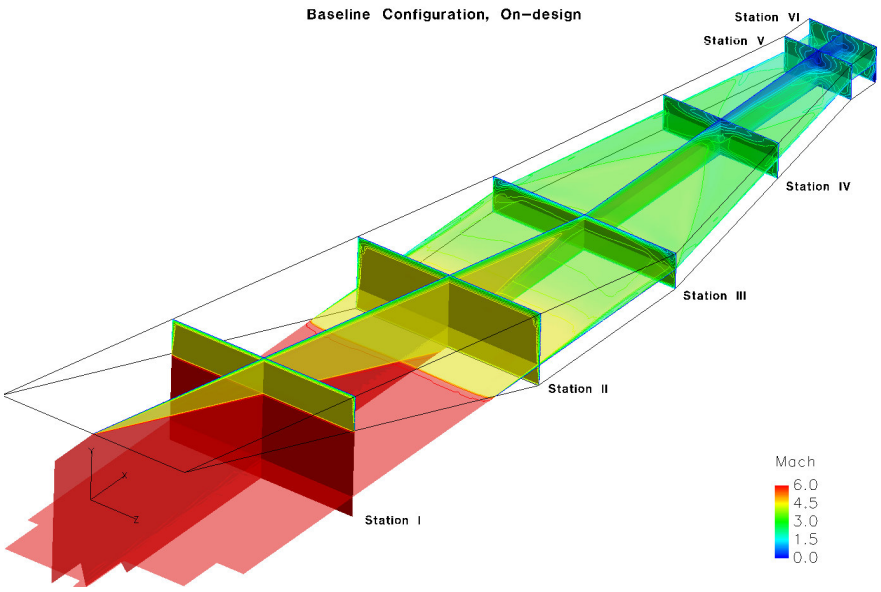

(a) Mach Number

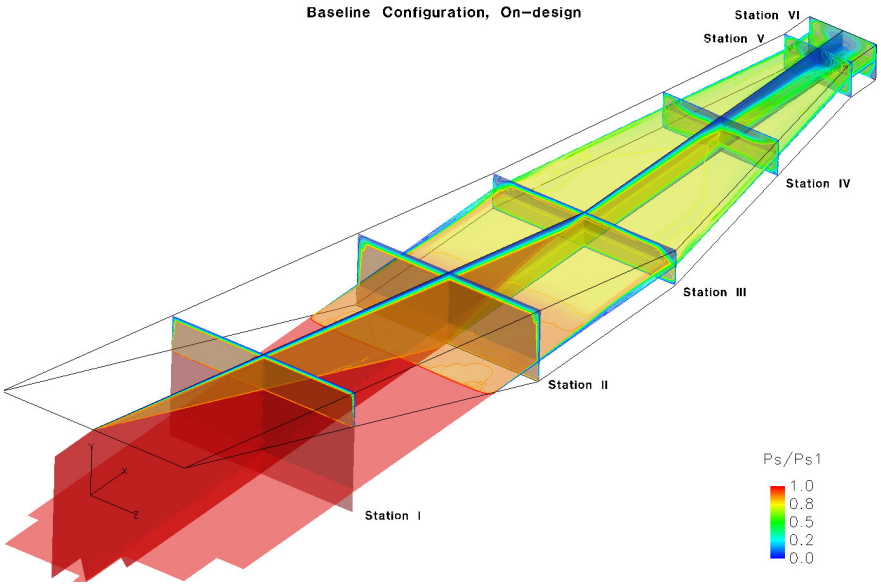

(b) Normalized Pitot Pressure

Figure 23: Baseline inlet results at symmetry plane and x-stations.

Figure 24 shows the temperature contours for the full Baseline inlet configuration as well as the streamline interactions detailing the flow separation

from the sidewalls on the upper and lower parts, respectively. Just like in the case of a high speed flow passing through a double fin ramp, the projected streamlines detail the flow separation due to the vertical side wall interactions on the floor and downstream on the ceiling of the Baseline inlet (as seen in Section 1.2.1).

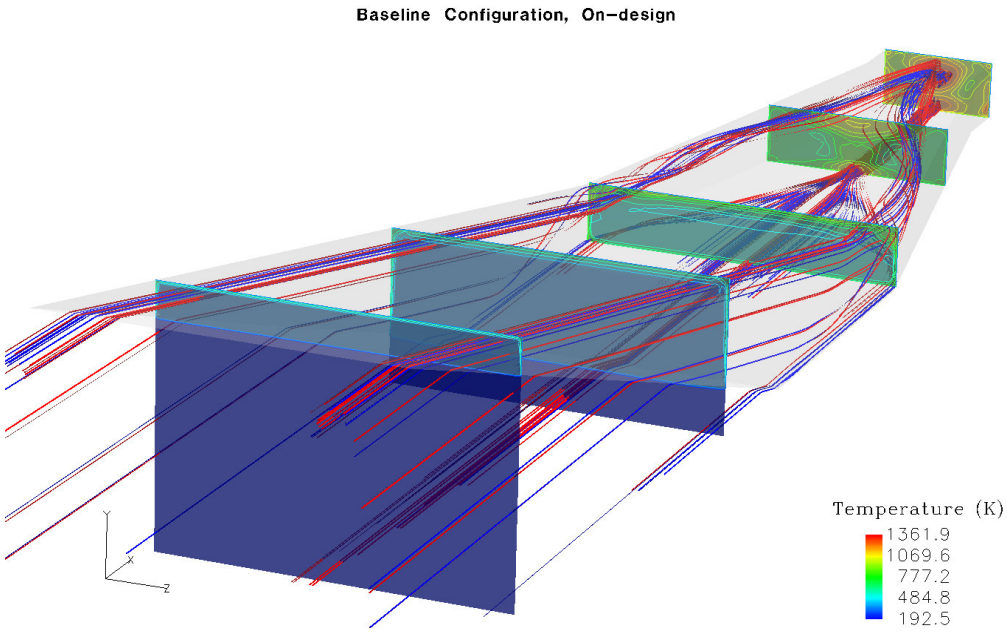

Figure 24: Viscous results for the on-design Baseline, Temperature (K) contours and streamlines.

Additional information is depicted in Figure 25a-c, showing Mach (top) and normalized pressure ratio (bottom) contours at the vertical symmetry (y_{min}) and exit plane (top and bottom respectively). The vertical symmetry delineates the initial shock boundary layer interaction on the second turn, which then yields a very severe flow separation at the center plane and upper/lower surfaces of the inlet, due to the sideways compression.

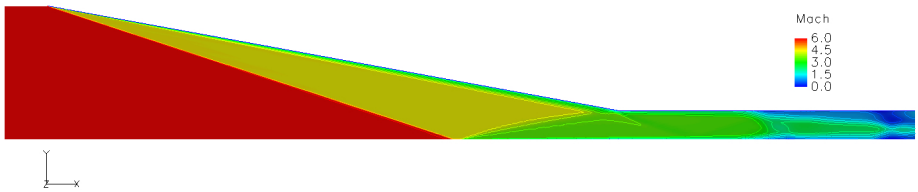

(a) Mach number, vertical symmetry plane

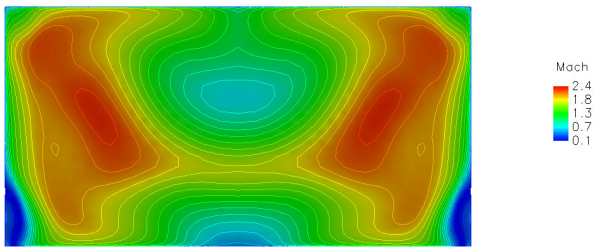

(b) Mach number, exit plane

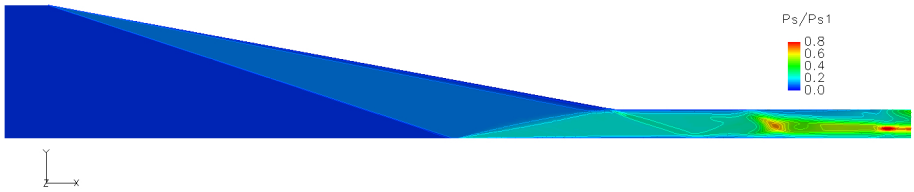

(c) Pressure ratio, vertical symmetry plane

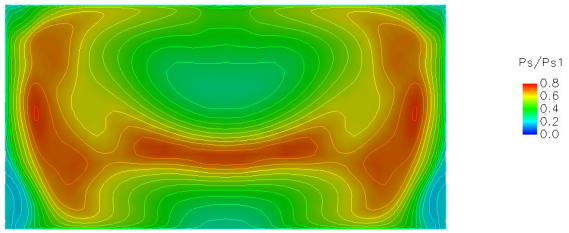

(d) Pressure ratio, exit plane

Figure 25: Turbulent Baseline solutions, on-design.

This analysis suggests that shock boundary layer interactions have a profound impact on the flow exiting the inlet. These non-ideal effects are

amplified with distance downstream, with the result that a shock/boundary layer interaction occurs downstream of the corner. When separation occurs in this context, there is a potential for a weak-interaction limit to be reached, for choking to occur downstream and possible degradation of isolator performance. This turbulent solution suggests avenues for redesigning the internal passages. The inlets could be modified by altering their lengths to accommodate for the shear layer growth or could be controlled with porous walls. These avenues are being explored in ongoing research (not shown herein).

The integrated thrust, averaged temperature and mass flow values calculated at the exit plane are 83.4KN, 59.1kg/sec and 1080.53K, respectively. These are then normalized for comparison to all other cases. The flow spillage and drag forces are calculated at the entrance and throughout the walls (the internal wetted area) in a non-dimensional manner as well. After completing the final thrust calculations for the most efficient combustor design, the drag to thrust ratio was near 33%. This measurement is a factor for the integrated airbreathing propulsion system and is directly proportional to the horizontal acceleration of the vehicle. These values obtained from the Baseline geometry are then utilized as a reference to compare the other two innovative configurations (see dimensions in Figure 1).

3.2.2 Jaws Inlet (On-Design)

An example of the on-design, inviscid shock structure for Jaws is shown in Figure 26 for just a quarter of its symmetry. The structures are clearly planar

as designed, even with the curvature of the inward turning inlet surface. The traces of various shocks are clearly evident in the iso-surface of the shock and contours observed. The Mach number drops from 6 to slightly above 4 after the first shock pair (since this reflects the point of reflection on the symmetry plane). A further reduction is observed after the second set of reflections towards the isolator to near 2.

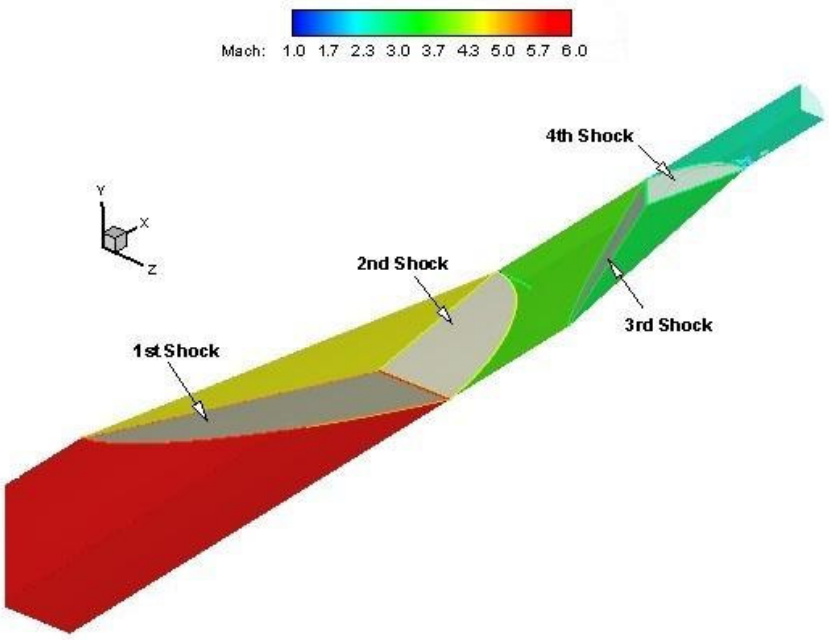

Figure 26: Inviscid shock structure and Mach number for Jaws.

The inviscid turbulent analysis for Jaws used to initialize all of the viscous cases (on-/off-design) converged in about 0.25 hours using 64 processors. The turbulent cases reached the L2 norm convergence about 7.6 hours later.

The turbulent on-design case for the Jaws concept is presented in more detail in Figure 27. This figure illustrates the flow in the two symmetry planes (z- and y-planes) and four other x-planes cutting along the inlet. Again, the boundary

layer growth and its interactions with the shocks significantly affect the downstream flow. As explained before in the case of Jaws, shockwaves emanate from both upper and lower surfaces. Although these sets of shocks are horizontally planar as in the Baseline counterpart, the first ramp encounters a shock-shock interaction that results differently (see horizontal center of Station I in Figure 27). These initial flow characteristics in the inlet direct the flow with fewer irregularities, smaller internal losses, less total heating at the lips and complete elimination of the cowl interaction.

At Station II, the second pair of shocks interacts with the surrounding wall, hugging the edge at the second turn (refer to the second planar shock shown in Figure 26 together with Figure 27). This second shock interaction affects the shear layer the most at the higher and lower locations (see the top and bottom of Station II, Figure 27). In this very location the 2nd ramp begins turning the flow inwards 90° from the first shock plane of interaction. Downstream, this unique shape offers an irregular boundary profile that is more predominant on the very top and bottom walls from the first two turns, and afterward interacts with the second pair of shocks (see Station III, Figure 27). At the 2nd Ramp the sidewalls of the inlet produce two vertical shock structures, one at each side; these effects are visible at the *y*-plane. Here, a second shock-shock interaction from the sidewalls (2nd Ramp), and the two vortices of flow separating from the top and bottom interact with the side compression waves.

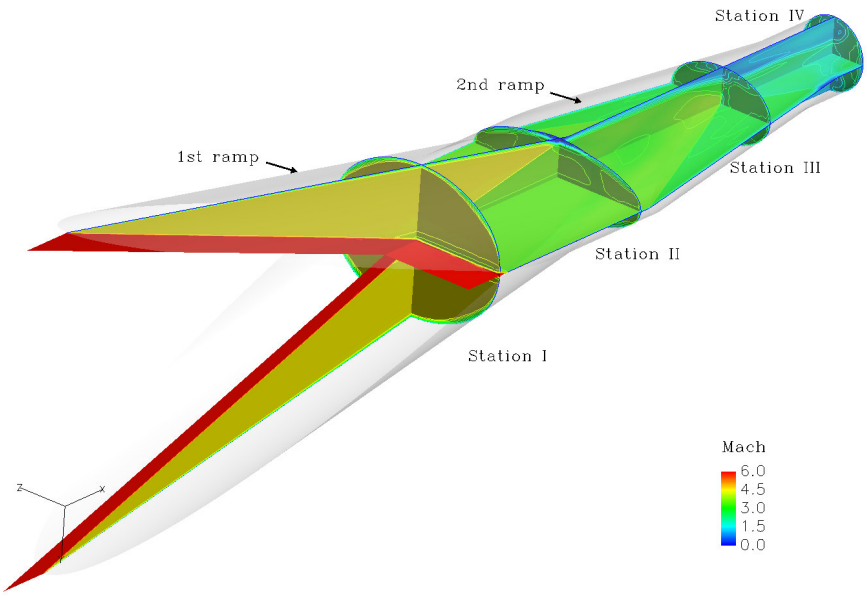

(a) Mach number

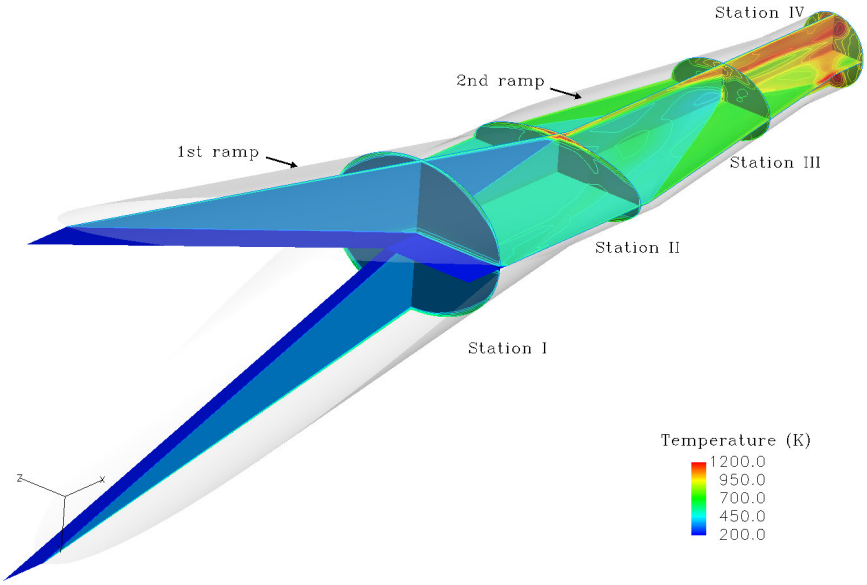

(b) Temperature contours

Figure 27: Turbulent solutions for Jaws, on-design.

The horizontal symmetry plane shows a second shock-boundary layer interaction at the sidewalls of the inlet, between Stations III and IV. Just as observed upstream in the 1st ramp, the pressure waves trip the flow into a more

severe separation than what was observed in the Baseline inlet, (seen on the *xy*-symmetry plane in Figure 23). In this region, at the end of the 2nd Ramp, the boundary layer begins to turn more predominantly from side to side than from the top and bottom. At the setting shown in Station IV, it confirms further development of the two vortices as they propagate downstream from the top, bottom and sides of the circular pattern.

Figure 28 exhibits turbulent results for the Jaws configuration (the figure is not to scale). In this case as in the prior one, many of the intricate features are observed. The dominant separation features persist for each turn of the inlet. Note particularly the swept interaction region where the spanwise compression is initiated. At the end of the 1st and 2nd ramps, the coalescent oil-flow lines at the wall delineate a characteristic steady local bifurcation structure as the flow changes behind a bluff body (Figure 28). As explained by Dallmann, this effect at this very location is noticeable in the vertical plane of symmetry as a separation bubble (see above, Figure 27).[63] As designed, downstream of the apex of the Jaws segments, a spanwise narrowing of the duct gives rise to spanwise shock segments. As shown in earlier work (Ref. 74), the laminar solution for this configuration also shows a relatively rich structure, which is not symmetric about the geometric planes of symmetry. The occurrence of laminar as well as the turbulence separations yield significant unsteadiness due to the low energy fluid observed on the top, bottom and both sides of the exit plane. Additionally, distinct regions are also evident in these turbulent simulations at the upper/lower center of the 2nd ramp, where folds of stream-surfaces are associated with the

formation of swirling flows or vortices (Figure 28). The upper and lower low total pressure regions are considerably larger than the side regions.

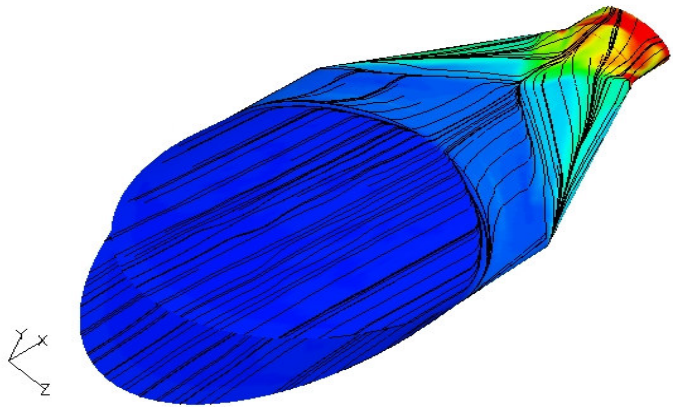

(a) Iso/top view

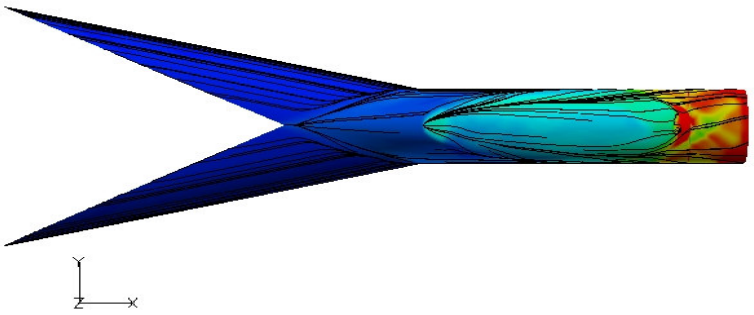

(b) Side view

Figure 28: Turbulent surface oil flow for the Jaws, on-design.

Following these shock interactions the boundary layer growth on the upper and lower walls remains fairly constant while the fourth pair of shocks intersects off course from its design locations. The distribution of Mach numbers is not uniform, with regions of lower values extending into the flow at the upper and lower edges, as well as the sides. These are effects of separation occurring

upstream, due to shock boundary layer interactions, similar to those documented earlier for the Baseline inlet configuration.[64] These phenomena typically degrade the performance of the inlet by increasing the distortion of the flow at the entrance to the combustor. Figure 29a exhibits simulated surface oil traces for the lower surface together with Mach number contours at four streamwise planes detailing the development of the shear layer separation. Figure 29b exhibits two groups of streamlines in blue (center-bottom streamline) and red (side-bottom lines) to further detail the flow structure forming this vortical structure, caused by the sidewall compression. Flow separation occurring near the lines of coalescence of the surface oil flow (Figure 29a) results in the region of low energy near the centerline. Iso-surfaces of the velocity gradient highlight the structure effectively in Figure 29c. Similar effects are also formed due to pitch plane compression; however these are relatively small because of differences in the strength of the corresponding swept shock boundary layer interaction. The origin of these structures bears some resemblance to the previous validation case of Mach 4 passing through two symmetrical fins (see the last bottom contour plane of Figure 29d). The genesis of a characteristic low total pressure pattern through the swept double fin viscous interactions is represented by pressure, oil flow and vortex streamlines at the bottom section of Jaws. In addition, three *x*-planes downstream are shown for comparison with the double-fin case, and are consistent with the low energy region observed in both situations (compare Jaws and Baseline, Figure 29c versus Figure 29d).

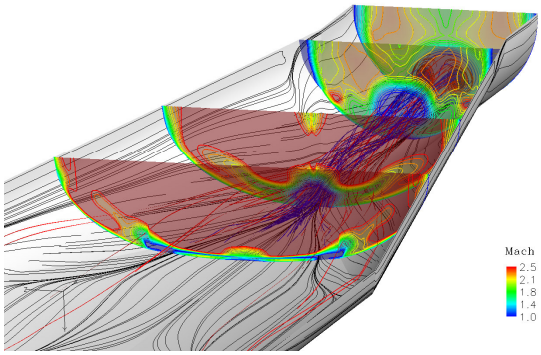

(a) Mach number

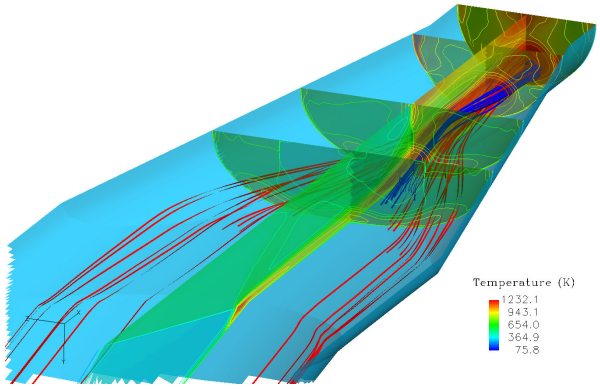

(b) Temperature (K)

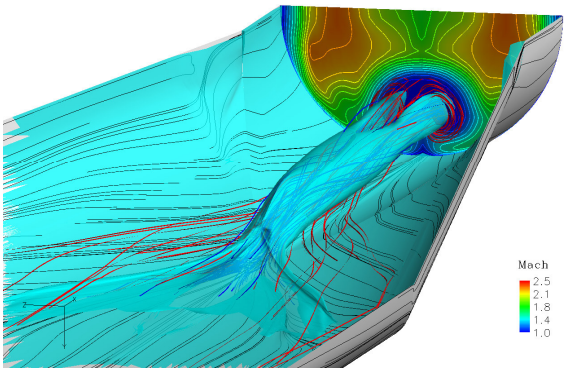

(c) Mach number and velocity iso-surfaces

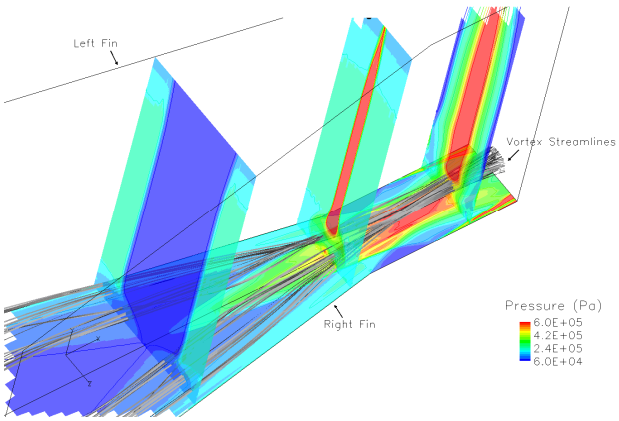

(d) Pressure (Pa) and velocity iso-surfaces

Figure 29: Bottom symmetry section of Jaws, with non-slip oil flow at the walls and streamlines depicted at the vortex separation (a-c) and (d) validation of a supersonic double 15° fin interaction.

In sum, the effect of multiple shock reflections in the pitch and subsequently the yaw plane give rise to separation and ultimately exhibit the distortion pattern shown in Figure 30 for the Mach contours.

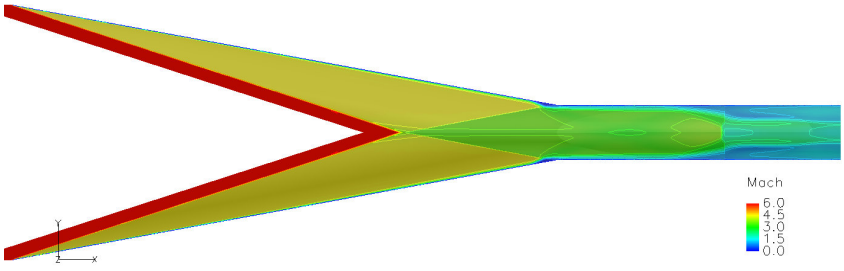

(a) Side view of vertical symmetry plane

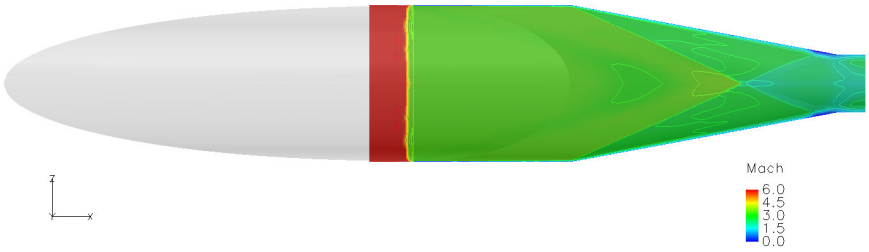

(b) Top view of horizontal symmetry plane

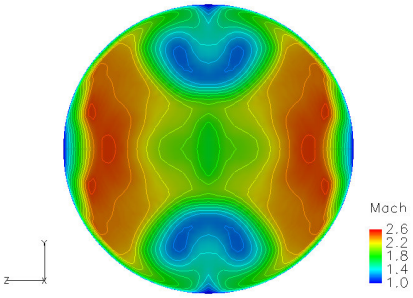

(c) Back/exit plane

Figure 30: Mach number contours for on-design Jaws.

The larger upper and lower lobes observed at the trailing sections distort the flow and may be expected to influence the performance of the downstream combustor component in a horseshoe vortex form.[65] Figure 31 shows the normalized pressure contours of Jaws at the vertical (xy), horizontal (xz) symmetry and exit planes respectively (from top to bottom).

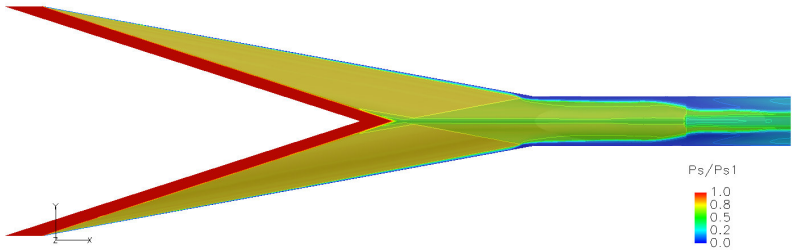

(a) Side view of vertical symmetry plane

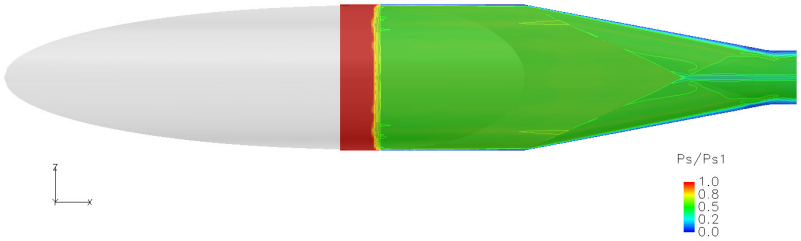

(a) Top view of horizontal symmetry plane

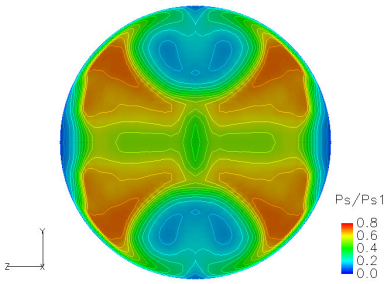

(c) Back/exit plane

Figure 31: Normalized Pitot pressure for on-design Jaws.

The integrated values at the exit plane yield a 7% increase in force, a 2% increase in mass captured and a 9.9% reduction in the average temperature compared to the Baseline. Earlier efforts explored under the USAF hypersonic research engine development programs found similar results in predecessor

configurations, such as the rectangular and triangular shaped Marquard dual mode scramjets.[66] These geometries yield higher combined skin friction and total drag forces in the engine of approximately 36% of the net thrust, divulging a frontal area equal to the Baseline herein.[67] The geometrical shape of Jaws provides some benefits at this section by having a smaller windward profile and less wall surface in contact with the flow (wedged area), which results in less boundary layer growth and overall friction drag (see 1st Ramp in Figure 27).

3.2.3 Scoop Inlet (On-Design)

The turbulent on-design case for Scoop reaches the L2 norm convergence in 7.8 hours using 64 processors without an inviscid initialization. Figure 32a-c displays Mach, pressure and temperature contours at six *x*-planes positioned perpendicular to the streamwise direction of the Scoop configuration. Together, these figures show the wall pressure, oil-flow patterns and some streamlines that originate flow separation from the sidewall interactions. The conically shaped shock structure is clearly evident in the Mach number and temperature contours (Figure 32a-c). In the initial segment, a curved shock originates at the leading edge of the device, turning the flow inward towards the surface (see the 1st and 2nd *x*-planes in Figure 32a,c respectively). Consecutively, a reflected conical shock emanates from the vicinity of the lower notched region, whose trace moves upward as the plane is moved downstream, initiating a sequence of reflections from the upper and lower surfaces. The initial pressure wave is designed to follow along the leading edges without converging to the rim at the bottom, but

rather, a small notch with an elliptical shape is removed from this region. Although this notch produces further spillage, this particular modification in the design mitigates an unwanted cowl lip interaction. At the trailing edge, the turbulent simulation showed a large separation coming from the surrounding walls, and pushed around towards the upper region as the flow twists downstream (observe the development of the 3rd - 6th *x*-planes, Figure 32a-c). In addition, a single, much smaller and shallower structure on the lower side is produced by the high pressure interaction near the notch. Downstream, between the 4th and 5th stations, this nearly imperceptible separation is enlarged by a second interaction at the bottom surface, where the wall pressure is the largest (marked with an arrow in Figure 32b). As in preceding cases, the reflected shocks significantly increase the size of the disturbed boundary layer region, yielding a diffuse low energy region on the upper side of the configuration as shown at the exit (6th *x*-plane, Figure 32a-c).

In contrast to earlier studies, Euler and laminar simulations showed a distinct three-lobed structure on the upper side of the cross section (see Ref. 74), while the turbulent solutions yield one low energy region on the upper part of the outflow. In comparison with the Scoop geometry, the average Mach number is lower but this is principally the effect of the compression ratio in association with the viscous flow interactions (compare Section 3.2.2 to 3.2.3).

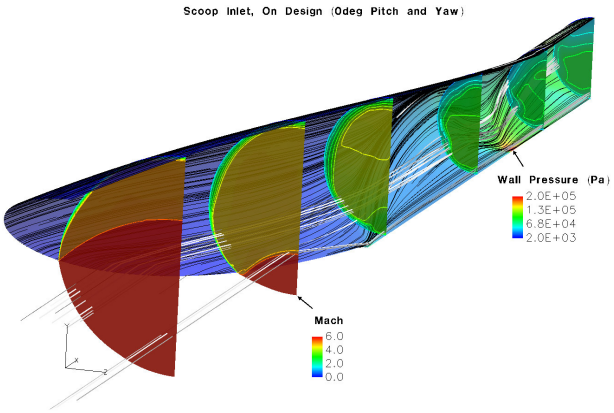

(a) Mach Number and wall Pressure (Pa)

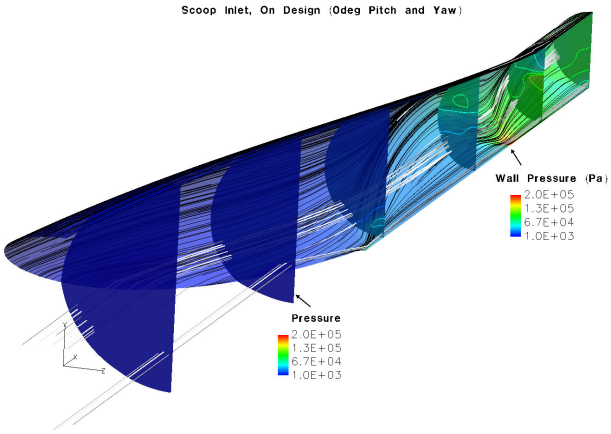

(b) Pressure (Pa)

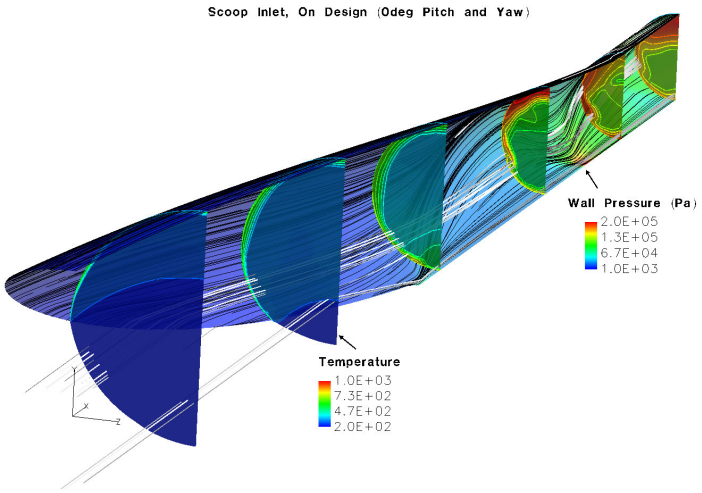

(c) Temperature (K) and wall Pressure (Pa)

Figure 32: Turbulent Scoop contours, on-design.

The turbulent solutions exhibited a modest degree of unsteadiness, and the low Mach number region does not develop into a choked or unstart situation (see Ref. 74). Since the inlet design considers the viscous effects in the positioning of the conical shocks and their interactions, previous inviscid patterns produced a richer structure compared to the turbulent simulation. Since the effect of

turbulence is to enhance the ability of the boundary layer to resist separation, the resultant mean turbulent structure is therefore simpler. [68, 69]

The oil-flow from the turbulent simulation (shown in Figure 33) exhibits further details of the flow. The previously observed regions of low energy (see Figure 32) are associated with the shock/boundary layer interaction and separation as shown in Figure 33. Note the coalescent lines on: 1) the upper walls where the inlet's second conical shock interacts, the same region where the geometry changes into a cylinder (see Figure 33a); and 2) the bottom notch region where another conical pressure wave collides further downstream (see Figure 33b). These surface flow structures show the region where the flow separates, caused by the local and sidewall pressure which perturbs the flow field and breaks up the separation bubble in the perpendicular downstream plane. Similar conclusions from the visualized oil flow were derived from the topological interpretations by Bippens and Turk (1983) and later described by Gaitonde et al. in hypersonic boundary layers.[70, 71]

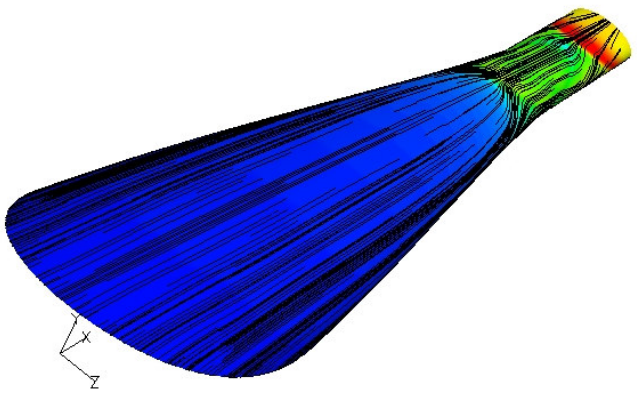

(a) Upper surfaces

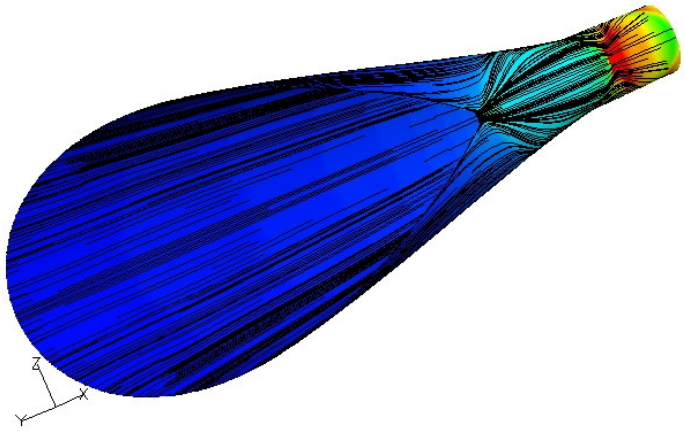

(b) Lower surfaces

Figure 33: Surface oil flow for the Scoop.

The viscous/inviscid interactions in the Scoop inlet, as previously observed in Jaws, result in a non-axisymmetric exit profile. The exit profiles in all three inlets show a double fold of stream-surfaces associated with the formation of pair vortices. The Scoop inlet yields such structure just on the upper region (see Figure 34a,b), while Jaws (see bottom of Figure 30a,b) and the Baseline (see Figure 25a,b) succumb to formations on the upper and lower regions. Although both innovative inlets have the same analogous circular configuration downstream, their designs are as sensitive to viscous interactions as their Baseline counterpart. These make them quite complex, reducing their design space, e.g., different flying conditions (altitudes and/or speeds). Also, the turbulence model's ability to accurately simulate details of such complex viscous/inviscid interactions is uncertain.[72] Nonetheless, this simulation shows a core region of a more uniform flow of relatively high Mach number (slightly over

2.5) and total pressure surrounded by lower speed fluid. The integrated values at the exit plane yield a 20% reduction of the force compared to its counterpart. In addition, 25% less mass was captured and average temperature was reduced 24% compared to the Baseline inlet. Although the cowl interaction was mitigated for the Scoop inlet, the spillage was much greater than the Baseline inlet by comparison. On the other hand, trying to mitigate such cowl interaction in the Baseline might result in a much larger spillage than Scoop due to a larger aperture at the bottom leading edge. Chapter 5 analyzes the Scoop profile incorporated to equivalent combustors. The Scoop inlet produced the least thrust compared to the other inlets, although the drag to thrust ratio was near 28%.

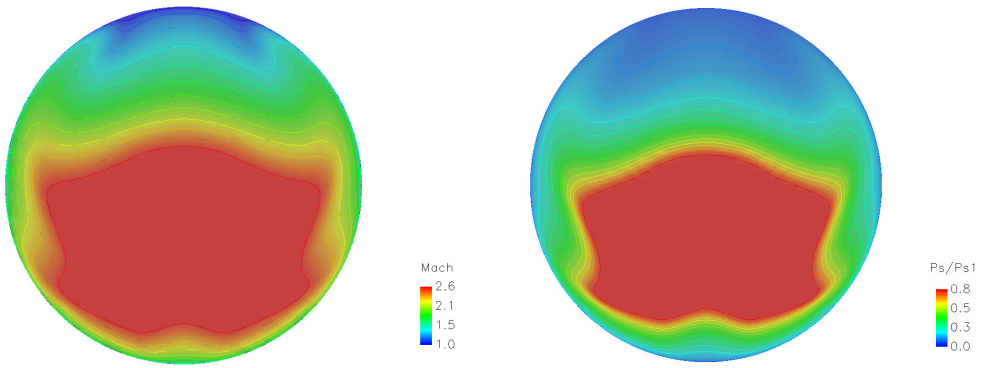

(a) Mach Number (b) Normalized Pitot Pressure

Figure 34: Scoop inlet exit profiles at on-design conditions.

As a note of precaution, the large low energy region at the exit profile that extends from the upper wall towards the core might allow the fuel and air mixture to propagate via its thick boundary layer and cause it to become thermally choked.

Additional attention must be taken when designing the combustor's entrance in order to diminish such probability. By comparison, the Jaws inlet resulted in a thinner shear layer accompanied by two strong vortices; one on the top and the other on the bottom section near the walls. These effects make it much more difficult for the reactions to flashback or propagate upstream, thus early predictions might be drawn from these innovative full scramjet systems by just comparing their exit silhouettes and inlet performances (compare Figure 30 to Figure 34).

3.2.4 Discussion of Results (On-Design Inlets)

Table 4 shows some of the integrated values at the exit plane and drag coefficients for all the on-/off-design cases. The calculated drag coefficients (C_d) for the on-design circular configurations with non-axisymmetric inflow profile yield values within previous measurements obtained by other authors on circular configurations, but with axisymmetric inflow profiles, of around 0.15 to 0.25 for similar flight conditions.[73]

Table 4: Normalized inlet results (On-Design).

Configuration	Pitch (^{o})	Yaw (^{o})	τ_i	m'	T_{ave}	C_d
Baseline	0	0	1.00	1.00	1.00	0.278
Jaws	0	0	1.07	1.02	0.90	0.186
Scoop	0	0	0.80	0.75	0.76	0.196

This research identified that even in streamline traced inlets, the flowfield distortions are present due to similar shock boundary layer interactions. [74] Both of these innovative inlets offer a well conditioned flow for their specific contoured geometries at on-design conditions compared to traditional configurations (see Ref. 6). Jaws yields the least drag coefficient and pressure loss compared to the other two geometries. Although the drag coefficient is lesser for Scoop than the Baseline, its total pressure losses across the system are about 20% higher. While these interactions result in increased losses, they can also engender a region of enhanced turbulence in the isolator, yielding better mixing of air and fuel. [75] This can significantly augment chemical reactions and improve the overall factor of the hypersonic propulsion system, which will be evaluated in Chapter 5. [76, 77] Thus, two principal issues must be considered when examining such configurations: 1) the three-dimensional interplay between viscous and inviscid interactions including shock-boundary layer and shock-shock interactions in the inlet and 2) the positive effects due to combustion of the reacting fuel-air mixture. [78, 79] Since much of the supersonic combustor work has been extended from subsonic combustors, aircraft engine designers try to reduce these inlet distortions in order to create a more uniform flow. Trying to accommodate and condition the flow to a linear combustion section returns further losses and complicates these hypersonic inward designs.

In this research, isolators are shortened to accentuate the inlet prototypes' performances, and to help clarify how these inlets might impact the combustor. A fully integrated analysis of the inlet to a common combustor advances comparison

and details of their interplay. The reduced straight zone measures about twice the inlet diameter from the last turn to the cavity where fuel ports are located. Consequently, the cross-flow profiles obtained from the inlets were employed to simulate the combustor, as shown in Chapter 5.

3.3 Off-Design Analysis

The previous cases provide a more detailed understanding of the internal viscous effects and describe the planar shocks and shock-shock interactions in the designs at 0^o pitch and yaw. Additional cases are analyzed for two different orientations: 3° pitch and 3° yaw angles for each of the three configurations, while holding to all other flight conditions for their given design. The off-design analysis investigates their performance degradation, and further compares their mean robustness. Earlier work examined different Mach numbers, angles of attack and altitudes (Ref. 6). The following viscous turbulent analyses conducted for all three inlets were similarly initialized from each of their respective inviscid solutions. The CFL was set to vary from 0.5 to 3.0, and the L2 norm convergence was reached around ~4.5 and 7 hours later using 64 processors, for when half geometries or full geometries were employed respectively.

3.3.1 Baseline Inlet (Off-Design)

Figure 35 shows the Mach number and temperature contours for a turbulent calculation of the Baseline inlet for a 3º pitch angle of attack. The plot illustrates the symmetry plane (k_{min}) and a horizontal *xz*-plane located 0.05m from

the bottom surface of the inlet, far over the boundary layer. The oblique shockwave caused by the first compression ramp is about 4º higher than previously seen (on-design). Distinctive Mach number contours show that the initial shockwave bypasses the cowl lip without colliding and flow spillage is apparent (see Figure 35a). The flow interacts with the boundary layer at the upper wall past the third turn. Subsequently, sidewall convergence produces a swept shock system to yield the highly three-dimensional flow as seen before but the Mach number variation is different from that observed previously in the on-design Baseline case. Although this small pitch deviation on the *xz*-plane does not display any notable change, the 4^{th} shock shifts position considerably from the on-design calculations. These effects produce a larger flow separation on the upper section than the bottom section downstream towards the combustor region. Again, this Baseline inlet exhibits the imperfect reflection of the shockwave from the wall, due to the displacement effect of the shocks and the boundary layer.

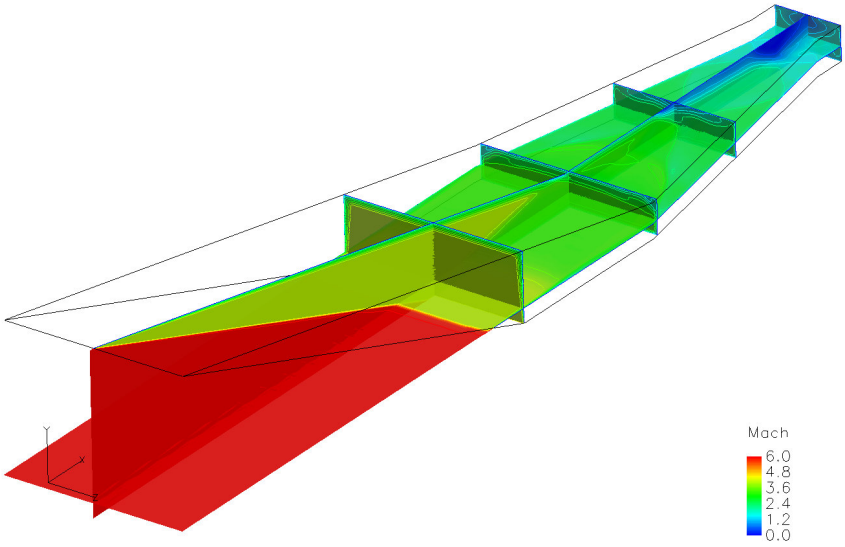

(a) Mach number

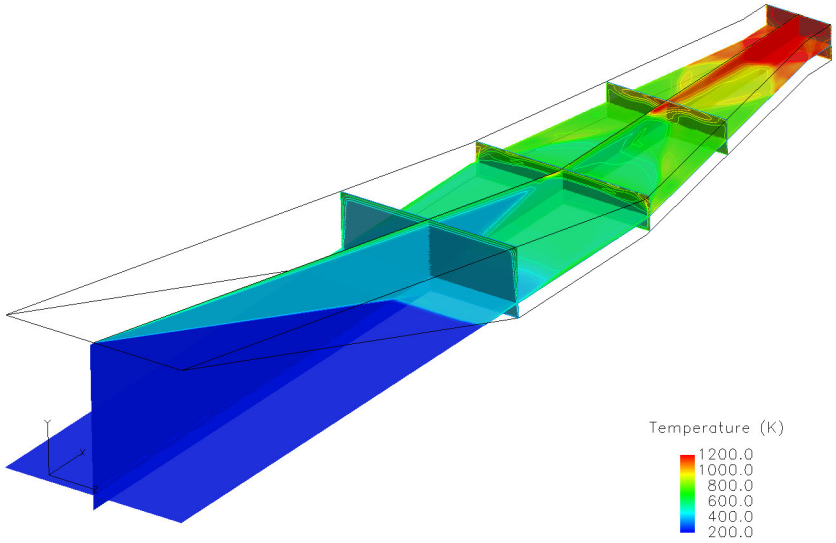

(b) Temperature (K)

Figure 35: Off-design (3° pitch) Baseline results.

Figure 36 shows the Mach number and Pitot pressure ratio contours at the exit plane of the Baseline inlet at an angle of attack of 3°. The displaced shock interaction produces additional pressure waves in the second ramp which then

cause the temperature to increase at the exit by 6.95% (see Figure 35b). In addition, the particular position at this angle of attack increases the mass flow rate of the air being captured by 10.77%, since the projected area upstream of the inlet is increased. Similarly, fluid forces meassured at the inlet exit augmented by 11.53%.

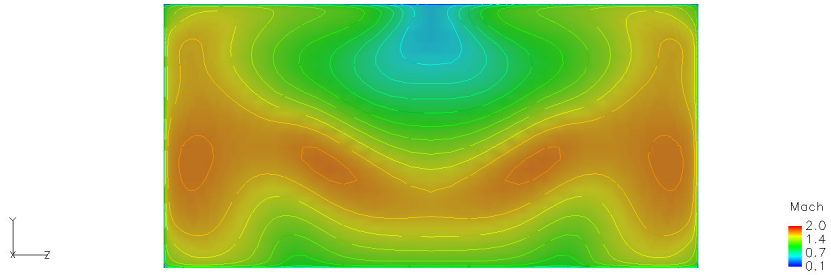

(a) Mach number

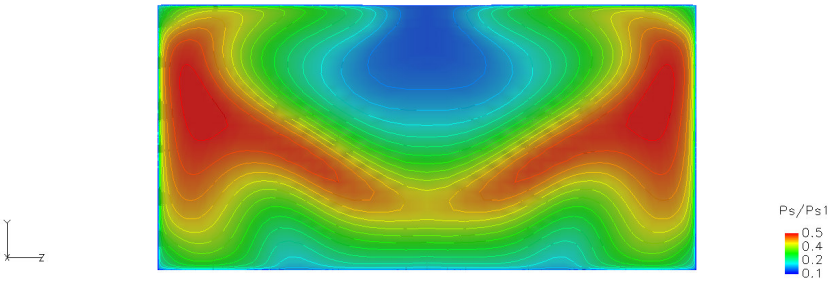

(b) Pitot pressure ratio

Figure 36: Off-design (3° pitch) results at the exit plane of Baseline inlet.

On the other hand, Figure 37 shows the Mach number and temperature contours for the Baseline inlet at 3º yaw. In this case, the flow enters the inlet from the right side looking downstream in the *xz*-plane. This produces a greater

spillage at the entrance of the inlet, thus reducing the mass capture. In addition, this effect, observed from the top view of the cutting plane at 0.05m from the bottom surface of the inlet, creates a sideward compression of the flow and greater boundary layer growth on the sidewalls. A large portion of the first shockwave bypasses the cowl lip (see 1st *x*-plane) and impinges toward the top wall right onto the third turn or second ramp (see 2nd *x*-plane); the vertical symmetry plane (k_{min}) has not shown any change until this location. The oblique shockwave caused by the second ramp diverges by 3º, interacting with the boundary layer at the side wall. The yawed inlet causes a larger compression on one side than the other. This interaction turns out a larger separation not only on the side but also on the upper region that gets propagated downstream (see 2nd to 4th *x*-planes). The position of the inlet at this angle of yaw decreases the mass flow rate of the air being captured compared to the on-design Baseline case by 3.3%. This effect can be explained in part by the change in the projected front area of the inlet which is reduced by the lateral freestream trajectory. Similarly, this insignificantly reduces the integrated exit forces and averaged temperature 3% and 4.2% respectively (see Figure 37b).

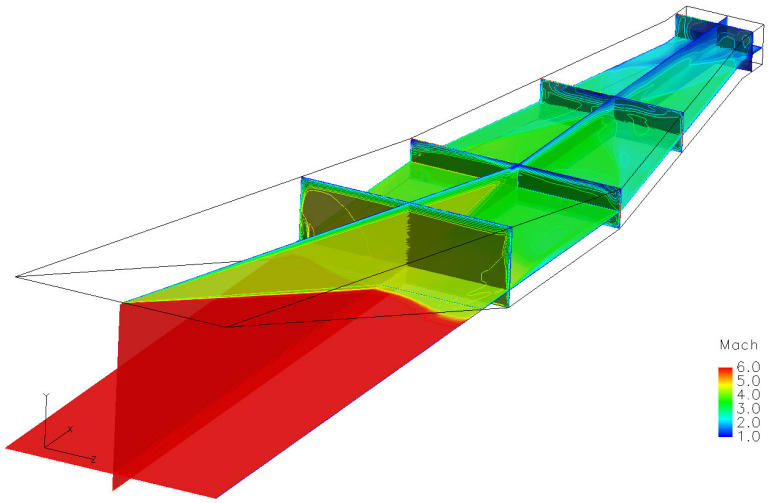

(a) Mach number

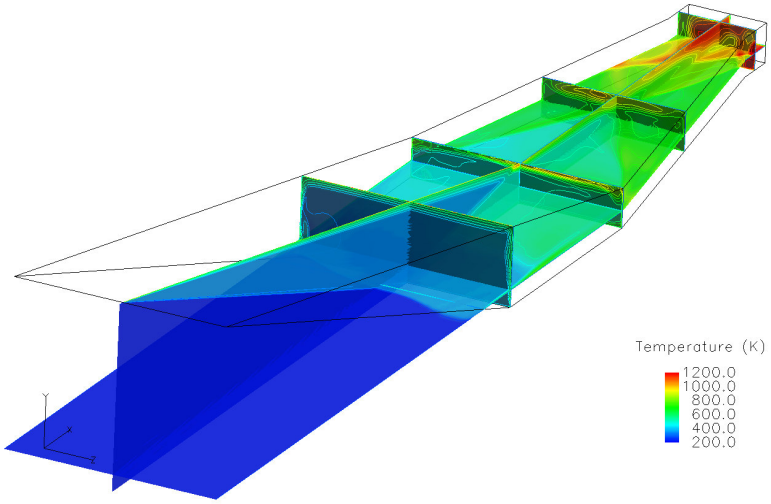

(b) Temperature (K)

Figure 37: Off-design (3^{o} yaw) Baseline results.

Although the overall integrated flow conditions were slightly altered by this small yaw deflection, the exiting flow has a profound contour. The exit plane for this Baseline case shows the most distorted profile due to the lateral offset interaction which generates a non-symmetrical flow pattern (see Figure 38). This

could result in a lesser thrust and affect its direction downstream in the combustor, causing uneven combustion, and a substantial boundary layer where reactions could propagate upstream. The earlier flow separation seen in the on-design Baseline case shifts counterclockwise, creating a much larger low energy region and thicker shear layer on the right side wall (as seen downstream).

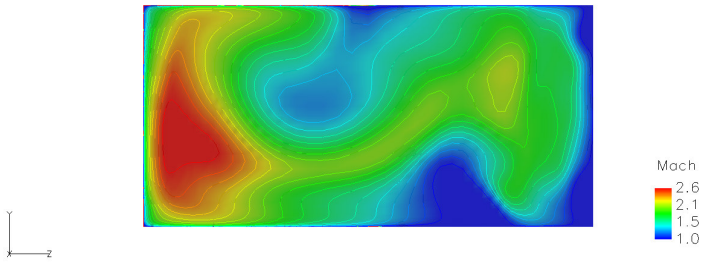

(a) Mach number

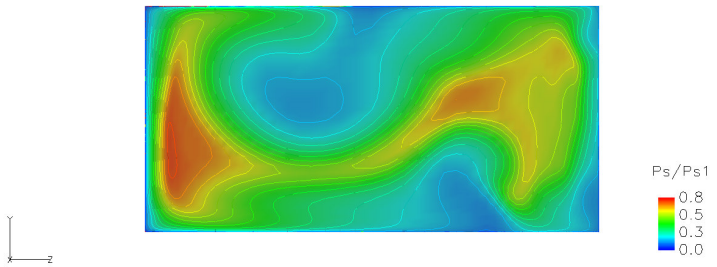

(b) Pitot pressure ratio

Figure 38: Off-design (3° yaw) results at the exit plane of the Baseline inlet.

Here, swirl can be defined differently than in most cases. Usually swirl is used for circular configurations where the center of rotation travels downstream at the geometrical axis or midpoint. Since none of the inlets nor their inflow profiles are axisymmetric, swirl is redefined herein as the integrated ratio of the velocity

magnitude at the *x*-plane (exit) by the velocity downstream, perpendicular to the plane (see Equation 18). This integrated value yields a downstream swirling effect of 10.3, meaning that about 10% of the entire exiting flow is revolving or positioned on the *x*-plane and in the general clockwise direction. Such knowledge could be exploited in perfecting injection strategies for the period of off-design conditions.

Equation 18: Swirl

$$S_i \equiv \int \frac{\sqrt{v^2 + w^2}}{u} dA$$

3.3.2 Jaws Inlet (Off-Design)

Figure 39 and Figure 40 show Mach number and static pressure contours at 3º angles of attack for the inward turning inlet respectively. The boundary layer patterns are generally similar to the on-design analysis. However, flow separation and shock interactions are shifted toward the bottom part of the inlet. From the vertical symmetry plane, on the top part of Figure 39, a higher low energy region is clearly observed at the upper section of the first inlet shoulder. This is caused by the offset shock interaction at this angle of attack, producing a flow separation downstream from this point. The effect is then further augmented by the second pair of unpaired shocks interacting at the center core by the second ramp. The top view or horizontal planes clearly resemble with few differences the on-design conditions for the Jaws inlet (see middle outlines of Figure 39).

Finally, the flow creates an effct as if the upper separation would have contracted as the lower grew compared to its on-design results at the exit of the inlet (compare the exit plane at the bottom of Figure 39 to Figure 30). The total swirl effect is not accounted for since there is symmetry, but the localized levels are greater on the bottom contoured section. The integrated swirl is near 6 and in opposite direction on each half of the exit.

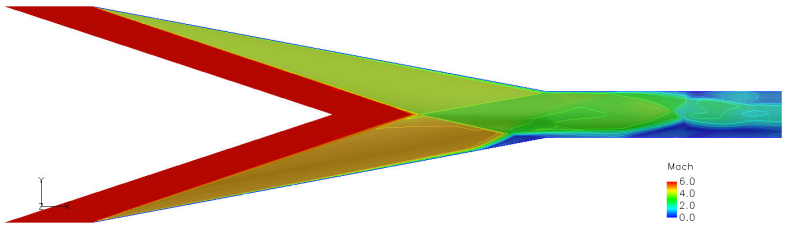

(a) Side view of vertical symmetry plane

(b) Top view of horizontal symmetry plane

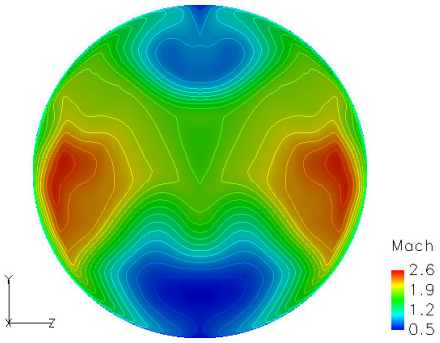

(c) Back/exit plane

Figure 39: Mach number contours for off-design (3° pitch) Jaws.

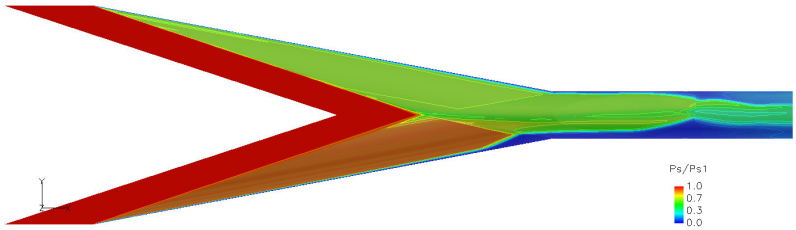

(a) Side view of vertical symmetry plane

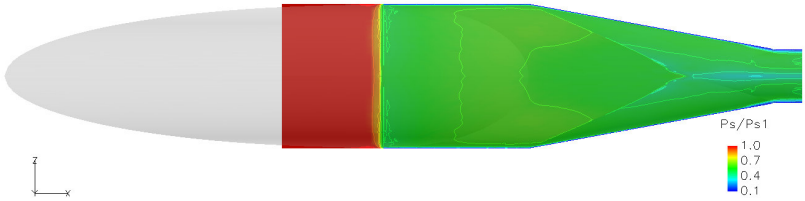

(b) Top view of horizontal symmetry plane

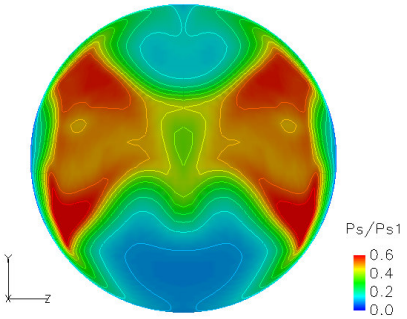

(b) Back/exit plane

Figure 40: Pitot pressure ratio contours for off-design (3° pitch) Jaws.

The position of the inlet at this angle of attack increases the integrated force and mass flow rate compared to the on-design Baseline case by 2.4% and 1.02%, respectively. This effect can be explained by increasing the arresting front area of the inlet, allowing it to capture more air mass although the spillage doubles. The average temperature at its exit plane is about 9.6% less than the

Baseline. The next figure shows just half of the Jaws vertical symmetry surface with its oil flow combined with: (a) Mach number contours at five equally spaced stations from the center of the 1st ramp towards the exit in the *x*-plane direction and transparent lines at the symmetry (see the shock-shock interaction between the 1st and 2nd stations), as well as a few ribbons positioned through the separation regions (Figure 41a); and (b) normalized pressure ratio (Figure 41b). From the oil flow solution at the concaved bottom floor of Jaws between the first two stations, the offset shock interaction prior to the 2nd turn (end of the 1st ramp) yields a rich owl shaped discontinuity, typical evidence of flow shock induced separation (Figure 41a). Next to this figure is a picture of a shock induced separation taken from a hypersonic experimental work done by Pitt Ford and Babinsky on oblique shock interaction past micro-ramps.[80] Also, similar shapes were found by Bippes and Turk (Ref. 70) in a hemisphere-cylinder at high angles of attack $\alpha \sim 30°$ and $Re \sim 6.5 \times 10^6$. Soon after the 2nd turn, between the 2nd and 3rd stations, the flow reattaches to the surface due to an increase in pressure in the upper and lower regions. Downstream from this point, between the 3rd and 4th stations, a recurrent flow separation is observed. This flow separation is just as extensively shown near the center of the 2nd ramp, but is much greater due to an earlier shift of the shock interaction from the sidewall direction. Another growth of the originally thinner shear layer is encountered from the top section; see the small bubble right on the top of the 4th station (Figure 41a,b).

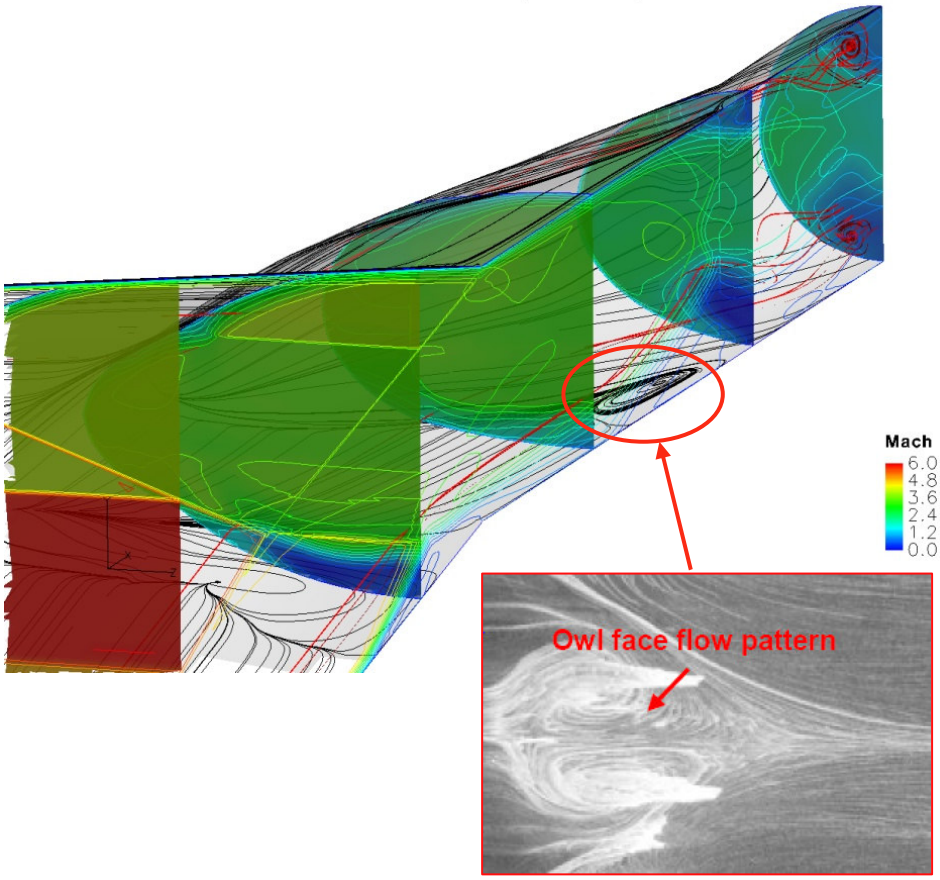

(a) Mach number contours and surface oil-flow comparison

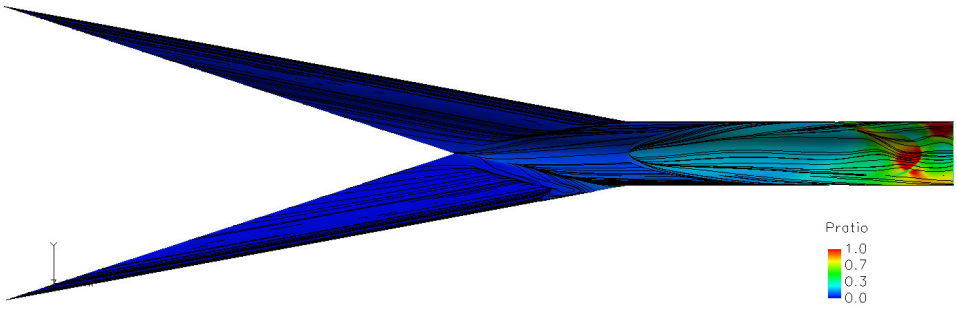

(b) Side view of the pressure ratio and oil flow at the surfaces

Figure 41: Off-design (3° pitch) Jaws.

Figure 42 show the Mach contours for a 3° angle of yaw and 0° angle of pitch, correspondingly. The boundary layer patterns are reversed or turned sideways from those previously described in the 3° pitch case, in that the lateral growth is greater than on the upper and lower surfaces. At this offset direction, flow separation and shock interactions are shifted sideways in the same direction as its counterpart (Baseline). The sideways position of this inlet is affected by an increase in the integrated force and mass flow rate compared to the on-design Baseline case by 6.69% and 0.12%, respectively. As recorded in all the other Jaws cases, the average temperature also decreases by 7.63%. The vertical symmetry plane (top of Figure 42a,b) shows no apparent differences from the on-design Jaws case, while the horizontal symmetry plane shows a difference in the shock interactions, boundary displacement and distortions (see top view of horizontal symmetry plane for both Figure 42 and Figure 43). In the pitch case, the opposite is true: change occurs in the horizontal, not the vertical, plane. Although the unique elliptical lips of Jaws allow it to increase the air capture during sideways maneuvers, as opposed to its Baseline counterpart, the exit profile results in very intricate distortion but quite familiar patterns. In this case, Jaws' geometry is symmetrical above its horizontal plane. Equivalent sidewall interactions can yield remarkably the same twisted pattern with counterclockwise rotation on the upper and lower lobes, larger separation and a lower energy region towards the right side compared to the left (compare the Mach number contours at the exit plane at the bottom of Figure 38 to those of Figure 42).

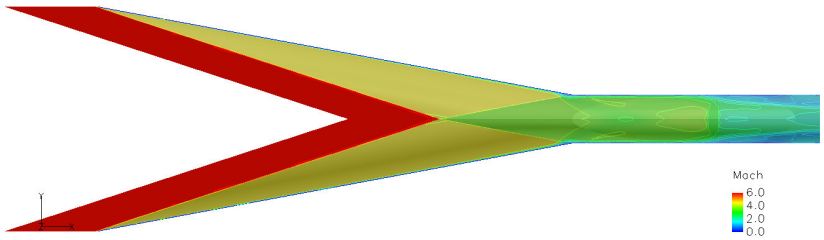

(a) Side view of vertical symmetry plane

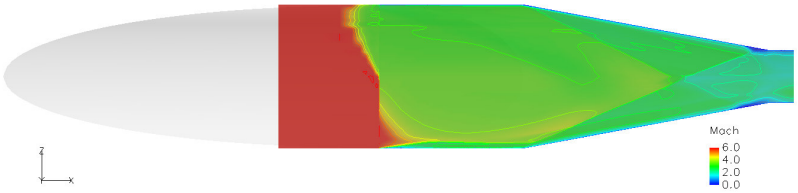

(b) Top view of horizontal symmetry plane

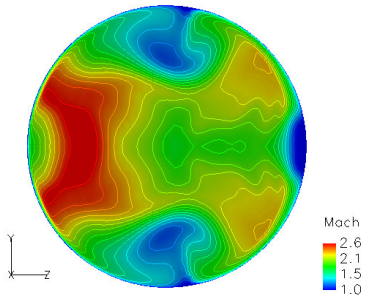

(c) Back/exit plane

Figure 42: Mach number contours for off-design (3° yaw) Jaws.

Figure 43 shows the normalized Pitot static pressure contours for a 3^{o} angle of yaw and 0^{o} angle of pitch, correspondingly.

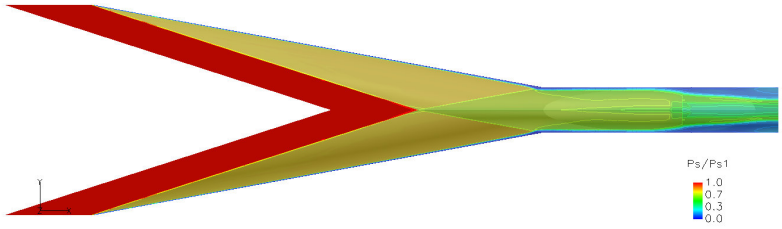

(a) Side view of vertical symmetry plane

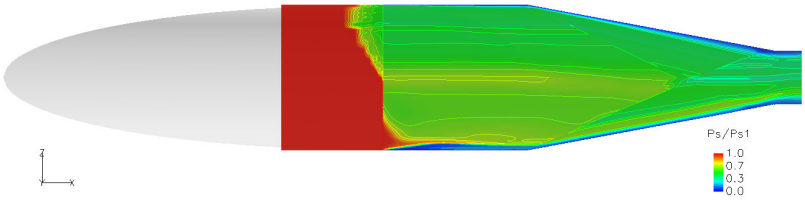

(b) Top view of horizontal symmetry plane

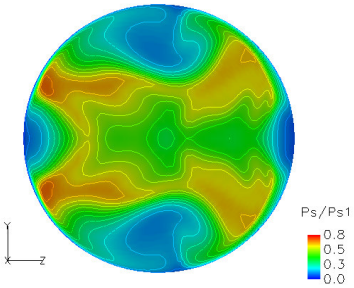

(c) Back/exit plane

Figure 43: Pitot pressure ratio contours for off-design (3° yaw) Jaws

In addition, the oil-flow at the surface of the bottom section of Jaws is plotted in Figure 44 in conjunction with the: a) Mach number, b) pressure contours at five stations downstream and c) normalized pressure ratios at the surface. As described in the initial (on-design) Jaws case the separations and surface flows are twisted, turned and shifted from the upper and bottom sides to the side to side positions. Note the larger separation at the middle right corner of

the 2nd ramp between the 2nd and 3rd stations, as well as the subsequent much smaller bubble past the 2nd ramp on the left corner of the 4th station (Figure 44a,b). Large three dimensional flow interaction and separations arise unexpectedly from a seemingly insignificant lateral deviation of only 3°.

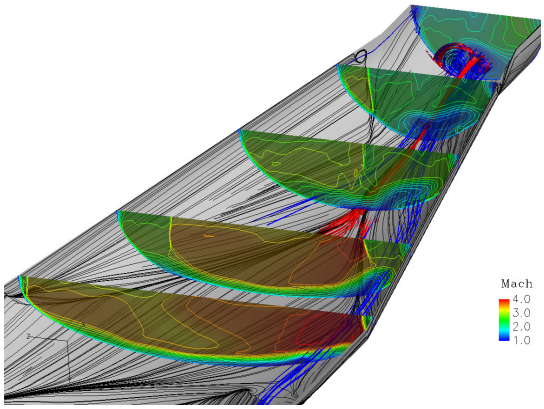

(a) Iso-view of upper half: Mach number

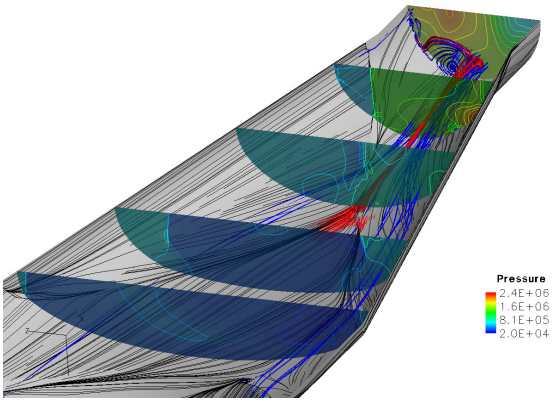

(b) Iso-view of upper half: Pressure (Pa)

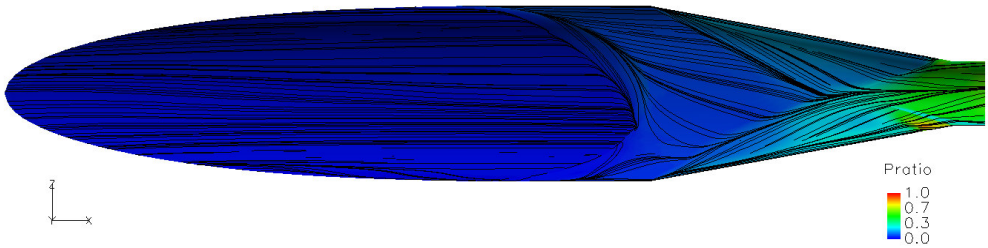

(c) Top view of pressure ratio and oil flow at surfaces

Figure 44: Off-design (3° yaw) Jaws results: x-planes contours, oil-flow and separated streamlines.

3.3.3 Scoop Inlet (Off-Design)

Figure 45a shows the Mach number contours at six different *x*-planes, oil-flow combined with wall pressure and a few streamlines extracted from the separation region at the exit. When the inlet is positioned at an angle of attack, the surrounding entrance's lips are further exposed to the freestream, causing the shock to further bow towards the passage, as seen in the Mach number contours. In addition to an increase in the mass capture, the small curved cowl on the bottom section separates the flow on the lower section more than the on-design case (see Figure 32a-c). This development is seen from the 3rd to the 6th Station (compare Figure 32a-c to Figure 45a). Figure 45b-c illustrates the Mach number and Pitot static pressure ratio at the exit plane of Scoop at a 3° angle of attack. The solutions seem to enlarge the low energy zone of the upper region, created by a greater shock boundary layer interaction, which induces a larger separation on the upper wall compared to the on-design case (compare Figure 34a,b to Figure 45b-c).

The Scoop's off-design mass capture increased by nearly 20% compared to its earlier on-design conditions. Scoop's integrated forces, mass flow rate and averaged temperature are significantly reduced compared to the on-design Baseline counterpart case, by 4.81%, 9.5% and 18.87%, respectively. At this point in the design, the recessed elliptical cowl lip modification still demonstrates its effectiveness, since a direct shock to wall interaction is very minimal.

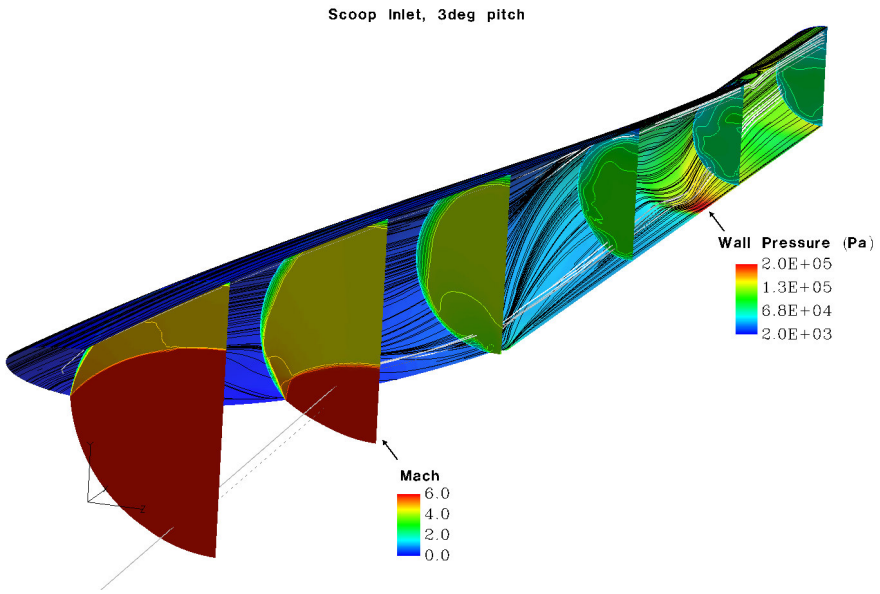

(a) Mach contours, oil-flow and Pressure (Pa) at the surface

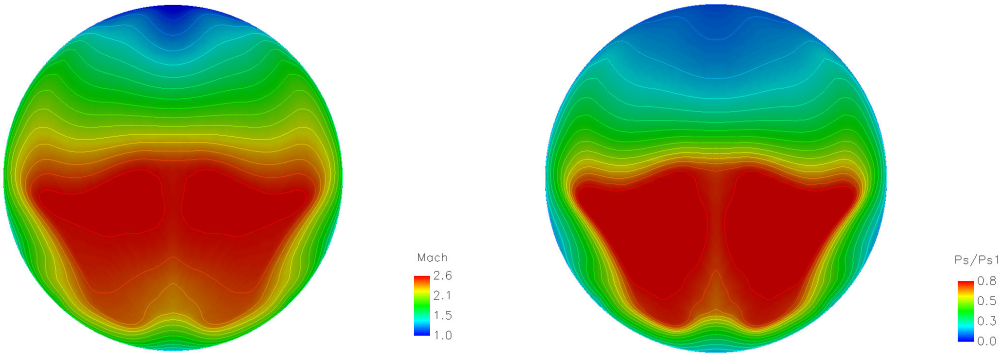

(b) Mach number

(c) Normalized Pitot Pressure

Figure 45: Off-design Scoop inlet results for 3° pitch.

Figure 46a,b provides two views of the oil flow results on the Scoop inlet pitched at 3º as seen from the upper back side, one of its entirety, and one of a close-up. These pictures identify the origin of a separation just past the conical curvature. This occurs as the second conical pressure wave interacts downstream with the surface at an off-design point. In this location, the inlet turns from an elliptical cone shape into a circular passage, causing a small expansion to occur

followed by a compression. During this pressure variation, the side wall shear layer coalesces with the top and then separates, similar to the effects captured in the cases above, unfolding a tight version of an owl structure typical of a shock boundary layer induced separation. These flow patterns show qualitative trends as those shown by similar shock to boundary layer interaction experiments (Ref. 10).

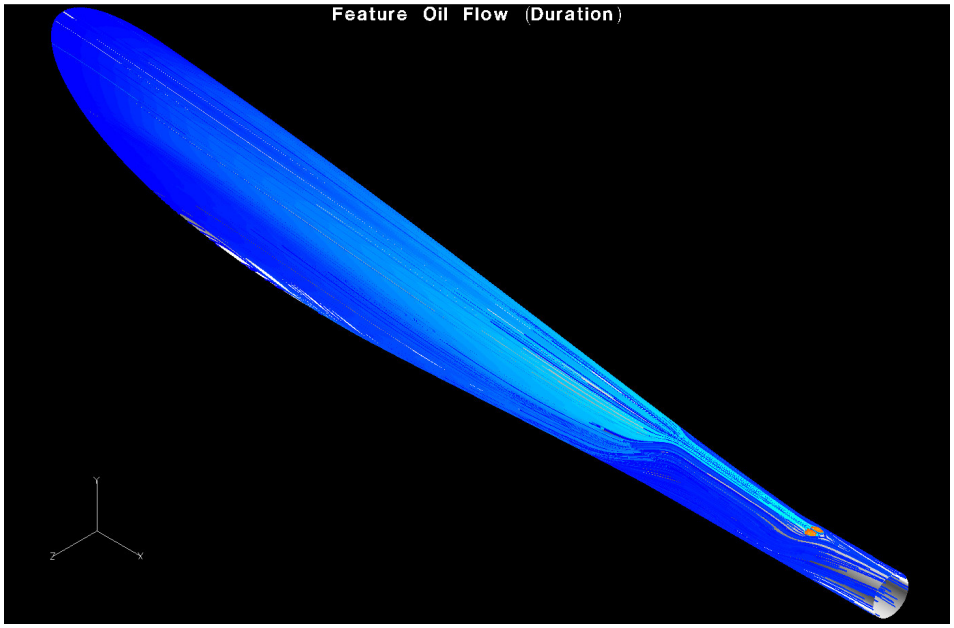

(a) Iso-view of the upper surface

Figure 46: Off-design (3° pitch) Scoop inlet oil-flow as normalized shear scalar.

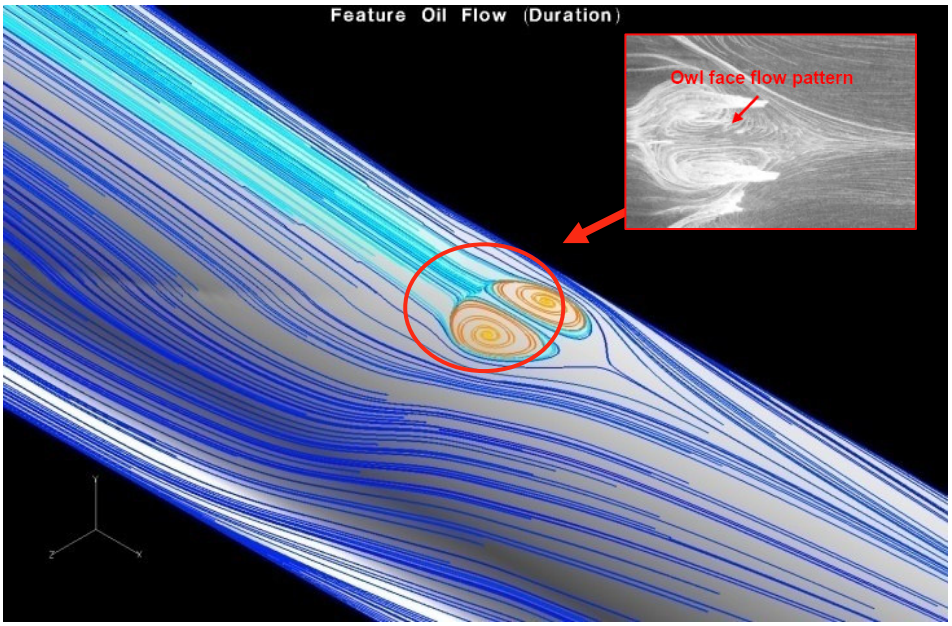

(b) Close-up of separation region at shoulder

"Figure 46 continued"

Figure 47a-c reveals a very complex three dimensional interplay of the entire non-symmetrical flow just as observed in the Baseline geometry. In Figure 47a, the Mach number contours are shown at four different *x*-planes, and the oil-flow is contoured to a normalized duration or time scale and combined with a few streamlines from the upcoming largest rear separation. When the inlet is positioned at a sideways angle of 3° yaw, the surrounding left side of the inlet is further exposed to the freestream, causing a small expansion from that side and a stronger bow shock interacting from the right side. This initial interaction later creates a strong turning of the flow which wraps around the walls, shearing off a larger growth layer and releases an integrated swirl of 11.2 (see 1st to 4th Stations, Figure 47a). Again, the low energy lobe of separated flow twisted counter-clockwise and clockwise like the others, but in a very coherent circular manner.

The oil flow as well as the streamlines selected illustrate the swirling effects and the more accented undulations of its trajectory (compare Figure 32a to Figure 47a). In contrast to the previous two Scoop cases, the oil flow solution at the walls shows a general coherent swirling surrounding the entire inlet in the counter-/clockwise direction as the compressed air travels downstream, rather than an undulation (up and down) throughout the inlet (compare Figure 47a to Figure 32a-c and Figure 45a). This development offered the worst values compared to all the other cases, due to a greater flow spillage, the largest drag and total pressure losses. In comparing this prototype to the on-design Baseline counterpart results, its integrated forces, mass flow rate and averaged temperature are significantly reduced by 22.18%, 28.47% and 23.95%, respectively. Figure 47b-c illustrates the Mach number and Pitot static pressure ratio at the exit plane of Scoop at 3° angle of yaw respectively. Similar to the previous case, the solution seems to enlarge the low energy zone on the upper region, in addition to creating a strong circulation in more than half of the left side. This lopsided separation can be traced back to the top left side of this configuration, originally produced by the offset inflow passing across the projected leading edges.

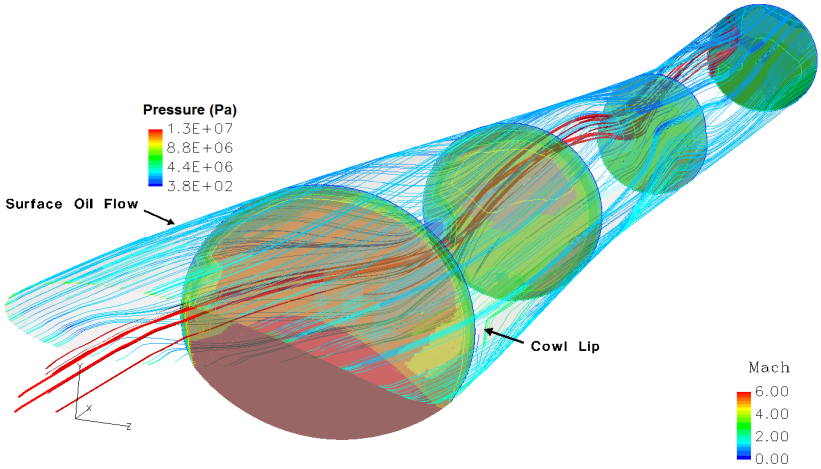

(a) Mach number, oil-flow scaled to P (Pa) and streamlines

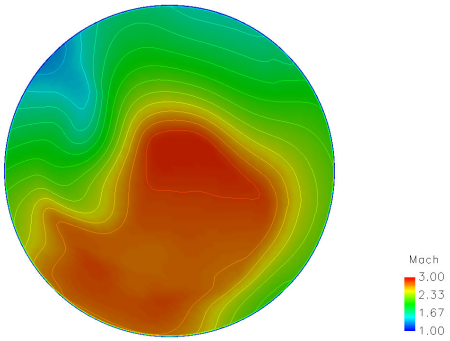

(b) Mach number at exit

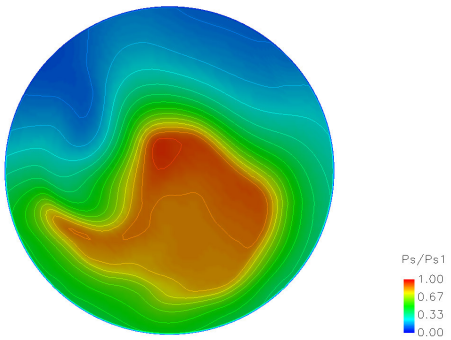

(c) Normalized Pitot Pressure at exit

Figure 47: Scoop inlet results at off-design (3° yaw).

Additional figures are shown below for: 1) six *x*-planes positioned along the inlet and frontal view of the surface's oil flow and *x*-plane over 2) the cowl and 3) the isolator/exit downstream point, Figure 49 and Figure 49a,b respectively.

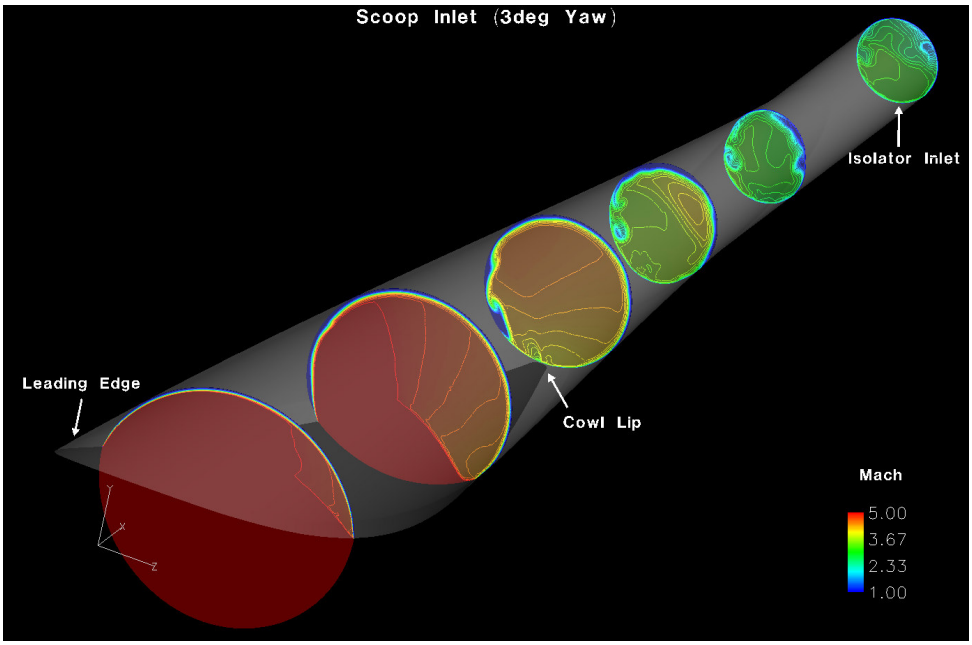

Figure 48: Upper iso-view Mach number contours at x-planes.

The oil flow unmistakably demonstrates how right after the cowl location, during the second (lopsided) pressure interaction before the configuration varies into a circular shape, the flow shifts its rotation from a counterclockwise into a clockwise direction. The variation of this rotary motion occurs from its bottom lip towards the upper region (see Figure 49b-c). This results in a larger shear layer separation and pressure losses as the flow travels downstream.

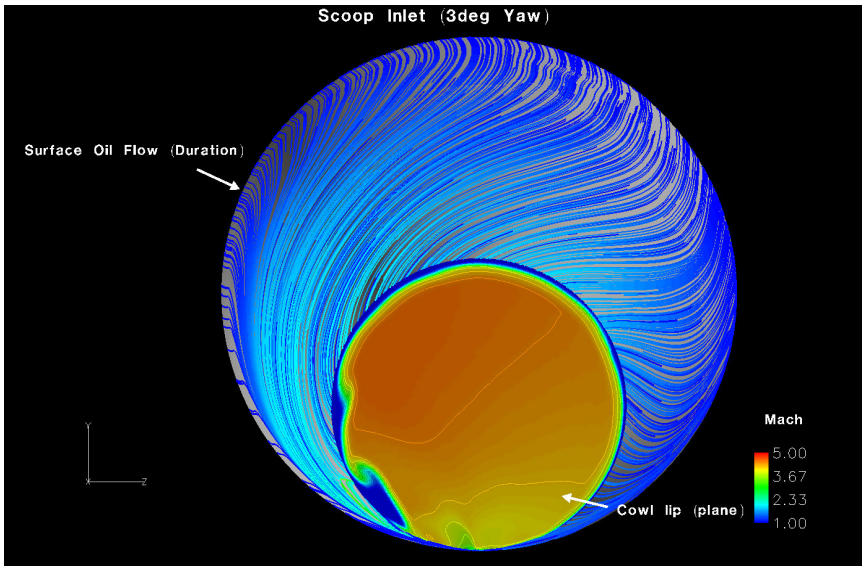

(a) Front view, oil flow and Mach number contour at cowl lip *x*-station

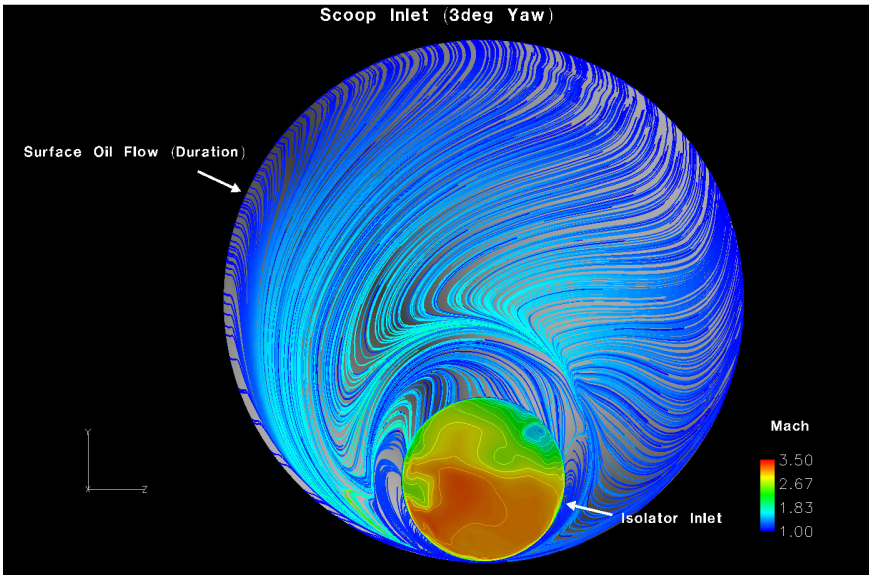

(b) Frontal view, oil flow and Mach number contour at exit *x*-plane

Figure 49: Scoop inlet results at off-design (3° yaw).

3.3.4 Discussion of Results (Off-Design Inlets)

Table 5 compares the integrated performance values at the exit plane and drag coefficients for all three geometries at off-design conditions.

Table 5: Normalized inlet results (Off-Design).

Configuration	Pitch (^{o})	Yaw (^{o})	τ_i	m'	T_{ave}	C_d
Baseline	3	0	1.07	1.11	1.12	0.543
	0	3	0.97	0.97	0.96	0.492
Jaws	3	0	1.02	1.01	0.90	0.223
	0	3	1.07	1.02	0.92	0.187
Scoop	3	0	0.95	0.91	0.81	0.224
	0	3	0.78	0.72	0.76	0.182

Again, Jaws yields the least drag coefficient compared to the other two geometries. The calculated thrust based on the pressure ratios at the exit plane reflects that Scoop and the Baseline inlets yield higher pressure losses and capture less mass at yaw versus pitch deviation. Jaws, on the other hand, increased its losses and while decreasing the mass captured for the pitch compare to the yaw. The drag coefficient for both innovative inlets is similar and much smaller than the Baseline design.

Final comparison is derived with a simple figure of merit. Traditional figures of merit used for typical aircraft engines retain their utility even in hypersonic propulsion systems such as those studied herein.[81] The physical quantities are generalized in terms of specific thrust, fuel consumption, impulse, air/fuel ratios and overall system factors. When comparing the inlet prototypes, the global performance parameters considered are limited to percentages or ratios of their thrust, drag and capture mass flow rates. The final points of merit are

evaluated by just the thrust, since they are all specifically designed for common freestream and fuel injection conditions. In Chapter 5, the thrust computed at the back of the shortened combustor section could be referred to as uninstalled, and includes the internal drag forces throughout the inlets.[82]

3.4 CONCLUSIONS REGARDING THE ISOLATED INLETS, ON-/OFF-DESIGN

The dual-plane compression strategy used in Jaws is less prone to interaction with the near wall flow than the other two inlets. In general, the Scoop flowfield gives rise to a relatively larger region of low pressure recovery on the upper surface, while the Jaws design yields a pattern of four such regions on the horizontal and vertical axes of symmetry.

The mass flow rate captured by the inlets and integrated forces across the exit plane is slightly higher for Jaws and lower for Scoop compared to their Baseline counterpart. The temperature always ends low for Jaws and much lower for the Scoop configuration relative to the normalized value. The overall values tabulated for Scoop seem lower due to lesser entrainment, but its drag coefficient and thrust to mass capture ratios are higher than the Baseline configuration (refer to Table 4 and Table 5).

In both streamline traced inlets (Jaws and Scoop), the flowfield distortions are due to shock boundary layer interactions as to those found in the Baseline inlet. Although interactions captured by the viscous simulations for the on-design conditions increase inlet losses, they create a region of enhanced turbulence in the

isolator, which later yields better mixing of air and fuel. This significantly augments chemical reactions and improves the overall factor of the hypersonic propulsion system. Overall, these innovative inlets mitigate some of the issues encountered in traditional configurations.

In general, Jaws inlet shows higher efficiency and less pressure losses at on-design, while both innovative inlets (Jaws and Scoop) underperform during off-design conditions when compared to the Baseline configurations.

CHAPTER 4: DEVELOPMENT OF A SUPERSONIC COMBUSTOR CONFIGURATION

In this chapter a series of design features are elaborated via a parametric study of a typical supersonic combustor, resulting in a desired circular combustor configuration to best fit these novel scramjets. The research begins with initial work conducted on rectangular configurations, moving from a single to multiple injection ports. The locations and directions of the fuel injections as well as the development of a single cavity used as a flame-holder are also critical features when designing an effective supersonic burner. Based on their overall performance (e.g. injection penetration, flame anchoring characteristics, mixing factor and ultimately thrust), the rectangular configurations with the highest mixing factor suggest equivalent circular prototypes. These circular combustors are transformed with many similar features and flow conditions for comparison of integrated inlet/combustor configurations.

4.1 SUPERSONIC COMBUSTOR'S CAVITY

Wall cavities have gained the attention of the scramjet community as promising flame-holding devices, owing to results obtained in flight tests and to feasibility demonstrations in laboratory scale supersonic combustors. However, comprehensive studies are needed to determine the optimal configuration which will yield the most effective performance. Numerous geometries have been tested to improve the mixing characteristics of fuel injection ports during the National

Aerospace Plane (NASP) program[83] and in recent years. The cavity flame holders, as an integrated fuel injection/flame-holding approach, have been proposed as a new concept for flame holding and stabilization in supersonic combustors.[84] Numerous examples of dual-mode scramjet flight tests (hydrogen fueled)[85] and other experiments (hydrocarbon, kerosene type fueled)[86, 87, 88 and 89] showed that the use of a cavity after the ramp injector significantly improved the hydrocarbon combustion factor in a supersonic flow. Similar flame stabilization zones have being investigated by Ben-Yakar et al. (Ref. 95) utilizing solid fuels.

In supersonic combustors we must mitigate the ignition delay effect: High air velocities through the engine make it difficult to keep the air/fuel mixture mixing and burning, due to low temperature and/or incomplete reactions. As a result, if the chemical time scales are equal to or greater than the residence time, the fuel will react outside the combustor. Extending the length of the combustor introduces further losses. Both might result in insufficient chemical energy to thrust for the vehicle (see Figure 50).

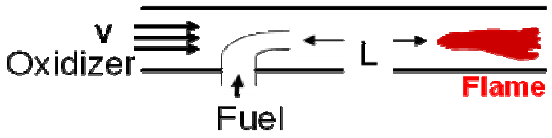

Figure 50: Schematic of key combustor physics

The solution is to create a cavity as a flame holder to reduce the ignition delay time and maximize combustion, improve fuel-air mixing and stabilize the flame. The trapped vortex combustor offers several advantages over more

conventional combustor designs. Relative to bluff-body and rearward facing steps, the trapped vortex approach is stable over a much wider operating range.[90, 91 and 92] Relative to swirl-stabilizer combustors, the main recirculation zone is shielded from minor flow upsets that may extinguish weakly stabilized swirl flames. Therefore, the trapped vortex combustor provides flame stabilization over a wide range of overall fuel-air mixtures, a simple and compact flame, enhanced heat-release rates, improved operability and lower weight, and even a lower cost.

The flow field inside the cavity is characterized by vortex formations and flow regions of recirculation which increase the residence time of the fluid entering the cavity. Because the drag associated with flow separation is much less over a cavity than a bluff-body, a cavity within the combustor region provides a stable flame holder and a relatively small pressure decrease. A rectangular cavity driven by a free shear layer provides a well-defined configuration to investigate the flow separation and reattachment process. Cavity flows are characterized by two basic types: open and closed cavities, as shown schematically in Figure 51.[93 and 94] The closed cavity has a coupling effect of the reflected acoustic waves and flow vortex writhing in the cavity secluded by the shear layer. As shown in Figure 51b, the open cavity design typically includes an angled rear wall that serves to suppress the unsteady nature of the free shear layer. Opposite the closed cavity, this configuration does not couple the reflected acoustic waves, while it reduces the cavity oscillations. This is accomplished by eliminating the generation of traveling shocks inside the cavity.[95 and 96] Studies conducted using supersonic scramjets have concluded that open cavities result in a smaller drag

penalty.[97] The longest cavities (*L/D>10*) produce vortex shedding, creating cavity oscillations and unstable flames. On the other hand, the shortest cavities do not produce vortex shedding issues, but lack sufficient air entrainment needed to sustain the combustion process.[98] For this research, medium-sized cavities (3<*L/D*>*5*) are examined.

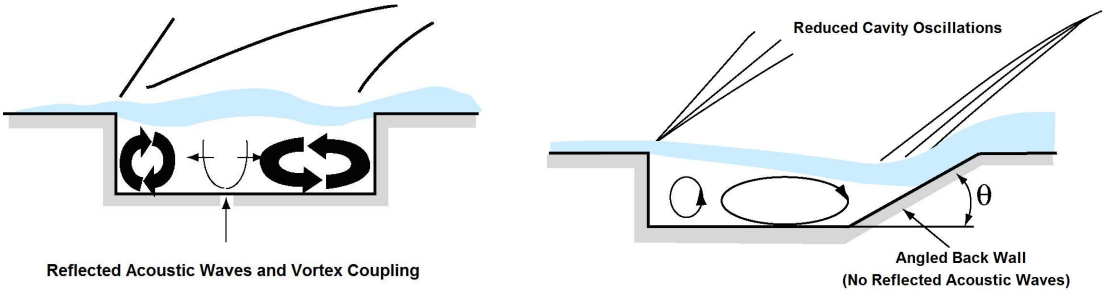

(a) Closed cavity (b) Open cavity

Figure 51: Typical cavity combustor designs

4.2 INJECTION STRATEGY

Critical to the performance of any air-breathing engine are the successful mixing of the fuel with the incoming flow, and the ability to initiate and maintain combustion. This is particularly true for the supersonic combustion process in a scramjet. The fuel should be injected with minimal disturbance to the airflow, yet maximum factor of fuel-air mixing. Scramjet fuel injectors can be conveniently categorized into three types:

(1) Flush wall injectors—In this design, fuel is injected into the scramjet duct flow from an orifice flush with the wall. Except for the presence of the

orifice itself, the duct wall shape is not altered by the injector. Therefore, flush wall injectors are considered non-intrusive;

(2) Ramp injectors—In this design, fuel is injected from an orifice located at the base or along a protuberance from the wall which is contoured to improve mixing and penetration of the fuel;

(3) Strut injectors – In this design, the injector orifice is suspended away from the wall by a strut. When compared with the flush wall injector, ramp and strut injectors are more intrusive to the primary combustor airflow stream.

A strategy which serves to enhance the fuel/air mixing process involves utilizing backward facing step geometry within the combustor region to produce streamwise vortices within the cavity formed by the step.[99] The backward facing step serves to generate a recirculation zone of hot gases within the cavity region located downstream of the step. The circulation of the hot gases provides a continuous ignition source within the combustor. Fuel injection locations can be optimized to take advantage of the vortex flow to supplement the fuel/air mixing and to stabilize the flame. While this approach can provide sustained combustion, it produces relatively-high stagnation pressure losses. This concept provides a fuel injection/flame-holding mechanism which has generated considerable interest as a new concept for flame holding and stabilization in supersonic combustors.[100] The cavity flame holder design is being developed as a means to provide sustained combustion and minimal stagnation pressure losses.

The current state-of-the-art in hydrocarbon scramjet technology relies heavily on non-intrusive flush wall fuel injectors coupled with a flame holding

cavity. The hardware structures for these devices are difficult to maintain inside the extremely harsh environment of a scramjet combustor and are often complex. The ignition issue may require scramjet-based propulsion systems to carry heavy solid-fueled gas generators, but liquid fuel designs are typically utilized. The heavy generators reduce available payload for fuel at the low speeds. The liquid-fueled generator design includes flush-wall fuel injection, wall-mounted flame holding structures, and techniques to enhance the atomization and vaporization characteristics of liquid fuels. [101, 102]

In the design of a scramjet combustor, the location of the fuel injection ports and the flame holding concept are significant considerations for flame stabilization and propagation downstream. To improve combustor performance, fuel and air must be mixed within the region near the fuel injection orifices (see examples in Ref. 62).

Angled fuel injection is an additional design consideration for achieving improved mixing and flame stabilization. Injection port angles of 30º, 60º, and 80º are typical along with the conventional practice of transverse, 90º injection of fuel from a wall orifice. As the fuel jet interacts with the supersonic cross flow, a bow shock is produced as shown in Figure 52 for a traverse injection scheme. As a result of the interaction, the upstream wall boundary layer separates, providing a region where the boundary layer and jet fluids mix within a subsonic region upstream of the fuel jet exit (Refs. 25 and 77). The separation region upstream of the injection location, the recirculation region downstream of the injection

location, the expansion-barrel shock and the bow shock formed by the fuel/air interactions are noted in Figure 52.

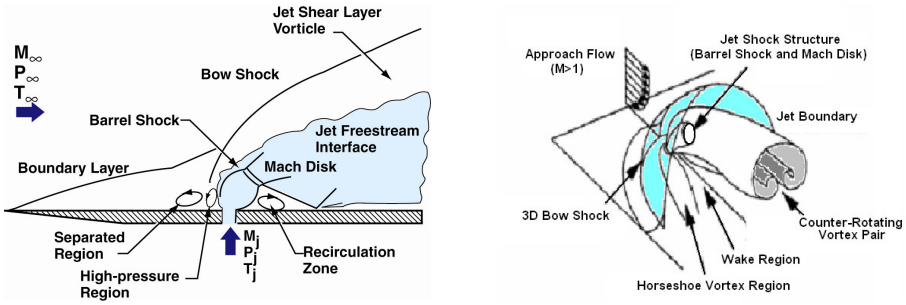

(a) 2-D (b) 3-D

Figure 52: Schematic of the under-expanded transverse fuel injection flow field structures.

This study numerically investigates the flame holding and combustion enhancement realized when a cavity is used simultaneously with fuel injection locations both upstream of the backward facing step and at strategic locations within the cavity and on the downstream ramp surface. With the use of a cavity mixer and flame holder, the location of the fuel injection and the angle of injection stream relative to the primary airflow stream are important parameters investigated in the numerical study. These parameters have an effect on the pressure loss, combustion stability, and the overall mixing factor. The computational study investigates the counter-balancing effects of pressure loss and combustion factor for various fuel injection locations and fuel stream angles to determine the optimum cavity-based fuel injection system.

4.3 RECTANGULAR COMBUSTOR DEVELOPMENT

As previously cited, numerous researchers in the supersonic combustion area have agreed on the most driven vortex results inside "open" cavities at Mach numbers from 2 to 3, yielding a L/D from 3 to 5. Closed cavities offer better flame holding characteristics for subsonic flow combustors, like those encountered in aircraft turbine engines. As described in Chapter 3, the entrance flow characteristics are near 2.5, thus the selected cavity design has a L/D=4. The flame holder at this specific dimension is utilized to: (1) provide a recirculation area where the fuel and air can be partially mixed at low velocities; (2) control shockwave interactions with partially or fully-mixed fuel and oxidizer; (3) form coherent flow structures containing unmixed fuel and air, wherein a diffusion flame occurs as the gases progress downstream; and (4) reduce the ignition delay time and provide a continuous source of chemical radicals to establish the chemical reactions within the shortest distance possible.

4.3.1 Analysis

In this section, three selected rectangular configurations are recalled from a previous study done by the author in collaboration with others on rectangular combustors (Ref. 22). The first case looked at a single normal injector, positioned on the top and L/2 upstream from the cavity (see top injection in Figure 54). The second case computed the effects when two perpendicular injectors are positioned upstream from each other (L/2) and at separated sides (see top and bottom injections in Figure 54). The third case is a fully coupled rectangular combustor

with two rows of injectors situated like the second case (in the downstream direction, x), with additional alternating or interlacing injectors in the span-wise direction, z, for a total of 18 injectors (see Figure 59). Figure 53 shows a sample of a computational domain for a combustor as computed herein. A structured mesh is employed to analyze the region of interest for the rectangular scramjet. The configuration is symmetric about the vertical z-plane, and thus only half of the scramjet is computed using a structured mesh. The computational domain was divided into many zones: one zone for each of the fuel injectors, one for the entire combustor rectangular core, and one for the cavity. As shown below, the grid was clustered near the walls to resolve the boundary layers and viscous/inviscid interactions (Figure 53). For the single and double fuel port cases, about 1.5 million points were employed. For the third configuration, nearly 10 million total points were utilized.

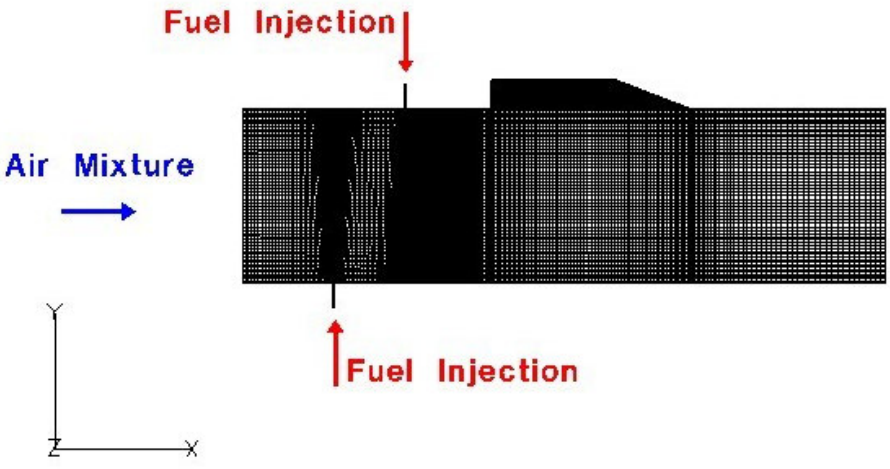

Figure 53: Grid structure for a combustor configuration.

The grid indices (*i*, *j* and *k*) are generally oriented in the streamwise (*x*), vertical (*y*) and spanwise (*z*) axes respectively as shown above. These subsequent cases were analyzed with the full 3-D steady Navier-Stokes equations together with a *k-w* model without body forces or external heat addition. The time and spatial accuracy used for all calculations was 2^{nd} and 3^{rd} order, with a Gauss-Seidel iterative matrix solution scheme correspondingly. The problems were initialized with uniform inflow conditions (M_∞=2.0, T_∞=1,000 K and ρ_∞=0.26 kg/m^3) throughout the combustor's core, fuel properties set (M_{fuel}=1.0, T_{fuel}=300 K and ρ_{fuel}=3.0 kg/m^3), and injectors aimed in their respective directions. The cavity domain was initialized at freestream conditions with the exception of velocity which was set at u= -0.01 m/s. CFL varied from 0.1 to 2.0, and the L2 norm convergence was reached around 86 and 408 hours later using 64 processors, when single/double injection or full geometry was employed respectively.

Top Single Injection:

In this analysis, only an axisymmetric slice of the combustor geometry was computed. Figure 54a,b shows the temperature surface of the liquid fuel droplets, the Mach (Figure 54a) and pressure (Figure 54b) contours of Jaws' combustor configuration at the center/symmetry plane (k_{min}).

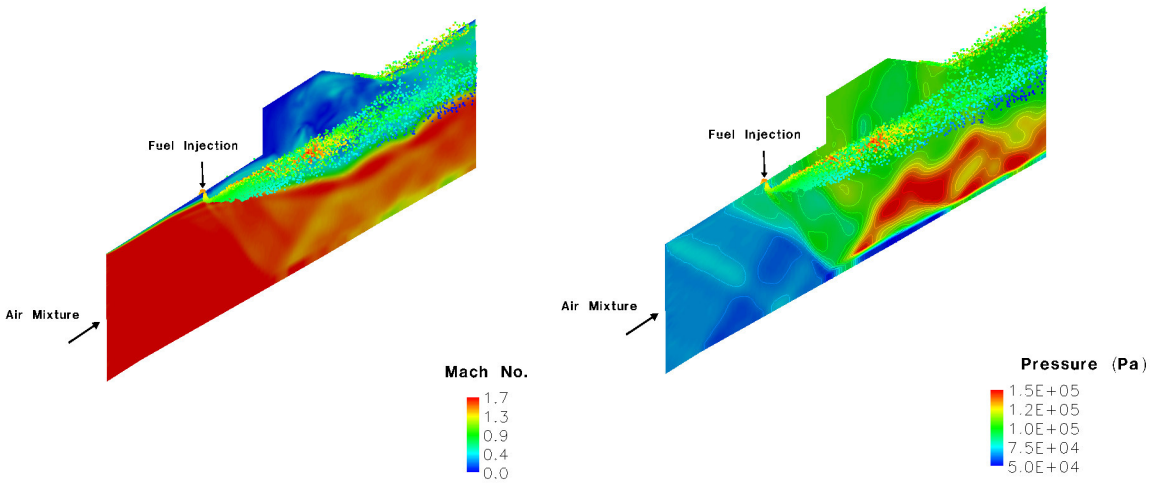

(a) Mach number (b) Pressure (Pa)

Figure 54: Contours at center z-plane, single perpendicular injection.

The jet penetration and complete combustion process is shown in Figure 55, which displays molar concentrations of various species. The cavity recirculation zone transports some of the hot combustion products back toward the combustor face (along the cavity's back wall) and ignites the incoming fuel and air as they mix in the combustion chamber.

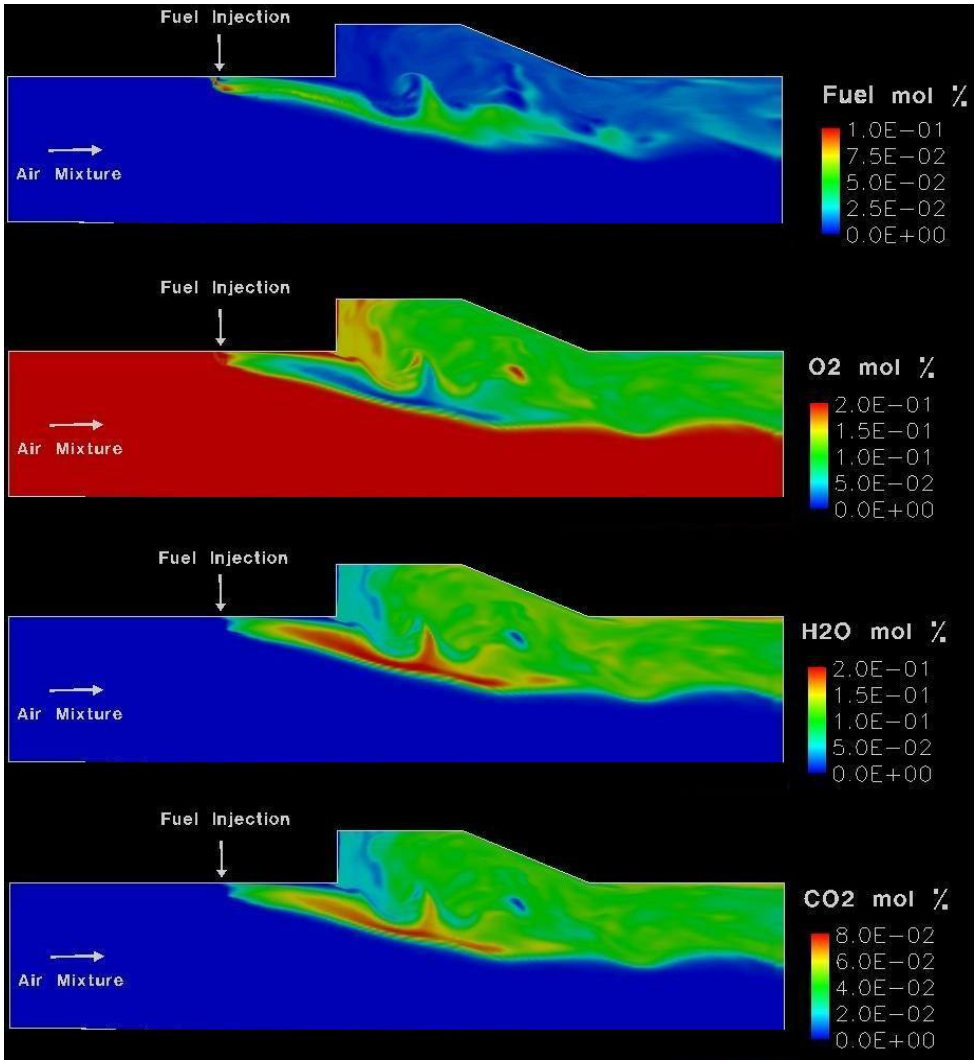

Figure 55: Fuel (JP8), Oxygen, Water and Carbon Dioxide mole fractions (from top to bottom) at the center plane for a single perpendicular injection configuration combustor.

The mean temperature in the cavity is close to the stagnation temperature of incoming airflow. The highest production of H_2O and CO_2 coincides with the highest heat addition. These recirculation zones form an exceptionally stable combustion region and are aerodynamically stable over a wide range of fuel-air ratios, temperatures and pressures. Furthermore, the products from the fuel-rich-

zone remain within the cavity (see the two upper figures in Figure 55) and drive a stable combustion system. Mixing occurs within the shear layer above the cavity as shown in Figure 54 and Figure 55. The vortex diameter is about the size of the cavity depth. By comparing the injected fuel to the burned mole fraction values at the exit, the combustion factor or burned fuel is estimated at about 70%.

Top and Bottom Injection:

The *JP* fuel is introduced into the engine through rounded injectors positioned perpendicularly into the airflow upstream of the combustor. For the Baseline inlet, injection occurs from the top and bottom walls (Case 3a). In this case, the center of the combustor is injected by two circular injectors mounted in the combustion chamber of the duct at different locations lengthwise. The bottom injector is upstream while the top injector is downstream. In addition, the cavity is positioned on the top surface, immediately after the second and last row of injectors with the dimensions noted (length equal to three times the height; and a 30^{o} ramp). These sections were designed by selecting optimal features from other common designs, coupled to determine a better combination of features.

Figure 56a,b depicts the Mach number and temperature contours of the rectangular combustor configuration at the symmetry plane (k_{mid}). It delineates this configuration and the complexity of reacting flow patterns by a double injection pattern. It also illustrates how the fuel stream originates from the top and bottom ports, mixing with the captured air, recirculating inside the combustor's cavity, acting as a vortex trap and subsequently dissipating or

burning downstream. A clear picture of the jet penetration and complete combustion process appears when these are considered together with those in Figure 56a,b, which exhibit mass concentrations of various species. The mixing and jet fuel penetration on the computed rectangular combustor geometry is very effective; the combustion factor is 81%.

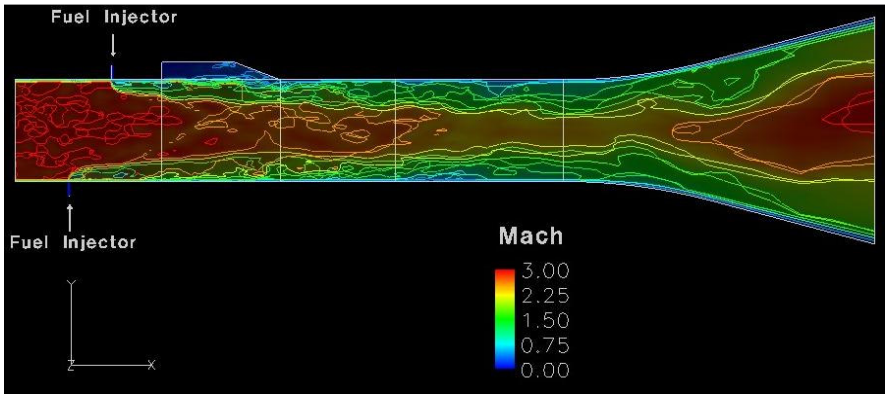

(a) Mach Number

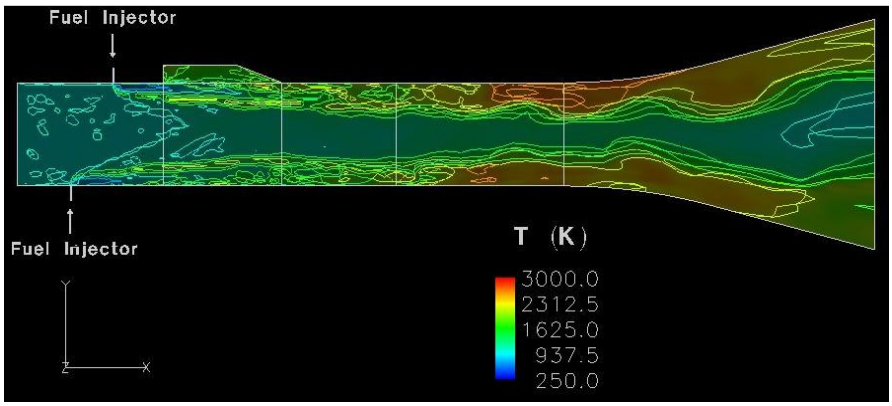

(b) Temperature (K)

Figure 56: Contours at z-planes, upper/lower dual injection.

Figure 57 (top and bottom) shows the mass fractions for the reactants (O_2 present in the captured air and hydrocarbon fuel); while Figure 58 (top and bottom) illustrates the main products CO_2 and H_2O at the symmetry plane (k_{min}). The mole fraction of the unburned fuel was further reduced by sheltering the second injection after the first one and creating additional eddies towards the TVC. Both of these figures illustrate the burning at the higher levels of water and carbon dioxide mass fractions (seen in red).

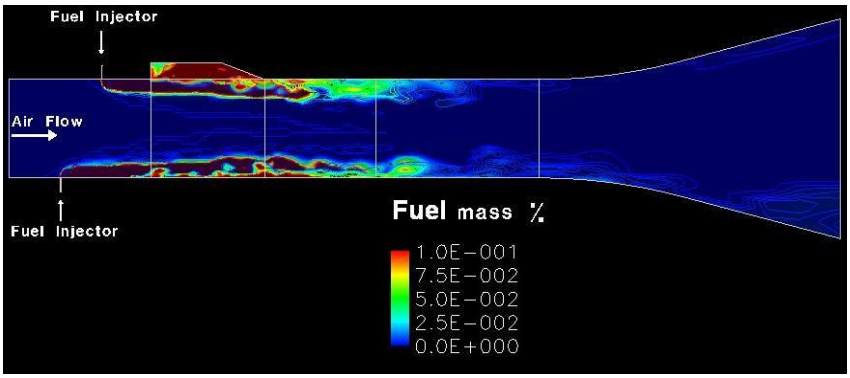

(a) $Y(C_7H_{16})$

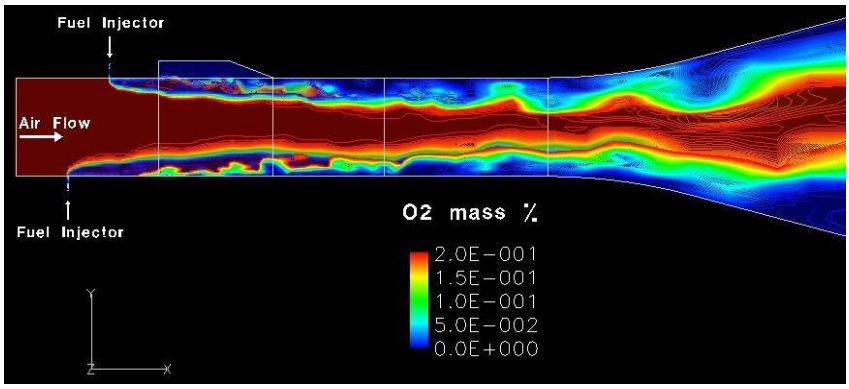

(b) $Y(O_2)$

Figure 57: Reactants at symmetry z-plane, upper/lower dual injection

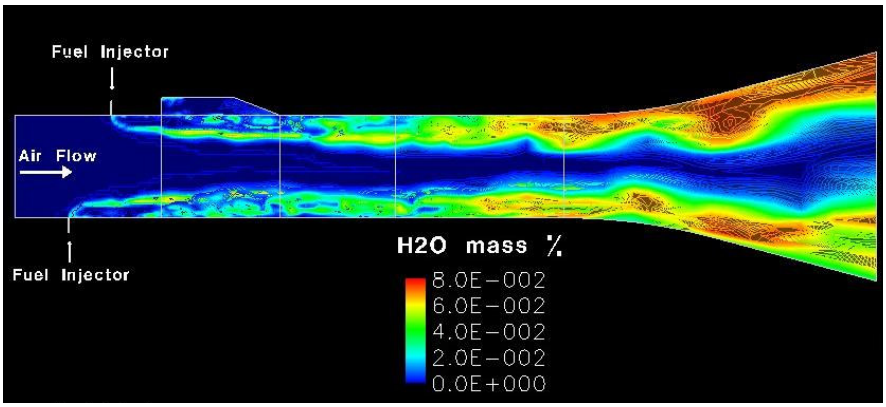

(a) Y(H_2O)

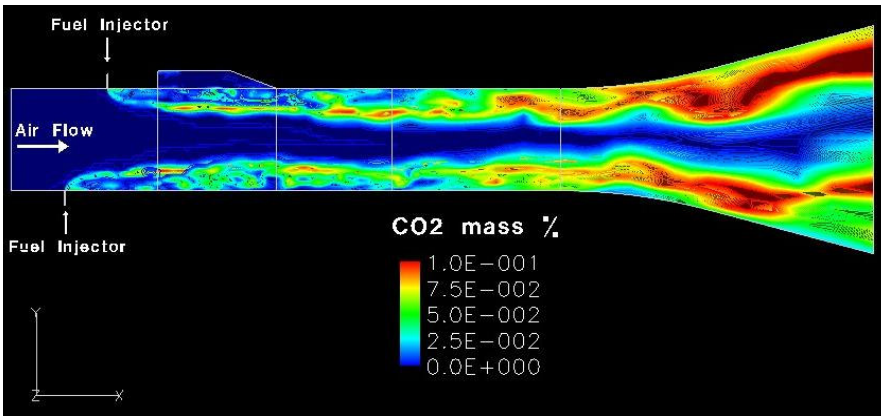

(b) Y(CO_2)

Figure 58: Products at symmetry *z*-plane, upper/lower dual injection.

Top, Bottom and Interlaced Injection:

Figure 59 shows a typical supersonic combustor with a single cavity acting as a flame holder. This configuration yielded the most effective injection strategy of those examined herein. The fuel-air mixing factor obtained was about 91%, by positioning the injectors sets 1) upstream from each other and prior to the cavity (*x*-direction), and 2) interlacing individual ports from each other (from top to bottom, *z*-direction).

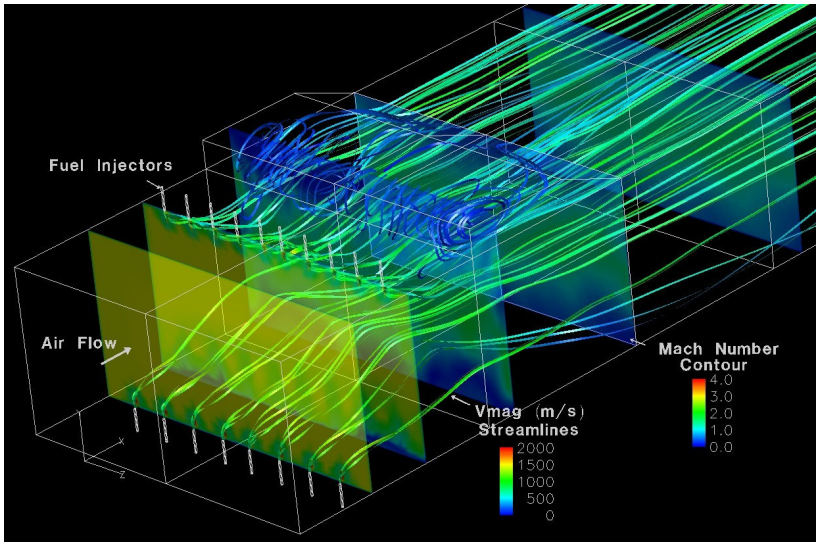

Figure 59: Dual row and interlaced injection strategy configuration.

As seen in Figure 60, the vortex created recirculates the hot combustion gases within the cavity, and the gases are exhausted out of the cavity and transported along the face of the combustor. The fuel injection has been strategically placed before the cavity to direct the flow up/downstream of the airflow. Locating the fuel injection points in the forward and aft walls of the cavity drives the vortex inside the cavities.

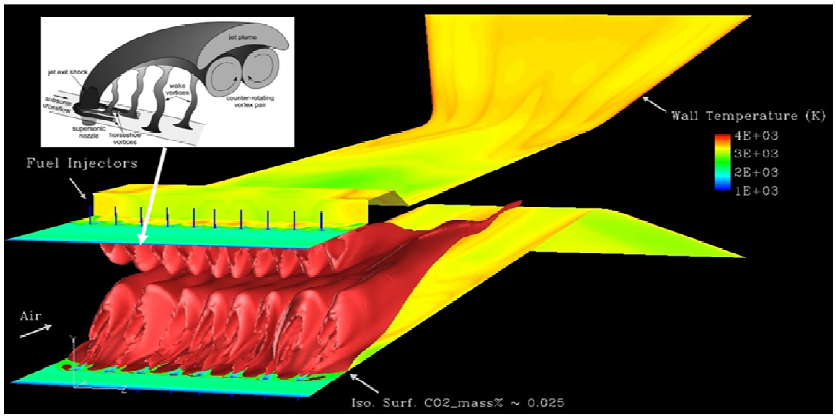

Figure 60: Temperature (K) at walls and iso-surface of Y(CO_2).

In these three analyzed cases, as in most, the intrusive fuel injectors and flame-holders are difficult to maintain inside the extremely harsh environment of a scramjet combustor and often yield very complex features with severe internal drag penalties.[103] In addition, external ignition aids are commonly employed at low flight Mach numbers (i.e., around M=4) and may require scramjet-based systems to carry potentially heavy generators. These devices reduce available payload for fuel at the low speed takeover point. These techniques include flush-wall fuel injection, wall-mounted flame holding, and devices to enhance the atomization and vaporization characteristics of liquid fuels. In the following cases, the trends will be drawn out by using much shorter combustors. For these cases, the analysis was done on a complete chemically reacting combustor section with a truncated straight nozzle.

In a hypersonic propulsion system, unwanted flow interactions upstream in the inlets can actually have a positive impact on the downstream section. These interactions can yield a region of enhanced turbulence in the isolator, shown to have a significant effect on the combustor, since a better mixing of air and fuel can significantly augment the chemical reactions and improve the overall factor of the hypersonic propulsion system.[104 and 105] It is important to understand: (1) the three-dimensional interplay between viscous and inviscid interactions including shock-boundary layer and shock-shock interactions in the inlet; as well as (2) the positive effects due to combustion of the reacting stoichiometric fuel-air mixture described above (Ref. 6).

Very few of the critical design fixtures that factor into these previously analyzed configurations can be applied to circular combustor configurations. Additional refinement work must be conducted into different injection strategies more suitable for comparison and practicality to employ into circular combustors with/out axisymmetric inflow profiles like that described herein. The work could be further simplified by analyzing the proper injection strategy trends of these new prototypes, assuming a single (gaseous) fuel, using much shorter combustors and reducing the computational cost by using RANS (see Ref. 79 and 106).

4.3.2 Discussion of Results (Previous Rectangular Combustors)

This preliminary analysis of the Baseline hypersonic propulsion system shows that the unwanted flow interactions upstream in the inlets can actually have a positive impact on the downstream section. The main overall performance is found when combining: 1) a bottom set of the injectors positioned upstream and interlaced from 2) a second set of injectors downstream for the first set, and 3) followed by an open single cavity on the upper region. This quite complex configuration yields a combustion coefficient of about 91%. Today's state of the art on rectangular configurations resembles these geometries and despite much work for the last half century, very few insights can be applied to future innovative circular combustor configurations. For example, circular combustors do not have a top and bottom. At equal contraction ratios, cross-sectional areas and injection pressure ratios, the penetration depth and tumbling effects will change.

4.4 COMBUSTOR PARAMETRIC STUDY

As previously explored, an efficient fuel injection and mixing scheme is paramount to successful scramjet combustor design (Ref. 62). The following fuel injection strategies must provide rapid mixing of the fuel and oxidizer streams while minimizing total-pressure losses, eliminating adverse effects on combustion flame holding capabilities and maintaining the structural integrity of the component hardware. Detailed information regarding optimized fuel management strategies, vortex residence times, entrainment of the cavity flow into the free stream, combustion stability, and interactions with disturbances in the main airflow are required to support future design process. And most importantly, the combustion flame holding process is a central factor in scramjet combustor design.

As previously described, various physical processes must be considered in CFD when modeling a realistic scramjet combustor configuration containing a cavity or backward step. Some of the complexity of the fluid path includes large regions of subsonic flow, shock-to-shock and shock-to-boundary layer interactions, separated flow regions, complex mixing phenomena, non-equilibrium transfer of turbulence energy, and interactions between turbulence and chemical kinetics that may impact both the chemical reactions and turbulence field. In current scramjet combustor design, fueling strategies are important factors to ensure a robust flame-holder and desired mixing combustion factor for the scramjet combustor. As part of this study, the optimum fuel injection location

and direction are explored. In addition, the effectiveness of a single passive cavity fueling was numerically examined in a non-reacting flow. The following section of the research compares ten prototype configurations using as the inflow the average values obtained from the Baseline's isolator on-design result.

4.4.1 Overview

The location of the fuel injectors and the directed angle of the injector orifices are varied to determine the optimum injection scheme and mixing factors when using non-chemically-reacting, and later, chemically-reacting flow. The fuel injector locations include the combustor inlet region upstream of the cavity, the cavity floor, and locations on the cavity upstream step and the downstream ramp. The fuel port injection slots include combinations of angles parallel to, 27 º from and perpendicular to the airflow inside the cavity. The comparative results will indicate the fuel injection configuration with the highest mixing factor. Although an additional parametric study could compare such effects when varying energy levels or injection pressure ratio inputs, this work is limited to a constant fuel/airflow conditions throughout. As shown by several researchers, the fuel/air pressure ratio (P_f/P_{air}) derives different flow structures in the core as well as interactions inside similar cavities, due to a differential in the vortex strength and required time scales for supersonic flame holders.[107, 108] The combustors of this parametric study are selected to allow comparisons between the Baseline inlet and both new circular inlet prototypes (Jaws and Scoop). Thus, in this research, the temperature effects at the walls are ignored and their performance evaluations

will be limited to basic parameters. These basic parameters are their combustion or mixing factors and produced kinetic energy (uninstalled thrust).

4.4.2 Computational Domain

The computational domain for the combustor was divided into several zones: four zones for each of the injectors, one for the main combustor passage and another for the cavity. All the scramjet combustor configurations analyzed herein employ a structured mesh. The combustors are symmetrical in the *z*-plane, so only half of the scramjet is computed. A 2.5 million point grid was selected with clustering being employed near the fuel injection to further resolve the shock, boundary layers and viscous/inviscid interactions. Refer again to Figure 53 for an example of how all combustor grids were constructed.

4.4.3 Parametric Analysis, Averaging Strategy

Assortments of fuel injectors were placed about the cavity; details of these sites are shown below. Each symmetrical configuration was made of four injectors, with most paired into two groups, with the exceptions of Cases 4 and 8. A single cavity is positioned 70mm from the combustor inlet and ends 140mm upstream from the exit. The common height and width of the combustors' inlets are 62.5mm and 76.5mm respectively. The flush-wall fuel injectors have diameters of 3.0mm. The injectors are positioned 30.6mm laterally apart from each other. The symmetry plane is 15.3mm away from the closest injector. The cavity is recessed from the combustor inlet with a 90-degree rearward-facing step.

The configuration of this cavity, which works as a flame-holder, has a depth of 16.5mm and a length of 66mm. All cases except Case 7 feature a 22.5^{o} ramp at the downstream wall of the cavity (see Figure 61g).

Figure 61 shows all the combustor configurations with their respective injector locations and directions for Cases 1 through 9. For Case 1, the injectors are positioned toward each other and inside the cavity. The first pair is oriented perpendicular to the upstream wall of the cavity at 33mm from the combustor floor while the other pair is located at the ramp 33mm away from the bottom of the cavity (Figure 61a). Case 2 differs from Case 1 by alternating the position height of the injection. The first pair is at 33mm from the bottom of the cavity while the second pair is located 33mm away from the combustor floor (Figure 61b). In addition, the length of cavity floor for the second case is 33mm instead of 66mm. The fuel was injected for Case 3 through a pair of fuel injectors located 35.6mm upstream of a recessed cavity and at an angle of 25 degrees (Figure 61c). Another pair is positioned perpendicular to the upstream wall of the cavity at 33mm from the combustor floor as seen in Case 1. Case 4 has a row of equally-spaced injectors; 35.6mm upstream of the cavity and leaning 25º downstream (Figure 61d). Case 5 combines the first pair of injectors as shown in Case 3, but the second pair injects out of the aft ramp toward the rearward-facing step parallel to the cavity floor at 33mm away from the bottom of the cavity (Figure 61e). For Cases 6 and 7, the first pair of injectors is positioned as in the previous case, but at half of the tilted angle (Figure 61f and g). The second pair is perpendicularly aimed from the very bottom of the cavity, and about 2.2mm away from the

backward facing step. In Case 6 each pair of injectors is staggered from one another along the width of the combustor (Z direction). Case 7 is the same as Case 6 except that the injectors are not staggered but aligned with each other in the combustor. Figure 61g shows Case 7, where the position of the injectors is the same as Case 1, except the cavity has no slope on the rear face (i.e., a closed cavity).

The injectors in Case 8 are positioned as in Case 1, while the cavity is designed to be closed. In Case 9, the dimensions of the combustor and cavity are the same as Case 1 except all 4 injectors are mounted vertically in the floor of the cavity at a constant streamwise station. For this particular case, the injectors are perpendicular to the freestream and located at 2.2 mm away from the backward facing step (Figure 61i). Finally, in Case 10 one pair of injectors is positioned as in Case 9, and the other pair is positioned at the rearward-facing step parallel to the cavity floor at 33mm away from the bottom of the cavity (as are the second pairs of injectors in Cases 1 and 5) (see Figure 61j).

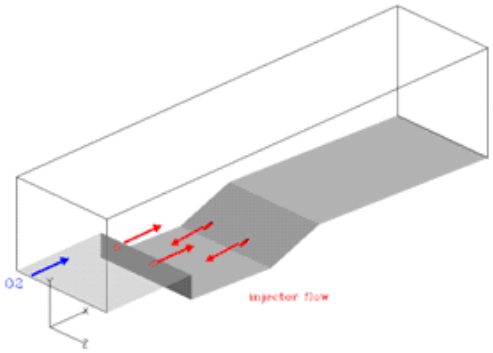

(a) Case 1

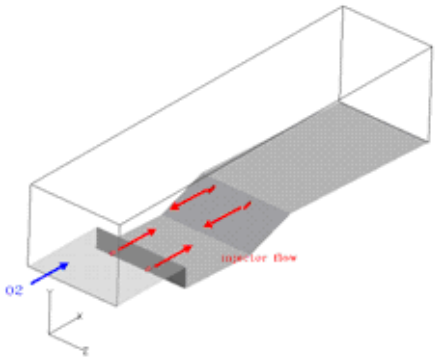

(b) Case 2

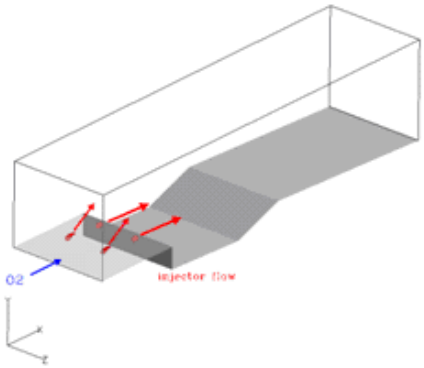

(c) Case 3

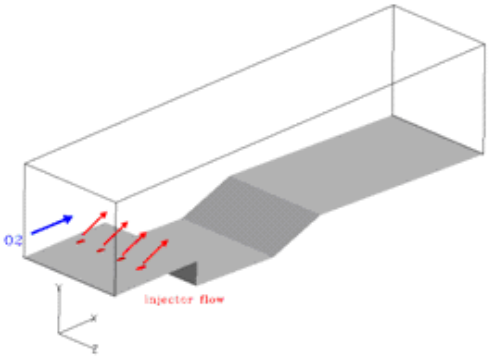

(d) Case 4

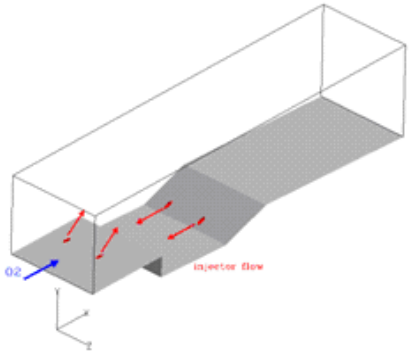

(e) Case 5

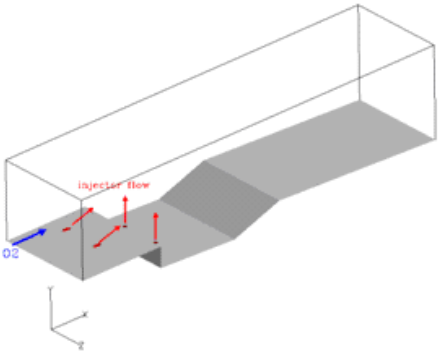

(f) Case 6

Figure 61: Rectangular scramjet combustor configurations.

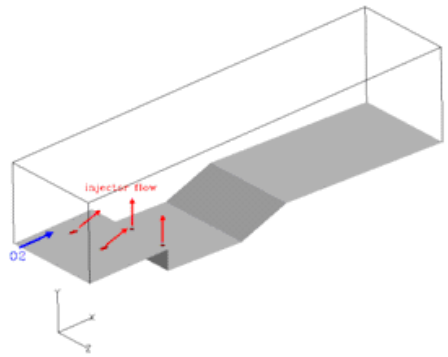

(g) Case 7

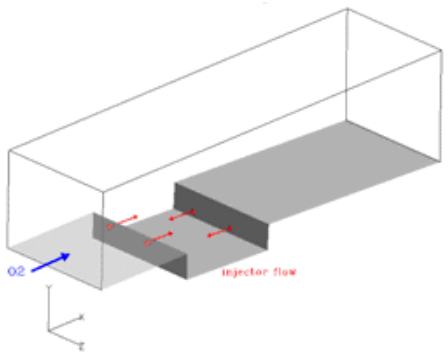

(h) Case 8

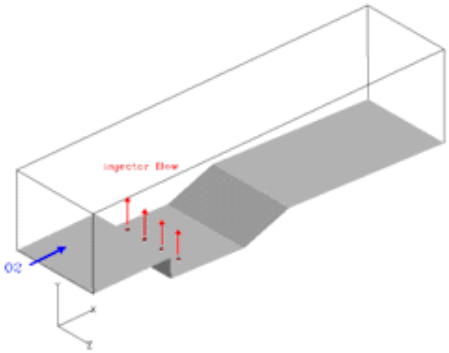

(i) Case 9

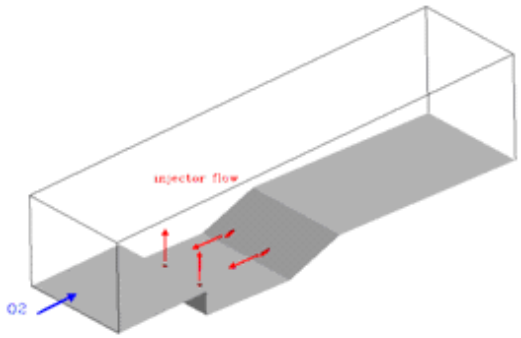

(j) Case 10

"Figure 61 continued"

Frozen Chemistry Assumption:

As explored herein, the position and direction of the fuel injection in or near the cavity can enhance vortices due to flow interactions. These vortices can yield a region of enhanced turbulence in the combustor, and produce a significant effect on the combustor, since a better mixing of air and fuel can augment the chemical reactions and improve the overall factor. Figure 62a-j shows the mass fraction of the fuel (C_2H_4) for Case 1 through Case 9 at the various selected axial locations and illustrates the complex aerodynamic flow interactions occurring in

the cavity zone as the jets interact with the incoming airflow. As expected, C_2H_4 mass fraction distribution for all cases with varying injection configurations differs from one another. However, the penetration rate for all cases with various injection locations does not appear to be significantly different.

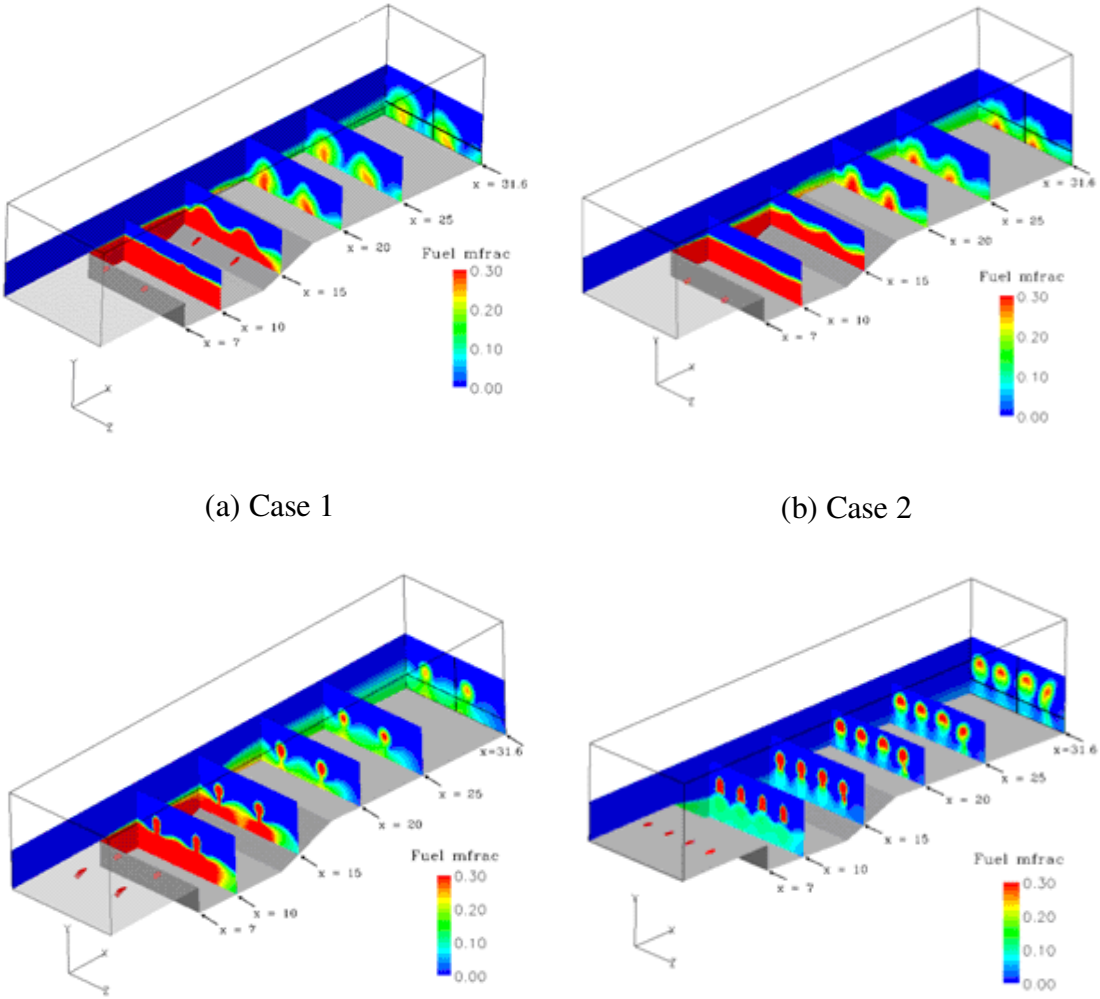

(a) Case 1

(b) Case 2

(c) Case 3

(d) Case 4

Figure 62: Fuel mass fraction at *z*- and several *x*- planes.

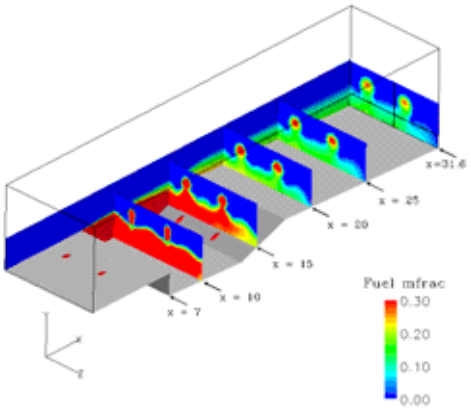

(e) Case 5

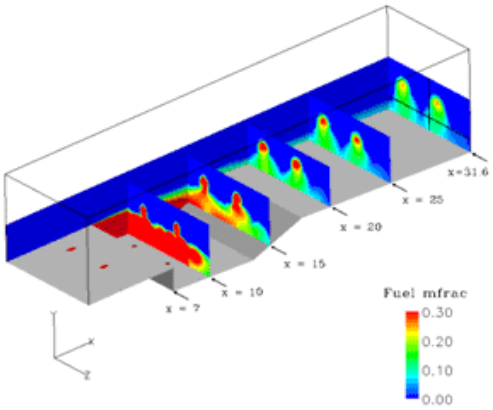

(f) Case 6

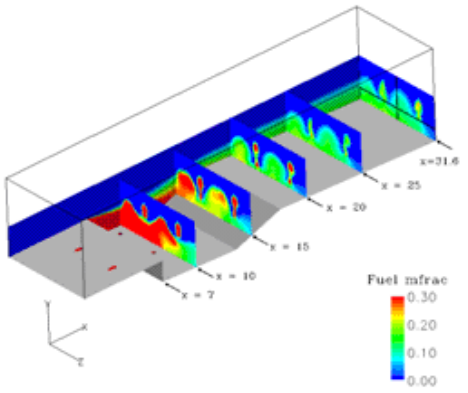

(g) Case 7

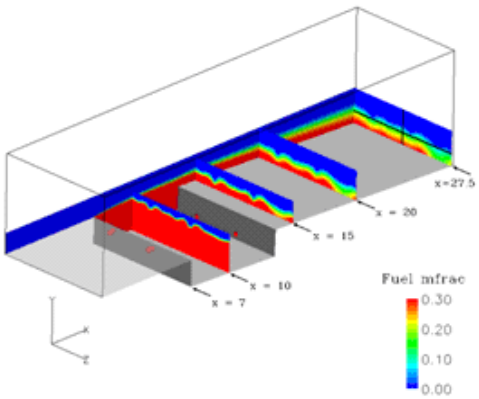

(h) Case 8

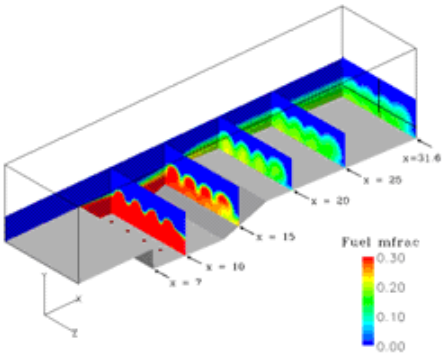

(i) Case 9

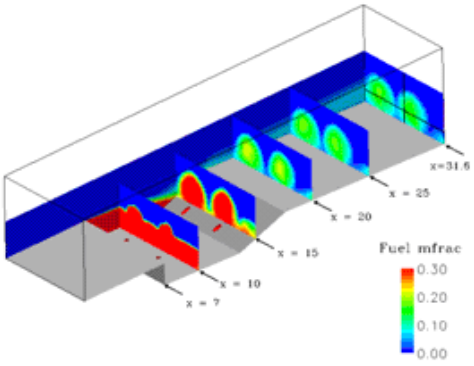

(j) Case 10

"Figure 62 continued"

For all 10 cases, the CFL was set constant around 1.0 and the L2 norm convergence was reached around 18.5 hours later using 64 processors. Since it is difficult to distinguish the mixing factor from the figure above for each case, the mass fraction of C_2H_4 and O_2 distribution was integrated at the end of the exit plane to find penetration and/or mixing for individual cases. The penetration depth is measured by the maximum distance from the walls towards the core, where the limit of the fuel is contoured throughout the length of the combustor. The mixing factor is assumed to be proportional to the fraction of the fuel mixed within the freestream for these frozen cases, versus the total amount of fuel added to the system. This mixing factor is then calculated by differentiating the integrated fuel to air ratios at the exit plane from the estimated ideal value, as if the total injected fuel mixes with air 100% (see Equation 19).

Equation 19: Frozen fuel/air mixing factor.

$$mf_{f\_mix}\% = \frac{\frac{1}{A_e}\int\left(\frac{Y_{C_2H_4}}{Y_{N_2}+Y_{O_2}}\right)\partial A}{\sum\left(\frac{Y_{C_2H_4}}{Y_{N_2}+Y_{O_2}}\right)}\times 100$$

On the other hand, for the chemically reactive cases (discussed later), the mixing factor is directly proportional to the combustion factor. For these cases, the mixing factor is measured rather as the ratio of the fuel that is consumed or depleted at the exit plane to the total amount injected (Equation 20).

Equation 20: Reactive fuel/air mixing factor.

$$mf_{r\_mix}\% = \int \frac{\sum Y_i - Y_{C_2H_4}}{\sum Y_i A_e} \partial A \times 100$$

The fuel mass fraction plots shown earlier provide insights into how the injection strategies displace fuel towards the core and spread it downstream while mixing it with air. For example: 1) for the open cavity geometry (Case 7), the fuel is highly concentrated inside the cavity with limited penetration rate (near the wall); 2) when all the injectors are positioned angled and upstream of the step (Case 4), the penetration is highest compared to all other cases and the fuel concentration remains conglomerated into a distinctive zone without mixing very well; and 3) Case 8 demonstrated a great spanwise mixing and average penetration when compared to others. Figure 63 shows integrated O_2 and fuel mixing factor at the exit of the combustor plane for all cases.

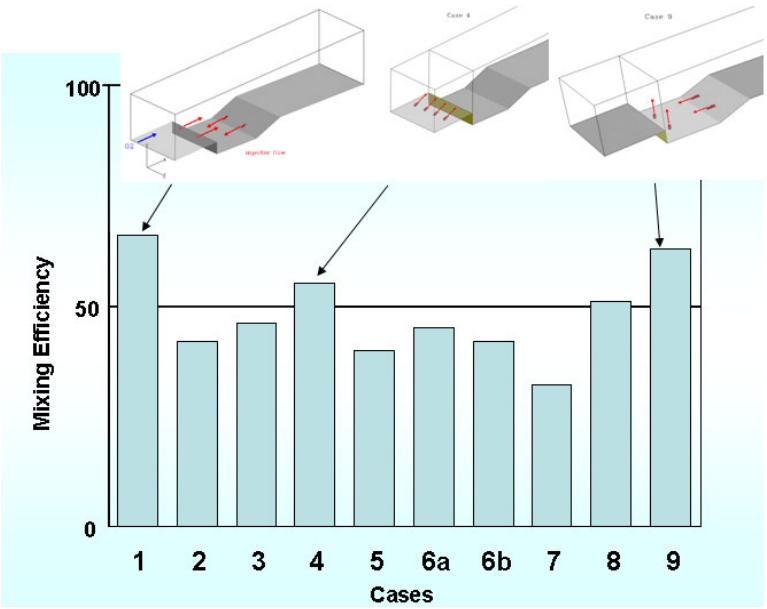

Figure 63: Mixing factor comparison; rectangular configurations.

Cases 1, 4 and 9 perform higher mixing factor than other cases. These combustors create higher turbulence which leads to higher mixing, and higher mixing results in a higher combustion factor. For Case 1, the fuel injector pattern helps drive the vortex inside the cavity continuously in its natural direction (refer to Figure 61 for geometry). The mixing factor for Case 1 at the exit plane is about 66%. The vertical penetration of the fuel in Case 4 is higher than all other cases. This is a direct result of having the injectors positioned upstream of the cavity and angled at 25 degrees, however the fuel does not mix as well in the *z*-direction (sideways). Finally, Case 9 is similar to Case 1, but shows a more dispersed pattern in the sideways direction, due to the first pair of injectors at the bottom of the cavity in the normal direction. This case did not show a higher penetration than Case 1 in the vertical direction.

The fuel penetration into the combustor in Cases 2, 5, 7 and 8 did not perform as well as in other cases. Case 2 was particularly different from the rest, due to the shorter cavity length (33mm instead of 66mm). In addition, the position of the injectors is switched compared to Case 1. The injection does not contribute to the natural driving motion of the vortex inside the cavity; in fact it is counterproductive. The configuration for Case 5 is similar to Case 1, except the first pair of injectors is upstream of the cavity at a 25 degree angle. By comparison, this injection pattern produced a mixing factor of only 40%. However, the vertical penetration for Case 5 was adequate as in Case 1, but with poor sideways dispersion. Case 7 produced only 32% mixing factor; due to its closed cavity the fuel tends to mix well only near the bottom wall of the combustor, resulting in much less penetration in the vertical direction. Case 8 is a borderline case. Having all normal fuel injectors lined at the cavity floor produces a very well distributed fuel in the z-direction. However, the fuel does not penetrate in the vertical direction as far as the three cases with the highest mixing factor.

Finite-Rate Chemistry Assumption:

The effect of chemistry was examined by performing finite rate simulation, utilizing the stipulated chemical model (refer to Section 2.3). This chemically reacting case was initialized from the previous frozen case, at a constant CFL of 2. Convergence was reached around 33.8 hours later using 64 processors. Results for Case 1 are shown in Figure 64a,b. Figure 64a shows the

Mach number contours in the XY-planes cutting in the plane of the jets as well as two YZ-planes downstream of the step cavity. The reacting calculation for Case 1 shows separation in the upper wall of the combustor while the non-reacting case does not (see the top of Figure 64a,b). This is due to strong trailing edge shockwave and boundary layer interaction in a reacting case. The bow shockwave produced by the injected fuel interferes with the boundary layer, thereby generating a separation zone in front of the injector. The recirculation zone upstream of the injector is broader than the non-reacting simulation's recirculation zone. This may result from the lifting effect of the higher temperature gas mixture reaction due to the vortices residing in the cavity. The reaction in the cavity acts to expand the gas, causing the shear layer to rise slightly. A strong trailing edge shockwave is also created as the shear layer reattaches at the angled back wall. The injected jet spans over the cavity until it reaches the trailing edge. Due to the interaction with the geometrical configuration, the shear layer over the cavity spreads vertically. The injected jet interacts with the strong trailing edge shockwave, which might play an important role in chemical reactions. Furthermore, when the trailing oblique shockwave increases the pressure and temperature of the mixture, a shock-induced chemical reaction takes place. A jet interaction with oblique shockwave results in an enhancement in the molecular mixing between supersonic air and jet fuel. The vortices generated by interaction between a shockwave and a shear layer have an immediate influence on mixing enhancement in supersonic flows, which then result in increasing the combustion efficiency. The trailing edge shock is

therefore expected to convey the flow direction behind it over the trailing edge of the cavity, increasing the mixing, the static pressure, the static temperature, and the reaction rate. The flame has lifted above the shear layer that separates the cavity fluid from the mainstream. Thus, much of the heat being released by the flow within the cavity mixes with the mainstream. The lower portion of the mainstream fuel reacts in the cavity opening. When a strong shock occurs, the flow turns and spreads the flame which is depicted by the region of high temperature (see temperature contours in Figure 64b); in return this increases the reaction rate and enhances the combustion.

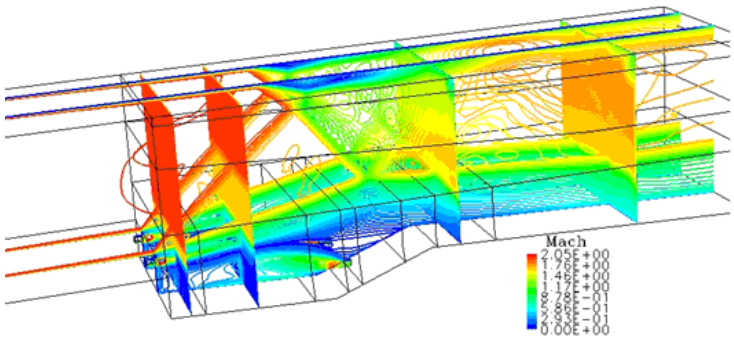

(a) Mach number

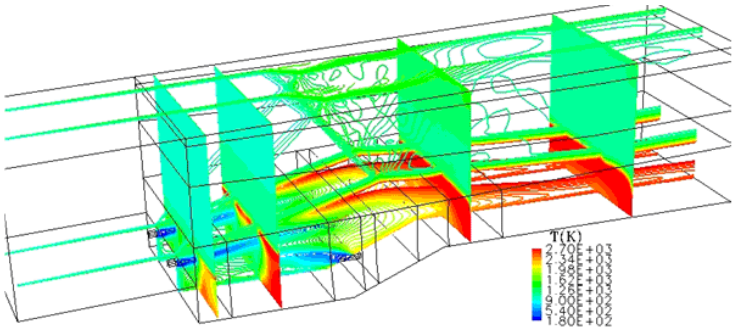

(b) Temperature (K)

Figure 64: Rectangular combustor Case 1, finite-rate chemistry.

The total mixing factor for this reacting Case 1 at the exit plane is about 72%, much better than the previously frozen case. In the reactive case, as in many others researched by the author, the chemically reacting assumption yielded about a 10% increase over the frozen postulations (Ref. 62). Considering that this geometry is quite short, about half of a realistic dimension, this configuration shows potential. The cavities of these rectangular configurations are designed to contain the recirculation of gases surrounded by sidewalls. This particular configuration produced a stronger driving vortex inside the cavity in the clockwise direction. This driving vortex will play a very important role when making comparisons with circular configurations later on. This configuration should yield an unstable solution, one that would be even more unstable if finite rate chemistry is assumed. In general, the parametric study simulations provided a guiding rule-of-thumb for developing such configurations.

4.4.4 Discussion of Results (Parametric Study)

A parametric study of ten different cavity-based flame-holders with various flush wall fuel injections for scramjet combustors in a uniform Mach 2 freestream was performed. For these calculations the inflow condition was set up from the earlier Baseline inlet solutions at on-design conditions, by averaging and assuming a gaseous Ethylene-air mixture (see Section 3.2). The effects of the cavity on the various fuel injection schemes into the supersonic airflow are investigated. The cavity increases both the total pressure loss and the temperature

of the combustor while enhancing the combustion of fuel and oxidizer. Cases 1 and 9 have a pair of 25° upstream fuel injectors and a pair of normal injectors in the cavity wall; in these cases the mixing factor seems improved. The mixing and jet fuel penetration of Case 1 is exceedingly effective; the mixing factor is about 66%. The fuel injector pattern causes this by helping to drive the vortex inside the cavity continuously in its natural direction. Case 4, with a row of injectors upstream of the cavity angled at 25°, also performs very well. In Cases 2 and 7 the fuel does not penetrate as far as in all other cases.

The rectangular prototype with the greater mixing factor, Case 1, is repeated with finite rate chemistry to further analyzed and reveals differences from its frozen counterpart. This reactive case exhibits an additional 10% mixing factor and shows much stronger pressure in the vicinity of the opening. The vortices generated by interaction between a shockwave and a shear layer have an immediate influence on the mixing enhancement in supersonic flows, increasing combustion factor and temperature for the finite-rate greater than frozen flow assumption. The combustion factor is directly related to the total length required for the combustor. With a higher combustion factor, the length of the combustor may be shortened. The cavity shape must be derived from flow stabilization and flame holding requirements. While the cavity depth can be estimated according to the required residence time which provides ignition, the length must be chosen to sustain a stable vortex inside the cavity. Additional improvements to injection schemes or devices for better flame-holding should be required for practical off-design and start-up conditions of any flight worthy supersonic combustor.

CHAPTER 5: CIRCULAR COMBUSTOR ANALYSIS

5.1 ANNULAR CONFIGURATION DEVELOPMENT

As noted in Chapter 3, downstream sections of the inlets show distortions due to the flow interactions. To further compare the innovative scramjet system as a whole, the inlets are coupled to three different proposed circular combustor configurations. The earlier flow interactions and/or separations upstream in the inlets might influence their overall performance. This chapter answers the question of whether these flow distortions can yield a region of enhanced turbulence downstream, and produce a significant (positive/negative) effect downstream into the combustor. Previous research has shown that with higher fuel-air mixing, chemical reactions will be enhanced and the overall combustor factor will improve (Ref. 93). Key phenomena influencing the flowfield include the three-dimensional interplay between viscous and inviscid interactions including shock-boundary layer and shock-shock interactions in the inlet, and the effects due to combustion of the reacting fuel-air mixture.

To set the stage for this part of the work, parametric studies on the earlier rectangular supersonic combustor configurations are summarized into the selected configurations. These three configurations with fuel injectors placed at different points inside and outside the cavity were examined for each of the innovative prototypes at on-design conditions. Of these, the three most promising cases (designated for the rectangular combustor as Cases 1, 4 and 9), were converted by

revolving them into circular geometries (now called Configurations A, B and C), while keeping the same cross-sectional area.

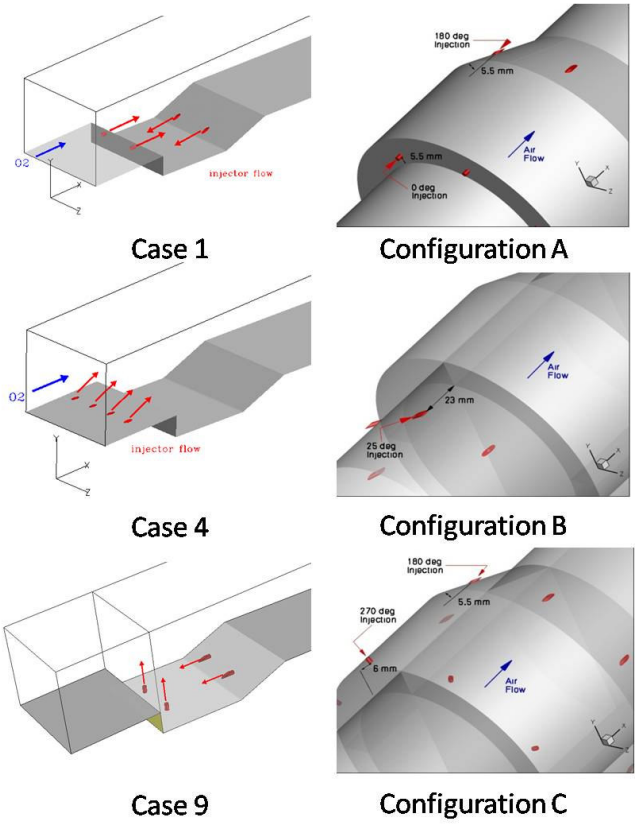

Figure 65: Previous rectangular combustors (left side, Cases 1, 4 and 9) converted into circular combustors (right side, Configurations A-C).

Although this will maintain geometrically the same single cavity depth and height values as well as the proper injection strategy, all 16 fuel ports are positioned further apart axially and create a larger volume in the cavity (see Figure 65). The circular geometries are then simulated with frozen flow

assumptions for the uniform inflow conditions and distorted inflows profiles obtained from Jaws and Scoop.[109]

The combustor with the most effective injector arrangement, detailed later in this chapter, is selected based on results of the rectangular/circular configurations assuming finite-rate chemistry. This configuration is then coupled to each of the above hypersonic inlet inflows (Jaws and Scoop). In addition, an average uniform inflow is further investigated as a baseline for comparison. Each simulation is analyzed to understand the phenomenology and guide further investigation. A sophisticated methodology is employed to analyze various complexities encountered in the flow path, including large regions of subsonic flow, shock-shock and shock-boundary layer interactions, separated flow regions, complex mixing phenomena, non-equilibrium transfer of turbulence energy, and interactions between turbulence and chemical kinetics that may impact both the chemical reactions and turbulence field.

The three selected injection strategies are represented in the lengthwise direction as follows: 1) Figure 66a, Configuration A has the first set of 8 injectors axially spaced at 45° and positioned D/3 from the front step aimed downstream, and the second set positioned 2D/3 at the ramp of the cavity aimed upstream; 2) Figure 66b, Configuration B has the 16 injectors axially and equally arranged at 22.5°, aimed at an angle of 25° towards the core and 2D downstream from the cavity's step; and finally 3) Figure 66c, Configuration C has the first set of 8 injectors axially spaced at 45° and positioned at the floor of the cavity D from the

front step aimed towards the core. Its second pair is located 2D/3 at the ramp of the cavity aimed upstream.

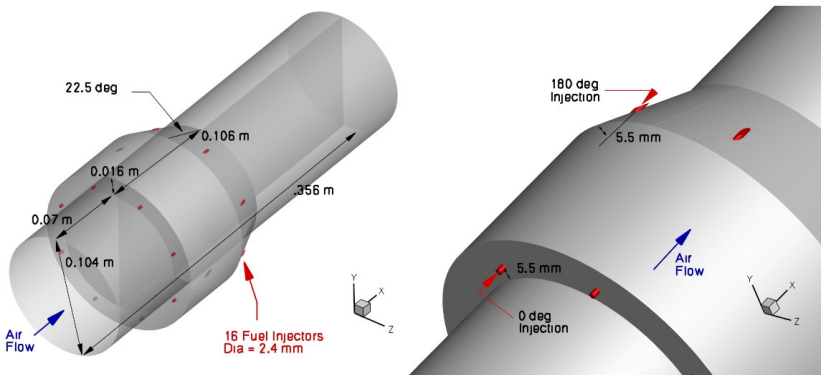

(a) Configuration A

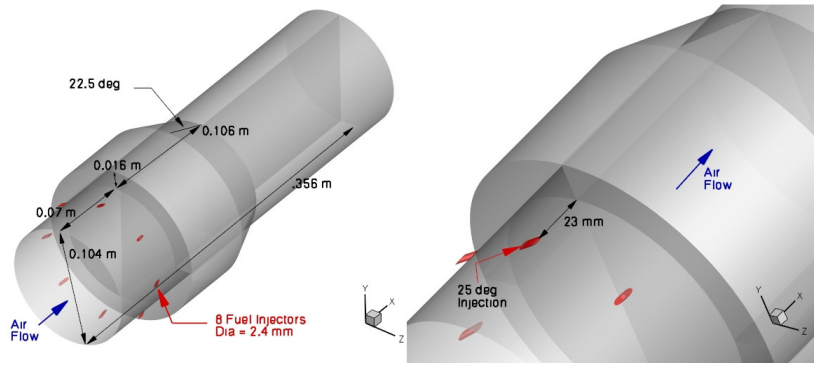

(b) Configuration B

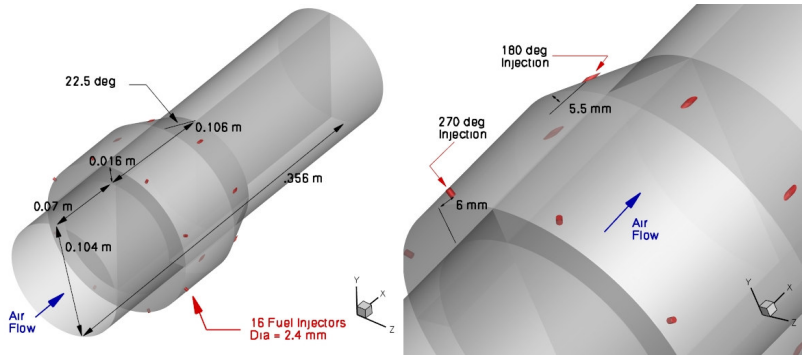

(c) Configuration C

Figure 66: Circular combustor prototypes.

As evident in Figure 67, the mesh of these circular configurations is clustered towards the outer walls and around the injectors to capture the correct flow physics and interactions for all cases. The quarter geometry utilized for the Jaws cases had a grid of 2 million points and for the Scoop cases the geometries were mirrored, thus the whole grid was 4 million points. The circular combustor configurations were conducted using a much finer grid, and topology (H-type) to ensure better solutions of the flow interactions traveling across the core of the combustor. In this manner the center averaging pole is substituted by a symmetry boundary condition.

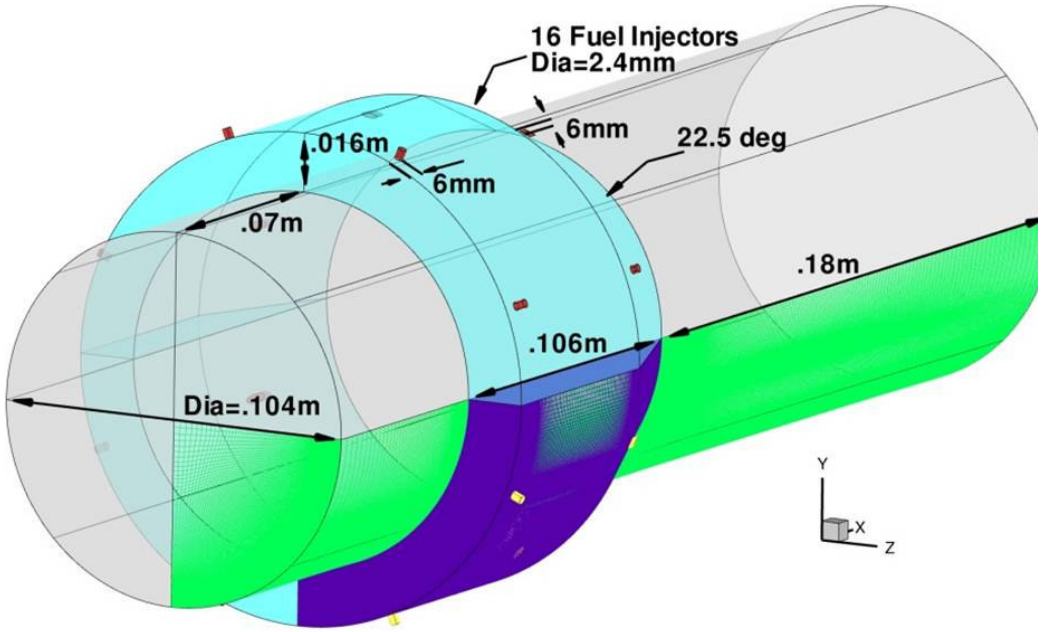

Figure 67: Configuration C, dimensions and structured mesh.

5.2 CIRCULAR SCRAMJET COMBUSTOR: FROZEN CHEMISTRY

As previously described, various physical processes must be considered in CFD when modeling a realistic scramjet combustor configuration containing a cavity or backward step. The three injector arrangements are examined with the following approach. First, the effectiveness of a single passive cavity fueling procedure is explored, assuming non-reacting and uniform flow; this creates a baseline for further analysis. Second and third, these configurations are repeated under the same assumption, but using the Jaws and Scoop inflow profile, respectively. The table below categorizes the cases studied in groups accordingly to their geometrical configuration, inflow conditions and chemistry assumptions (Table 6). For these cases, the subscript "a-c" is used for referring to the circular Configurations A-C.

Table 6: Circular cross-section scramjet combustor Cases.

Cases	Configurations	Inflow
1a	A	Uniform
1b	B	
1c	C	
2a	A	Jaws
2b	B	
2c	C	
3a	A	Scoop
3b	B	
3c	C	

5.2.1 Uniform Inflow, Frozen Chemistry

For Cases 1a-c, the combustors were initialized by assuming a constant inflow condition in the entire configuration, with the exception of the cavity's

domain where the velocity was reduced to u= -0.01 m/s. The CFL was increased from 0.1 to 1.0 for the first 2000 iterations, and then maintained constant at 1.0 until convergence was achieved in around 46 hours total using 64 processors. The results obtained for Case 1c are plotted in Figure 68. The Mach number, pressure, temperature and mass fraction of fuel contours are shown for four cutting planes parallel to the k-direction: 2 planes positioned through the center of the injector pairs, and 2 others on the boundaries of xy- and xz-symmetry planes. Pressure waves are evident, originating around the walls from the shear layer separation where the flow turns into the cavity. These pressure waves essentially reflect at the center line (they intersect the system from the other side of the symmetry plane) and further interact downstream with another set of waves emanating from the back ramped wall of the step, where the shear layer is pushed further away from the wall. The fuel mixing factor is modest near the shear layer. The fuel does not penetrate towards the core of the combustor as observed in the rectangular case in the vertical direction. Since there is volumetric expansion of the cavity, the driven vortex is much weaker than initially predicted. If the temperature and pressure are high enough, auto ignition may result in a circular flame sheet surrounding the inside perimeter of the combustor.

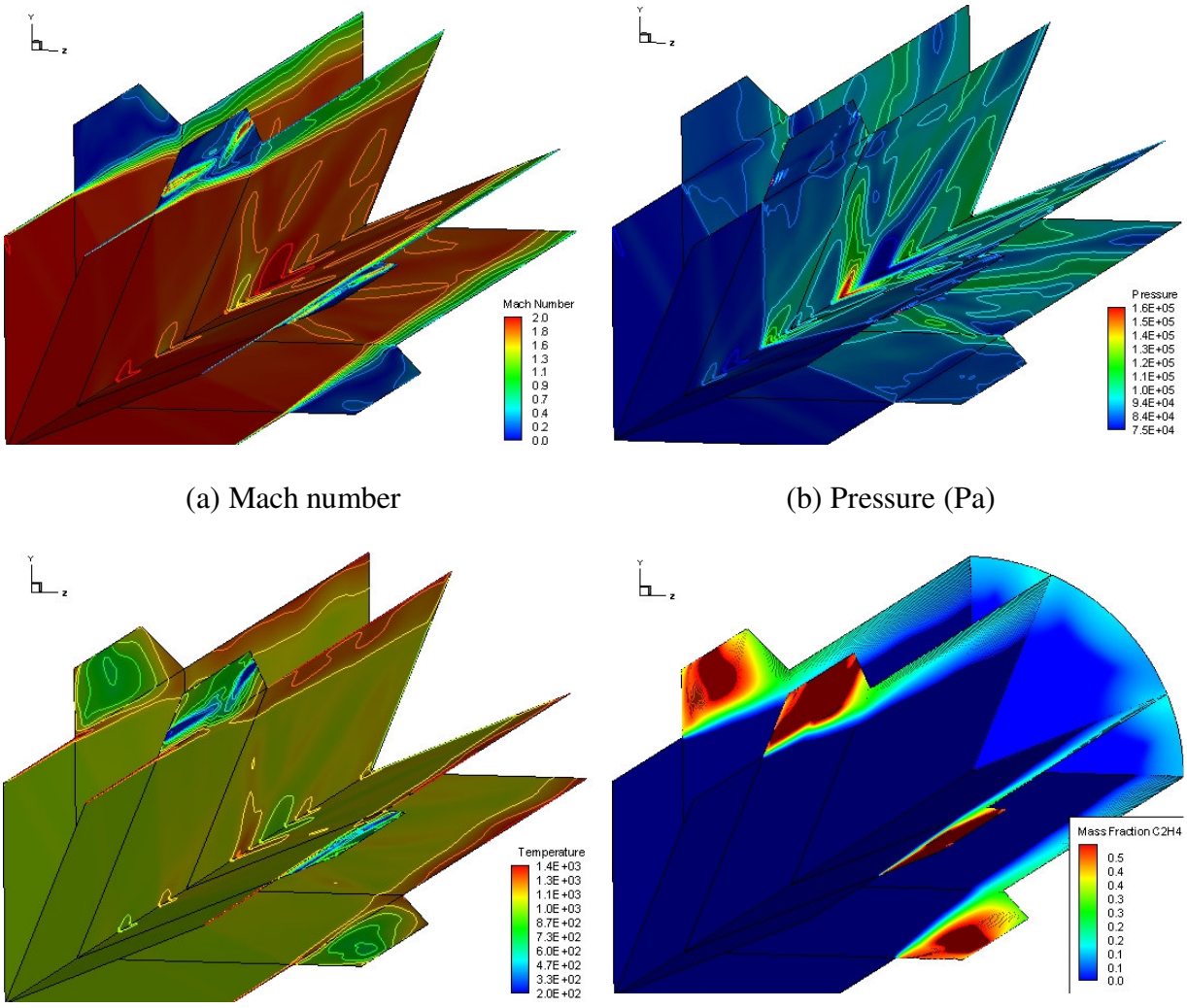

(a) Mach number

(b) Pressure (Pa)

(c) Temperature (K)

(d) $Y(C_2H_4)$

Figure 68: Configuration A results, uniform flow (Case 1a).

Figure 69 shows the fuel mass fraction contours on azimuthal cutting planes. Two planes are located through the center of the injector pairs, and a third is centered between the injectors. In addition, a few streamlines are released from each of the fuel ports to examine their trajectories inside and downstream of the cavity. As shown by these streamlines, this configuration demonstrates a much richer fuel region in and around the cavity where it circulates and mixes with the

incoming air. In addition to its natural vortex rotation in the *ij*-direction, an axial rotation (*jk*-direction) occurs as the fluid interacts within the cavity, allowing it to break away from the cavity by traveling downstream near the wall. This circular configuration did not achieve as high of a mixing factor as its rectangular counterpart (see Case 1 in Chapter 4). Note that although the combustor inlets were designed with equal areas, the revolved cavity has a larger volume; this caused more of the fuel to remain trapped in this region, exiting near the wall and without reaching further towards the center compared to its rectangular counterpart.

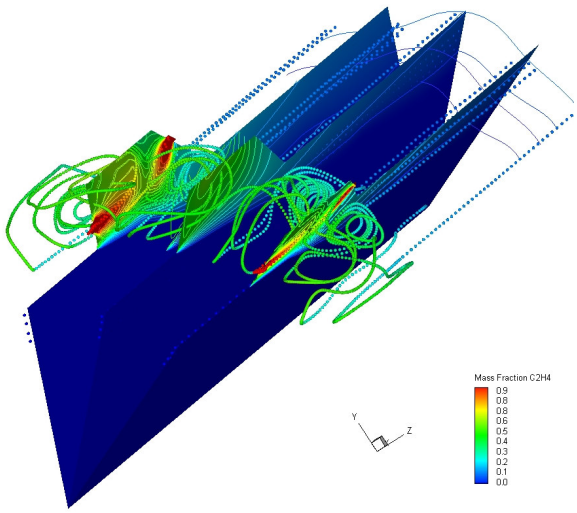

Figure 69: Y_{fuel} contours and injection streamline traces (Case 1a).

The results obtained for Case 1b are plotted in Figure 70. The Mach number, pressure, temperature and mass fraction of fuel contours are shown for three cutting planes parallel to the *k*-direction, positioned through the center of the injectors. As is typical of such injection strategies where fuel is angled into the

airflow, two small circulation regions are present in the front and rear of the jets. This pushes the shear layer away from the wall, producing an unsteady shock/boundary layer interaction, in addition to a pronounced bow shock standing in front of the injectors. Pressure waves are also present in the back wall of the cavity, where the shear layer is further pushed away from the wall.

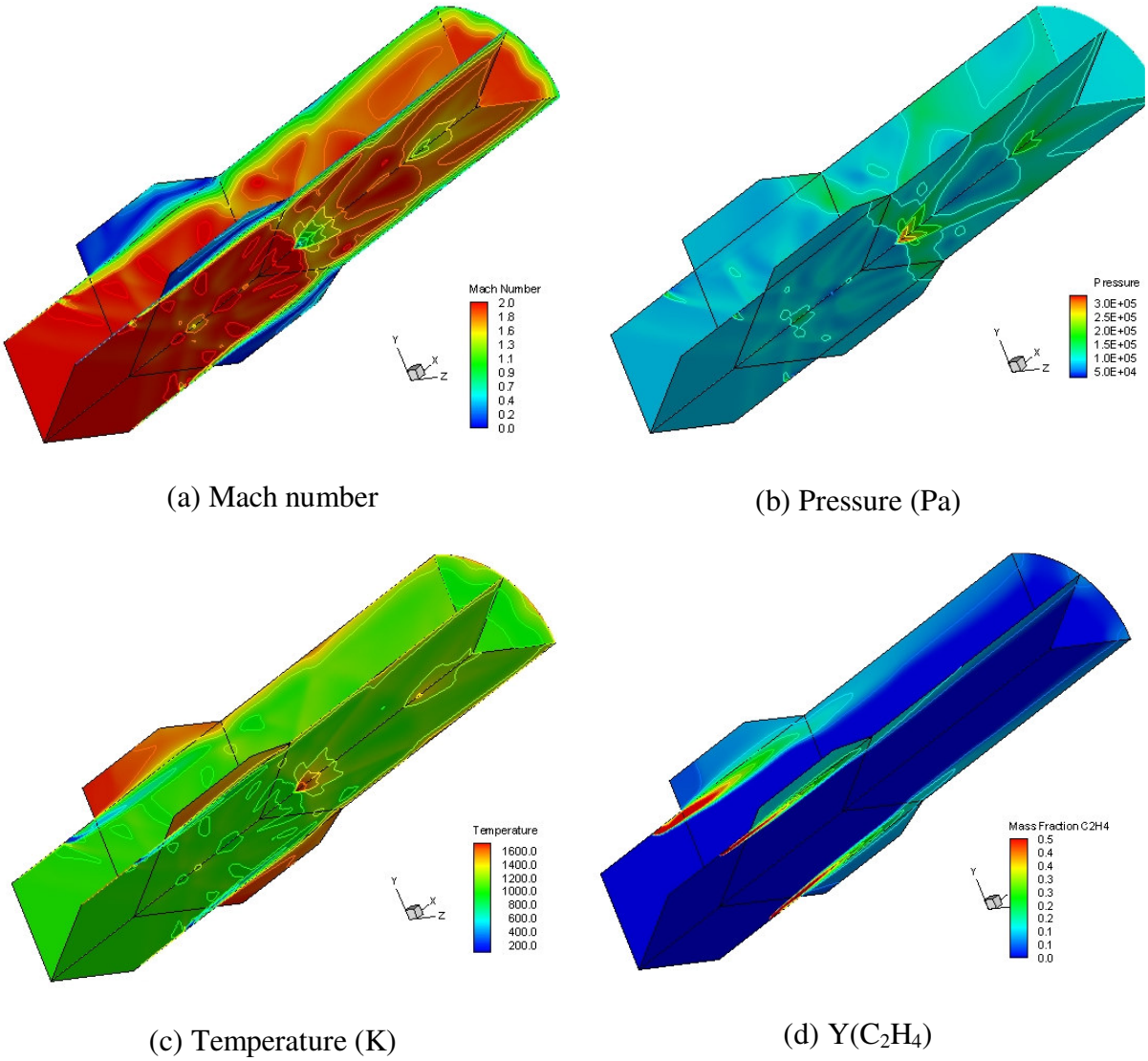

(a) Mach number

(b) Pressure (Pa)

(c) Temperature (K)

(d) $Y(C_2H_4)$

Figure 70: Configuration B results, uniform flow (Case 1b).

Again, the fuel appears to mix just near the shear layer. In the cavity, temperature and pressure are higher, and the fuel/air mixture is leaner than in the previous case since the fuel is positioned outside the opening. The fuel turns into this region, but does not penetrate or mix further into the core.

A close-up of the Mach number, pressure, temperature and mass fraction of fuel contours is shown in Figure 71. A $1/4^{th}$ symmetrical geometry is displayed for the vertical, horizontal, and two other cutting planes positioned through the center of the injectors for Case 1c near the cavity region. One set of injectors is positioned perpendicular to the airflow and in the floor of the cavity. These jets affect the shear layer, preventing it from reaching the front of the step, creating a greater compression at the core while opening the recirculation region around the cavity.

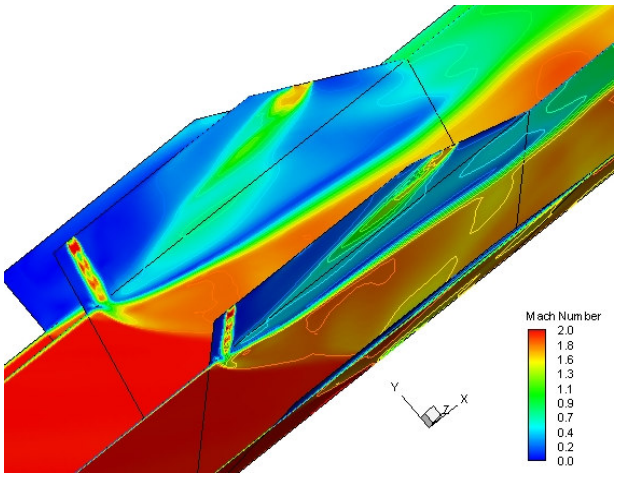

(a) Mach number

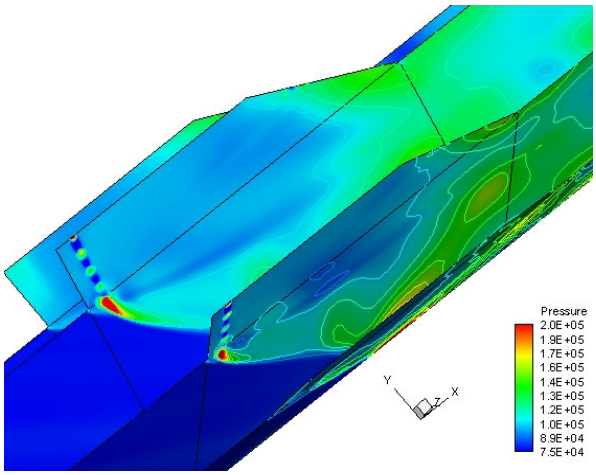

(b) Pressure (Pa)

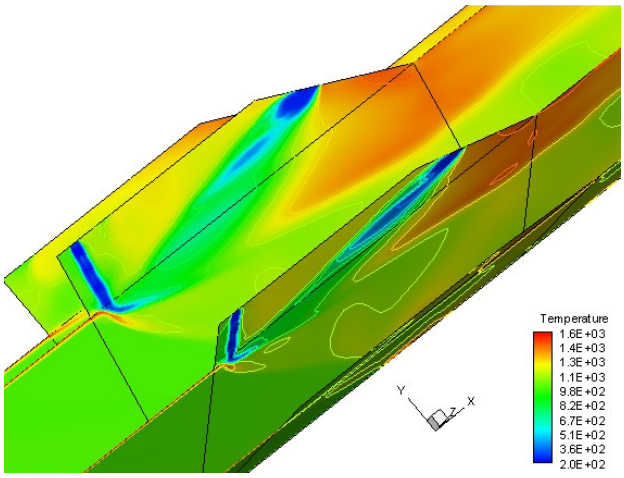

(c) Temperature (K)

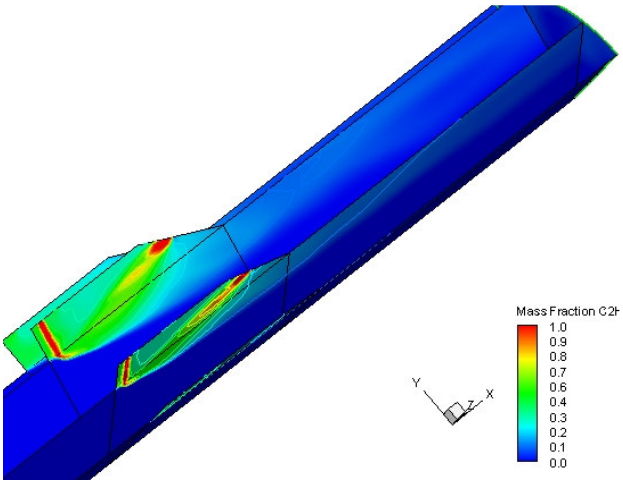

(d) Y(C_2H_4)

Figure 71: Configuration C results, uniform flow (Case 1c).

Figure 72 shows the entire computational domain for the Mach number, pressure, mass fraction of fuel and temperature contours (Case 1c). Again, each quantity is plotted on the y- and z- symmetry planes, as well as four other cross-flow planes along the length of the combustor. As noted earlier, the first set of injectors is positioned perpendicular to the airflow on the floor of the cavity. These jets interrupt the development of the shear layer, creating a greater

compression at the core while expanding the recirculation region around the cavity.

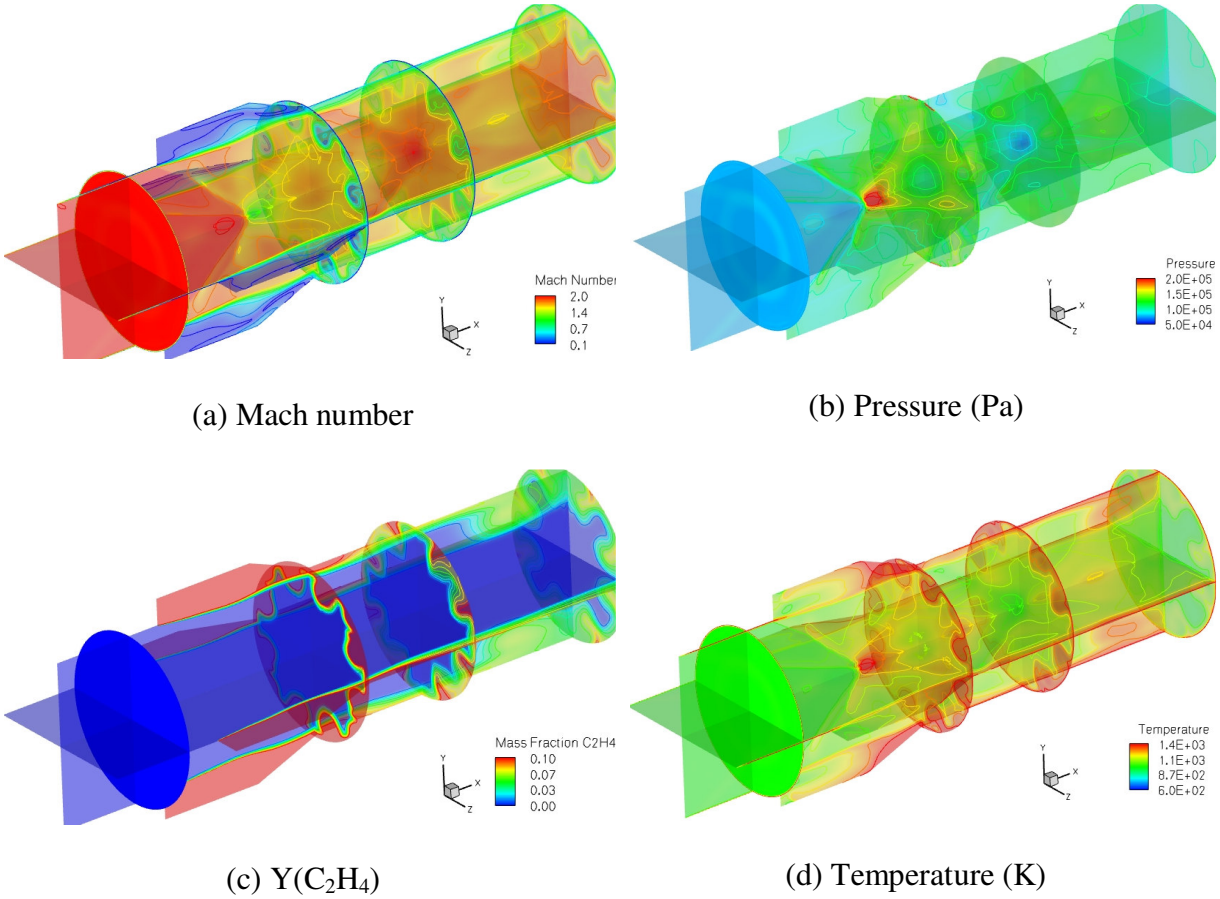

(a) Mach number

(b) Pressure (Pa)

(c) $Y(C_2H_4)$

(d) Temperature (K)

Figure 72: Case 1c, frozen chemistry and uniform inflow.

Figure 72 also shows a small disk formed on the centerline through the convergence of two sets of conical pressure waves. The first originates at the leading edge of the combustor, while the second arises due to the displacement of the cavity shear layer by the first injector set. This wave structure then interacts with the rear of the cavity ramp and other locations downstream.

The second set of injectors, positioned at the ramp and facing the front wall, is intended to aid fuel-air mixture rotation in the natural counter-clock-wise direction. However, this second set did not enhance the intended rotation, since the orientation of the flow past its first set of injectors was followed by a larger stagnation region near the floor of the cavity. The second set of injectors lies in the shadow of the effects associated with the first set, consistent with prior observation of the rectangular combustor prototype (see Case 1 in Chapter 4). Mixing factor is 57% and the integrated local Φ inside the cavity is around 1.0. The volumetric averaged temperature and pressure inside the cavity were 1,150 K and 0.15 M Pa, respectively.

Figure 73a-c compares the Mach number contours for Cases 1c, 2c and 3c on azimuthal planes passing through the center of the injection pairs. Configuration A produces a more equally distributed flow downstream with less loss due to boundary layer and/or shock interactions, and very rich conditions near the cavity (Figure 73a). Configuration B shows a greater shear layer growth than Configuration A, and greater shock/boundary layer interactions (Figure 73b). Finally, Configuration C results in greater fuel penetration and a recirculation region at the cavity region with an air-fuel ratio around stoichiometric proportions (Figure 73c).

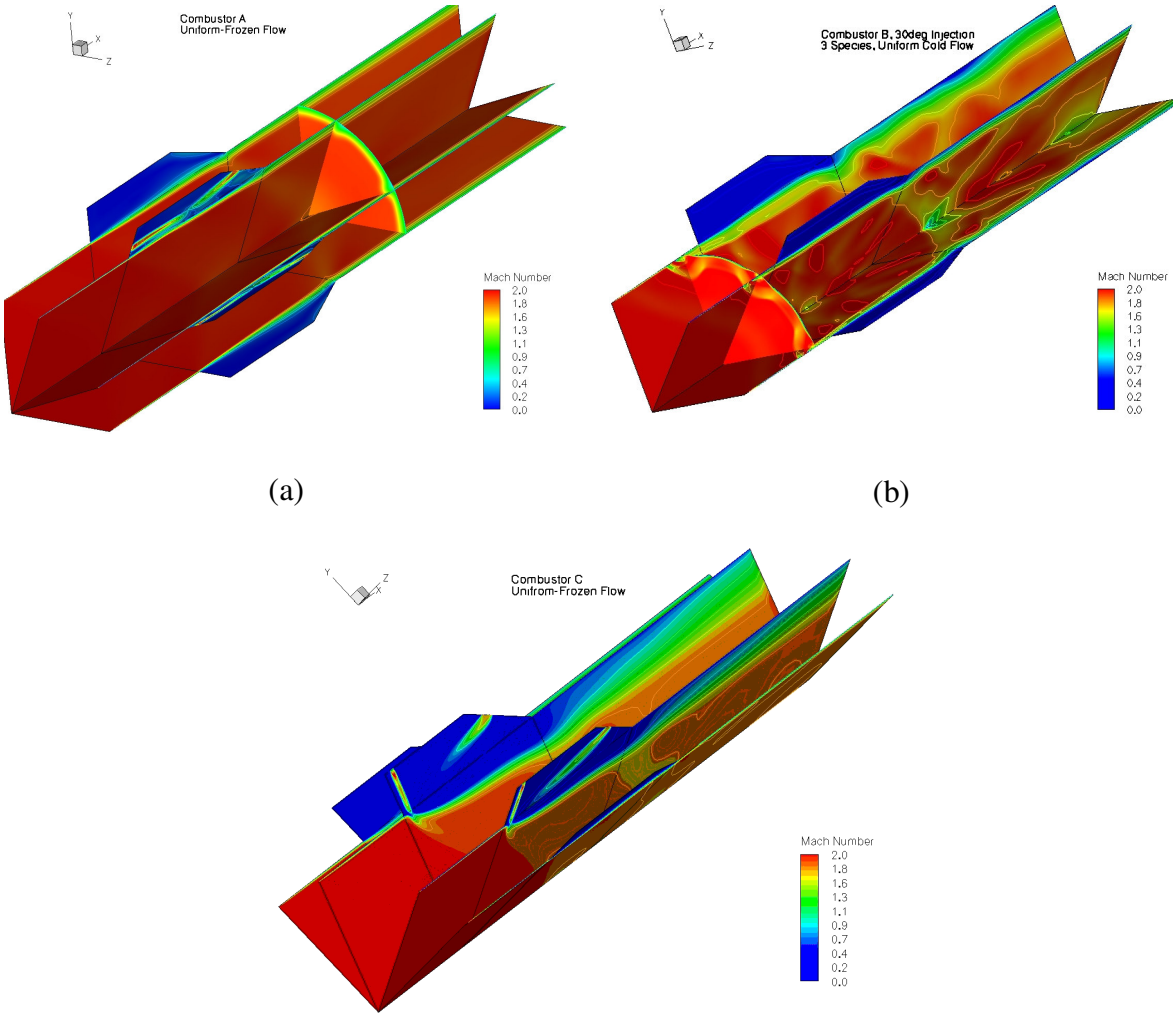

Figure 73: Mach number contours for Cases 1-3c, a-c respectively.

The injection strategy of Configuration C promises a greater mixing factor than the other two configurations, and it compares well to its rectangular counterpart (see Case 9 in Chapter 4). Although the rotating vortex in the cavity was weaker than in Case 1, the mixing was as effective and its integrated air/fuel ratio inside the cavity remained closer to an equivalence ratio of one. Table 2 shows the equivalent ratios integrated inside the cavity for Cases 1-3c. This air-

fuel ratio, together with the proper temperature and pressure, produces the most desirable conditions to anchor a robust flame near the cavity and auto-ignition. Note that the other cases result in lean or overly rich fuel/air ratios inside the cavity, falling outside the flammability limits (Cases 1a and b). The estimated mixing factors for Cases 1a-c are approximated to be 53, 41 and 57 percent respectively.

Table 7: Integration analysis for frozen Cases 1a-c

Cases	**Configuration**	**Inflow**	**Phi in Cavity**	**Mixing factor %**
1a	A	Uniform	2.47	53
1b	B		0.15	41
1c	C		1.05	57

As noted in Chapter 3, downstream sections of the inlets show distortions due to the flow interactions. These can yield a region of enhanced turbulence in the isolator, and produce a significant effect on the combustor, since better mixing of air and fuel can augment chemical reactions and improve the overall factor. Key phenomena influencing the flowfield include the three-dimensional interplay between viscous and inviscid interactions including shock-boundary layer and shock-shock interactions in the inlet and the positive effects due to combustion of the reacting fuel-air mixture (Ref. 94). This analysis is now presented for only the Scoop and Jaws configurations, assuming a chemically reactive hydrocarbon-air mixture. Since the geometries are scaled so that the exit of each inlet is circular,

and has the same diameter, the combustor configuration is assumed to be identical. The principal difference is the profile of the flow entering the combustor, which, as described above, is profoundly different for the two geometries.

5.2.2 Jaws Inflow, Frozen Chemistry

For Cases 2a-c, the inflow condition was imposed from Jaws' exit plane solution and the entire computational domain was initialized using the results of Cases 1a-c, respectively. The CFL was again set to increase from 0.1 to 1.0 for the first 2000 iterations, and then maintained constant at 1.0 until convergence was achieved in around 32.2 hours total using 64 processors. The results obtained for Case 2a are plotted in Figure 74. The Mach number, pressure, temperature and mass fraction of fuel contours are shown for four cutting planes positioned through the center of the injector pairs, and two others on the vertical and horizontal symmetry boundaries. Asymmetric pressure waves are once again present, originating around the walls from the shear layer separation where the flow turns into the cavity, varying with the inflow profile produced by Jaws. These waves collide and further interact downstream with another set of waves formed by the back ramped wall of the step. The shear is pushed away from the wall at the end of the cavity ramp near the low speed zone entering the burner (see the horizontal symmetry plane of Mach number contours in the top left of Figure 74), further than in the vertical symmetry plane.

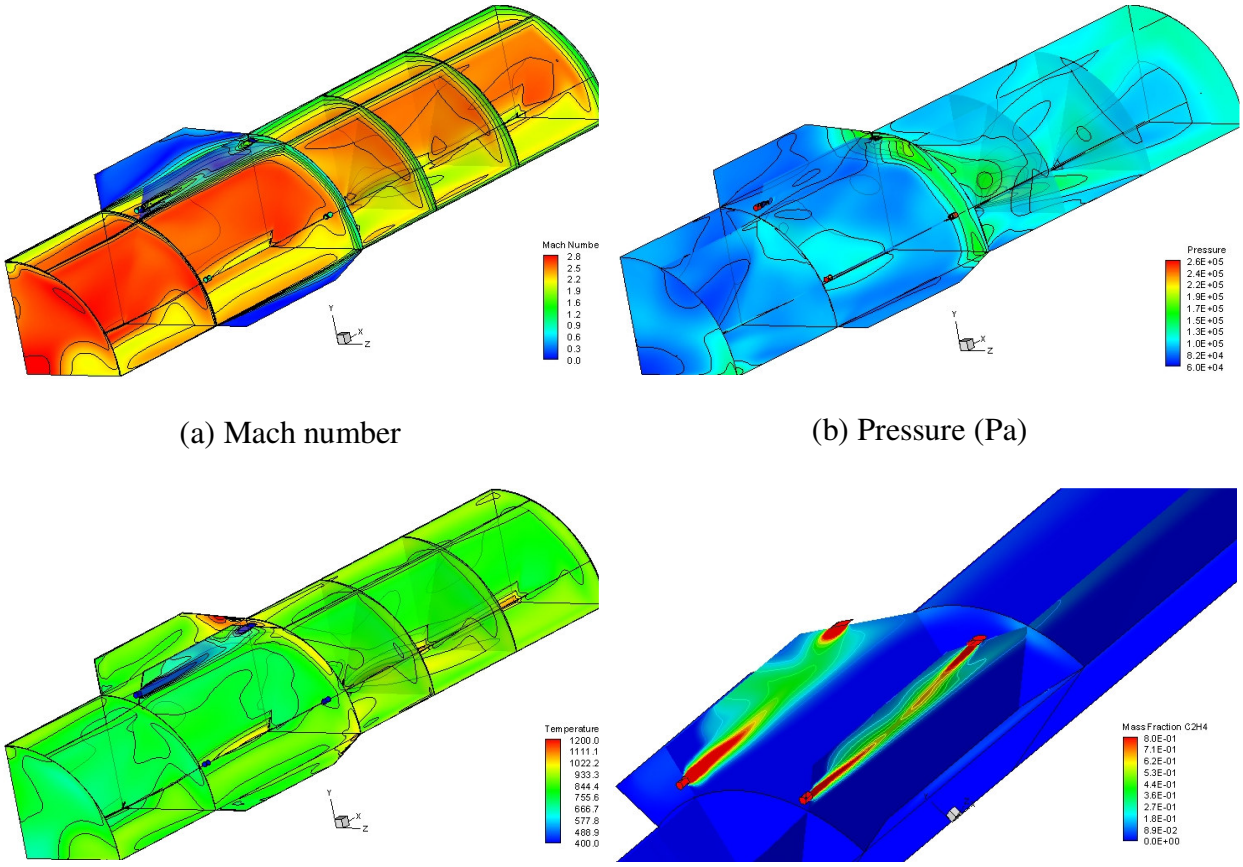

(a) Mach number

(b) Pressure (Pa)

(c) Temperature (K)

(d) Y(C_2H_4)

Figure 74: Configuration A results; Jaws inflow and frozen chemistry (Case 2a).

For this case, the Jaws inflow conditions into combustor Configuration A yield a high pressure and temperature region near the back (ramp) wall of the cavity. This indicates a zone where the chemical reactions will most likely occur or advance. Subsequent forward displacement through the detached shear layer into the front wall of the step will then yield a more distorted circular flame near the combustor's circumference. In this case, the air and fuel seem to mix better inside the cavity than in Case 1a (the case with a uniform inflow).

Figure 75 depicts the Mach number, pressure, temperature and fuel fraction contours for Configuration B assuming the Jaws inflow profile (Case 2b). In general, the jets interact with the distorted air inflow in a manner similar to Case 1b, except that the fuel penetrates unevenly in the low speed region of the profile located at the *xz*-plane (horizontal) where the lower energy flow enters the combustor.

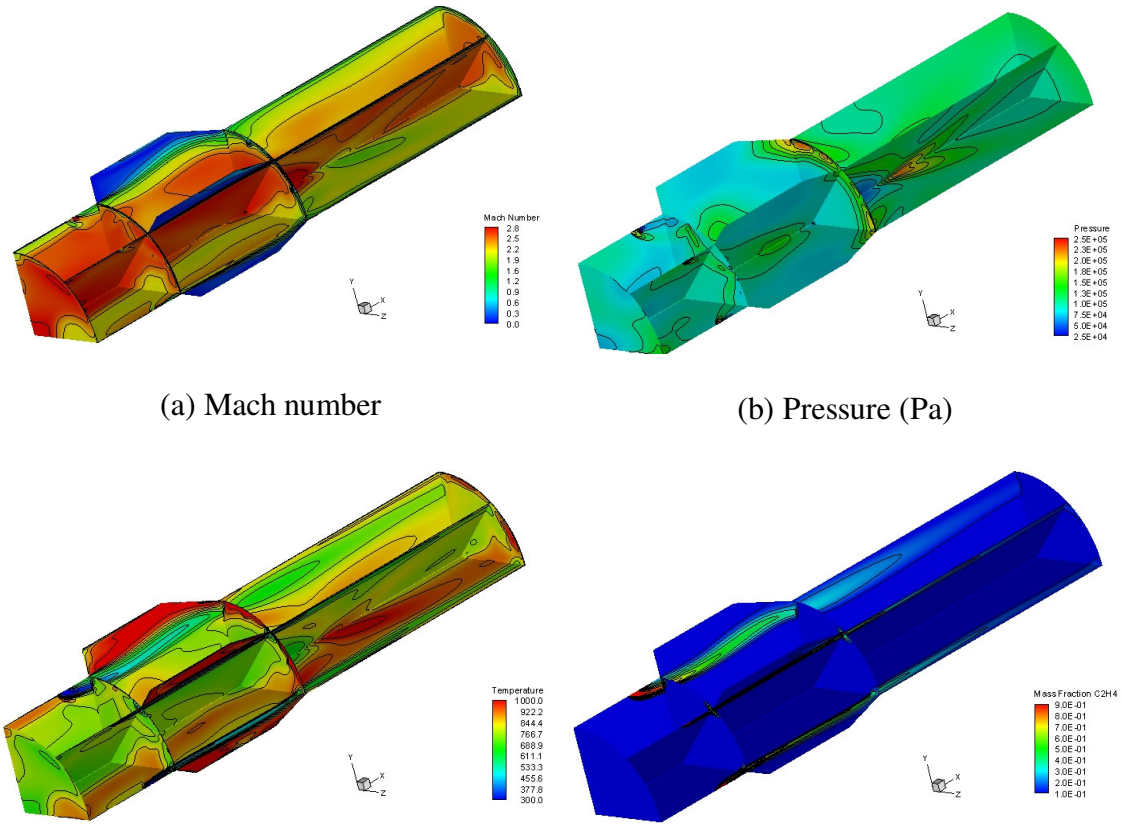

(a) Mach number

(b) Pressure (Pa)

(c) Temperature (K)

(d) Y(C_2H_4)

Figure 75: Configuration B results, Jaws inflow and frozen chemistry (Case 2b).

Although the velocities, temperature and pressure vary along the flowpath, the conditions in the cavity do not indicate significant variation except for the

amount of fuel within. The mass fraction of fuel shows a leaner area on the *xz*-plane, due to better diffusion occurring along the shear layer crossing this region of the opening (see Figure 75).

Results for Case 2c are shown in Figure 76. As in Case 1c, the fuel jets influence the development of the shear layer. This creates a greater compression at the core and a greater aperture in the recirculation region around the cavity near the low speed region. In this non-reacting case, the mixing was more effective than seen in all other cases. Although the air/fuel ratio coefficient inside the cavity is larger than for Cases 2a and 2b, the stoichiometric proportions within the cavity volume are within the flammability limits, an important factor when desiring an effective cavity design that could act as a flame holder. Note that the while the volumetric integrated fuel/air mixture might seem low, the localized values near the outside of the step and within the highly diffusive shear layer will become higher as it crosses the cavity.

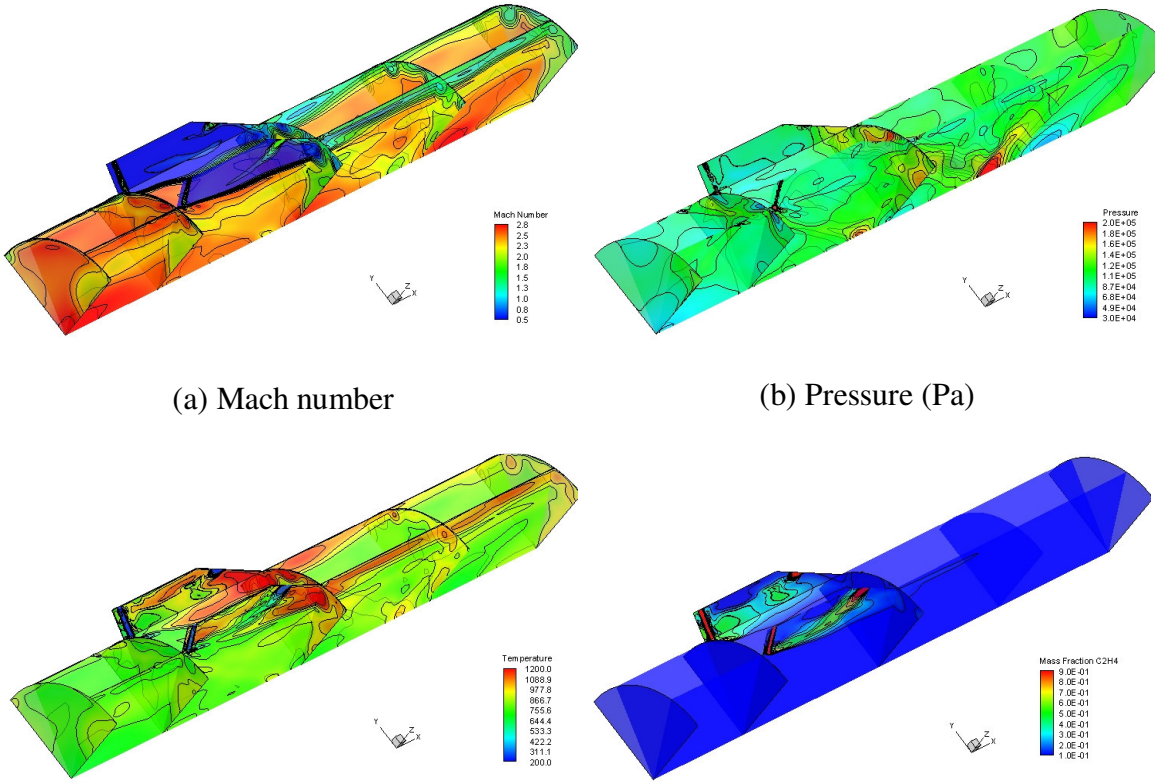

(a) Mach number

(b) Pressure (Pa)

(c) Temperature (K)

(d) $Y(C_2H_4)$

Figure 76: Case 2c results, 1/4th view.

Figure 77 shows the entire configuration. As in Case 1c, the fuel jets influence the development of the shear layer. Greater compression is observed along the centerline. In this non-reacting case, the mixing was slightly more effective (at 63%) than the uniform case (57%). The calculated volumetric Φ inside the cavity was much leaner at 0.6, though temperature and pressure remained similar to Case 1c. This reveals that the distortion, for the case of Jaws, helps to extract fuel from the cavity and mix the fuel with the air away from the vicinity of the cavity. Numerous but weaker pressure wave interactions around the combustor maintained a larger region of supersonic flow than in the previous

uniform case. A higher velocity flow region near the walls, with less temperature and higher pressure levels in close proximity to the ramp, results in poorer fuel penetration than the uniform case (Case 1c). This effect pushes the fuel closer to the walls downstream from the cavity's ramp.

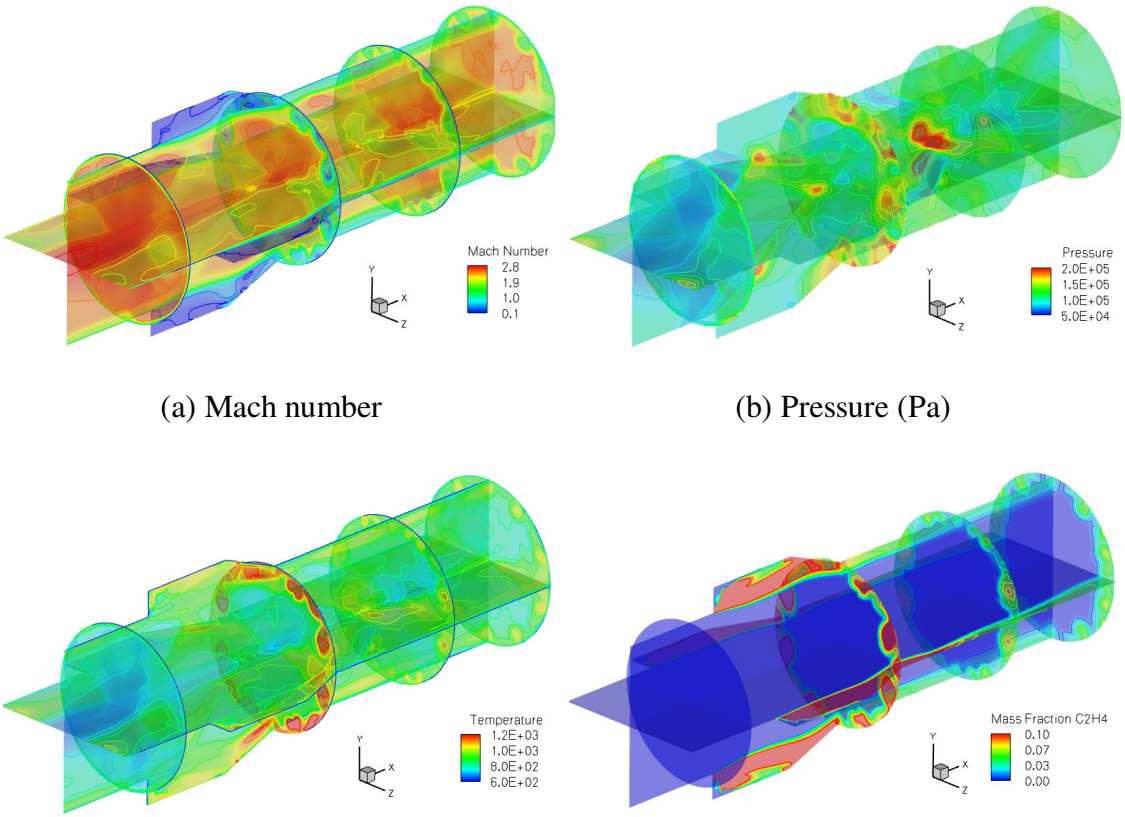

(a) Mach number (b) Pressure (Pa)

(c) Temperature (K) (d) Y(C_2H_4)

Figure 77: Case 2c results at symmetry planes, full view.

Table 3 shows the equivalent ratios integrated inside the cavity for Cases 2a-c. The fuel/air ratio inside the opening results in much leaner volumetric proportions, significantly more different for Configurations A and B, due to a higher circulation inside the cavity. This is produced by the vortex rotation

introduced from the Jaws inlet which penetrates into the opening, further diffusing and mixing the fuel outwards. Although the integrated dispersion area at the exit plane is less than for the uniform non-reacting cases (Cases 1a-c), the estimated mixing factors are 57, 45 and 63 percent respectively, i.e., modestly better within the cavity.

Table 8: Integration analysis for frozen Cases 2a-c.

Cases	Configuration	Inflow	Phi in Cavity	Mixing factor %
2a	A	Jaws	0.28	57
2b	B		0.08	45
2c	C		0.60	63

5.2.3 Scoop Inflow, Frozen Chemistry

For Cases 3a-c, the inflow condition was imposed from Scoop's exit plane solution and the entire computational domain was initialized using the results of Cases 1a-c, respectively. The CFL was again increased from 0.1 to 1.0 for the first 2000 iterations, and then maintained constant at 1.0 until convergence was achieved in around 61.3 hours using 64 processors. The results obtained for Case 3a are plotted in Figure 78. The Mach number, pressure, temperature and mass fraction of fuel contours (from top to bottom respectively) are shown for the vertical symmetry boundary and four *x*-plane stations: positioned at the entrance, forward step, back ramp and outlet. As opposed to Case 1a, the inflow profile causes a series of non-asymmetric pressure waves around the walls and near the

shear layer separation where the flow turns into the cavity. Though the shock interactions caused by the unique Scoop profile are not planar, they intermingle from the top and/or bottom towards its core rather than the surrounding walls radial to the core as seen in Case 1-2a. These waves collide and further interact downstream with another set of waves formed by the back ramped wall of the step in a disorganized manner due to the larger low energy region dominating at the bottom section of the combustor. For this case, the shear is not pushed as far from the wall at the end of the cavity ramp near the low speed zone entering the burner (see *y*-plane) compared to Cases 1a and 2a. Note the shear layer development from the 2nd to the 3rd *x*-plane station (from right to left); as if turning into the radial direction the shear layer is further developed from the top (clockwise) towards the bottom. This case demonstrates a poor injection strategy, since fuel penetration appears insignificant at the edges of the 3rd station downstream. This is caused by a high pressure region near the back wall of the cavity, which prevents a strong circulation from extracting the fuel.

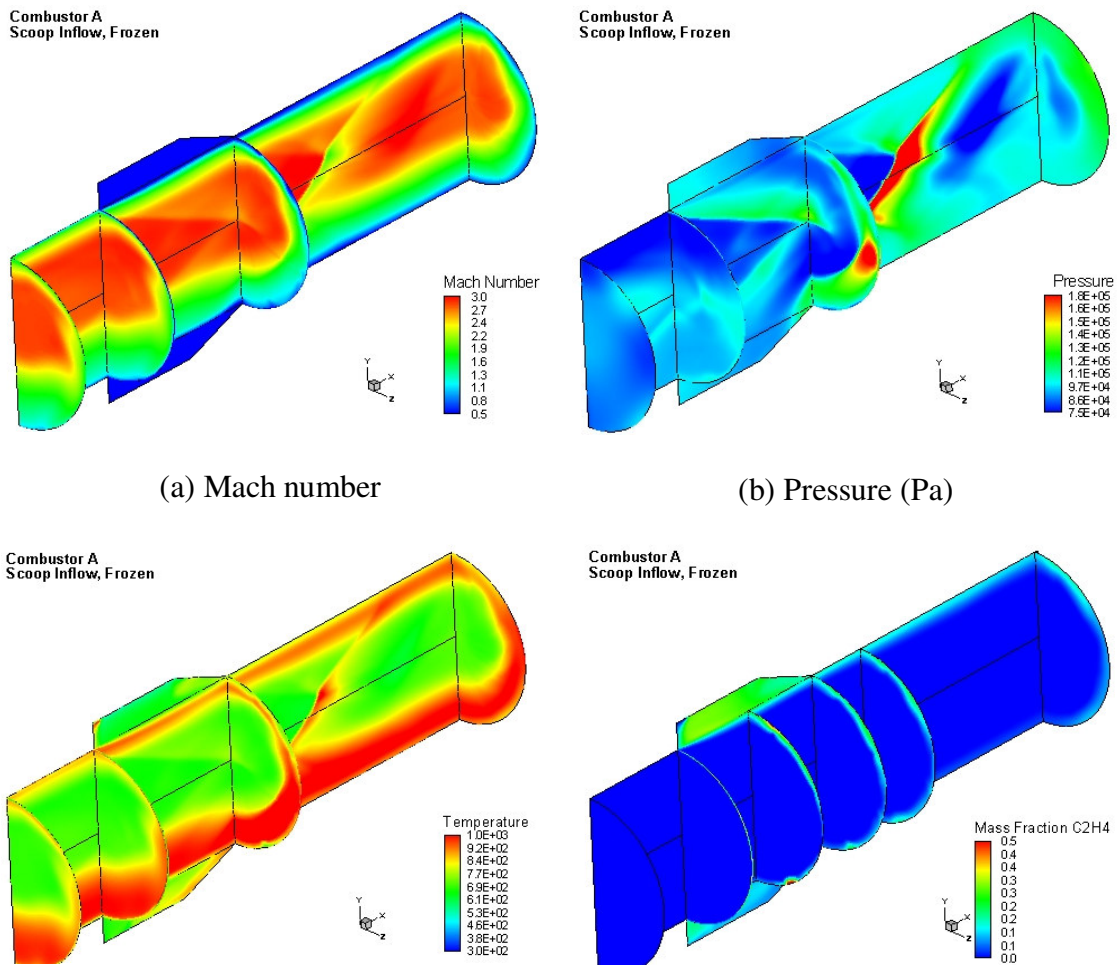

(a) Mach number

(b) Pressure (Pa)

(c) Temperature (K)

(d) Y(C_2H_4)

Figure 78: Configuration A results, Scoop profile and frozen chemistry.

When examining the more flammable levels of temperature and pressure plots near the lesser energized region, it appears that the reactions will most likely settle in the bottom portion of this combustor if finite-rate chemistry is considered (see Figure 78). Subsequent forward displacement through the detached shear layer into the front wall of the step will then yield a more distorted non-circular flame near the combustor's circumference on the more energized upper section.

For the Scoop, as well as for the Jaws profile, the air and fuel seem to mix better towards the outflow and inside the cavity than in Case 1a.

Figure 79 depicts the Mach number, pressure, fuel mass fraction and temperature contours for Configuration B assuming the Scoop inflow profile (from top to bottom, Case 3b). The pressure contours clearly show the jets' interaction with the distorted supersonic air inflow differently than in Case 3a (see the top-right corner of Figure 78). Also, as in Case 3a, the upper and lower pressure waves seem to interact further up from the center of the combustor (see the symmetry plane for the Mach number and pressure contours of Figure 79).

Since the injection takes place upstream of the cavity, there are larger pressure losses due to bowed shock interactions formed by the angled jets into the supersonic flow. In this case, similar to Case 1b, the fuel mainly remains over the shear layer as it crosses the cavity, and allows for further penetration into the core rather than seeping into the opening. And in contrast to the uniform flow assumption (Case 1b), the same fueling strategy penetrates unevenly in the low speed region of the profile. Although the volume inside the cavity is left with a very lean fuel/air mixture, there is a favorable region at the edge of the step. This could possibly anchor a reaction sheet that later promotes further burning downstream. The velocities, pressure and mass fraction conditions in the cavity do not indicate significant variation in the radial θ-direction, except for the temperature contours. In Case 3b, the temperature is higher in the upper region than the lower section with the lower energy zone, as opposed to Case 3a. This outcome is produced by a combination of factors. The upper region has a higher

velocity, which causes the fuel to flow near the walls, whereas the lower region has a lower velocity, allowing the fuel to penetrate deeper into the core of the combustor (see the symmetry plane and 2nd station of the pressure contours in Figure 79).

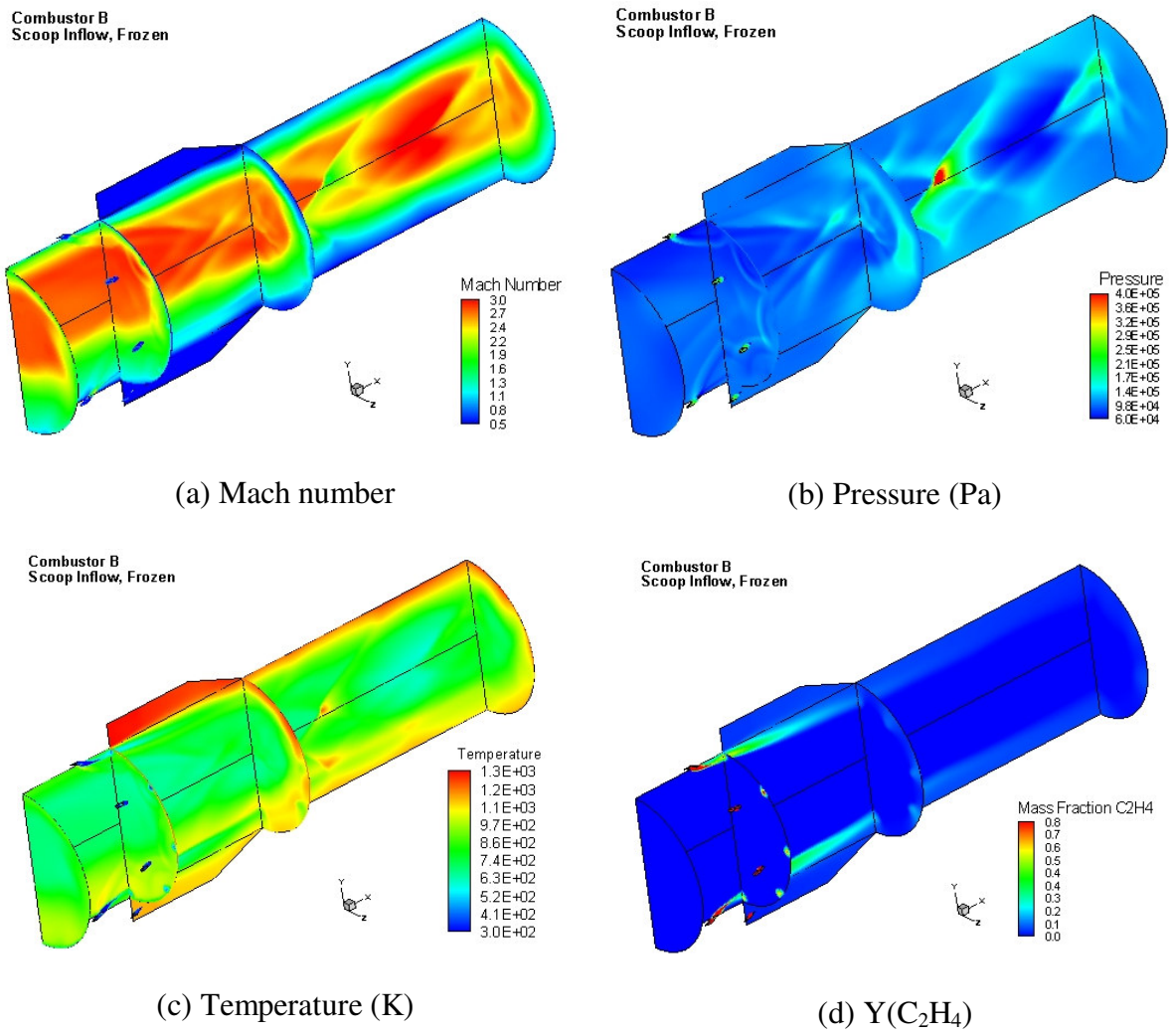

(a) Mach number

(b) Pressure (Pa)

(c) Temperature (K)

(d) $Y(C_2H_4)$

Figure 79: Configuration B results, Scoop profile and frozen chemistry.

In the lower region of Case 3b, the fuel prevents the hot profile from entering the cavity. The fuel temperature is about three times lower than the air,

thus the fuel cools down the shear layer as it travels across the bottom step more than the upper area of the combustor. Even if this bottom set of injectors might shelter the hot profile from entering the cavity, this region has more favorable conditions for flammability due to higher mixing and a lower velocity profile. Therefore, as in Case 3a, the reactions most likely settle in the bottom portion of this combustor if finite-rate chemistry is considered, and flashback might occur.

Figure 80 shows results for the Scoop inflow or Case 3c. In this case, mixing factor was computed to be 60% at the exit of the combustor, and its integrated Φ inside the cavity remained closer to 0.5 (i.e., much leaner than Case 1a). Again, the integrated volumetric temperature and pressure in the cavity are similar to those of Jaws. However, in contrast to Case 2c, the temperature increases and pressure decreases near the end of the ramp cavity, allowing the fuel to travel further away from the walls. The Scoop profile generates a larger low velocity region near the cavity. Due to the horizontal asymmetry in the distorted Scoop profile, which results in higher pressures and temperatures in the lower region, a correspondingly augmented fuel penetration pattern is observed in the combustor. Similarly, the uneven interactions of the shear and pressure waves yield an asymmetric contour map of the fuel dispersion inside the cavity. Just as in Case 3a and Case 3b, the pressure interactions are very planar, moving from the upper walls to the low energy profile at the bottom region of these configurations (see the symmetry plane and 2^{nd} to 4^{th} stations for the Mach number, pressure and temperature contours of Figure 80).

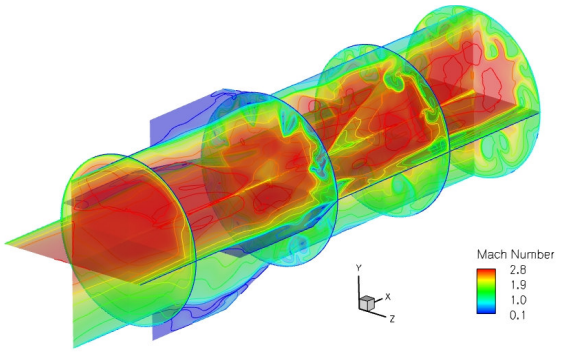

(a) Mach number

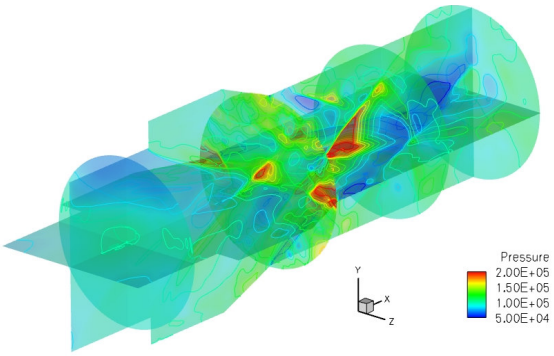

(b) Pressure (Pa)

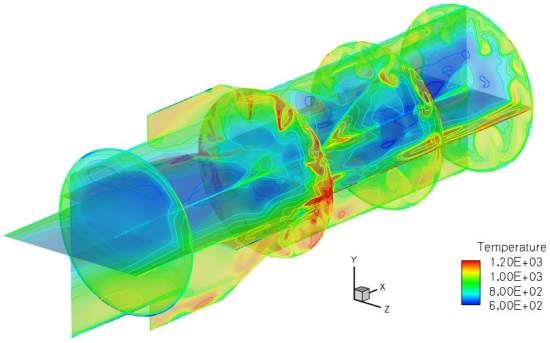

(c) Temperature (K)

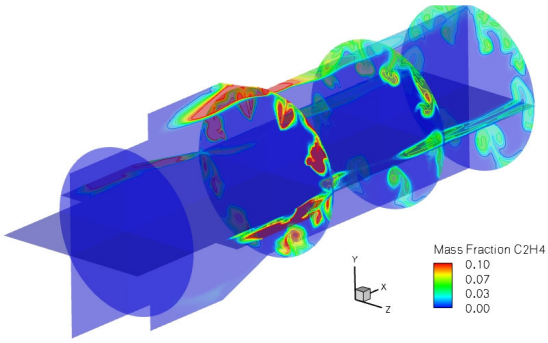

(d) Y(C2H4)

Figure 80: Case 3c results, Scoop profile with frozen chemistry.

Table 9 shows the computed results for the volumetric fuel/air ratio inside the cavity and the overall mixing factor using the frozen and Scoop entrance profile assumptions.

Table 9: Integration analysis for frozen Cases 3a-c.

Cases	**Configuration**	**Inflow**	**Phi in Cavity**	**Mixing factor %**
3a	A	Scoop	2.01	56
3b	B		0.12	45
3c	C		0.56	60

5.2.4 Uniform, Jaws vs. Scoop inflow, Frozen Assumptions

Figure 81a,b compares the mass fraction contours of fuel for the distorted profiles, Jaws and Scoop for frozen chemistry, i.e, Cases 2-3c respectively. Eight cross-flow planes are employed to depict the evolution of the fuel distribution with streamwise direction. In these cases, the combined effect of the chosen air-fuel ratio, together with high temperature and pressure, produces the most desirable conditions to anchor a robust flame near the cavity and supports auto-ignition. Although the combustor geometry is the same, the uniform averaged inlet profile case (Case 1c, bottom left of Figure 72) exhibits a higher fuel concentration in the cavity and penetration towards the core than the other two cases with distorted inlet profiles (Cases 2-3c). Both coupled inlet profiles considered here slightly increase the diffusion of fuel due to incoming vorticity and localized swirl (symmetrically opposing each half of the symmetrical profile), which helps reduce the fuel concentration in the cavity.

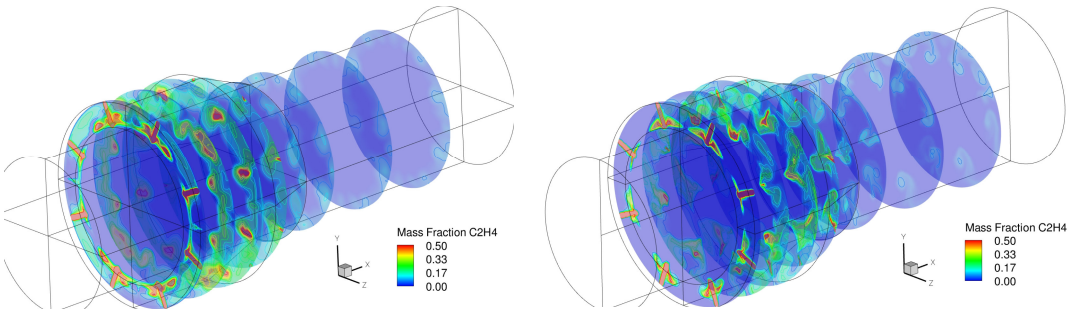

(a) Jaws Inlet Profiles (b) Scoop Inlet Profiles

Figure 81: Fuel mass fraction at 8 x-planes at the cavity region.

Figure 82a-c shows the Mach number contours at the azimuthal z-plane passing through the center of the injectors for the uniform, Jaws and Scoop chemically frozen cases (Cases 1-3c, Figure 82a-c). Cases 1c and 2c are symmetric about the horizontal, while, as anticipated, Case 3c results in a very different pattern due to its characteristic distortion and subsequent interaction with the injection strategy. The Jaws inlet generates a much smaller shear layer and weaker interactions than the uniform or Scoop cases, which translates to lesser losses. Figure 82a, in particular, shows the ineffectiveness of the second pair of injectors inside the cavity in further enhancing circulation in the natural direction. Instead, these injectors push the shear layer away from the cavity, contracting the flow downstream into additional shock interactions. Thus, the uniform inflow results in the lowest mixing factor of all cases, considered in this section.

In addition, Figure 82d shows the pressure lines at the center of the combustor Configuration C with frozen chemistry for the three inflow assumptions, Cases 1-3c. The uniform inflow assumption shows a higher pressure spike due the conical (3D oblique) shock interaction from the cavity leading edge towards the core and around the middle of the cavity the length. Unlike the uniform inflow assumption, both inlet profiles (Jaws and Scoop) produce a higher pressure further downstream from the cavity ramp. In addition to this figure, together with the Mach contours (see Figure 82a-c), the variation in the inflow profile causes a unique series of contractions and expansions through the configuration past the cavity.

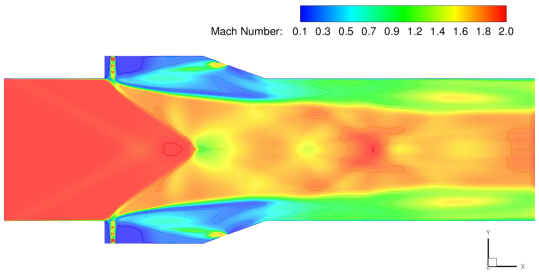

(a) Mach Number, Uniform inflow

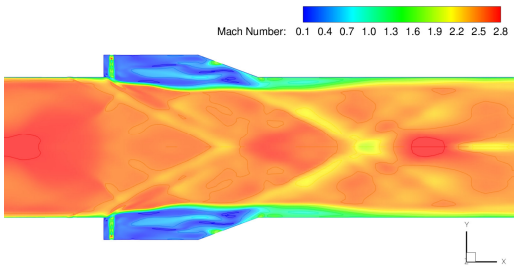

(b) Mach Number, Jaws inflow

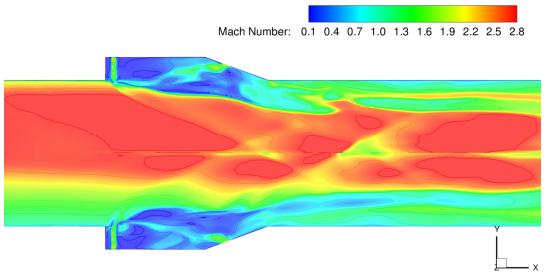

(c) Mach Number, Scoop inflow

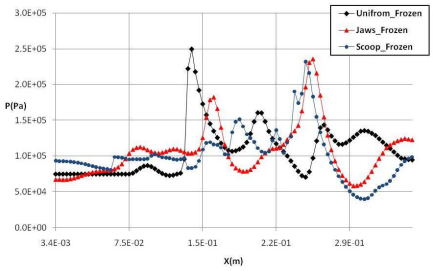

(d) Centerline Pressure (Pa)

Figure 82: Results comparison for Cases 1-3c.

The table below compares the integrated values inside the cavity volume for the three different inflow profiles when assuming chemistry for the combustor Configuration C, Cases 1-3c (Table 10).

Table 10: Integrated pressure and temperature averaged for Cases 1-3c.

Inflow Profile	**P_{ave}(Pa)**	**T_{ave}(K)**
Uniform	6.53×10^4	9.82×10^2
Jaws	9.64×10^4	9.70×10^2
Scoop	9.96×10^4	9.71×10^2

5.2.5 Rectangular vs. Circular Combustors

Figure 83 shows the mixing factor comparison between the rectangular and circular combustors for several conditions, including the effect of assuming frozen or finite-rate chemistry as well as uniform or distorted profiles. When modifying these rectangular combustor configurations into circular ones, the geometries were kept similar with the same injection strategies, area cross sections and flow conditions (of the inlet entrance and injectors). Chapter 4 shows that the fuel distributions differed significantly from one another for the different injection strategies, even though the penetration rate was generally similar. Since it is difficult to distinguish mixing factor based on these qualitative features, the mass fractions of C_2H_4 and O_2 distribution were integrated at the end of the exit plane to find penetration or mixing factor for individual cases, and translate directly to greater overall combustor factor. For the rectangular Configuration A, the fuel injector pattern helps drive the vortex inside the cavity continuously in its natural direction. Although the vertical penetration of the fuel in the rectangular Configuration B was higher than all other cases, its mixing factor was lower because when the injectors are positioned upstream of the cavity (and angled at 25º), mixing in the span-wise direction is poor. Finally, results with Configuration C, which combines injection normal to the cavity floor and ramp, are similar to those with Configuration A. Even though the fuel penetration is similar to that with Configuration A, more dispersion in the cross-flow direction is observed with Configuration C, due to normal injection at the bottom of the cavity. Overall, when comparing rectangular with circular geometries, the

former configuration has a superior performance. However, such a comparison should be qualified by the fact that the cavity volume for the circular case is larger.

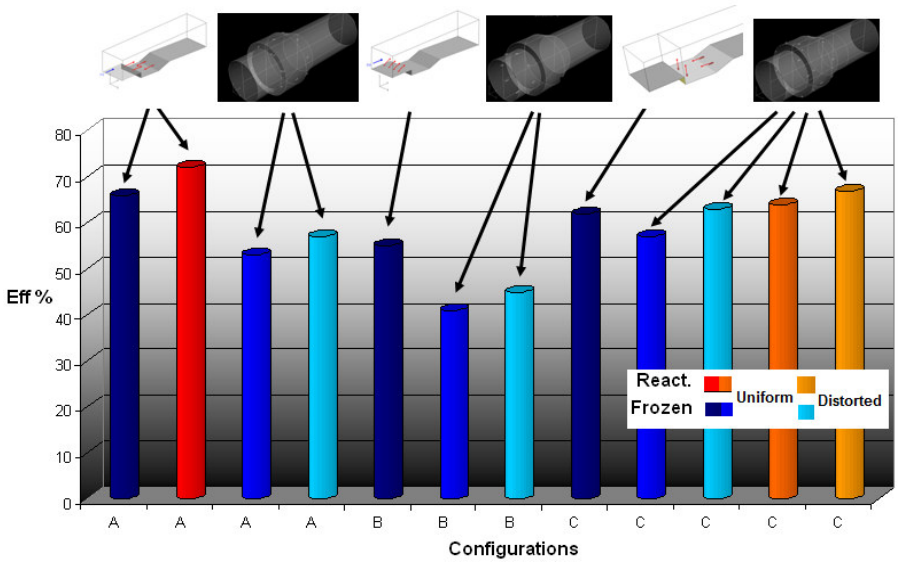

Figure 83: Mixing factor comparison for rectangular and circular combustors Configurations A-C, with/out chemistry and inflow profiles.

In general, despite good auto-ignition characteristics and better inlet performance, Cases 1-3a (circular configurations) showed relatively poor air-fuel mixing factor values of 57%, 63% and 60% when compared to their rectangular counterpart ~70%. The innovative circular inlets mitigate some of the issues encountered in the Baseline configuration (traditional hypersonic inlets), but the combustor deficits might balance or overcome the complete integration of the scramjet. This is due to the diminished strength of the rotating vortex in the

cavity and the flow interaction in the injection strategies used. As shown above, these non-reacting calculations (see Table 7 for uniform, Table 8 for Jaws and Table 9 for Scoop inflow profiles) indicate that Configuration C is the most efficient. Further analysis assuming uniform/Jaws inflow with chemical reactions will be limited to this configuration.

The following figure shows a comparison of the fuel mass fraction for the rectangular configuration of Case 4 to the circular equivalent, Configuration B. Due to variations in geometry, fuel port distances and cavity volumes, fuel penetration and downstream dispersion are quite dissimilar.

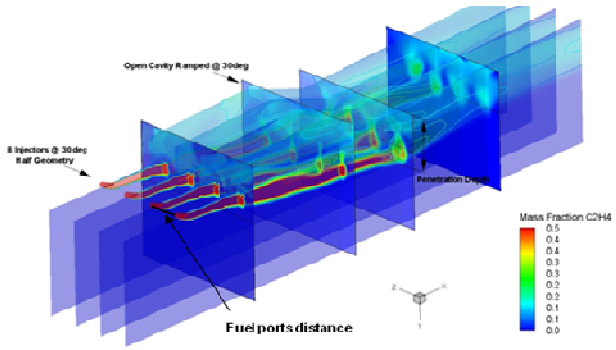

(a) Rectangular

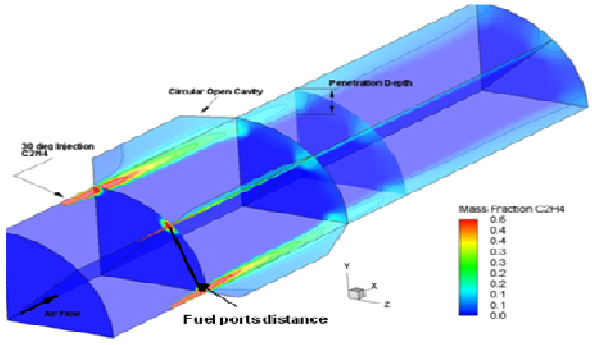

(b) Circular

Figure 84: Fuel penetration depth comparison of configurations.

Figure 85 shows the similarity of the rectangular and circular combustor configuration area cross sections and their relation to the fuel penetration depth comparison.

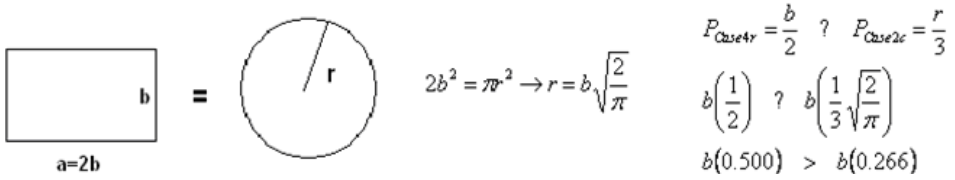

Figure 85: Cross sectional area relationships to the fuel penetration: Rectangular versus Circular combustor.

5.2.5 Discussion of Results (Circular Combustor, Frozen Chemistry)

From the selected three rectangular combustor configurations (Cases 1, 4 and 9) found in Chapter 4, several simulations are performed to explore the effect of these injector configurations with a circular cross-section modified into Configurations A-C (Cases 1-3c) respectively. The effect of inflow profile (uniform versus distorted either by a Jaws or a Scoop inlet), steady state assumptions and frozen chemical kinetics are delineated. The distorted inflow profiles yield higher fuel/air mixing factor than the uniform inflow profiles, due to additional vortical structures and circulation near the wall. This increases shock/boundary layer interactions, which then aids diffusion.

As foreseen, the boundary/shock interactions cause the Jaws inflow conditions to slightly increase the mixing factor and thrust ratio because of its higher profile pattern distortion compared to Scoop. However, the increase is not

as high as anticipated. The selected fuel injection strategy is apparently not designed efficiently enough to take advantage of the normal horseshoe vortex created by Jaws, and further strategies might be explored specifically considering these inflow distortions. Finally, the circular Configuration C is the most efficient of all the circular configurations, but it does not perform as well as the rectangular configuration (see Case 4 in Chapter 4).

The results suggest that the fuel injection strategy may be further optimized for this specific Configuration C by: 1) considering the features present at the exits of the inlets, 2) positioning the smaller and numerous fuel ports closer together (as in the rectangular configuration) to further drive the cavity's vortex and disperse the fuel, while maintaining the same stoichiometric value, and 3) reducing the volumetric cavity proportional to the rectangular counterpart with an equivalent length to depth ratio, rather than equal length and depth. Note that these design changes are not considered earlier, since other factors are held constant across three circular configurations to assume equal dimensions, fuel mass flow rates/pressure ratios, number of injectors and achievable penetration depth compared to the rectangular counterpart cases.

5.3 CIRCULAR COMBUSTOR SELECTION: INFLOW ASSUMPTIONS AND FINITE-RATE CHEMISTRY

In the following simulations, gaseous Ethene fuel (C_2H_4) is injected through flush-wall injectors located upstream of the cavity with the same conditions as before. The inflow conditions are set by specifying either 1) the

averaged uniform or 2) point-wise primitive variables corresponding to Jaws and Scoop inflow profiles. The outflow boundary condition is modeled using 1st-order extrapolation. The combustor and injector walls are modeled with a no-slip, adiabatic boundary condition. Combustion is modeled using a finite-rate, Ethene-air chemistry model and Gordon/McBride thermodynamic curve fits. Thirteen chemical species are considered (C_2H_4, C_2H_2, CO_2, CO, OH, O_2, O, H_2, H, H_2O, NO, N and N_2) with 20 chemical reactions applicable to a reduced reaction mechanism for reactants and products (described in Chapter 1).

As shown in the previous section, Configuration C also resulted in greater fuel penetration relative to other circular cases, and a stronger recirculation region in the cavity. Temperature and pressure, together with an air-fuel ratio at approximately stoichiometric proportions in the cavity region, were found to be ideal for auto-ignition in this configuration. Injection strategies that drove the cavity vortex in its natural direction were particularly significant, and suggested the existence of a highly unsteady situation, especially when reactions were considered.

Focusing now only on the circular Configuration C cases, as anticipated, the distortions due to shock/boundary layer interactions in Jaws/Scoop inflow increase the mixing factor slightly. One possibility is that the injection strategy does not take as much advantage of the vortical structure created by these innovative inlets, and other strategies may be superior in this case. When comparing all the non-reacting cases, Combustor Configuration C was the most efficient due to the first pair of injectors located at the front-bottom wall of the

cavity, and directed perpendicular to the air upstream. The second pair of injectors, located on the ramp and directed against the air inflow, did not enhance the natural vortex rotation in the cavity as previously observed in the rectangular analysis. Further work in this area should be considered if a more detailed design analysis of these scramjet combustors is desired.

Table 11 groups the cases studied for this section according to their geometrical configuration, inflow conditions and chemistry assumptions. For these cases, the subscript "cr" is used to refer to circular Configuration C when chemical reactions are assumed. For Cases 1-3cr, the combustors were initialized from their previous frozen solutions of Cases 1-3c, respectively. The CFL was set constant at 1.0 until convergence was achieved in around 30.3, 34.5 and 61.2 hours using 64 processors for Cases 1-3cr, correspondingly.

Table 11: Circular combustor cases with finite-rate chemistry.

Cases	**Configuration**	**Inflow**
1_{cr}	C	Uniform
2_{cr}		Jaws
3_{cr}		Scoop

5.3.1 Uniform Inflow (Finite-Rate Chemistry)

The results obtained for the uniform inflow conditions are shown in Figure 86 for Case 1cr. Examination of the Mach number and pressure contours on the xy-symmetry plane of the reacting case reveals a high compression disk-shaped area upstream of the cavity. This feature originates because of the chemical

reactions taking place upstream of the cavity prior to the injection location. Although not observed in the frozen chemistry case, the phenomenon reveals the mechanism for upstream displacement of the reaction region. As in previous cases, the shear layer in this configuration is pushed away from the vicinity of the step where the perpendicular injectors at the bottom of the cavity are situated. This causes a larger circulation region ahead of the jet and near the back wall, opening a low speed pocket that allows the injection to pierce deeper toward its annular core. In addition, this creates a region of high temperature and mixture (see Figure 86) where rapid reactions propagate forward and outside the cavity through the shear layer. The results indicate that chemical reactions are initiated upstream of the cavity, even prior to the injection location. A principal cause of this is the upstream influence of the injection on the cavity floor, which results in an earlier detachment of the cavity shear layer, even before the step. The ideal temperature and balanced fuel/air mixture at the boundary layer outside the cavity results in an upstream propagation of the reactions away from the cavity. The fuel mass fraction (see Figure 86c) shows, in contrast to the non-reacting and uniform case (Case 1c), a good diffusion within the cavity region resulting in a mixing factor of about 64%. As previously anticipated in the frozen assumption of Case 1c, this shows a relatively rapid reaction rate. The CO_2 contours indicate locations of maximum burning and correspond to high temperature regions.

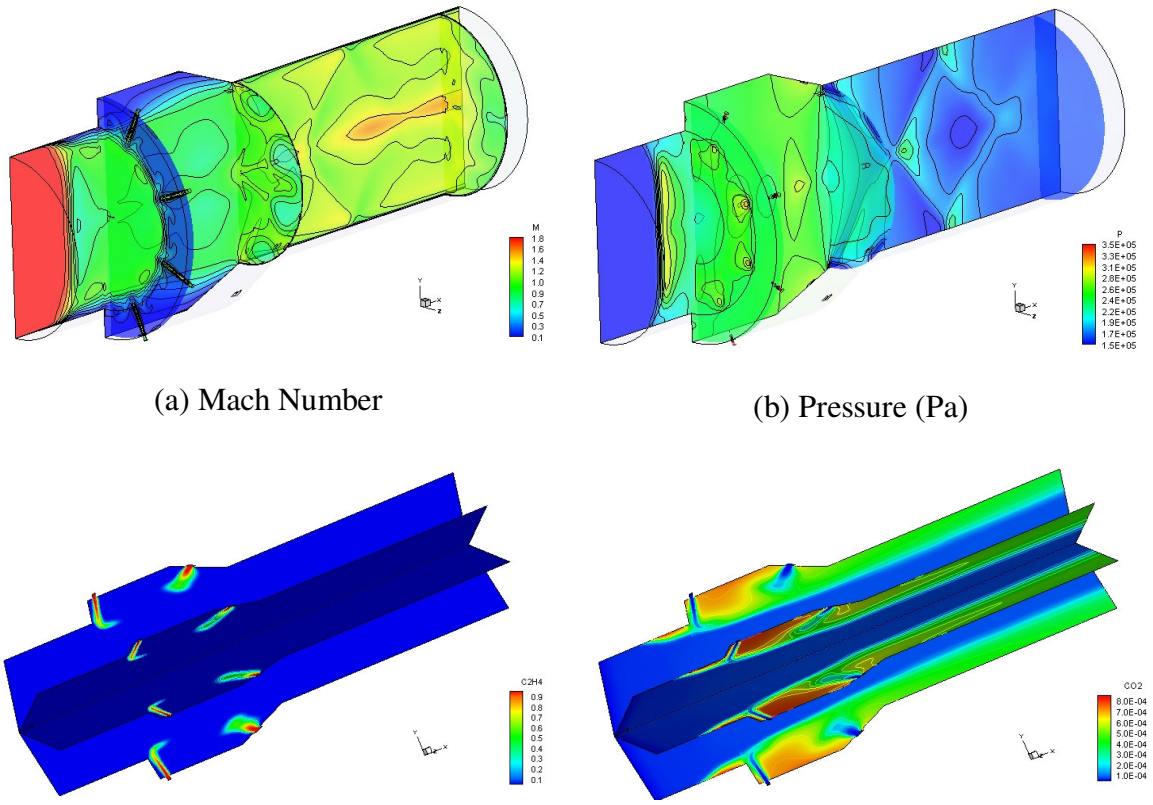

(a) Mach Number

(b) Pressure (Pa)

(c) $Y(C_2H_4)$

(d) $Y(CO_2)$

Figure 86: Case 1cr results, uniform flow and chemically reactive.

Figure 87 shows the entire geometry at the symmetry planes and four additional *x*-plane stations for Case 1cr. Again, several conclusions are readily apparent when these figures are compared to equivalent results in the frozen cases.

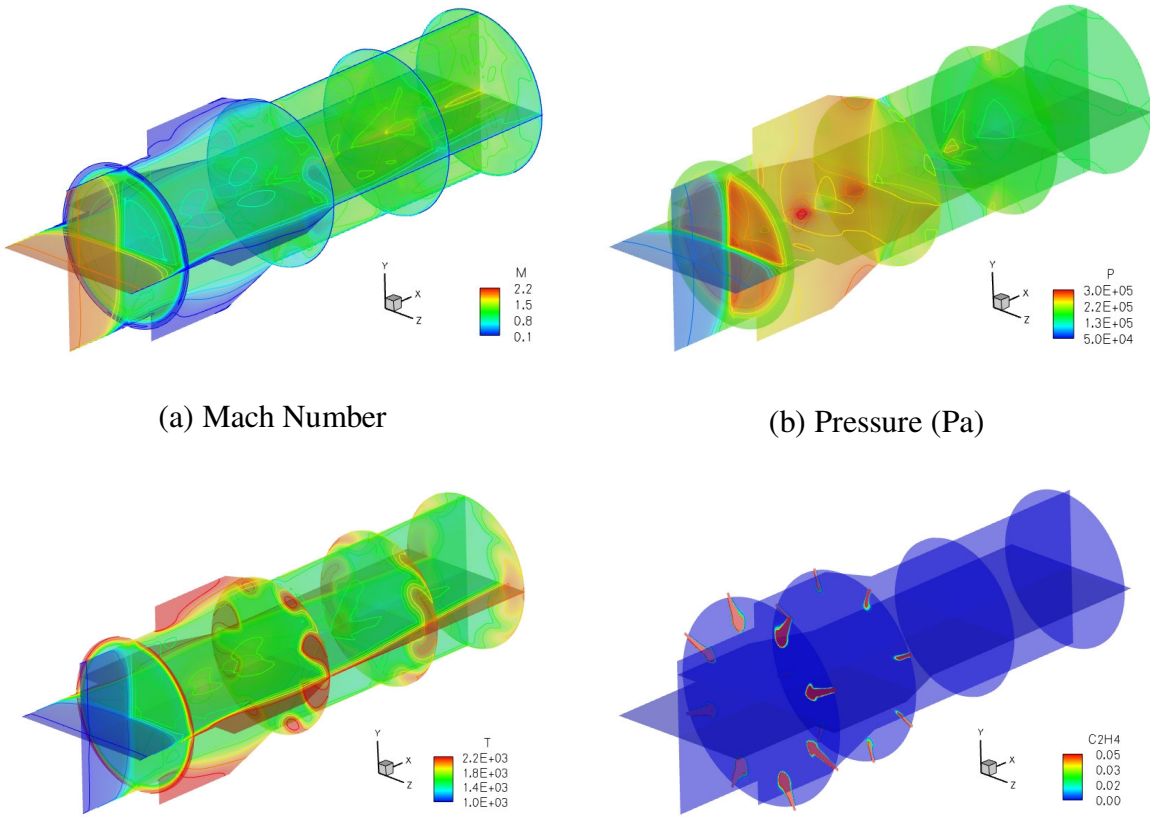

(a) Mach Number

(b) Pressure (Pa)

(c) Temperature (K)

(d) $Y(C_2H_4)$

Figure 87: Case 1cr results, uniform chemical reactive.

Note that both Mach Number and pressure contours on the *z*-plane of the reacting case reveal a high compression disk-shaped area upstream of the cavity, which is absent in the frozen simulation (Figure 87). Section 5.5 of this chapter will further analyze the causes and effects of these flashback phenomena with a time-accurate (unsteady) computation on this Configuration C. In that section, a much finer grid with the same 3rd spatial order is utilized with the LES turbulence model described in Chapter 1.

5.3.2 Jaws Inflow (Finite-Rate Chemistry)

Figure 88 shows the quarter symmetry results obtained for the Jaws inflow conditions (Case 2cr). In comparison to Case 1cr, the Mach number and pressure contours do not show such a high compression area upstream of the cavity, or chemical reactions taking place far upstream of the cavity prior to the injection location. In comparison with the frozen case (Case 2c), the bowed shock from the interacting jet and shear layer shows a larger compression towards the center of the combustor and moved upstream. The variation in the boundary layer profile upstream of the cavity indicates that the flame is positioned right on the edge, in front of the opening as predicted in the frozen chemistry case (Case 2c). A larger region of low Mach numbers is observed inside the cavity, caused by the larger temperature values produced by chemical reactions. As seen in Case 1c, the shear layer in this configuration is pushed away from the vicinity of the step where the perpendicular injectors at the bottom of the cavity are situated, causing a leaner circulation region in front of the jet and near the back wall. This shows a bit superior penetration and layer development near the opening than with chemically frozen assumptions, since the reactions are taking place a bit upstream of the step, increasing the pressure in this region which then moves the shock interaction forward closer to the step. As shown by the CO_2 mass fraction contours (Figure 88c), many of the reactions take place in the vicinity of the shear layer while under the opening and further downstream near the wall, also corresponding to high temperature regions. The Danköhler number contours in Figure 88 show the

non-axisymmetric reaction patterns that occur within the cavity, from the two cutting planes positioned through two pairs of injections.

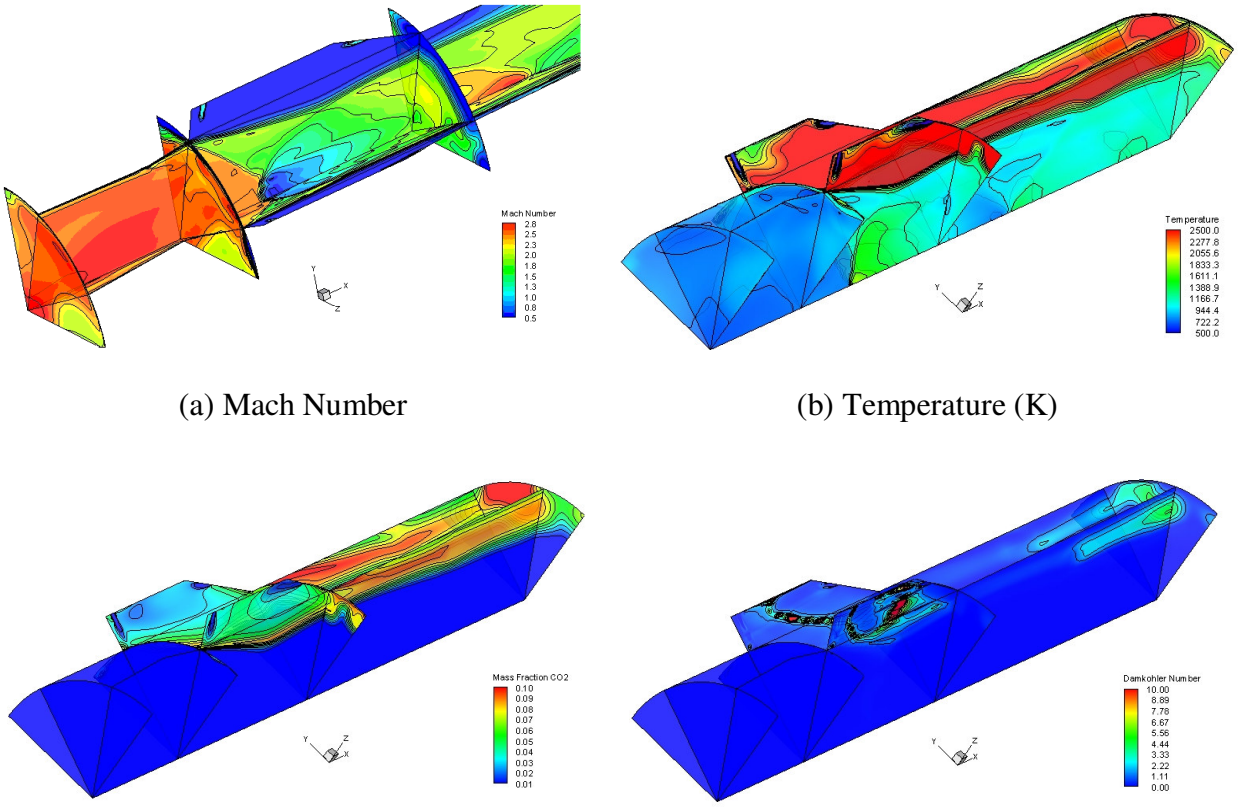

(a) Mach Number

(b) Temperature (K)

(c) Y(CO_2)

(d) Danköhler Number

Figure 88: Case 2cr results, Jaws inflow with chemistry.

Figure 89 shows the Mach number, vorticity magnitude, fuel mass fraction and temperature results obtained for Case 2cr, at the symmetry planes and four other *x*-plane stations. In comparison to the reacting but uniform profile case (Case 1cr), the Mach number and temperature contours do not show as high a compression area upstream of the cavity. Thus, chemical reactions take place far upstream of the cavity prior to the injection location. Considering frozen versus

finite rate chemistry for the Jaws inflow profile, the latter case shows larger compression towards the center of the combustor due to the bowed shock from the interacting jet. The shear layer separation does show upstream movement, but not as much as in the reactive uniform case. The variation in the boundary layer profile upstream of the cavity indicates that the flame is positioned on the edge of the step, in front of the opening, as predicted in the frozen chemistry case. A larger region of low Mach numbers is observed inside the cavity, caused by the larger temperature values produced by chemical reactions. In this case, the distorted incoming profile mitigates the upstream propagation of shear layer separation and thus reduces local pressure losses. The average fuel mixing factor calculated under the steady state assumption reaches 67%, marginally higher than the previous case, and less than its chemically reactive rectangular counterpart (Case 4 ~72%). The vorticity magnitude contours on Figure 89 show the asymmetric velocity flow patterns that occur near the walls. As computed from the inlet (see Chapter 3), stronger vortical structures are observed on the upper and bottom region with diminished shear on the sides of the Jaws profile. The effect on the shear layer across the cavity increases the diffusion. In addition, this interaction further disperses fuel from the opening and aids combustion, as evident on the z-plane (see fuel mass fraction and temperature in Figure 89).

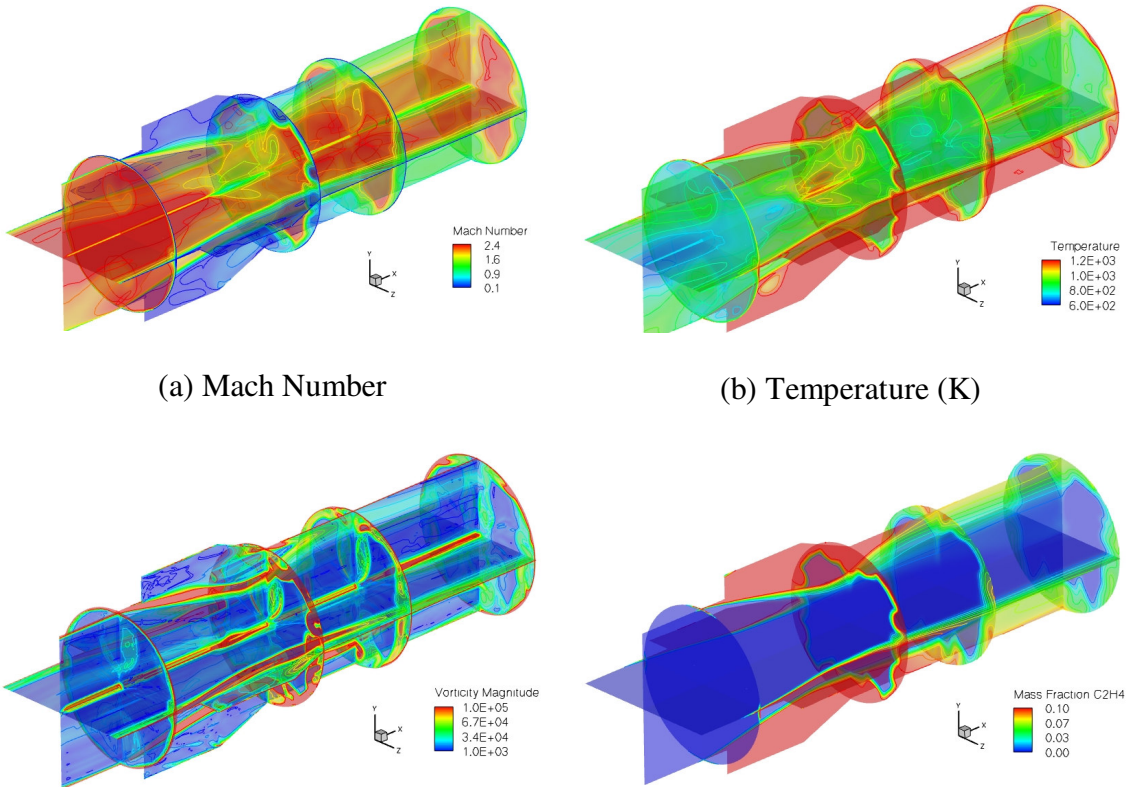

(a) Mach Number

(b) Temperature (K)

(c) Vorticity

(d) Y(C_2H_4)

Figure 89: Case 2cr solutions at symmetry planes.

5.3.3 Scoop Inflow (Finite-Rate Chemistry)

The results obtained for the Scoop inflow conditions are shown in Figure 90 (Case 3cr). A cursory examination reveals significant differences from the Jaws profile. Examination of the Mach number and pressure contours on the xy-symmetry plane of this reacting case reveals a three dimensional oblique compression area upstream of the cavity. Its conical shape is distorted by the low velocity region on the lower part (recall that the Scoop profile does not display symmetry about the horizontal plane), which positions the shock further upstream from the step than in the frozen case (Case 3_a).

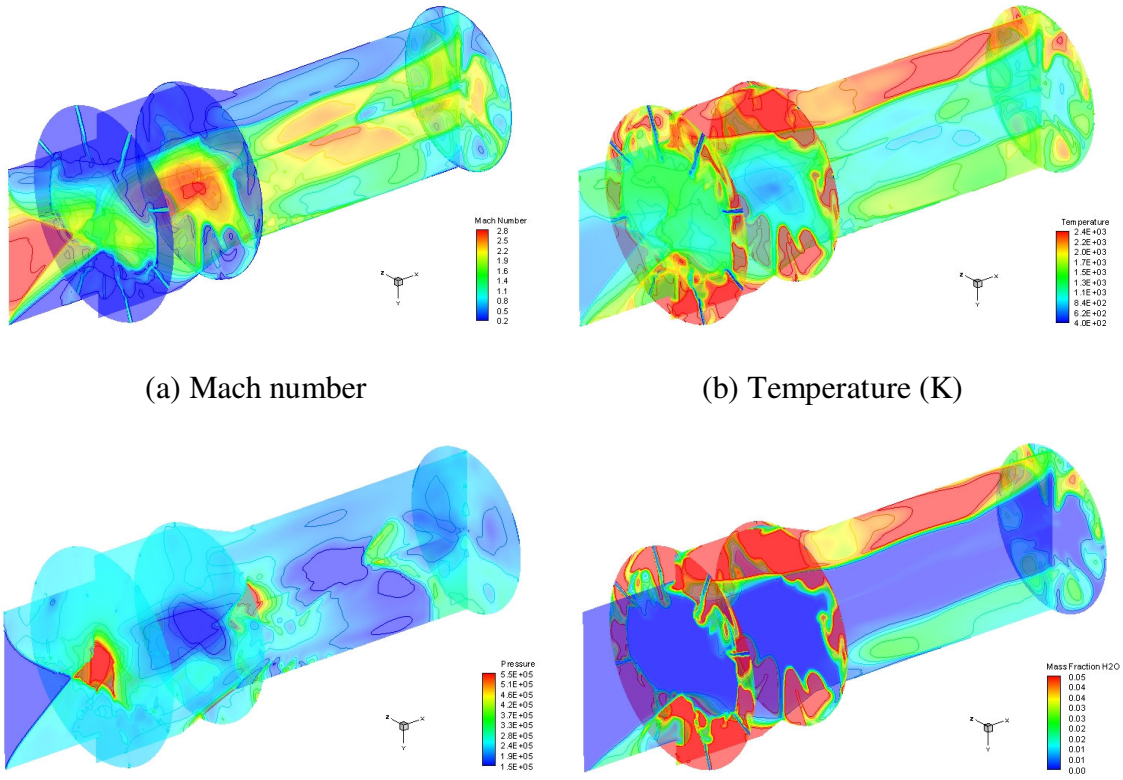

(a) Mach number (b) Temperature (K)

(c) Pressure (Pa) (d) Y(H_2O)

Figure 90: Case 3cr solutions at the vertical symmetry plane.

The mechanism is similar to that observed for Case 1b but specifics of the pattern are different because of the variation in the entrance profile. Scoop exhibits a larger circulation region ahead of the jet, further allowing the fuel to travel forward. The pressure contours illustrate the uneven primary and secondary shock interactions prior to and past the cavity zone (see Figure 90). As experiments have shown, if the fuel air mixture is within flammability limits, one or two flame zones might be present within the light and re-light high pressure regions.[110] The water mass fraction (Figure 90d) shows the region of higher production inside the cavity, which coincides with the high temperature region

(Figure 90b). The finite-rate shows a better diffusion within the cavity region than the frozen case, resulting in a mixing factor of about 63%. In this case (Case 3cr), as in the other reactive cases, the prominent reaction region lies in the vicinity of the cavity shear layer and further downstream near the wall, which also corresponds to high temperature contours.

5.3.5 Uniform, Jaws vs. Scoop inflow, Finite Rate Assumptions

The chemical reacting temperature contours for Jaws reveal a more uniform flow at the exit of the combustor compared to the Scoop results shown in Chapter 3. The Jaws case displays more uniform combustion in the angular, θ, direction compared to the Scoop case. In the Scoop case combustion was not as uniform in the θ direction, and a region of reduced burning was observed in the upper section of the flame holder. An initial assessment of the flow in the recessed cavity region (in the low burning section of the combustor) indicated that the streamwise (xxr-direction) recirculation was not as strong as in the Jaws case. This resulted in reduced entrainment of O_2 from the core flow and therefore lower O_2 concentrations in the cavity. Furthermore, the flow pattern in the recessed cavity exhibits a circulation component in the x- θ direction that aids in combining the ethylene from the upper two injectors. The net effect is a fuel-rich condition that produces less burning. Additional burning occurs downstream of the recessed cavity in this section of the combustor as more O_2 becomes available through macroscopic and diffusive mixing processes.

A comparison of the effect of inflow profile on reactive cases is summarized in Figure 91, which shows CO radical mass fraction contours for the uniform and also the two distorted inflow profiles (Jaws and Scoop, respectively). These solutions indicate that both Jaws and Scoop non-uniform inlet profiles can significantly lower the fuel-air ratio levels inside the cavity, helping distribute the fuel towards the core.

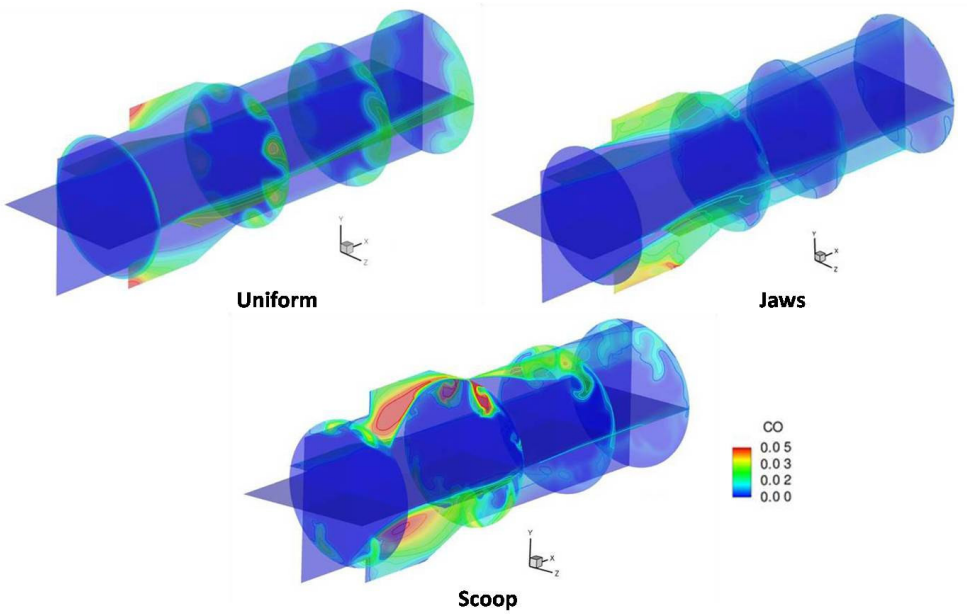

Figure 91: Mass fraction CO contours at symmetry planes for Cases 1-3cr.

Figure $92_{a\text{-}c}$, in particular, shows profile differences on the Mach number contours at the z-plane positioned through a set of injectors (Uniform, Jaws and Scoop, respectively). The uniform inflow, with no developed shear layer at its entrance, positions a normal (three-dimensional disk) shock halfway between the entrance and the step. This is caused by the combustion pressure rise and forward movement of the fuel (Figure 92_a). Jaws' profile mitigates the effects captured by

the uniform assumption, while Scoop's develops a thermal shocking effect that develops further upstream towards the conditioned inflow boundary (see Figure $92_{b\text{-}c}$). A comparison of the effect of each inflow profile on reactive cases is summarized in Figure 92_d, which shows the pressure line at the center of the combustor Configuration C. Jaws' profile results in a much higher combustion pressure that spikes at the core of the combustor right before the cavity's ramp produced by a conical shock interaction, and followed by an expansion (see Figure $92_{a\text{-}c}$). On the other hand, the Scoop profile did not show much difference at the center pressure line compared to the uniform inflow.

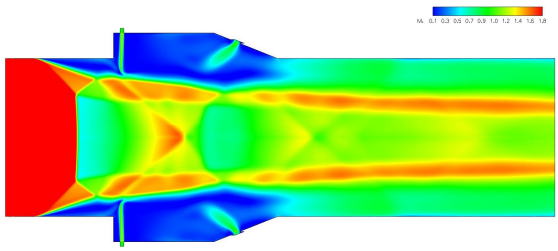

(a) Mach Number, Uniform inflow

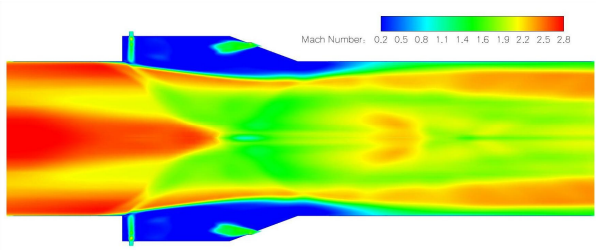

(b) Mach Number, Jaws inflow

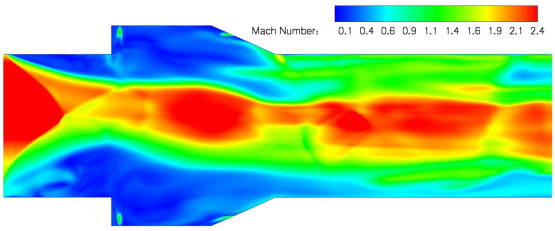

(c) Mach Number, Scoop inflow

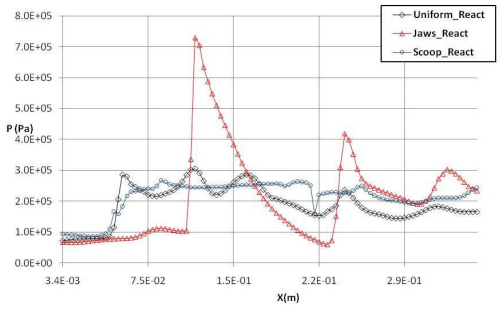

(d) Centerline Pressure (Pa)

Figure 92: Results comparison for Cases 1-3cr.

Table 12 summarizes the integrated pressure and temperature averaged inside the cavity volume for the tree inflow profiles assuming chemistry, Cases 1-3cr.

Table 12: Pressure and temperature inside cavity (Cases 1-3cr).

Inflow Profile	**P_{ave}(Pa)**	**T_{ave}(K)**
Uniform	2.56×10^5	1.31×10^3
Jaws	2.25×10^5	1.26×10^3
Scoop	2.45×10^5	2.23×10^3

In addition to the fuel/air mixing factor, which correlates with combustion, the normalized integrated thrust per unit area ratio (Equation 21) is computed as shown below.

Equation 21: Thrust per unit area ratio.

$$F = \dot{m}_e u_e - \dot{m}_i u_i + A_e P_e - A_i P_i, \dot{m}_e = \dot{m}_i + \dot{m}_f \quad and \quad A_e = A_i$$

$$\rightarrow \Im = \int \frac{(\dot{m}_i + \dot{m}_f) u_e / A_i + P_e}{\dot{m}_i u_i / A_i + P_i} \partial A_i$$

For the final assessment of the inlet and combustor integration for all of the above on-/off-design conditions, see Table 13. From the earlier calculations done across the inlets and combustors, the total thrust *($\Im$)* and drag *(D)* are computed and normalized to obtain their combined uninstall magnitudes at the

exit *(F_e-D)*. The combustor factor is considered analogous to the amount of fuel consumed from the total input into the burner or equivalent to the chemically reactive mixing factor as described above. The calculated total drag forces on all these cases in terms of thrust percentage *(D/ τ)* are shown in Table 13.

Note that these configurations are relatively short (about half of their projected length), and extend only a few cavity lengths downstream. When considering such designs, a much larger combustor length must be considered due to the flow and chemical time scales. The motivation for these shortened simulations was to quickly measure their performances in order to obtain trend information.

Table 13: Integrated scramjet performance results.

Configuration	**Pitch (^{o})**	**Yaw (^{o})**	ℑ	***Ce %***	***(F_e-D)***	**(D/ τ)%**
Baseline	0	0	2.23	71	1.00	32.79
	3	0			1.40	30.65
	0	3			1.27	33.80
Jaws	0	0	2.63	67	1.19	24.15
	3	0			1.14	25.23
	0	3			1.18	24.21
Scoop	0	0	2.22	63	0.83	27.85
	3	0			0.99	23.34
	0	3			0.81	28.55

5.3.6 Discussion of Results (Circular Combustor, Finite-Rate Chemistry)

The circular configuration that yields the highest mixing factor from earlier in this chapter, Configuration C, was simulated with a 13 species and 20 reactions chemical model. Then, three cases were computed for the uniform, Jaws and Scoop inflow profiles (Cases 1-3cr, respectively). In general, the solutions indicate once more that the inlet profiles can significantly lower the equivalent ratio levels inside the cavity, helping to move the fuel towards the core. The trends observed with and without chemical reactions are the same, though the former yields roughly 10% higher mixing factor. Unlike at frozen conditions, when chemical reactions are considered, a high compression disk-shaped area is observed upstream of the cavity for Case 1cr. The upstream reactions from the cavity have a significant impact on the development of the shear layers and downstream development of the entire combustion. This is caused by the chemical reactions situated upstream of the cavity prior to the injection location. The shear layer in this configuration is pushed away from the vicinity of the step where the fuel is injected perpendicular to the incoming air and positioned at the bottom of the cavity. This increases the circulation region in and around the cavity, allowing the reactions to propagate forward through the shear layer. These physical effects are not present when modeling Jaws inflow with chemistry (Case 2cr). In Scoop, these effects are exacerbated due to the thicker low energy profile surrounding the walls and most of the lower section of the combustor.

The flashback effect is further analyzed with a time-accurate (unsteady) computation of Configuration C. Section 5.5 uses a much finer grid with the same spatial order (3^{rd}), but coupled to an LES turbulence model. This is conducted in the interest of flame stabilization and to gain further insight into the starting conditions.

5.4 UNSTEADY ANALYSIS: URANS VS. LES

Two additional approaches, Unsteady Reynolds-Averaged-Navier-Stokes (URANS) and Large-Eddy Simulation (LES), further highlight the flow instability and reveal the differences when applying each tool to these non-premixed cases. For all previous cases, the key performance of combustion is not realistically captured, since the chemical time scales are not assumed to be directly coupled to the turbulent effects. For these unsteady cases, on the other hand, chemistry and turbulence are assumed to be directly coupled to help capture these trends and understand the starting characteristics and/or thermal shocking effects. The essential issues regarding supersonic combustion, such as fuel-air mixing, ignition, flame anchoring via open cavities as holders, and flame adaptation as hypersonic inlet conditions varies, have never been properly addressed. This is partly due to a lack of accurate and physically consistent numerical prediction codes (since experimental evaluation of actual flight envelopes is very expensive, if not impossible). In this section, the research focuses on analyzing the unsteadiness of the flow and how the mixing/combustion performance efficiencies vary for the selected circular combustor. Again, as in the RANS

modeling analysis of Configuration C, a uniform averaged profile is assumed. The use of a cavity, combined with a proper fuel injection strategy, applies as a flame holder in supersonic conditions. Our selected scramjet combustor prototype yielded the highest fuel/air mixing factor from a previous parametric analysis. This configuration contains a single cavity and two arrays of fuel ports: a first set of injectors at the cavity floor directed 90° to the airflow; and a second set positioned at the bottom of the ramp, aimed upstream with respect to the airflow.

These assessments are computed using the identical finite rate chemical kinetic model for the combustion of Ethene fuel and air on Configuration C as used in Section 5.4. The URANS modeling is used as an engineering tool to understand overall flow structure and to compare to more costly LES calculations. LES is employed in the combustor domains to accurately capture the physics of unsteady mixing and combustion instabilities by providing vortex shedding, an indication for cavity oscillations and unstable flames. The dominating flow field inside the cavity, characterized by vortex formation and recirculation regions, is noticeably different in each approach.

A main difficulty in providing a mathematical description for prediction of cavity flow arises from the presence of turbulence and its interactions with other dominant features of these flow fields. Due to the complex physical phenomena in scramjet combustion and difficulties in experimental investigation, simulations are expected to play an ever increasing role in the design process. In addition to access to flow conditions and flow features which cannot be obtained

experimentally, CFD can greatly reduce the length and cost of the design cycle. However, conventional CFD techniques such as Reynolds-Averaged Navier Stokes (RANS) approaches have failed in the past to resolve many of the issues related to scramjet combustor fuel-air mixing, since this is primarily an unsteady phenomenon. In a majority of industries, unsteady RANS is still the method of choice for practical situations. However, it suffers from fundamental deficiencies in its depiction of turbulent behavior that significantly limits solution accuracy. [111] A promising technique for predicting the effects of turbulence in unsteady cavity flow is Large Eddy Simulation (LES). In the unsteady RANS, the solution utilizes time-averaged variables, in which all scales are modeled in the same way. In this approach, there is no difference between large-scale turbulence structures and small, dissipative turbulent scales. In the LES, the large-scale motion is fully resolved on the computational grid using a time- and space-accurate scheme. In LES, only the small scales are modeled. For smaller, dissipative scales (*i.e.*, smaller than the grid size), LES utilizes subgrid models, including sub-grid scale models (*SGS*) for turbulence and turbulence-combustion interactions (Ref. *44*). LES modeling techniques require large computational resources which limit practical and routine applications. However, due to the HPC parallel computer clusters, the computational cost of LES is becoming more reasonable for medium sized problems such as this research.

5.4.1 Computational Modeling

The objective of this section is to numerically investigate the scramjet combustor fuel-air mixing, reacting, and cavity interaction with main stream flow using two different turbulence methodologies: URANS and LES approaches. The configuration adopted and the inflow conditions are common in supersonic combustion.

The cavity is considered to be the state of the art approach to stabilizing a flame by trapping a vortex of flammable mixture. In conventional flame stabilization approaches, swirl, bluff-body, and rearward facing steps are used to create low velocity recirculation zones into which hot combustion products are entrained to stabilize the reaction. In these conventional approaches, the location, strength, and stability (temporal and/or spatial) of the recirculation zones are coupled to the main flow in the combustor. Previous steady state calculations concluded that in this part of the research, the flame is stabilized by a vortex that is virtually independent of the main stream due to the selected injection strategy (Configuration C). This recirculation zone transports some of the hot combustion products back toward the combustor face and ignites the incoming fuel and air as it mixes in the combustion chamber.

The complexity of the scramjet with cavity includes large regions of subsonic flow, shock-to-shock and shock-to-boundary-layer interactions, separated flow regions, complex mixing phenomena, non-equilibrium transfer of turbulence energy, and interactions between turbulence and chemical kinetics that may impact both the chemical reactions and the turbulence field, as seen in earlier

sections. GPACT code has been applied towards simulating scramjet combustor flowfields and many other propulsion systems.[112]

This LES methodology and URANS both used the exact same structured grid. The computational details included a fully implicit and strongly conservative finite-volume formulation. As shown in Figure 67, the entire configuration has 8 pairs of injectors, thus the simulation is reduced to just a $1/8^{th}$ slice (see Figure 93). The structured computational grid is made out of ~7.8 million points and resolves the flow in the cavity and around the fuel injector, near the edges and around the corners of the cavity, and the towards wall (see Figure 93). The volumetric average grid cell size is about $5x10^{-11}$ m^3, clustered near the walls and around the cavity to yield an average y^+~0.6. The time step for these unsteady cases is $1x10^{-7}$ sec. The boundary conditions for the periodic sides were assumed to be symmetrical, averaged at the axis-symmetry pole, fixed uniform inlet at the entrance and fuel ports, and 1^{st} order extrapolation at the exit plane.

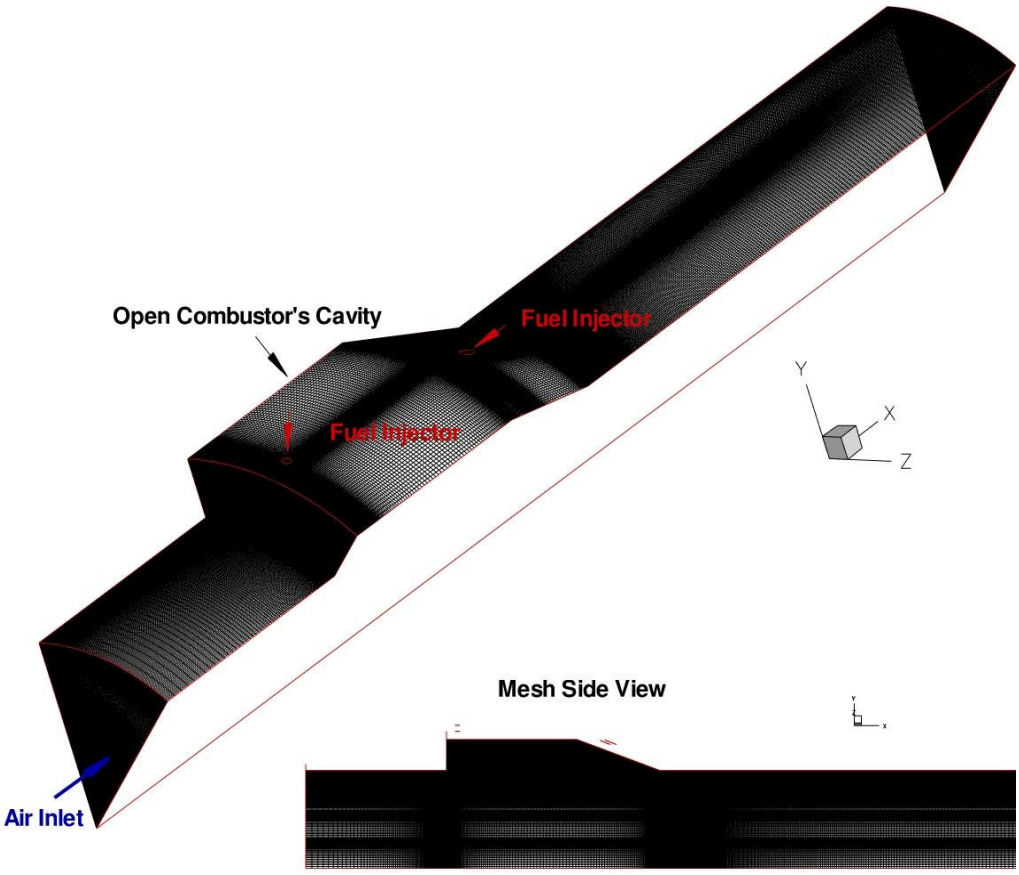

Figure 93: Computational grid for a 1/8th section with symmetrical boundary conditions, circular combustor.

Both of these problems were initialized by the uniform inflow condition throughout the combustor, except for the cavity region where the velocity was reduced to u= -0.01 m/s. When injection into the cavity began, the T_{fuel}=600K was prescribed for the first 1,000 iterations. This was reduced to T_{fuel}=300K thereafter. The time steps were set constant at $1x10^{-7}$ sec, until a final time of about 3.0 msec was achieved in about 105 and 612 hours using 64 processors, for the URANS and LES cases accordingly.

5.4.2 URANS with Finite-Rate Chemistry

The results of the URANS analysis for Mach number, pressure and temperature contours at 5 different time frames is shown in Figure 95. The picture depicts the development of the flow as time frames change from 0.6 to 1.0 msec by increments of 0.2 msec, at half-symmetry of a z-plane located through the center of both injector sets. Note that both URANS and LES were initialized by achieving a steady state condition of just the airflow with no injection. This facilitated the establishment of the airflow inside the cavity region, as well as the shear layer.

The URANS solution reveals the flow development as it reacts chemically, as well as the interactions between the shear layer and pressure waves. The high temperature contours initiate in the cavity where two injectors are mounted, and propagate upstream and further downstream near the periphery of the walls towards the exit. The results for URANS rapidly attained asymptotic solutions around 1.0 msec, when limited and cyclical variation was noted.

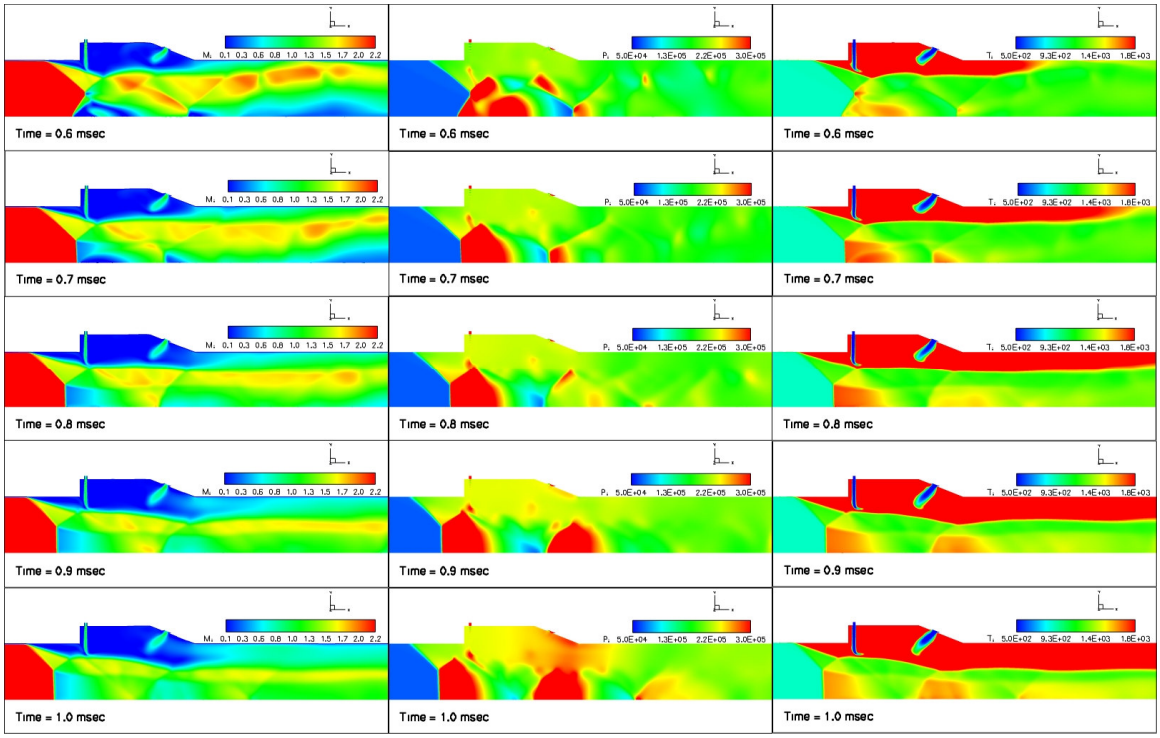

Figure 94: URANS results with finite-rate assumption, Configuration C: Mach Number, Pressure (Pa) and Temperature (K) from left to right columns.

5.4.3 LES with Finite-Rate Chemistry

The results of the LES analysis for Mach number, pressure and temperature contours at 12 different time frames is shown in Figure 95. The picture depicts the development of the flow as time frames change from 0.44 to 1.32 msec at half-symmetry of a *z*-plane located through the center of both injector sets. The LES solution captures the large-scale unsteady structures in the combustor flowfield region. The flowfield in the initial part of the mixing section consists of a periodic vortex shedding downstream of the cavity trailing edge. This organized vortex shedding then rapidly transitions to a turbulent structure.

The Mach number contours reveal the sizeable region of circulation, which appears to extend further into the free stream when reaction occurs. High levels of kinetic energy are observed inside of the cavity due to the chemical reactions. These rapid reactions within the shear layer and cavity increase the wall temperature. They also enhance a cavity interaction with the flowfield in the combustor.

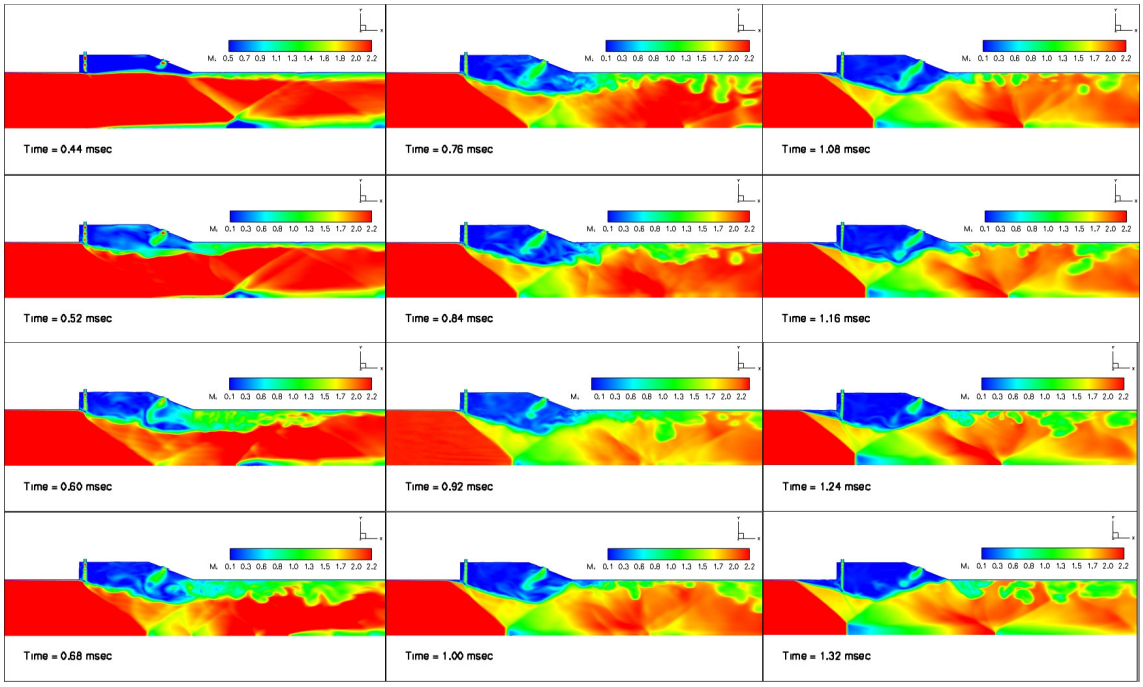

(a) Mach Number

Figure 95: LES with finite-rate assumption, Configuration C.

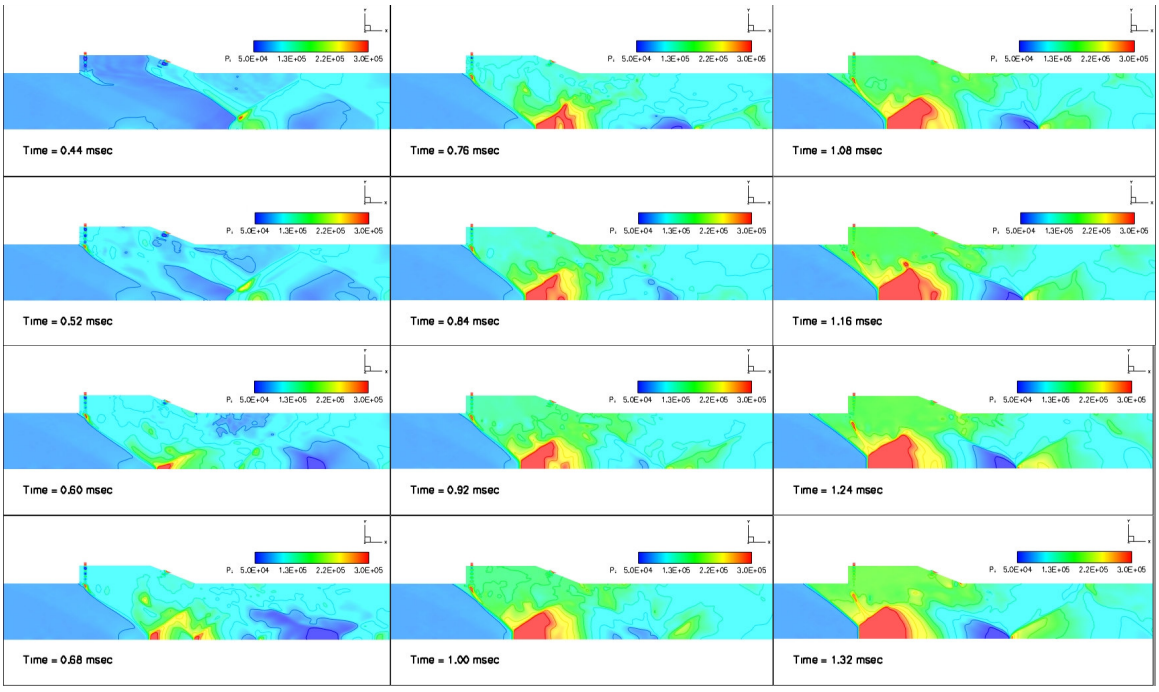

(b) Pressure (Pa)

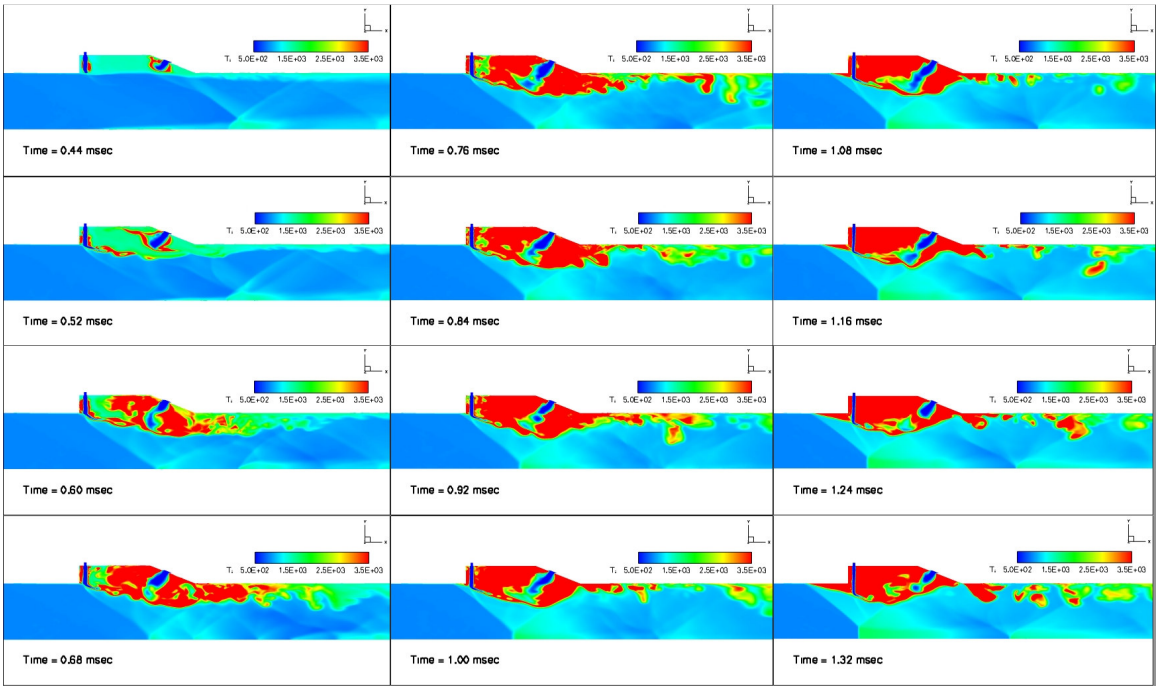

(c) Temperature (K)

"Figure 95 continued"

Figure 96 shows the Mach number and pressure contours for the LES case after t=1.32 msec from the previous figures. The plots on the left hand side of Figure 96 display the time progression from 1.4 to 1.8 msec, while the right hand side shows the time from 2.4 to 2.8 msec. Note the variation on the Mach number plot for: 1) the shear layer as it progresses across the cavity, large eddies develop and move downstream near the walls past the ramp, and 3) a shock interaction which reflects at the core of the combustor and near the end of the ramp yields a small subsonic region that fluctuates in size. The pressure contours show how the secondary pressure waves cycle in strength and location slightly back and forth at the centerline, downstream from the step. This pattern cycles in a similar matter over a period of about 0.6 msec.

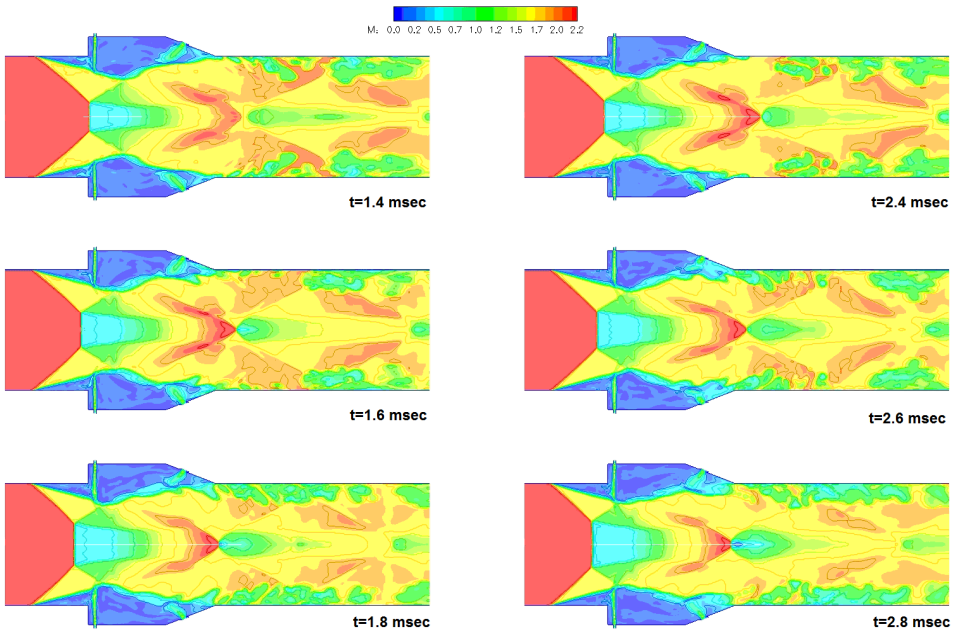

(a) Mach Number

Figure 96: Asymptotic behavior of LES after t=1.4 msec.

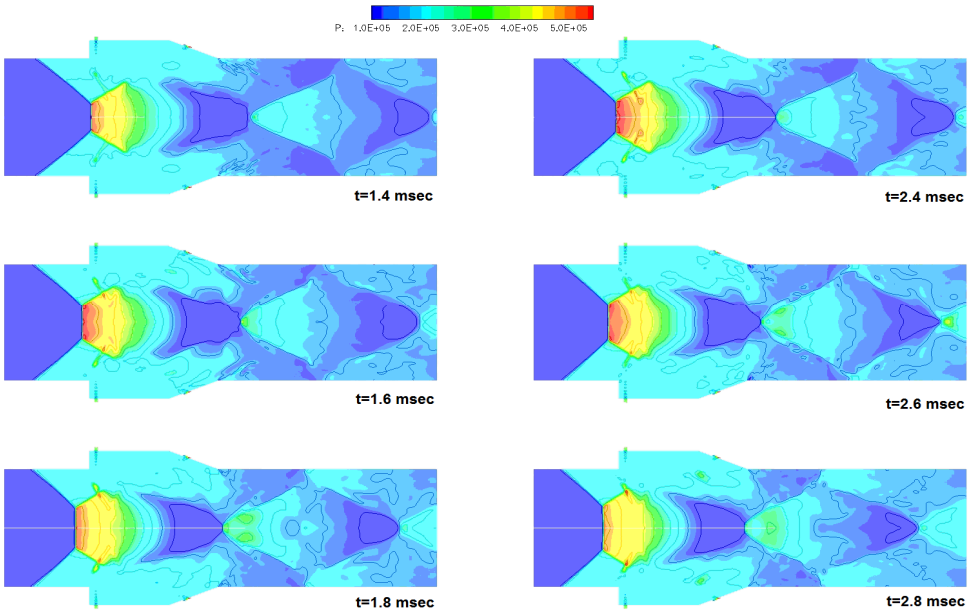

(b) Pressure (Pa)

"Figure 96 continued"

5.4.4 URANS vs. LES

The Mach number and Y(CO_2) contours for the LES and URANS calculations at four different time frames are shown side by side in Figure 97 for comparison. Figure 97a depicts the development of the flow as time frames change from 0.6 to 1.0 msec at half-symmetry of a z-plane located through the center of both injector sets. Observe how the subsonic region near the cavity, the shock interactions and their positions significantly differ from each other. Also, the exit planes for the LES, compared to URANS, yield a larger and more supersonic zone. In Figure 97b, the value of Y(CO_2) is scaled higher for the LES than the URANS simulation, which shows a major difference in the production of radicals, and in general, their reaction rates between both methodologies. When

solving for the finer scales in the LES model, solutions indicate an earlier appearance of and higher concentration of CO_2 than when using URANS.

In Figure 97c, reactions take place in the vicinity of the shear layer, within the opening and further downstream near the wall, all high radical production and temperature regions. Comparison of LES and URANS simulations shows that LES captures the large-scale unsteady structures in the flowfield of the cavity region, and yields higher levels and larger zones of temperature. This is because turbulent combustion is inherently unsteady. The vortex shedding and shear layer mixing cannot be properly captured by URANS. URANS also yields a deficit in the production of radicals, combustion temperature and pressure compared to LES. The flame anchoring and prediction of the shock location near the leading edge of the cavity differ drastically in each approach.

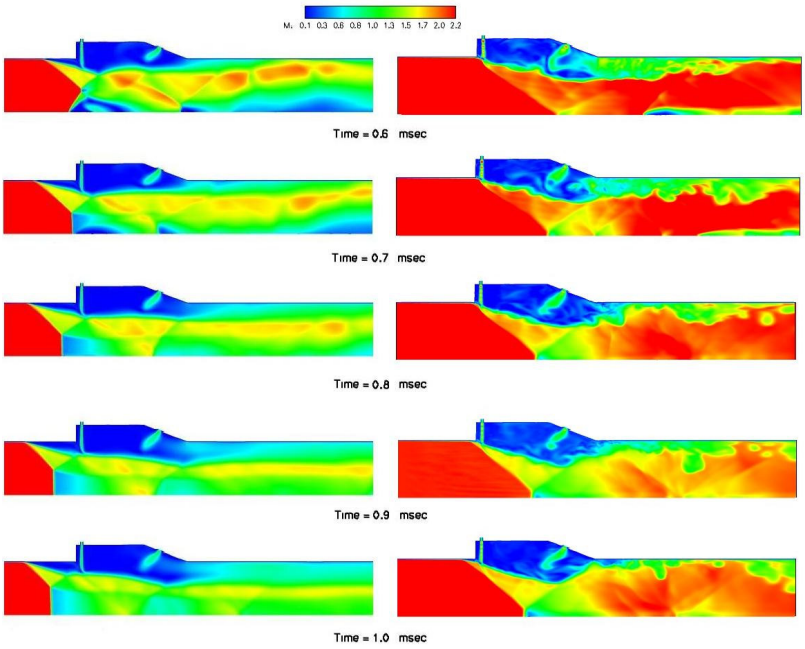

(a) Mach Number

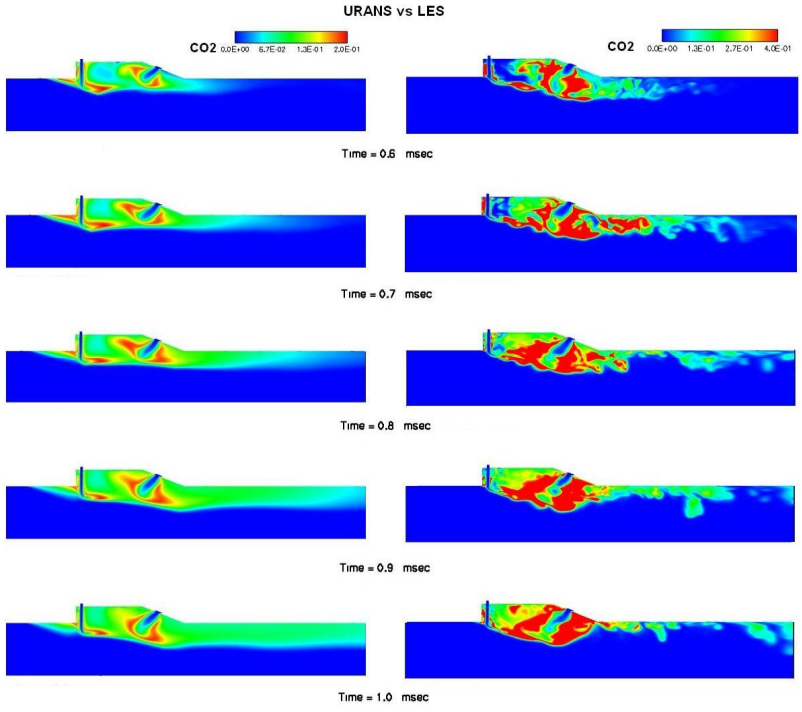

(b) Y (CO_2)

Figure 97: URANS (left side) versus LES (right side).

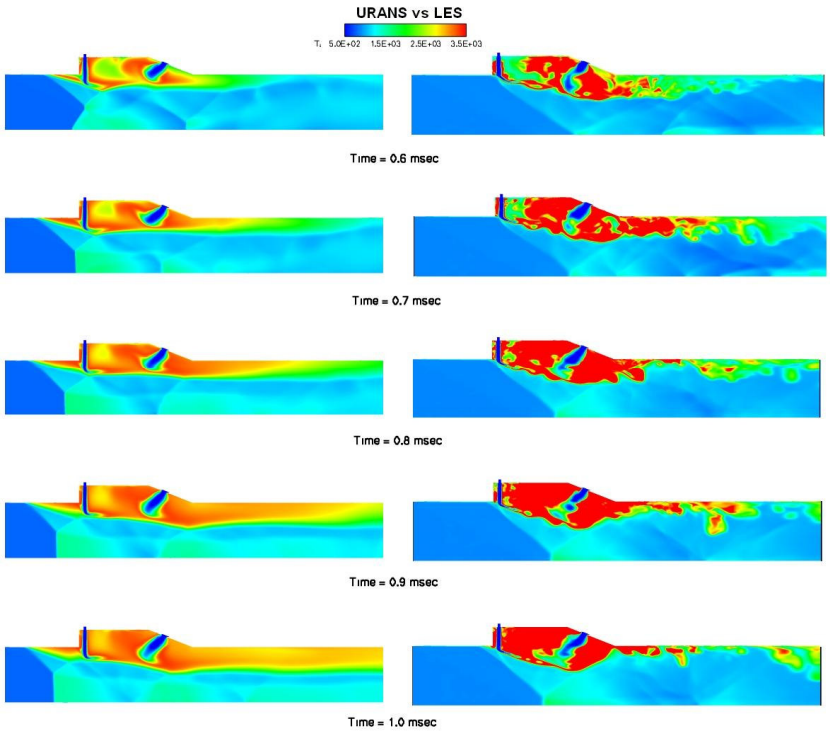

(c) Temperature (K)

"Figure 97 continued"

5.4.5 Discussion of Results (URANS vs. LES, Finite-Rate Chemistry)

Two unsteady modeling methods, RANS and LES, are used to explore overall flow structure and histories for comparison of individual numerical methods. This study shows that LES is capable of capturing the large-scale unsteady structures in the flowfield region. This is because turbulent combustion is inherently unsteady and RANS might fail to properly capture the flowfield inside the cavity.

As seen in earlier cases (Cases 1-3cr), the shear layer on this configuration is pushed away from the vicinity of the step housing the perpendicular injectors at

the bottom of the cavity. This causes a larger circulation region ahead of the jet and near the back wall, opening a low speed pocket that allows the fuel to flash back toward the combustor's entrance. As the shear layer detaches at the step, a reverse penetration flow at the edge of the step brings hot products upstream of the cavity. The chemical reactions that occur within the cavity are promoted by higher temperature and pressure, which then result in increased expansion of the gas mixture. This expansion forces the shear layer to be pushed upward (i.e., to rise away from the step towards the core) in the radial direction. The first injection set, on the floor of the step, further interacts with the strong trailing edge of the shockwave and might play an important role in enhancing chemical reactions. A trailing-edge shockwave is created as the shear layer reattaches near the angled ramp. Furthermore, the trailing oblique shockwave increases the temperature of the mixture by the surrounding walls, causing shock-induced chemical reactions to occur downstream.

Focusing on the cavity analysis, additional differences were observed between LES and URANS solutions: 1) a larger circulation region exists for LES, 2) more detailed vortex shedding is seen in LES, which causes 3) higher mixing in LES and interaction with main stream flow, 4) deeper and earlier fuel penetration towards the core, and 5) overall, LES yields around 9% higher combustion factor. In URANS, most of the fuel stayed at the wall close to the opening due to the lack of cavity interaction and lower vortex interaction with mainstream. As shown before, the shear layer in this configuration is pushed away from the vicinity of the step where the perpendicular injectors at the bottom

of the cavity are. This causes a larger circulation region ahead of the jet and near the back wall, opening a low speed pocket that allows the fuel to flash back toward the combustor's entrance. This reverse penetration flow at the edge of the step brings hot products upstream of the cavity in LES, but not as far upstream as predicted by the URANS simulation. Also, both unsteady simulations show that this effect is not as far upstream as predicted by RANS (in Section 5.4). This cavity with reactive flows is inherently unsteady (including vortex shedding, shear layer mixing, and acoustic wave propagation), and RANS cannot capture counter-gradient diffusion and other unsteady phenomena seen in the combustor flowfield.

These last two unsteady cases are crucial to show how the starting process develops. The cavity recirculation zone transports some of the hot combustion products back toward the combustor face (along the cavity's back wall) and ignites the incoming fuel and air as they mix in the combustion chamber. For this unsteady analysis, the uniform inflow condition initially provides a mean temperature in the cavity close to the stagnation temperature of incoming airflow, and higher than the fuel's ignition temperature.

In general, the interactions of the fuel jet with the oblique shockwave in the vicinity of the cavity result in an enhancement in the molecular mixing between the supersonic air and the jet fuel. Also, downstream from the cavity, the vortices generated by earlier interactions with the shear layer have an additional influence on the mixing factor. These recirculation zones form an exceptionally stable combustion region and are aerodynamically stable over a wide range of

fuel-air ratios and inlet conditions (temperatures and pressures). Furthermore, the products from the fuel-rich-zone remain within the cavity, driving a stable combustion system. Mixing can be seen within the shear layer above/across the cavity as a reaction sheet. The vortex diameter is about the size of the cavity depth. This ignition process will develop quite differently if the non-averaged profiles are coupled into the isolator setting (combustor entrance), due to a much lower temperature and higher shear layer profile near the walls. Future work must be extended into the full unsteady integration for starting conditions to advance design optimization.

When comparing the unsteady cases to the RANS analysis (Case 1cr), the normal shock effect is positioned farthest upstream, about L(2/3) from the combustor entrance (refer to Figure 92a). An asymptotic solution is reached around 1.5msec and 2.0msec, for the URANS and LES respectively. As seen for the URANS case (Figure 97), this effect is between the entrance and the step (~L/2) and follows an oblique shock about L/3 from the entrance. URANS methodology has more dissipation compared to the LES solution, resulting in an under-predicted ignition time. This means that reactions are taking place earlier inside the cavity, given a larger pressure and expansion that causes much stronger upstream effects.

In LES, an initial oblique shock is positioned around L/2 and a slight normal shock interaction is affected near the edge of the step. The LES results show a less likely un-start or thermally choking combustor than URANS. Thus, the turbulence model and/or inflow assumptions can critically affect the total

outcome of such devices. Comparing the injected fuel to the burned mole fraction values at the exit, the mixing factor or burned fuel is estimated about 10% higher than the previous steady state assumptions limited to RANS. Thus the overall integrated configuration mixing factor increases again an additional 10% from the previous calculations, yielding for Jaws values near 74% at half of the expected combustor length. Also, it favors the total drag/thrust ratio by reducing it to around 22%.

This reveals the need for future efforts to examine the effect of unsteadiness on the entire flowpath (from the inlet entrance to the combustor exit) and to develop a flow model with a more advanced, higher-order accurate methodology-based LES turbulence model. Although these time accurate computations are more extensive and costly, the complex profiles throughout the scramjet system must be considered, from the interplay of the in-/visicid shock interactions to the chemically reactive supersonic flow in an unsteady manner, most critically during its starting conditions.

CHAPTER 6: CONCLUSIONS

6.1 OVERVIEW:

The main objective of this research is to conduct a high-fidelity multi-physics CFD analysis of two innovative hypersonic inlets, Jaws and Scoop, and compare them to a Baseline inlet. The internal flow paths and overall coupled effects of these non-rectangular, non-axisymmetric scramjet engines are detailed for on-design and off-design conditions of their tip-to-tail configurations. All inlets are designed for equal flight conditions, equal contraction ratios and exit cross-sectional areas, thus facilitating their comparison and integration to a common combustor design.

The flowfield structure in these three inward turning inlet-combustor combination configurations is described for the selected flight trajectory conditions of Mach 6 and a dynamic pressure of 1,500 psf (71.82 kPa). Additional cases are analyzed for each of the three inlets with two different orientations: 3^o pitch and 3^o yaw. The off-design analysis investigates performance degradation and robustness for the configurations tested. The conclusions provided in this chapter are organized for the separate inlet analysis first, followed by their integrated system analysis, and finally for the group of suggested circular and rectangular combustor configurations.

6.2 HYPERSONIC INLETS (ON-/OFF-DESIGN)

Isolated Hypersonic Inlet Analysis:

The following conclusions are derived from the analysis of isolated (not integrated) streamline traced inlets on Jaws and Scoop.

1. The flowfield distortions occur due to shock boundary layer interactions similar to those found in the Baseline inlet.
2. The low momentum region caused by the viscous interactions increases inlet losses.
3. The innovative inlets mitigate issues encountered in the Baseline: the cowl-lip interactions, corner flows, spillage and parasite drag.
4. Only the Jaws inlet shows higher efficiency and less pressure losses at on-design.
5. Both innovative inlets (Jaws and Scoop) underperform during off-design conditions when compared to the Baseline configuration.
6. The dual-plane compression strategy used in Jaws is less prone to interaction with the near wall flow than the other two inlets.
7. The Scoop flowfield gives rise to a larger region of low pressure recovery on the upper surface.
8. The mass flow rate captured by the inlets and integrated forces across the exit plane is slightly higher for Jaws and lower for Scoop compared to the Baseline.

9. The average temperature at the exit plane of the inlet is low for Jaws and much lower for the Scoop configuration relative to the baseline value. For the Scoop, the lower temperature appears to be due to reduced entrainment. However, its drag coefficient and thrust to mass capture ratios are higher than the Baseline configuration.

Inlet and Combustor Integration:

The final assessment of the inlet and combustor integration using the best performing combustor configurations is concluded below.

1. When considering the effect of internal passages, the innovative Jaws and Scoop configurations performed better in terms of thrust-to-drag ratio relative to configurations commonly described in the literature.
2. Although the Jaws inlet demonstrates a quite valuable design with higher performance than the Baseline, its overall performance decreases to comparable values downstream in the combustor, due to a drop in the mixing factor to the level of the Baseline.
3. The Baseline and Jaws performance attributes are similarly strong, but Jaws accomplishes this while eradicating the cowl lip interaction, and lowering the total drag and spillage penalties at its lips for off-design conditions.

4. The region of enhanced turbulence in the isolator later yields better mixing of air and fuel in the combustor, significantly augmenting chemical reactions and improving the overall thrust of the hypersonic propulsion system.
5. The innovative geometries, especially Jaws, yield higher values of thrust over drag ratios, equivalent to a larger forward acceleration compared to the Baseline design.
6. In general, the off-design results of the Baseline design do better than Jaws due to an increase in the mass captured, and particularly yawed.
7. Overall, the integrated Scoop configuration performs poorly in turns of thrust, overall efficiency and drag compared to the others at on-/off-design conditions.

6.3 SUPERSONIC COMBUSTORS

Steady state Inflow and Chemical Assumptions (Rectangular vs. Circular Configurations):

1. The preliminary analysis on the rectangular (current state of the art) configurations shows that the unwanted flow interactions upstream in the inlets can actually have a positive impact on the downstream section.
2. The greatest rectangular combustion coefficient performance of ~91% was found when combining: 1) a bottom set of the injectors positioned

upstream and interlaced from 2) a second set of injectors downstream for the first set, and 3) followed by an open single cavity on the upper region.

3. From the succeeding parametric study of ten different cavity-based flame-holders with various flush wall fuel injections, the cavity increases both the total pressure loss and the temperature of the combustor while enhancing the combustion of fuel and oxidizer.
4. The mixing factor seems to improve for cases where a pair of injectors is positioned downstream of the ramp facing forward and a second pair is perpendicular to the flow at the cavity floor.
5. The rectangular combustor prototypes yield a much greater mixing factor compared to the circular configurations.
6. The trends observed with and without chemical reactions are the same, though the former yields roughly a 10% higher mixing factor.
7. The vortices generated by interaction between a shockwave and a shear layer have an immediate influence on the mixing enhancement in supersonic flows, increasing the combustion factor and temperature for the finite-rate greater than frozen flow assumption.
8. The effect of the distorted inflow profiles (Jaws or Scoop), steady state assumptions and frozen chemical kinetics yield a higher fuel/air mixing factor than the uniform inflow profile, due to additional vortical structures and circulation near the wall.
9. The shock/boundary layer interactions increase as the mixing factor augments, which then aids diffusion downstream.

10. Jaws inflow conditions slightly increase the mixing factor and thrust ratio because of its higher profile pattern distortion compared to Scoop.
11. When chemical reactions were considered, the uniform inflow assumption resulted in a large separation region underneath the cavity and pressure disk upstream of the step.
12. Both inlet profile assumptions significantly lower the equivalent ratio levels inside the cavity, helping to move the fuel towards the core.
13. The Jaws inlet distortion with/out chemical assumptions mitigates the upstream displacement of fuel, the shear layer and pressures, yielding the highest mixing factor.
14. Unlike at frozen conditions, when chemical reactions are considered, a high compression disk-shaped area is observed upstream of the cavity for uniform inflow assumptions.
15. The upstream, displaced reactions from the cavity have a significant impact on the development of the shear layers and downstream development of the entire combustion. This is caused by the chemical reactions situated upstream of the cavity prior to the injection location. The shear layer in this configuration is pushed away from the vicinity of the step where the fuel is injected perpendicular to the incoming air and positioned at the bottom of the cavity. This increases the circulation region in and around the cavity, allowing the reactions to propagate forward through the shear layer.

16. In Scoop, the chemical reactions yield a strong flashback effect, due to the thicker low energy profile surrounding the walls and most of the lower section of the combustor.

Unsteady Assumptions (URANS vs. LES):

In this section, the URANS and LES assessment and comparisons are summarized.

1. LES is capable of capturing the large-scale unsteady structures in the flowfield region, since supersonic turbulent combustion is inherently unsteady and RANS might fail to properly capture the flowfield near the cavity.
2. In RANS, the normal shock effect is followed by an oblique shock from the combustor entrance and is positioned further upstream compared to the LES solution.
3. URANS methodology has more dissipation compared to the LES solution, resulting in an under-predicted ignition time, meaning that reactions are taking place earlier inside the cavity, resulting in higher pressure that causes much stronger upstream effects.
4. Comparing the injected fuel to the burned mole fraction values at the exit, the mixing factor or burned fuel is estimated about 10% higher than the previous steady state assumptions limited to RANS. This reveals the need for future efforts to examine the effect of unsteadiness on the entire flowpath (from the inlet entrance to the combustor exit) and to develop a

flow model with a higher-order accurate methodology-based LES turbulence model.

5. Although these time accurate computations are more extensive and costly, the complex profiles throughout the scramjet system must be considered, from the interplay of the in-/visicid shock interactions to the chemically reactive supersonic flow in an unsteady manner, most critically during its starting conditions.

6.4 SUMMARY

In summary, all the research objectives were met to characterize the scramjet flowfields in circular combustors with non-axisymmetric inflow profiles. Two innovative inlets were analyzed and compared to a traditional Baseline inlet for on/off-design conditions.

The analysis of the three selected hypersonic inlets was extended to investigate their distortion effects downstream in common generic combustors (which include a single cavity acting as flame holder and strategically positioned fuel injection ports). The isolated and coupled combustor numerical experiments contribute to the development of pioneering inlets for scramjets. This work on the common configuration demonstrated the significant impact of distortion when analyzing the fully integrated system.

A systematic parametric analysis enabled insight into mixing enhancement of injection strategies from rectangular to circular supersonic combustors. Design guidance principles were derived to evolve air-breathing propulsion systems for

future hypersonic vehicles. Thereafter, a rigorous analysis was conducted on numerical methodologies, chemical and inflow assumptions.

The most effective coupled configuration with the lowest losses was identified. The flow physics was investigated and the integrated performance impact of two novel scramjet inlet designs was quantified. These results affect not only inlet designs but also the selection of methodologies when designing scramjets. The key conclusions of this research are summarized as follows:

1. *Flow distortion in the innovative inlets is similar to some of the distortion in the Baseline inlet, despite design differences.*

2. *The innovative inlets work best on-design, whereas for off-design, the traditional inlet yields a higher performance.*

3. *Early pressure losses and flow distortions actually aid downstream combustion in all cases*

4. *A parametric study of the location and direction of injection was conducted to select the configuration for fuel penetration, mixing factor (factor) and other combustion qualities.*

5. *Steady and unsteady simulations were conducted to characterize the ignition process, flame anchoring and flashback effects.*

6. *Unsteady Reynolds Average Navier-Stokes (URANS) and Large Eddy Simulation (LES) modeling were compared to explore overall flow structure and for comparison of individual numerical methods.*

Insights from this research drove design modifications to a Jaws geometry tested at NASA Langley and upcoming Hifire-II flight program, and are used to support of a collaboration of the United States and the Australian Departments of Defense. The results of the parametric study are being used for a direct-connect scramjet combustor configuration tested at AFRL facilities. Towards the end of this research, an additional three year HPC challenge award of over 2 million hours was provided to AFRL. This award will allow further investigations and support of additional flight and ground testing. Ultimately, this research will facilitate the development of improved scramjets.

APPENDIX A

Auto-ignition Data of Ethylene-Air mixture (Ref. 33):

Table 14: ER=0.5, $X(C_2H_4)$=0.007 and $X(O_2)$=0.042.

T (K)	P (atm)	Time (sec)	[fuel] mol/cc	[O2] mol/cc	10,000/T (K)
1210	5.27	3.16×10^{-4}	3.72×10^{-7}	2.23×10^{-6}	8.26
1223	5.82	2.90×10^{-4}	4.06×10^{-7}	2.44×10^{-6}	8.18
1127	4.83	9.00×10^{-4}	3.65×10^{-7}	2.19×10^{-6}	8.87
1186	5.45	4.00×10^{-4}	3.92×10^{-7}	2.35×10^{-6}	8.43
1291	6.46	1.06×10^{-4}	4.27×10^{-7}	2.56×10^{-6}	7.75
1232	5.82	2.22×10^{-4}	4.03×10^{-7}	2.42×10^{-6}	8.12
1308	6.62	9.35×10^{-4}	4.31×10^{-7}	2.59×10^{-6}	7.64
1158	5.22	5.54×10^{-4}	3.84×10^{-7}	2.31×10^{-6}	8.64
1229	5.96	2.67×10^{-4}	4.14×10^{-7}	2.48×10^{-6}	8.14
1149	5.73	7.42×10^{-4}	4.26×10^{-7}	2.55×10^{-6}	8.71
1125	5.62	9.48×10^{-4}	4.26×10^{-7}	2.56×10^{-6}	8.89
1201	6.72	3.06×10^{-4}	4.77×10^{-7}	2.86×10^{-6}	8.33
1198	7.01	3.26×10^{-4}	5.00×10^{-7}	3.00×10^{-6}	8.35
1219	7.62	2.64×10^{-4}	5.33×10^{-7}	3.20×10^{-6}	8.2
1210	7.89	2.34×10^{-4}	5.56×10^{-7}	3.34×10^{-6}	8.26
1176	7.05	5.37×10^{-4}	5.11×10^{-7}	3.07×10^{-6}	8.5

Table 15: ER=0.75, $X(C_2H_4)$=0.007 and $X(O_2)$=0.028.

T (K)	P (atm)	Time (sec)	[fuel] mol/cc	[O2] mol/cc	10,000/T (K)
1350	6.97	8.55×10^{-5}	4.41×10^{-7}	1.76×10^{-6}	7.41
1333	7.07	9.20×10^{-5}	4.53×10^{-7}	1.81×10^{-6}	7.5
1182	5.76	5.24×10^{-5}	4.15×10^{-7}	1.66×10^{-6}	8.46
1334	7.53	8.90×10^{-5}	4.82×10^{-7}	1.93×10^{-6}	7.5

Table 16: ER=1.0, $X(C_2H_4)$=0.007 and $X(O_2)$=0.021.

T (K)	P (atm)	Time (sec)	[fuel] mol/cc	[O2] mol/cc	10,000/T (K)
1276	6.94	1.73×10^{-4}	4.64×10^{-7}	1.85×10^{-6}	7.83
1197	6.16	4.42×10^{-4}	4.39×10^{-7}	1.76×10^{-6}	8.35
1233	6.6	3.45×10^{-4}	4.57×10^{-7}	1.83×10^{-6}	8.11
1191	6.18	6.36×10^{-4}	4.43×10^{-7}	1.77×10^{-6}	8.4
1414	7.09	9.05×10^{-4}	4.28×10^{-7}	1.28×10^{-6}	7.07
1346	6.58	1.36×10^{-4}	4.17×10^{-7}	1.25×10^{-6}	7.43
1380	7.64	1.02×10^{-4}	4.72×10^{-7}	1.42×10^{-6}	7.25

Table 17: ER=1.0, X(C_2H_4)=0.00145 and X(O_2)=0.021.

T (K)	P (atm)	Time (sec)	[fuel] mol/cc	[O2] mol/cc	10,000/T (K)
1348	4.01	4.59×10^{-4}	7.88×10^{-8}	1.52×10^{-6}	7.42
1324	3.93	5.46×10^{-4}	7.88×10^{-8}	1.52×10^{-6}	7.55
1449	6.77	1.74×10^{-4}	8.26×10^{-8}	1.20×10^{-6}	6.9
1439	6.88	2.31×10^{-4}	8.45×10^{-8}	1.22×10^{-6}	6.95
1344	6.23	6.03×10^{-4}	8.19×10^{-8}	1.19×10^{-6}	7.44
1351	5.83	6.99×10^{-4}	7.62×10^{-8}	1.10×10^{-6}	7.4
1372	6.26	4.75×10^{-4}	8.05×10^{-8}	1.17×10^{-6}	7.29
1499	3.16	1.71×10^{-4}	3.72×10^{-8}	5.39×10^{-6}	6.67

APPENDIX B

Reaction Rates in a Linear Form (Ethylene-Air Mixture):

From the chemical reactions shown in Table 3, the mass fraction production for each of the 13 different species are given in Equation 22 through Equation 34:

Equation 22: Production of $C_2H_{4(g)}$ mass fraction.

$$\dot{Y}_{C_2H_4} = -k_{f_1} Y_{C_2H_4} + k_{b_1} Y_{C_2H_2} Y_{H_2}$$

Equation 23: Production of $C_2H_{2(g)}$ mass fraction.

$$\dot{Y}_{C_2H_2} = k_{f_1} Y_{C_2H_4} - k_{b_1} Y_{C_2H_2} Y_{H_2} - 2k_{f_2} Y_{C_2H_2} Y_{O_2} + 2k_{b_2} Y_{CO}{}^2 Y_{H_2}$$

Equation 24: Production of $O_{2(g)}$ mass fraction.

$$\dot{Y}_{O_2} = -2k_{f_2} Y_{C_2H_2} Y_{O_2} + 2k_{b_2} Y_{CO}{}^2 Y_{H_2} - k_{f_4} Y_{CO} Y_{O_2} + k_{b_4} Y_{CO_2} Y_O + k_{f_7} Y_O Y_{OH} - k_{b_7} Y_{O_2} Y_H + 2k_{f_{13}} Y_O{}^2 Y_M$$
$$- 2k_{b_{13}} Y_{O_2} Y_M - k_{f_{15}} Y_N Y_{O_2} + k_{b_{15}} Y_{NO} Y_O - 2k_{f_{17}} Y_{H_2} Y_{O_2} + 2k_{b_{17}} Y_{OH}{}^2$$

Equation 25: Production of $O_{(g)}$ mass fraction.

$$\dot{Y}_O = -k_{f_3} Y_{CO} Y_O Y_M + k_{b_3} Y_{CO_2} Y_M + k_{f_4} Y_{CO} Y_{O_2} - k_{b_4} Y_{CO_2} Y_O - k_{f_7} Y_O Y_{OH} + k_{b_7} Y_{O_2} Y_H - k_{f_8} Y_O Y_{H_2} + k_{b_8} Y_{OH} Y_H$$
$$+ 2k_{f_9} Y_{OH}{}^2 - 2k_{b_9} Y_O{}^2 Y_{H_2O}$$

Equation 26: Production of $H_{2\,(g)}$ mass fraction.

$$\dot{Y}_{H_2} = k_{f_1} Y_{C_2H_4} - k_{b_1} Y_{C_2H_2} Y_{H_2} + 2k_{f_2} Y_{C_2H_2} Y_{O_2} - 2k_{b_2} Y_{CO}{}^2 Y_{H_2} - k_{f_6} Y_{OH} Y_{H_2} + k_{b_6} Y_{H_2O} Y_H - k_{f_8} Y_O Y_{H_2} + k_{b_8} Y_{OH} Y_H + 2k_{f_{10}} Y_H{}^2 Y_M - 2k_{b_{10}} Y_{H_2} Y_M - 2k_{f_{17}} Y_{H_2} Y_{O_2} + 2k_{b_{17}} Y_{OH}{}^2 - 2k_{f_{18}} Y_H{}^2 Y_{H_2} + 2k_{b_{18}} Y_{H_2}{}^2 + 2k_{f_{19}} Y_H{}^2 Y_{H_2O} - 2k_{b_{19}} Y_{H_2} Y_{H_2O} + 2k_{f_{20}} Y_H{}^2 Y_{CO_2} - 2k_{b_{20}} Y_{H_2} Y_{CO_2}$$

Equation 27: Production of $H_{(g)}$ mass fraction.

$$\dot{Y}_H = k_{f_5} Y_{CO} Y_{OH} - k_{b_5} Y_{CO_2} Y_H + k_{f_6} Y_{OH} Y_{H_2} - k_{b_6} Y_{H_2O} Y_H + k_{f_7} Y_O Y_{OH} - k_{b_7} Y_{O_2} Y_H + k_{f_8} Y_O Y_{H_2} - k_{b_8} Y_{OH} Y_H - 2k_{f_{10}} Y_H{}^2 Y_M + 2k_{b_{10}} Y_{H_2} Y_M - k_{f_{11}} Y_H Y_{OH} Y_M + k_{b_{11}} Y_{H_2O} Y_M - k_{f_{12}} Y_H Y_O Y_M + k_{b_{12}} Y_{OH} Y_M + k_{f_{16}} Y_N Y_{OH} - k_{b_{16}} Y_{NO} Y_H - 2k_{f_{18}} Y_H{}^2 Y_{H_2} + 2k_{b_{18}} Y_{H_2}{}^2 - 2k_{f_{19}} Y_H{}^2 Y_{H_2O} + 2k_{b_{19}} Y_{H_2} Y_{H_2O} - 2k_{f_{20}} Y_H{}^2 Y_{CO_2} + k_{b_{20}} Y_{H_2} Y_{CO_2}$$

Equation 28: Production of $OH_{(g)}$ mass fraction.

$$\dot{Y}_{OH} = -k_{f_5} Y_{CO} Y_{OH} + k_{b_5} Y_{CO_2} Y_H - k_{f_6} Y_{OH} Y_{H_2} + k_{b_6} Y_{H_2O} Y_H - k_{f_7} Y_O Y_{OH} + k_{b_7} Y_{O_2} Y_H + k_{f_8} Y_O Y_{H_2} - k_{b_8} Y_{OH} Y_H - 2k_{f_9} Y_{OH}{}^2 + 2k_{b_9} Y_O Y_{H_2O} - k_{f_{11}} Y_H Y_{OH} Y_M + k_{b_{11}} Y_{H_2O} Y_M + k_{f_{12}} Y_H Y_O Y_M - k_{b_{12}} Y_{OH} Y_M - k_{f_{16}} Y_N Y_{OH} + k_{b_{16}} Y_{NO} Y_H + 2k_{f_{17}} Y_{H_2} Y_{O_2} - 2k_{b_{17}} Y_{OH}{}^2$$

Equation 29: Production of $H_2O_{(g)}$ mass fraction.

$$\dot{Y}_{H_2O} = k_{f_6} Y_{OH} Y_{H_2} - k_{b_6} Y_{H_2O} Y_H + 2k_{f_9} Y_{OH}{}^2 - 2k_{b_9} Y_O Y_{H_2O} + k_{f_{11}} Y_H Y_{OH} Y_M - k_{b_{11}} Y_{H_2O} Y_M$$

Equation 30: Production of $N_{2\,(g)}$ mass fraction.

$$\dot{Y}_{N_2} = k_{f_{14}} Y_N Y_{NO} - k_{b_{14}} Y_{N_2} Y_O$$

Equation 31: Production of $N_{(g)}$ mass fraction.

$$\dot{Y}_N = k_{f_{14}} Y_N Y_{NO} - k_{b_{14}} Y_{N_2} Y_O - k_{f_{15}} Y_N Y_{O_2} + k_{b_{15}} Y_{NO} Y_O - k_{f_{16}} Y_N Y_{OH} + k_{b_{16}} Y_{NO} Y_H$$

Equation 32: Production of $NO_{(g)}$ mass fraction.

$$\dot{Y}_{NO} = -k_{f_{14}} Y_N Y_{NO} + k_{b_{14}} Y_{N_2} Y_O + k_{f_{15}} Y_N Y_{O_2} - k_{b_{15}} Y_{NO} Y_O + k_{f_{16}} Y_N Y_{OH} - k_{b_{16}} Y_{NO} Y_H$$

Equation 33: Production of $CO_{2(g)}$ mass fraction.

$$\dot{Y}_{CO_2} = k_{f_3} Y_{CO} Y_O Y_M - k_{b_3} Y_{CO_2} Y_M + k_{f_4} Y_{CO} Y_{O_2} - k_{b_4} Y_{CO_2} Y_O + k_{f_5} Y_{CO} Y_{OH} - k_{b_5} Y_{CO_2} Y_H + 2k_{f_{20}} Y_H Y_{CO_2} - k_{b_{20}} Y_{H_2} Y_{CO_2}$$

Equation 34: Production of $CO_{(g)}$ mass fraction.

$$\dot{Y}_{CO} = k_{f_2} Y_{C_2H_2} Y_{O_2} - 2k_{b_2} Y_{CO} Y_{H_2} - k_{f_3} Y_{CO} Y_O Y_M + k_{b_3} Y_{CO_2} Y_M - k_{f_4} Y_{CO} Y_{O_2} + k_{b_4} Y_{CO_2} Y_O - k_{f_5} Y_{CO} Y_{OH} + k_{b_5} Y_{CO_2} Y_H$$

The net reaction rate for the nonlinear equations can be transformed into a linear form by using a Two- and Three-Body reaction for the source term and mass fraction (see Equation 35 through Equation 37):

Equation 35: Linear form for the produced mass fraction.

$$\dot{Y}_i = \partial[Y_i] / \partial t \approx \left(Y_i^{n+1} - Y_i^n\right) / \Delta t \rightarrow Y_i^{n+1} = \dot{Y}_i \Delta t + Y_i^n$$

Equation 36: Two-Body reaction

$$\left(Y_i Y_j\right)^{n+1} = -Y_i^n Y_j^n + Y_i^n Y_j^{n+1} + Y_i^{n+1} Y_j^n$$

Equation 37: Three-Body reaction.

$$\left(Y_i Y_j Y_k\right)^{n+1} = -2Y_i^n Y_j^n Y_k^n + Y_i^n Y_j^n Y_k^{n+1} + Y_i^n Y_j^{n+1} Y_k^n + Y_i^{n+1} Y_j^n Y_k^n$$

The species mass productions from the previous functions (see Equation 22 to Equation 34) are transformed into linear terms by substituting the 2- and 3-body terms into the linear form for the produced mass fraction (Equation 38-50).

Equation 38: $C_2H_{4(g)}$ mass production.

$$\frac{\left(Y_{C_2H_4}{}^{n+1} - Y_{C_2H_4}{}^{n}\right)}{\Delta t} = -k_{f_1} Y_{C_2H_4}{}^{n+1} + k_{b_1}\begin{pmatrix} -Y_{C_2H_2}{}^{n} Y_{H_2}{}^{n} + Y_{C_2H_2}{}^{n} Y_{H_2}{}^{n+1} \\ +Y_{C_2H_2}{}^{n+1} Y_{H_2}{}^{n} \end{pmatrix}$$

Equation 39: $C_2H_{2(g)}$ mass production.

$$\frac{\left(Y_{C_2H_2}{}^{n+1} - Y_{C_2H_2}{}^{n}\right)}{\Delta t} = k_{f_1} Y_{C_2H_4}{}^{n+1} - k_{b_1}\begin{pmatrix} -Y_{C_2H_2}{}^{n} Y_{H_2}{}^{n} + Y_{C_2H_2}{}^{n} Y_{H_2}{}^{n+1} \\ +Y_{C_2H_2}{}^{n+1} Y_{H_2}{}^{n} \end{pmatrix} - 2k_{f_2}\begin{pmatrix} -Y_{C_2H_2}{}^{n} Y_{O_2}{}^{n} + Y_{C_2H_2}{}^{n} Y_{O_2}{}^{n+1} \\ +Y_{C_2H_2}{}^{n+1} Y_{O_2}{}^{n} \end{pmatrix}$$
$$+ 2k_{b_2}\begin{pmatrix} -2Y_{CO}{}^{2n} Y_{H_2}{}^{n} + Y_{CO}{}^{2n} Y_{H_2}{}^{n+1} \\ +2Y_{CO}{}^{2n+n} Y_{H_2}{}^{n} \end{pmatrix}$$

Equation 40: $O_{2(g)}$ mass production.

$$\frac{\left(Y_{O_2}{}^{n+1} - Y_{O_2}{}^{n}\right)}{\Delta t} = -2k_{f_2}\begin{pmatrix} -Y_{C_2H_2}{}^{n} Y_{O_2}{}^{n} + Y_{C_2H_2}{}^{n} Y_{O_2}{}^{n+1} \\ +Y_{C_2H_2}{}^{n+1} Y_{O_2}{}^{n} \end{pmatrix} + 2k_{b_2}\begin{pmatrix} -2Y_{CO}{}^{2n} Y_{H_2}{}^{n} + Y_{CO}{}^{2n} Y_{H_2}{}^{n+1} \\ +Y_{CO}{}^{2n+n} Y_{H_2}{}^{n} \end{pmatrix} - k_{f_4}\begin{pmatrix} -Y_{CO}{}^{n} Y_{O_2}{}^{n} + Y_{CO}{}^{n} Y_{O_2}{}^{n+1} \\ +Y_{CO}{}^{n+1} Y_{O_2}{}^{n} \end{pmatrix}$$
$$+ k_{b_4}\begin{pmatrix} -Y_{CO_2}{}^{n} Y_{O}{}^{n} + Y_{CO_2}{}^{n} Y_{O}{}^{n+1} \\ +Y_{CO_2}{}^{n+1} Y_{O}{}^{n} \end{pmatrix} + k_{f_7}\begin{pmatrix} -Y_{O}{}^{n} Y_{OH}{}^{n} + Y_{O}{}^{n} Y_{OH}{}^{n+1} \\ +Y_{O}{}^{n+1} Y_{OH}{}^{n} \end{pmatrix} - k_{b_7}\begin{pmatrix} -Y_{O_2}{}^{n} Y_{H}{}^{n} + Y_{O_2}{}^{n} Y_{H}{}^{n+1} \\ +Y_{O_2}{}^{n+1} Y_{H}{}^{n} \end{pmatrix} + 2k_{f_{13}}\begin{pmatrix} -2Y_{O}{}^{2n} Y_{M}{}^{n} + Y_{O}{}^{2n} Y_{M}{}^{n+1} \\ +Y_{O}{}^{2n+n} Y_{M}{}^{n} \end{pmatrix}$$
$$- 2k_{b_{13}}\begin{pmatrix} -Y_{O_2}{}^{n} Y_{M}{}^{n} + Y_{O_2}{}^{n} Y_{M}{}^{n+1} \\ +Y_{O_2}{}^{n+1} Y_{M}{}^{n} \end{pmatrix} - k_{f_{15}}\begin{pmatrix} -Y_{N}{}^{n} Y_{O_2}{}^{n} + Y_{N}{}^{n} Y_{O_2}{}^{n+1} \\ +Y_{N}{}^{n+1} Y_{O_2}{}^{n} \end{pmatrix} + k_{b_{15}}\begin{pmatrix} -Y_{NO}{}^{n} Y_{O}{}^{n} + Y_{NO}{}^{n} Y_{O}{}^{n+1} \\ +Y_{NO}{}^{n+1} Y_{O}{}^{n} \end{pmatrix} - 2k_{f_{17}}\begin{pmatrix} -Y_{H_2}{}^{n} Y_{O_2}{}^{n} + Y_{H_2}{}^{n} Y_{O_2}{}^{n+1} \\ +Y_{H_2}{}^{n+1} Y_{O_2}{}^{n} \end{pmatrix}$$
$$+ 2k_{b_{17}}\begin{pmatrix} -Y_{OH}{}^{2n} \\ +2Y_{OH}{}^{n(n+1)} \end{pmatrix}$$

Equation 41: $O_{(g)}$ mass production.

$$\frac{\left({Y_O}^{n+1}-{Y_O}^{n}\right)}{\Delta t}=-k_{f_3}\begin{pmatrix}-{Y_{CO}}^{n}{Y_O}^{n}{Y_M}^{n}+{Y_{CO}}^{n}{Y_O}^{n}{Y_M}^{n+1}\\+{Y_{CO}}^{n}{Y_O}^{n+1}{Y_M}^{n}+{Y_{CO}}^{n+1}{Y_O}^{n}{Y_M}^{n}\end{pmatrix}+k_{b_3}\begin{pmatrix}-{Y_{CO_2}}^{n}{Y_M}^{n}+{Y_{CO_2}}^{n}{Y_M}^{n+1}\\+{Y_{CO_2}}^{n+1}{Y_M}^{n}\end{pmatrix}+k_{f_4}\begin{pmatrix}-{Y_{CO}}^{n}{Y_{O_2}}^{n}+{Y_{CO}}^{n}{Y_{O_2}}^{n+1}\\+{Y_{CO}}^{n+1}{Y_{O_2}}^{n}\end{pmatrix}$$
$$-k_{b_4}\begin{pmatrix}-{Y_{CO_2}}^{n}{Y_O}^{n}+{Y_{CO_2}}^{n}{Y_O}^{n+1}\\+{Y_{CO_2}}^{n+1}{Y_O}^{n}\end{pmatrix}-k_{f_7}\begin{pmatrix}-{Y_O}^{n}{Y_{OH}}^{n}+{Y_O}^{n}{Y_{OH}}^{n+1}\\+{Y_O}^{n+1}{Y_{OH}}^{n}\end{pmatrix}+k_{b_7}\begin{pmatrix}-{Y_{O_2}}^{n}{Y_H}^{n}+{Y_{O_2}}^{n}{Y_H}^{n+1}\\+{Y_{O_2}}^{n+1}{Y_H}^{n}\end{pmatrix}-k_{f_8}\begin{pmatrix}-{Y_O}^{n}{Y_{H_2}}^{n}+{Y_O}^{n}{Y_{H_2}}^{n+1}\\+{Y_O}^{n+1}{Y_{H_2}}^{n}\end{pmatrix}$$
$$+k_{b_8}\begin{pmatrix}-{Y_{OH}}^{n}{Y_H}^{n}+{Y_{OH}}^{n}{Y_H}^{n+1}\\+{Y_{OH}}^{n+1}{Y_H}^{n}\end{pmatrix}+2k_{f_9}\begin{pmatrix}-{Y_{OH}}^{2n}\\+2{Y_{OH}}^{n(n+1)}\end{pmatrix}-2k_{b_9}\begin{pmatrix}-2{Y_O}^{2}{Y_{H_2O}}+{Y_O}^{2}{Y_{H_2O}}^{n+1}\\+{Y_O}^{2(n+1)}{Y_{H_2O}}^{n}\end{pmatrix}$$

Equation 42: $H_{2(g)}$ mass production.

$$\frac{\left({Y_{H_2}}^{n+1}-{Y_{H_2}}^{n}\right)}{\Delta t}=k_{f_1}{Y_{C_2H_4}}^{n+1}-k_{b_1}\begin{pmatrix}-{Y_{C_2H_2}}^{n}{Y_{H_2}}^{n}+{Y_{C_2H_2}}^{n}{Y_{H_2}}^{n+1}\\+{Y_{C_2H_2}}^{n+1}{Y_{H_2}}^{n}\end{pmatrix}+2k_{f_2}\begin{pmatrix}-{Y_{C_2H_2}}^{n}{Y_{O_2}}^{n}+{Y_{C_2H_2}}^{n}{Y_{O_2}}^{n+1}\\+{Y_{C_2H_2}}^{n+1}{Y_{O_2}}^{n}\end{pmatrix}-2k_{b_2}\begin{pmatrix}-2{Y_{CO}}^{2n}{Y_{H_2}}^{n}+{Y_{CO}}^{2n}{Y_{H_2}}^{n+1}\\+2{Y_{CO}}^{n(n+1)}{Y_{H_2}}^{n}\end{pmatrix}$$
$$-k_{f_6}\begin{pmatrix}-{Y_{OH}}^{n}{Y_{H_2}}^{n}+{Y_{OH}}^{n}{Y_{H_2}}^{n+1}\\+{Y_{OH}}^{n+1}{Y_{H_2}}^{n}\end{pmatrix}+k_{b_6}\begin{pmatrix}-{Y_{H_2O}}^{n}{Y_H}^{n}+{Y_{H_2O}}^{n}{Y_H}^{n+1}\\+{Y_{H_2O}}^{n+1}{Y_H}^{n}\end{pmatrix}-k_{f_8}\begin{pmatrix}-{Y_O}^{n}{Y_{H_2}}^{n}+{Y_O}^{n}{Y_{H_2}}^{n+1}\\+{Y_O}^{n+1}{Y_{H_2}}^{n}\end{pmatrix}+k_{b_8}\begin{pmatrix}-{Y_{OH}}^{n}{Y_H}^{n}+{Y_{OH}}^{n}{Y_H}^{n+1}\\+{Y_{OH}}^{n+1}{Y_H}^{n}\end{pmatrix}$$
$$+2k_{f_{10}}\begin{pmatrix}-2{Y_H}^{2n}{Y_M}^{n}+{Y_H}^{2n}{Y_M}^{n+1}\\+2{Y_H}^{2(n+1)}{Y_M}^{n}\end{pmatrix}-2k_{b_{10}}\begin{pmatrix}-{Y_{H_2}}^{n}{Y_M}^{n}+{Y_{H_2}}^{n}{Y_M}^{n+1}\\+{Y_{H_2}}^{n+1}{Y_M}^{n}\end{pmatrix}-2k_{f_{17}}\begin{pmatrix}-{Y_{H_2}}^{n}{Y_{O_2}}^{n}+{Y_{H_2}}^{n}{Y_{O_2}}^{n+1}\\+{Y_{H_2}}^{n+1}{Y_{O_2}}^{n}\end{pmatrix}+2k_{b_{17}}\begin{pmatrix}-{Y_{OH}}^{2n}\\+2{Y_{OH}}^{n(n+1)}\end{pmatrix}$$
$$-2k_{f_{18}}\begin{pmatrix}-2{Y_H}^{2n}{Y_{H_2}}^{n}+{Y_H}^{2n}{Y_{H_2}}^{n+1}\\+2{Y_H}^{n(n+1)}{Y_{H_2}}^{n}\end{pmatrix}+2k_{b_{18}}\begin{pmatrix}-{Y_{H_2}}^{2n}\\+2{Y_{H_2}}^{n(n+1)}\end{pmatrix}+2k_{f_{19}}\begin{pmatrix}-2{Y_H}^{2n}{Y_{H_2O}}^{n}+{Y_H}^{2n}{Y_{H_2O}}^{n+1}\\+2{Y_H}^{n(n+1)}{Y_{H_2O}}^{n}\end{pmatrix}-2k_{b_{19}}\begin{pmatrix}-{Y_{H_2}}^{n}{Y_{H_2O}}^{n}+{Y_{H_2}}^{n}{Y_{H_2O}}^{n+1}\\+{Y_{H_2}}^{n+1}{Y_{H_2O}}^{n}\end{pmatrix}$$
$$+2k_{f_{20}}\begin{pmatrix}-2{Y_H}^{2n}{Y_{CO_2}}^{n}+{Y_H}^{2n}{Y_{CO_2}}^{n+1}\\+2{Y_H}^{n(n+1)}{Y_{CO_2}}^{n}\end{pmatrix}-2k_{b_{20}}\begin{pmatrix}-{Y_{H_2}}^{n}{Y_{CO_2}}^{n}+{Y_{H_2}}^{n}{Y_{CO_2}}^{n+1}\\+{Y_{H_2}}^{n+1}{Y_{CO_2}}^{n}\end{pmatrix}$$

Equation 43: $H_{(g)}$ mass production.

$$\frac{\left({Y_H}^{n+1}-{Y_H}^{n}\right)}{\Delta t}=k_{f_5}\begin{pmatrix}-{Y_{CO}}^{n}{Y_{OH}}^{n}+{Y_{CO}}^{n}{Y_{OH}}^{n+1}\\+{Y_{CO}}^{n+1}{Y_{OH}}^{n}\end{pmatrix}-k_{b_5}\begin{pmatrix}-{Y_{CO_2}}^{n}{Y_H}^{n}+{Y_{CO_2}}^{n}{Y_H}^{n+1}\\+{Y_{CO_2}}^{n+1}{Y_H}^{n}\end{pmatrix}+k_{f_6}\begin{pmatrix}-{Y_{OH}}^{n}{Y_{H_2}}^{n}+{Y_{OH}}^{n}{Y_{H_2}}^{n+1}\\+{Y_{OH}}^{n+1}{Y_{H_2}}^{n}\end{pmatrix}-k_{b_6}\begin{pmatrix}-{Y_{H_2O}}^{n}{Y_H}^{n}+{Y_{H_2O}}^{n}{Y_H}^{n+1}\\+{Y_{H_2O}}^{n+1}{Y_H}^{n}\end{pmatrix}$$
$$+k_{f_7}\begin{pmatrix}-{Y_O}^{n}{Y_{OH}}^{n}+{Y_O}^{n}{Y_{OH}}^{n+1}\\+{Y_O}^{n+1}{Y_{OH}}^{n}\end{pmatrix}-k_{b_7}\begin{pmatrix}-{Y_{O_2}}^{n}{Y_H}^{n}+{Y_{O_2}}^{n}{Y_H}^{n+1}\\+{Y_{O_2}}^{n+1}{Y_H}^{n}\end{pmatrix}+k_{f_8}\begin{pmatrix}-{Y_O}^{n}{Y_{H_2}}^{n}+{Y_O}^{n}{Y_{H_2}}^{n+1}\\+{Y_O}^{n+1}{Y_{H_2}}^{n}\end{pmatrix}-k_{b_8}\begin{pmatrix}-{Y_{OH}}^{n}{Y_H}^{n}+{Y_{OH}}^{n}{Y_H}^{n+1}\\+{Y_{OH}}^{n+1}{Y_H}^{n}\end{pmatrix}$$
$$-2k_{f_{10}}\begin{pmatrix}-2{Y_H}^{2n}{Y_M}^{n}+{Y_H}^{2n}{Y_M}^{n+1}\\+2{Y_H}^{2(n+1)}{Y_M}^{n}\end{pmatrix}+2k_{b_{10}}\begin{pmatrix}-{Y_{H_2}}^{n}{Y_M}^{n}+{Y_{H_2}}^{n}{Y_M}^{n+1}\\+{Y_{H_2}}^{n+1}{Y_M}^{n}\end{pmatrix}-k_{f_{11}}\begin{pmatrix}-2{Y_H}^{n}{Y_{OH}}^{n}{Y_M}^{n}+{Y_H}^{n}{Y_{OH}}^{n}{Y_M}^{n+1}\\+{Y_H}^{n}{Y_{OH}}^{n+1}{Y_M}^{n}+{Y_H}^{n+1}{Y_{OH}}^{n}{Y_M}^{n}\end{pmatrix}+k_{b_{11}}\begin{pmatrix}-{Y_{H_2O}}^{n}{Y_M}^{n}+{Y_{H_2O}}^{n}{Y_M}^{n+1}\\+{Y_{H_2O}}^{n+1}{Y_M}^{n}\end{pmatrix}$$
$$-k_{f_{12}}\begin{pmatrix}-2{Y_H}^{n}{Y_O}^{n}{Y_M}^{n}+{Y_H}^{n}{Y_O}^{n}{Y_M}^{n+1}\\+{Y_H}^{n}{Y_O}^{n+1}{Y_M}^{n}+{Y_H}^{n+1}{Y_O}^{n}{Y_M}^{n}\end{pmatrix}+k_{b_{12}}\begin{pmatrix}-{Y_{OH}}^{n}{Y_M}^{n}+{Y_{OH}}^{n}{Y_M}^{n+1}\\+{Y_{OH}}^{n+1}{Y_M}^{n}\end{pmatrix}+k_{f_{16}}\begin{pmatrix}-{Y_N}^{n}{Y_{OH}}^{n}+{Y_N}^{n}{Y_{OH}}^{n+1}\\+{Y_N}^{n+1}{Y_{OH}}^{n}\end{pmatrix}-k_{b_{16}}\begin{pmatrix}-{Y_{NO}}^{n}{Y_H}^{n}+{Y_{NO}}^{n}{Y_H}^{n+1}\\+{Y_{NO}}^{n+1}{Y_H}^{n}\end{pmatrix}$$
$$-2k_{f_{18}}\begin{pmatrix}-2{Y_H}^{2n}{Y_{H_2}}^{n}+{Y_H}^{2n}{Y_{H_2}}^{n+1}\\+2{Y_H}^{n(n+1)}{Y_{H_2}}^{n}\end{pmatrix}+2k_{b_{18}}\begin{pmatrix}-{Y_{H_2}}^{2n}\\+2{Y_{H_2}}^{n(n+1)}\end{pmatrix}-2k_{f_{19}}\begin{pmatrix}-2{Y_H}^{2n}{Y_{H_2O}}^{n}+{Y_H}^{2n}{Y_{H_2O}}^{n+1}\\+2{Y_H}^{n(n+1)}{Y_{H_2O}}^{n}\end{pmatrix}+2k_{b_{19}}\begin{pmatrix}-{Y_{H_2}}^{n}{Y_{H_2O}}^{n}+{Y_{H_2}}^{n}{Y_{H_2O}}^{n+1}\\+{Y_{H_2}}^{n+1}{Y_{H_2O}}^{n}\end{pmatrix}$$
$$-2k_{f_{20}}\begin{pmatrix}-2{Y_H}^{2n}{Y_{CO_2}}^{n}+{Y_H}^{2n}{Y_{CO_2}}^{n+1}\\+2{Y_H}^{n(n+1)}{Y_{CO_2}}^{n}\end{pmatrix}+2k_{b_{20}}\begin{pmatrix}-{Y_{H_2}}^{n}{Y_{CO_2}}^{n}+{Y_{H_2}}^{n}{Y_{CO_2}}^{n+1}\\+{Y_{H_2}}^{n+1}{Y_{CO_2}}^{n}\end{pmatrix}$$

Equation 44: $OH_{(g)}$ mass production.

$$\frac{\left({Y_{OH}}^{n+1}-{Y_{OH}}^{n}\right)}{\Delta t}=-k_{f_5}\begin{pmatrix}-{Y_{CO}}^{n}{Y_{OH}}^{n}+{Y_{CO}}^{n}{Y_{OH}}^{n+1}\\+{Y_{CO}}^{n+1}{Y_{OH}}^{n}\end{pmatrix}+k_{b_5}\begin{pmatrix}-{Y_{CO_2}}^{n}{Y_H}^{n}+{Y_{CO_2}}^{n}{Y_H}^{n+1}\\+{Y_{CO_2}}^{n+1}{Y_H}^{n}\end{pmatrix}-k_{f_6}\begin{pmatrix}-{Y_{OH}}^{n}{Y_{H_2}}^{n}+{Y_{OH}}^{n}{Y_{H_2}}^{n+1}\\+{Y_{OH}}^{n+1}{Y_{H_2}}^{n}\end{pmatrix}+k_{b_6}\begin{pmatrix}-{Y_{H_2O}}^{n}{Y_H}^{n}+{Y_{H_2O}}^{n}{Y_H}^{n+1}\\+{Y_{H_2O}}^{n+1}{Y_H}^{n}\end{pmatrix}$$
$$-k_{f_7}\begin{pmatrix}-{Y_O}^{n}{Y_{OH}}^{n}+{Y_O}^{n}{Y_{OH}}^{n+1}\\+{Y_O}^{n+1}{Y_{OH}}^{n}\end{pmatrix}+k_{b_7}\begin{pmatrix}-{Y_{O_2}}^{n}{Y_H}^{n}+{Y_{O_2}}^{n}{Y_H}^{n+1}\\+{Y_{O_2}}^{n+1}{Y_H}^{n}\end{pmatrix}+k_{f_8}\begin{pmatrix}-{Y_O}^{n}{Y_{H_2}}^{n}+{Y_O}^{n}{Y_{H_2}}^{n+1}\\+{Y_O}^{n+1}{Y_{H_2}}^{n}\end{pmatrix}-k_{b_8}\begin{pmatrix}-{Y_{OH}}^{n}{Y_H}^{n}+{Y_{OH}}^{n}{Y_H}^{n+1}\\+{Y_{OH}}^{n+1}{Y_H}^{n}\end{pmatrix}$$
$$-2k_{f_9}\begin{pmatrix}-{Y_{OH}}^{2n}\\+2{Y_{OH}}^{n(n+1)}\end{pmatrix}+2k_{b_9}\begin{pmatrix}-2{Y_O}^{2}{Y_{H_2O}}+{Y_O}^{2n}{Y_{H_2O}}^{n+1}\\+{Y_O}^{2(n+1)}{Y_{H_2O}}^{n}\end{pmatrix}-k_{f_{11}}\begin{pmatrix}-2{Y_H}^{n}{Y_{OH}}^{n}{Y_M}^{n}+{Y_H}^{n}{Y_{OH}}^{n}{Y_M}^{n+1}\\+{Y_H}^{n}{Y_{OH}}^{n+1}{Y_M}^{n}+{Y_H}^{n+1}{Y_{OH}}^{n}{Y_M}^{n}\end{pmatrix}+k_{b_{11}}\begin{pmatrix}-{Y_{H_2O}}^{n}{Y_M}^{n}+{Y_{H_2O}}^{n}{Y_M}^{n+1}\\+{Y_{H_2O}}^{n+1}{Y_M}^{n}\end{pmatrix}$$
$$+k_{f_{12}}\begin{pmatrix}-2{Y_H}^{n}{Y_O}^{n}{Y_M}^{n}+{Y_H}^{n}{Y_O}^{n}{Y_M}^{n+1}\\+{Y_H}^{n}{Y_O}^{n+1}{Y_M}^{n}+{Y_H}^{n+1}{Y_O}^{n}{Y_M}^{n}\end{pmatrix}-k_{b_{12}}\begin{pmatrix}-{Y_{OH}}^{n}{Y_M}^{n}+{Y_{OH}}^{n}{Y_M}^{n+1}\\+{Y_{OH}}^{n+1}{Y_M}^{n}\end{pmatrix}-k_{f_{16}}\begin{pmatrix}-{Y_N}^{n}{Y_{OH}}^{n}+{Y_N}^{n}{Y_{OH}}^{n+1}\\+{Y_N}^{n+1}{Y_{OH}}^{n}\end{pmatrix}+k_{b_{16}}\begin{pmatrix}-{Y_{NO}}^{n}{Y_H}^{n}+{Y_{NO}}^{n}{Y_H}^{n+1}\\+{Y_{NO}}^{n+1}{Y_H}^{n}\end{pmatrix}$$
$$+2k_{f_{17}}\begin{pmatrix}-{Y_{H_2}}^{n}{Y_{O_2}}^{n}+{Y_{H_2}}^{n}{Y_{O_2}}^{n+1}\\+{Y_{H_2}}^{n+1}{Y_{O_2}}^{n}\end{pmatrix}-2k_{b_{17}}\begin{pmatrix}-{Y_{OH}}^{2n}\\+2{Y_{OH}}^{n(n+1)}\end{pmatrix}$$

Equation 45: $H_2O_{(g)}$ mass production.

$$\frac{\left({Y_{H_2O}}^{n+1}-{Y_{H_2O}}^{n}\right)}{\Delta t}=k_{f_6}\begin{pmatrix}-{Y_{OH}}^{n}{Y_{H_2}}^{n}+{Y_{OH}}^{n}{Y_{H_2}}^{n+1}\\+{Y_{OH}}^{n+1}{Y_{H_2}}^{n}\end{pmatrix}-k_{b_6}\begin{pmatrix}-{Y_{H_2O}}^{n}{Y_H}^{n}+{Y_{H_2O}}^{n}{Y_H}^{n+1}\\+{Y_{H_2O}}^{n+1}{Y_H}^{n}\end{pmatrix}+2k_{f_9}\begin{pmatrix}-{Y_{OH}}^{2n}\\+2{Y_{OH}}^{n(n+1)}\end{pmatrix}-2k_{b_9}\begin{pmatrix}-2{Y_O}^{2}{Y_{H_2O}}+{Y_O}^{2n}{Y_{H_2O}}^{n+1}\\+{Y_O}^{2(n+1)}{Y_{H_2O}}^{n}\end{pmatrix}$$
$$+k_{f_{11}}\begin{pmatrix}-2{Y_H}^{n}{Y_{OH}}^{n}{Y_M}^{n}+{Y_H}^{n}{Y_{OH}}^{n}{Y_M}^{n+1}\\+{Y_H}^{n}{Y_{OH}}^{n+1}{Y_M}^{n}+{Y_H}^{n+1}{Y_{OH}}^{n}{Y_M}^{n}\end{pmatrix}-k_{b_{11}}\begin{pmatrix}-{Y_{H_2O}}^{n}{Y_M}^{n}+{Y_{H_2O}}^{n}{Y_M}^{n+1}\\+{Y_{H_2O}}^{n+1}{Y_M}^{n}\end{pmatrix}$$

Equation 46: $N_{2(g)}$ mass production.

$$\frac{\left({Y_{N_2}}^{n+1}-{Y_{N_2}}^{n}\right)}{\Delta t}=k_{f_{14}}\begin{pmatrix}-{Y_N}^{n}{Y_{NO}}^{n}+{Y_N}^{n}{Y_{NO}}^{n+1}\\+{Y_N}^{n+1}{Y_{NO}}^{n}\end{pmatrix}-k_{b_{14}}\begin{pmatrix}-{Y_{N_2}}^{n}{Y_O}^{n}+{Y_{N_2}}^{n}{Y_O}^{n+1}\\+{Y_{N_2}}^{n+1}{Y_O}^{n}\end{pmatrix}$$

Equation 47: $N_{(g)}$ mass production.

$$\frac{\left({Y_N}^{n+1}-{Y_N}^{n}\right)}{\Delta t}=k_{f_{14}}\begin{pmatrix}-{Y_N}^{n}{Y_{NO}}^{n}+{Y_N}^{n}{Y_{NO}}^{n+1}\\+{Y_N}^{n+1}{Y_{NO}}^{n}\end{pmatrix}-k_{b_{14}}\begin{pmatrix}-{Y_{N_2}}^{n}{Y_O}^{n}+{Y_{N_2}}^{n}{Y_O}^{n+1}\\+{Y_{N_2}}^{n+1}{Y_O}^{n}\end{pmatrix}-k_{f_{15}}\begin{pmatrix}-{Y_N}^{n}{Y_{O_2}}^{n}+{Y_N}^{n}{Y_{O_2}}^{n+1}\\+{Y_N}^{n+1}{Y_{O_2}}^{n}\end{pmatrix}+k_{b_{15}}\begin{pmatrix}-{Y_{NO}}^{n}{Y_O}^{n}+{Y_{NO}}^{n}{Y_O}^{n+1}\\+{Y_{NO}}^{n+1}{Y_O}^{n}\end{pmatrix}$$
$$-k_{f_{16}}\begin{pmatrix}-{Y_N}^{n}{Y_{OH}}^{n}+{Y_N}^{n}{Y_{OH}}^{n+1}\\+{Y_N}^{n+1}{Y_{OH}}^{n}\end{pmatrix}+k_{b_{16}}\begin{pmatrix}-{Y_{NO}}^{n}{Y_H}^{n}+{Y_{NO}}^{n}{Y_H}^{n+1}\\+{Y_{NO}}^{n+1}{Y_H}^{n}\end{pmatrix}$$

Equation 48: $NO_{(g)}$ mass production.

$$\frac{\left({Y_{NO}}^{n+1}-{Y_{NO}}^{n}\right)}{\Delta t}=-k_{f_{14}}\begin{pmatrix}-{Y_N}^{n}{Y_{NO}}^{n}+{Y_N}^{n}{Y_{NO}}^{n+1}\\+{Y_N}^{n+1}{Y_{NO}}^{n}\end{pmatrix}+k_{b_{14}}\begin{pmatrix}-{Y_{N_2}}^{n}{Y_O}^{n}+{Y_{N_2}}^{n}{Y_O}^{n+1}\\+{Y_{N_2}}^{n+1}{Y_O}^{n}\end{pmatrix}+k_{f_{15}}\begin{pmatrix}-{Y_N}^{n}{Y_{O_2}}^{n}+{Y_N}^{n}{Y_{O_2}}^{n+1}\\+{Y_N}^{n+1}{Y_{O_2}}^{n}\end{pmatrix}-k_{b_{15}}\begin{pmatrix}-{Y_{NO}}^{n}{Y_O}^{n}+{Y_{NO}}^{n}{Y_O}^{n+1}\\+{Y_{NO}}^{n+1}{Y_O}^{n}\end{pmatrix}$$
$$+k_{f_{16}}\begin{pmatrix}-{Y_N}^{n}{Y_{OH}}^{n}+{Y_N}^{n}{Y_{OH}}^{n+1}\\+{Y_N}^{n+1}{Y_{OH}}^{n}\end{pmatrix}-k_{b_{16}}\begin{pmatrix}-{Y_{NO}}^{n}{Y_H}^{n}+{Y_{NO}}^{n}{Y_H}^{n+1}\\+{Y_{NO}}^{n+1}{Y_H}^{n}\end{pmatrix}$$

Equation 49: $CO_{2(g)}$ mass production.

$$\frac{\left({Y_{CO_2}}^{n+1}-{Y_{CO_2}}^{n}\right)}{\Delta t}=k_{f_3}\begin{pmatrix}-{Y_{CO}}^{n}{Y_O}^{n}{Y_M}^{n}+{Y_{CO}}^{n}{Y_O}^{n}{Y_M}^{n+1}\\+{Y_{CO}}^{n}{Y_O}^{n+1}{Y_M}^{n}+{Y_{CO}}^{n+1}{Y_O}^{n}{Y_M}^{n}\end{pmatrix}-k_{b_3}\begin{pmatrix}-{Y_{CO_2}}^{n}{Y_M}^{n}+{Y_{CO_2}}^{n}{Y_M}^{n+1}\\+{Y_{CO_2}}^{n+1}{Y_M}^{n}\end{pmatrix}+k_{f_4}\begin{pmatrix}-{Y_{CO}}^{n}{Y_{O_2}}^{n}+{Y_{CO}}^{n}{Y_{O_2}}^{n+1}\\+{Y_{CO}}^{n+1}{Y_{O_2}}^{n}\end{pmatrix}-k_{b_4}\begin{pmatrix}-{Y_{CO_2}}^{n}{Y_O}^{n}+{Y_{CO_2}}^{n}{Y_O}^{n+1}\\+{Y_{CO_2}}^{n+1}{Y_O}^{n}\end{pmatrix}$$
$$+k_{f_5}\begin{pmatrix}-{Y_{CO}}^{n}{Y_{OH}}^{n}+{Y_{CO}}^{n}{Y_{OH}}^{n+1}\\+{Y_{CO}}^{n+1}{Y_{OH}}^{n}\end{pmatrix}-k_{b_5}\begin{pmatrix}-{Y_{CO_2}}^{n}{Y_H}^{n}+{Y_{CO_2}}^{n}{Y_H}^{n+1}\\+{Y_{CO_2}}^{n+1}{Y_H}^{n}\end{pmatrix}+2k_{f_{20}}\begin{pmatrix}-2{Y_H}^{2n}{Y_{CO_2}}^{n}+{Y_H}^{2n}{Y_{CO_2}}^{n+1}\\+2{Y_H}^{n(n+1)}{Y_{CO_2}}^{n}\end{pmatrix}-2k_{b_{20}}\begin{pmatrix}-{Y_{H_2}}^{n}{Y_{CO_2}}^{n}+{Y_{H_2}}^{n}{Y_{CO_2}}^{n+1}\\+{Y_{H_2}}^{n+1}{Y_{CO_2}}^{n}\end{pmatrix}$$

Equation 50: $CO_{(g)}$ mass production.

$$\frac{\left({Y_{CO}}^{n+1}-{Y_{CO}}^{n}\right)}{\Delta t}=2k_{f_2}\begin{pmatrix}-{Y_{C_2H_2}}^{n}{Y_{O_2}}^{n}+{Y_{C_2H_2}}^{n}{Y_{O_2}}^{n+1}\\+{Y_{C_2H_2}}^{n+1}{Y_{O_2}}^{n}\end{pmatrix}-2k_{b_2}\begin{pmatrix}-2{Y_{CO}}^{2n}{Y_{H_2}}^{n}+{Y_{CO}}^{2n}{Y_{H_2}}^{n+1}\\+2{Y_{CO}}^{n(n+1)}{Y_{H_2}}^{n}\end{pmatrix}-k_{f_3}\begin{pmatrix}-{Y_{CO}}^{n}{Y_O}^{n}{Y_M}^{n}+{Y_{CO}}^{n}{Y_O}^{n}{Y_M}^{n+1}\\+{Y_{CO}}^{n}{Y_O}^{n+1}{Y_M}^{n}+{Y_{CO}}^{n+1}{Y_O}^{n}{Y_M}^{n}\end{pmatrix}+k_{b_3}\begin{pmatrix}-{Y_{CO_2}}^{n}{Y_M}^{n}+{Y_{CO_2}}^{n}{Y_M}^{n+1}\\+{Y_{CO_2}}^{n+1}{Y_M}^{n}\end{pmatrix}$$
$$-k_{f_4}\begin{pmatrix}-{Y_{CO}}^{n}{Y_{O_2}}^{n}+{Y_{CO}}^{n}{Y_{O_2}}^{n+1}\\+{Y_{CO}}^{n+1}{Y_{O_2}}^{n}\end{pmatrix}+k_{b_4}\begin{pmatrix}-{Y_{CO_2}}^{n}{Y_O}^{n}+{Y_{CO_2}}^{n}{Y_O}^{n+1}\\+{Y_{CO_2}}^{n+1}{Y_O}^{n}\end{pmatrix}-k_{f_5}\begin{pmatrix}-{Y_{CO}}^{n}{Y_{OH}}^{n}+{Y_{CO}}^{n}{Y_{OH}}^{n+1}\\+{Y_{CO}}^{n+1}{Y_{OH}}^{n}\end{pmatrix}+k_{b_5}\begin{pmatrix}-{Y_{CO_2}}^{n}{Y_H}^{n}+{Y_{CO_2}}^{n}{Y_H}^{n+1}\\+{Y_{CO_2}}^{n+1}{Y_H}^{n}\end{pmatrix}$$

Then, solving for each produced species, the linear set of equations is organized into the equations below:

Equation 51: Linearization of $C_2H_{4(g)}$ mass production.

$${Y_{C_2H_4}}^{n+1}=\frac{k_{b_1}\left(-{Y_{C_2H_2}}^{n}{Y_{H_2}}^{n}+{Y_{C_2H_2}}^{n}{Y_{H_2}}^{n+1}+{Y_{C_2H_2}}^{n+1}{Y_{H_2}}^{n}\right)+{Y_{C_2H_4}}^{n}/\Delta t}{1/\Delta t+k_{f_1}}$$

Equation 52: Linearization of $C_2H_{2(g)}$ mass production.

$$Y_{C_2H_2}^{n+1} = \frac{k_{f_1} Y_{C_2H_4}^{n+1} - k_{b_1}\left(\begin{matrix}-Y_{C_2H_2}^{n} Y_{H_2}^{n} \\ +Y_{C_2H_2}^{n} Y_{H_2}^{n+1}\end{matrix}\right) - 2k_{f_2}\left(\begin{matrix}-Y_{C_2H_2}^{n} Y_{O_2}^{n} \\ +Y_{C_2H_2}^{n} Y_{O_2}^{n+1}\end{matrix}\right) + 2k_{b_2}\left(\begin{matrix}-2Y_{CO}^{2n} Y_{H_2}^{n} + Y_{CO}^{2n} Y_{H_2}^{n+1} \\ +2Y_{CO}^{2n+n} Y_{H_2}^{n}\end{matrix}\right) + \frac{Y_{C_2H_2}^{n}}{\Delta t}}{1/\Delta t + k_{b_1} Y_{H_2}^{n} + 2k_{f_2} Y_{O_2}^{n}}$$

Equation 53: Linearization of $O_{2(g)}$ mass production.

$$Y_{O_2}^{n+1} = \frac{\begin{matrix} -2k_{f_2}\left(\begin{matrix}-Y_{C_2H_2}^{n} Y_{O_2}^{n} \\ +Y_{C_2H_2}^{n+1} Y_{O_2}^{n}\end{matrix}\right) + 2k_{b_2}\left(\begin{matrix}-2Y_{CO}^{2n} Y_{H_2}^{n} + Y_{CO}^{2n} Y_{H_2}^{n+1} \\ +Y_{CO}^{2n+n} Y_{H_2}^{n}\end{matrix}\right) - k_{f_4}\left(\begin{matrix}-Y_{CO}^{n} Y_{O_2}^{n} \\ +Y_{CO}^{n+1} Y_{O_2}^{n}\end{matrix}\right) + k_{b_4}\left(\begin{matrix}-Y_{CO_2}^{n} Y_O^{n} + Y_{CO_2}^{n} Y_O^{n+1} \\ +Y_{CO_2}^{n+1} Y_O^{n}\end{matrix}\right) \\ + k_{f_7}\left(\begin{matrix}-Y_O^{n} Y_{OH}^{n} + Y_O^{n} Y_{OH}^{n+1} \\ +Y_O^{n+1} Y_{OH}^{n}\end{matrix}\right) - k_{b_7}\left(\begin{matrix}-Y_{O_2}^{n} Y_H^{n} \\ +Y_{O_2}^{n} Y_H^{n+1}\end{matrix}\right) + 2k_{f_{13}}\left(\begin{matrix}-2Y_O^{2n} Y_M^{n} + Y_O^{2n} Y_M^{n+1} \\ +Y_O^{2n+n} Y_M^{n}\end{matrix}\right) - 2k_{b_{13}}\left(\begin{matrix}-Y_{O_2}^{n} Y_M^{n} \\ +Y_{O_2}^{n} Y_M^{n+1}\end{matrix}\right) \\ - k_{f_{15}}\left(\begin{matrix}-Y_N^{n} Y_{O_2}^{n} \\ +Y_N^{n+1} Y_{O_2}^{n}\end{matrix}\right) + k_{b_{15}}\left(\begin{matrix}-Y_{NO}^{n} Y_O^{n} + Y_{NO}^{n} Y_O^{n+1} \\ +Y_{NO}^{n+1} Y_O^{n}\end{matrix}\right) - 2k_{f_{17}}\left(\begin{matrix}-Y_{H_2}^{n} Y_{O_2}^{n} \\ +Y_{H_2}^{n+1} Y_{O_2}^{n}\end{matrix}\right) + 2k_{b_{17}}\left(\begin{matrix}-Y_{OH}^{2n} \\ +2Y_{OH}^{n(n+1)}\end{matrix}\right) + \frac{Y_{O_2}^{n}}{\Delta t} \end{matrix}}{1/\Delta t + 2k_{f_2} Y_{C_2H_2}^{n} + k_{f_4} Y_{CO}^{n} + k_{b_7} Y_H^{n} + 2k_{b_{13}} Y_M^{n} + k_{f_{15}} Y_N^{n} + 2k_{f_{17}} Y_{H_2}^{n}}$$

Equation 54: Linearization of $O_{(g)}$ mass production.

$$Y_O^{n+1} = \frac{\begin{matrix} -k_{f_3}\left(\begin{matrix}-Y_{CO}^{n} Y_O^{n} Y_M^{n} + Y_{CO}^{n} Y_O^{n} Y_M^{n+1} \\ +Y_{CO}^{n+1} Y_O^{n} Y_M^{n}\end{matrix}\right) + k_{b_3}\left(\begin{matrix}-Y_{CO_2}^{n} Y_M^{n} + Y_{CO_2}^{n} Y_M^{n+1} \\ +Y_{CO_2}^{n+1} Y_M^{n}\end{matrix}\right) + k_{f_4}\left(\begin{matrix}-Y_{CO}^{n} Y_{O_2}^{n} + Y_{CO}^{n} Y_{O_2}^{n+1} \\ +Y_{CO}^{n+1} Y_{O_2}^{n}\end{matrix}\right) \\ - k_{b_4}\left(\begin{matrix}-Y_{CO_2}^{n} Y_O^{n} \\ +Y_{CO_2}^{n+1} Y_O^{n}\end{matrix}\right) - k_{f_7}\left(\begin{matrix}-Y_O^{n} Y_{OH}^{n} \\ +Y_O^{n} Y_{OH}^{n+1}\end{matrix}\right) + k_{b_7}\left(\begin{matrix}-Y_{O_2}^{n} Y_H^{n} + Y_{O_2}^{n} Y_H^{n+1} \\ +Y_{O_2}^{n+1} Y_H^{n}\end{matrix}\right) - k_{f_8}\left(\begin{matrix}-Y_O^{n} Y_{H_2}^{n} \\ +Y_O^{n} Y_{H_2}^{n+1}\end{matrix}\right) \\ + k_{b_8}\left(\begin{matrix}-Y_{OH}^{n} Y_H^{n} + Y_{OH}^{n} Y_H^{n+1} \\ +Y_{OH}^{n+1} Y_H^{n}\end{matrix}\right) + 2k_{f_9}\left(\begin{matrix}-Y_{OH}^{2n} \\ +2Y_{OH}^{n(n+1)}\end{matrix}\right) - 2k_{b_9}\left(\begin{matrix}-2Y_O^{2} Y_{H_2O} \\ +Y_O^{2n} Y_{H_2O}^{n+1}\end{matrix}\right) + \frac{Y_O^{n}}{\Delta t} \end{matrix}}{1/\Delta t + k_{f_3} Y_{CO}^{n} Y_M^{n} + k_{b_4} Y_{CO_2}^{n} + k_{f_7} Y_{OH}^{n} + k_{f_8} Y_{H_2}^{n} + 2k_{b_9} Y_O^{(n+1)} Y_{H_2O}^{n}}$$

Equation 55: Linearization of $H_{2(g)}$ mass production.

$$
\begin{aligned}
&k_{f_1} {Y_{C_2H_4}}^{n+1} - k_{b_1}\begin{pmatrix} -{Y_{C_2H_2}}^{n}{Y_{H_2}}^{n} \\ +{Y_{C_2H_2}}^{n+1}{Y_{H_2}}^{n}\end{pmatrix} + 2k_{f_2}\begin{pmatrix} -{Y_{C_2H_2}}^{n}{Y_{O_2}}^{n} + {Y_{C_2H_2}}^{n}{Y_{O_2}}^{n+1} \\ +{Y_{C_2H_2}}^{n+1}{Y_{O_2}}^{n}\end{pmatrix} - 2k_{b_2}\begin{pmatrix} -2{Y_{CO}}^{2n}{Y_{H_2}}^{n} \\ +2{Y_{CO}}^{n(n+1)}{Y_{H_2}}^{n}\end{pmatrix} - k_{f_6}\begin{pmatrix} -{Y_{OH}}^{n}{Y_{H_2}}^{n} \\ +{Y_{OH}}^{n+1}{Y_{H_2}}^{n}\end{pmatrix} \\
&+ k_{b_6}\begin{pmatrix} -{Y_{H_2O}}^{n}{Y_H}^{n} + {Y_{H_2O}}^{n}{Y_H}^{n+1} \\ +{Y_{H_2O}}^{n+1}{Y_H}^{n}\end{pmatrix} - k_{f_8}\begin{pmatrix} -{Y_O}^{n}{Y_{H_2}}^{n} \\ +{Y_O}^{n+1}{Y_{H_2}}^{n}\end{pmatrix} + k_{b_8}\begin{pmatrix} -{Y_{OH}}^{n}{Y_H}^{n} + {Y_{OH}}^{n}{Y_H}^{n+1} \\ +{Y_{OH}}^{n+1}{Y_H}^{n}\end{pmatrix} + 2k_{f_{10}}\begin{pmatrix} -2{Y_H}^{2n}{Y_M}^{n} + {Y_H}^{2n}{Y_M}^{n+1} \\ +2{Y_H}^{2(n+1)}{Y_M}^{n}\end{pmatrix} \\
&- 2k_{b_{10}}\begin{pmatrix} -{Y_{H_2}}^{n}{Y_M}^{n} \\ +{Y_{H_2}}^{n}{Y_M}^{n+1}\end{pmatrix} - 2k_{f_{17}}\begin{pmatrix} -{Y_{H_2}}^{n}{Y_{O_2}}^{n} \\ +{Y_{H_2}}^{n}{Y_{O_2}}^{n+1}\end{pmatrix} + 2k_{b_{17}}\begin{pmatrix} -{Y_{OH}}^{2n} \\ +2{Y_{OH}}^{n(n+1)}\end{pmatrix} - 2k_{f_{18}}\begin{pmatrix} -2{Y_H}^{2n}{Y_{H_2}}^{n} \\ +2{Y_H}^{n(n+1)}{Y_{H_2}}^{n}\end{pmatrix} - 2k_{b_{18}}{Y_{H_2}}^{2n} \\
&+ 2k_{f_{19}}\begin{pmatrix} -2{Y_H}^{2n}{Y_{H_2O}}^{n} + {Y_H}^{2n}{Y_{H_2O}}^{n+1} \\ +2{Y_H}^{n(n+1)}{Y_{H_2O}}^{n}\end{pmatrix} - 2k_{b_{19}}\begin{pmatrix} -{Y_{H_2}}^{n}{Y_{H_2O}}^{n} \\ +{Y_{H_2}}^{n}{Y_{H_2O}}^{n+1}\end{pmatrix} + 2k_{f_{20}}\begin{pmatrix} -2{Y_H}^{2n}{Y_{CO_2}}^{n} + {Y_H}^{2n}{Y_{CO_2}}^{n+1} \\ +2{Y_H}^{n(n+1)}{Y_{CO_2}}^{n}\end{pmatrix} - 2k_{b_{20}}\begin{pmatrix} -{Y_{H_2}}^{n}{Y_{CO_2}}^{n} \\ +{Y_{H_2}}^{n}{Y_{CO_2}}^{n+1}\end{pmatrix} + \frac{{Y_{H_2}}^{n}}{\Delta t} \\
{Y_{H_2}}^{n+1} = &\frac{}{\begin{pmatrix} 1/\Delta t + k_{b_1}{Y_{C_2H_2}}^{n} + 2k_{b_2}{Y_{CO}}^{2n} + k_{f_6}{Y_{OH}}^{n} + k_{f_8}{Y_O}^{n} + 2k_{b_{10}}{Y_M}^{n} \\ +2k_{f_{17}}{Y_{O_2}}^{n} + 2k_{f_{18}}{Y_H}^{2n} - 4k_{b_{18}}{Y_{H_2}}^{n} + 2k_{b_{19}}{Y_{H_2O}}^{n} + 2k_{b_{20}}{Y_{CO_2}}^{n}\end{pmatrix}}
\end{aligned}
$$

Equation 56: Linearization of $H_{(g)}$ mass production.

$$
\begin{aligned}
&k_{f_5}\begin{pmatrix} -{Y_{CO}}^{n}{Y_{OH}}^{n} + {Y_{CO}}^{n}{Y_{OH}}^{n+1} \\ +{Y_{CO}}^{n+1}{Y_{OH}}^{n}\end{pmatrix} - k_{b_5}\begin{pmatrix} -{Y_{CO_2}}^{n}{Y_H}^{n} \\ +{Y_{CO_2}}^{n+1}{Y_H}^{n}\end{pmatrix} + k_{f_6}\begin{pmatrix} -{Y_{OH}}^{n}{Y_{H_2}}^{n} + {Y_{OH}}^{n}{Y_{H_2}}^{n+1} \\ +{Y_{OH}}^{n+1}{Y_{H_2}}^{n}\end{pmatrix} - k_{b_6}\begin{pmatrix} -{Y_{H_2O}}^{n}{Y_H}^{n} \\ +{Y_{H_2O}}^{n+1}{Y_H}^{n}\end{pmatrix} \\
&+ k_{f_7}\begin{pmatrix} -{Y_O}^{n}{Y_{OH}}^{n} + {Y_O}^{n}{Y_{OH}}^{n+1} \\ +{Y_O}^{n+1}{Y_{OH}}^{n}\end{pmatrix} - k_{b_7}\begin{pmatrix} -{Y_{O_2}}^{n}{Y_H}^{n} \\ +{Y_{O_2}}^{n+1}{Y_H}^{n}\end{pmatrix} + k_{f_8}\begin{pmatrix} -{Y_O}^{n}{Y_{H_2}}^{n} + {Y_O}^{n}{Y_{H_2}}^{n+1} \\ +{Y_O}^{n+1}{Y_{H_2}}^{n}\end{pmatrix} - k_{b_8}\begin{pmatrix} -{Y_{OH}}^{n}{Y_H}^{n} \\ +{Y_{OH}}^{n+1}{Y_H}^{n}\end{pmatrix} - 2k_{f_{10}}\begin{pmatrix} -2{Y_H}^{2n}{Y_M}^{n} \\ +{Y_H}^{2n}{Y_M}^{n+1}\end{pmatrix} \\
&+ 2k_{b_{10}}\begin{pmatrix} -{Y_{H_2}}^{n}{Y_M}^{n} + {Y_{H_2}}^{n}{Y_M}^{n+1} \\ +{Y_{H_2}}^{n+1}{Y_M}^{n}\end{pmatrix} - k_{f_{11}}\begin{pmatrix} -2{Y_H}^{n}{Y_{OH}}^{n}{Y_M}^{n} + {Y_H}^{n}{Y_{OH}}^{n}{Y_M}^{n+1} \\ +{Y_H}^{n}{Y_{OH}}^{n+1}{Y_M}^{n}\end{pmatrix} + k_{b_{11}}\begin{pmatrix} -{Y_{H_2O}}^{n}{Y_M}^{n} + {Y_{H_2O}}^{n}{Y_M}^{n+1} \\ +{Y_{H_2O}}^{n+1}{Y_M}^{n}\end{pmatrix} \\
&- k_{f_{12}}\begin{pmatrix} -2{Y_H}^{n}{Y_O}^{n}{Y_M}^{n} + {Y_H}^{n}{Y_O}^{n}{Y_M}^{n+1} \\ +{Y_H}^{n}{Y_O}^{n+1}{Y_M}^{n}\end{pmatrix} + k_{b_{12}}\begin{pmatrix} -{Y_{OH}}^{n}{Y_M}^{n} + {Y_{OH}}^{n}{Y_M}^{n+1} \\ +{Y_{OH}}^{n+1}{Y_M}^{n}\end{pmatrix} + k_{f_{16}}\begin{pmatrix} -{Y_N}^{n}{Y_{OH}}^{n} + {Y_N}^{n}{Y_{OH}}^{n+1} \\ +{Y_N}^{n+1}{Y_{OH}}^{n}\end{pmatrix} - k_{b_{16}}\begin{pmatrix} -{Y_{NO}}^{n}{Y_H}^{n} \\ +{Y_{NO}}^{n+1}{Y_H}^{n}\end{pmatrix} \\
&- 2k_{f_{18}}\begin{pmatrix} -2{Y_H}^{2n}{Y_{H_2}}^{n} \\ +{Y_H}^{2n}{Y_{H_2}}^{n+1}\end{pmatrix} + 2k_{b_{18}}\begin{pmatrix} -{Y_{H_2}}^{2n} \\ +2{Y_{H_2}}^{n(n+1)}\end{pmatrix} - 2k_{f_{19}}\begin{pmatrix} -2{Y_H}^{2n}{Y_{H_2O}}^{n} \\ +{Y_H}^{2n}{Y_{H_2O}}^{n+1}\end{pmatrix} + 2k_{b_{19}}\begin{pmatrix} -{Y_{H_2}}^{n}{Y_{H_2O}}^{n} + {Y_{H_2}}^{n}{Y_{H_2O}}^{n+1} \\ +{Y_{H_2}}^{n+1}{Y_{H_2O}}^{n}\end{pmatrix} \\
&- 2k_{f_{20}}\begin{pmatrix} -2{Y_H}^{2n}{Y_{CO_2}}^{n} \\ +{Y_H}^{2n}{Y_{CO_2}}^{n+1}\end{pmatrix} + 2k_{b_{20}}\begin{pmatrix} -{Y_{H_2}}^{n}{Y_{CO_2}}^{n} + {Y_{H_2}}^{n}{Y_{CO_2}}^{n+1} \\ +{Y_{H_2}}^{n+1}{Y_{CO_2}}^{n}\end{pmatrix} + \frac{{Y_H}^{n}}{\Delta t} \\
{Y_H}^{n+1} = &\frac{}{\begin{pmatrix} 1/\Delta t + k_{b_5}{Y_{CO_2}}^{n} + k_{b_6}{Y_{H_2O}}^{n} + k_{b_7}{Y_{O_2}}^{n} + k_{b_8}{Y_{OH}}^{n} + 4k_{f_{10}}{Y_H}^{(n+1)}{Y_M}^{n} + k_{f_{11}}{Y_{OH}}^{n}{Y_M}^{n} \\ +k_{f_{12}}{Y_O}^{n}{Y_M}^{n} + k_{b_{16}}{Y_{NO}}^{n} + 4k_{f_{18}}{Y_H}^{n}{Y_{H_2}}^{n} + 4k_{f_{19}}{Y_H}^{n}{Y_{H_2O}}^{n} + 4k_{f_{20}}{Y_H}^{n}{Y_{CO_2}}^{n}\end{pmatrix}}
\end{aligned}
$$

Equation 57: Linearization of $OH_{(g)}$ mass production.

$$\left(Y_{OH}{}^{n+1}-Y_{OH}{}^{n}\right)/\Delta t=-k_{f_5}\begin{pmatrix}-Y_{CO}{}^{n}Y_{OH}{}^{n}+Y_{CO}{}^{n}Y_{OH}{}^{n+1}\\+Y_{CO}{}^{n+1}Y_{OH}{}^{n}\end{pmatrix}+k_{b_5}\begin{pmatrix}-Y_{CO_2}{}^{n}Y_{H}{}^{n}+Y_{CO_2}{}^{n}Y_{H}{}^{n+1}\\+Y_{CO_2}{}^{n+1}Y_{H}{}^{n}\end{pmatrix}-k_{f_6}\begin{pmatrix}-Y_{OH}{}^{n}Y_{H_2}{}^{n}+Y_{OH}{}^{n}Y_{H_2}{}^{n+1}\\+Y_{OH}{}^{n+1}Y_{H_2}{}^{n}\end{pmatrix}+k_{b_6}\begin{pmatrix}-Y_{H_2O}{}^{n}Y_{H}{}^{n}+Y_{H_2O}{}^{n}Y_{H}{}^{n+1}\\+Y_{H_2O}{}^{n+1}Y_{H}{}^{n}\end{pmatrix}$$
$$-k_{f_7}\begin{pmatrix}-Y_{O}{}^{n}Y_{OH}{}^{n}+Y_{O}{}^{n}Y_{OH}{}^{n+1}\\+Y_{O}{}^{n+1}Y_{OH}{}^{n}\end{pmatrix}+k_{b_7}\begin{pmatrix}-Y_{O_2}{}^{n}Y_{H}{}^{n}+Y_{O_2}{}^{n}Y_{H}{}^{n+1}\\+Y_{O_2}{}^{n+1}Y_{H}{}^{n}\end{pmatrix}+k_{f_8}\begin{pmatrix}-Y_{O}{}^{n}Y_{H_2}{}^{n}+Y_{O}{}^{n}Y_{H_2}{}^{n+1}\\+Y_{O}{}^{n+1}Y_{H_2}{}^{n}\end{pmatrix}-k_{b_8}\begin{pmatrix}-Y_{OH}{}^{n}Y_{H}{}^{n}+Y_{OH}{}^{n}Y_{H}{}^{n+1}\\+Y_{OH}{}^{n+1}Y_{H}{}^{n}\end{pmatrix}$$
$$-2k_{f_9}\begin{pmatrix}-Y_{OH}{}^{2n}\\+2Y_{OH}{}^{n(n+1)}\end{pmatrix}+2k_{b_9}\begin{pmatrix}-2Y_{O}{}^{2}Y_{H_2O}+Y_{O}{}^{2n}Y_{H_2O}{}^{n+1}\\+Y_{O}{}^{2(n+1)}Y_{H_2O}{}^{n}\end{pmatrix}-k_{f_{11}}\begin{pmatrix}-2Y_{H}{}^{n}Y_{OH}{}^{n}Y_{M}{}^{n}+Y_{H}{}^{n}Y_{OH}{}^{n}Y_{M}{}^{n+1}\\+Y_{H}{}^{n}Y_{OH}{}^{n+1}Y_{M}{}^{n}+Y_{H}{}^{n+1}Y_{OH}{}^{n}Y_{M}{}^{n}\end{pmatrix}+k_{b_{11}}\begin{pmatrix}-Y_{H_2O}{}^{n}Y_{M}{}^{n}+Y_{H_2O}{}^{n}Y_{M}{}^{n+1}\\+Y_{H_2O}{}^{n+1}Y_{M}{}^{n}\end{pmatrix}$$
$$+k_{f_{12}}\begin{pmatrix}-2Y_{H}{}^{n}Y_{O}{}^{n}Y_{M}{}^{n}+Y_{H}{}^{n}Y_{O}{}^{n}Y_{M}{}^{n+1}\\+Y_{H}{}^{n}Y_{O}{}^{n+1}Y_{M}{}^{n}+Y_{H}{}^{n+1}Y_{O}{}^{n}Y_{M}{}^{n}\end{pmatrix}-k_{b_{12}}\begin{pmatrix}-Y_{OH}{}^{n}Y_{M}{}^{n}+Y_{OH}{}^{n}Y_{M}{}^{n+1}\\+Y_{OH}{}^{n+1}Y_{M}{}^{n}\end{pmatrix}-k_{f_{16}}\begin{pmatrix}-Y_{N}{}^{n}Y_{OH}{}^{n}+Y_{N}{}^{n}Y_{OH}{}^{n+1}\\+Y_{N}{}^{n+1}Y_{OH}{}^{n}\end{pmatrix}+k_{b_{16}}\begin{pmatrix}-Y_{NO}{}^{n}Y_{H}{}^{n}+Y_{NO}{}^{n}Y_{H}{}^{n+1}\\+Y_{NO}{}^{n+1}Y_{H}{}^{n}\end{pmatrix}$$
$$+2k_{f_{17}}\begin{pmatrix}-Y_{H_2}{}^{n}Y_{O_2}{}^{n}+Y_{H_2}{}^{n}Y_{O_2}{}^{n+1}\\+Y_{H_2}{}^{n+1}Y_{O_2}{}^{n}\end{pmatrix}-2k_{b_{17}}\begin{pmatrix}-Y_{OH}{}^{2n}\\+2Y_{OH}{}^{n(n+1)}\end{pmatrix}$$

Equation 58: Linearization of $H_2O_{(g)}$ mass production.

$$Y_{H_2O}{}^{n+1}=-1/\Delta t+k_{b_6}Y_{H}{}^{n}+2k_{b_9}Y_{O}{}^{2n}$$
$$k_{f_6}\begin{pmatrix}-Y_{OH}{}^{n}Y_{H_2}{}^{n}+Y_{OH}{}^{n}Y_{H_2}{}^{n+1}\\+Y_{OH}{}^{n+1}Y_{H_2}{}^{n}\end{pmatrix}-k_{b_6}\begin{pmatrix}-Y_{H_2O}{}^{n}Y_{H}{}^{n}\\+Y_{H_2O}{}^{n}Y_{H}{}^{n+1}\end{pmatrix}+2k_{f_9}\begin{pmatrix}-Y_{OH}{}^{2n}\\+2Y_{OH}{}^{n(n+1)}\end{pmatrix}-2k_{b_9}\begin{pmatrix}-2Y_{O}{}^{2}Y_{H_2O}\\+Y_{O}{}^{2(n+1)}Y_{H_2O}{}^{n}\end{pmatrix}$$
$$+k_{f_{11}}\begin{pmatrix}-2Y_{H}{}^{n}Y_{OH}{}^{n}Y_{M}{}^{n}+Y_{H}{}^{n}Y_{OH}{}^{n}Y_{M}{}^{n+1}\\+Y_{H}{}^{n}Y_{OH}{}^{n+1}Y_{M}{}^{n}+Y_{H}{}^{n+1}Y_{OH}{}^{n}Y_{M}{}^{n}\end{pmatrix}-k_{b_{11}}\begin{pmatrix}-Y_{H_2O}{}^{n}Y_{M}{}^{n}+Y_{H_2O}{}^{n}Y_{M}{}^{n+1}\\+Y_{H_2O}{}^{n+1}Y_{M}{}^{n}\end{pmatrix}+\frac{Y_{H_2O}{}^{n}}{\Delta t}$$

Equation 59: Linearization of $N_{2(g)}$ mass production.

$$Y_{N_2}{}^{n+1}=\frac{k_{f_{14}}\begin{pmatrix}-Y_{N}{}^{n}Y_{NO}{}^{n}+Y_{N}{}^{n}Y_{NO}{}^{n+1}\\+Y_{N}{}^{n+1}Y_{NO}{}^{n}\end{pmatrix}-k_{b_{14}}\begin{pmatrix}-Y_{N_2}{}^{n}Y_{O}{}^{n}\\+Y_{N_2}{}^{n}Y_{O}{}^{n+1}\end{pmatrix}+\frac{Y_{N_2}{}^{n}}{\Delta t}}{1/\Delta t+k_{b_{14}}Y_{O}{}^{n}}$$

Equation 60: Linearization of $N_{(g)}$ mass production.

$$Y_{N}{}^{n+1}=\frac{\begin{array}{l}k_{f_{14}}\left(-Y_{N}{}^{n}Y_{NO}{}^{n}+Y_{N}{}^{n}Y_{NO}{}^{n+1}\right)-k_{b_{14}}\begin{pmatrix}-Y_{N_2}{}^{n}Y_{O}{}^{n}+Y_{N_2}{}^{n}Y_{O}{}^{n+1}\\+Y_{N_2}{}^{n+1}Y_{O}{}^{n}\end{pmatrix}-k_{f_{15}}\begin{pmatrix}-Y_{N}{}^{n}Y_{O_2}{}^{n}\\+Y_{N}{}^{n}Y_{O_2}{}^{n+1}\end{pmatrix}+k_{b_{15}}\begin{pmatrix}-Y_{NO}{}^{n}Y_{O}{}^{n}+Y_{NO}{}^{n}Y_{O}{}^{n+1}\\+Y_{NO}{}^{n+1}Y_{O}{}^{n}\end{pmatrix}\\-k_{f_{16}}\begin{pmatrix}-Y_{N}{}^{n}Y_{OH}{}^{n}\\+Y_{N}{}^{n}Y_{OH}{}^{n+1}\end{pmatrix}+k_{b_{16}}\begin{pmatrix}-Y_{NO}{}^{n}Y_{H}{}^{n}+Y_{NO}{}^{n}Y_{H}{}^{n+1}\\+Y_{NO}{}^{n+1}Y_{H}{}^{n}\end{pmatrix}+\frac{Y_{N}{}^{n}}{\Delta t}\end{array}}{1/\Delta t-k_{f_{14}}Y_{NO}{}^{n}+k_{f_{15}}Y_{O_2}{}^{n}+k_{f_{16}}Y_{OH}{}^{n}}$$

Equation 61: Linearization of $NO_{(g)}$ mass production.

$$Y_{NO}^{\,n+1} = \frac{\begin{matrix} -k_{f_{14}}\begin{pmatrix} -Y_N^{\,n}Y_{NO}^{\,n} \\ +Y_N^{\,n+1}Y_{NO}^{\,n} \end{pmatrix} + k_{b_{14}}\begin{pmatrix} -Y_{N_2}^{\,n}Y_O^{\,n} + Y_{N_2}^{\,n}Y_O^{\,n+1} \\ +Y_{N_2}^{\,n+1}Y_O^{\,n} \end{pmatrix} + k_{f_{15}}\begin{pmatrix} -Y_N^{\,n}Y_{O_2}^{\,n} + Y_N^{\,n}Y_{O_2}^{\,n+1} \\ +Y_N^{\,n+1}Y_{O_2}^{\,n} \end{pmatrix} - k_{b_{15}}\begin{pmatrix} -Y_{NO}^{\,n}Y_O^{\,n} \\ +Y_{NO}^{\,n}Y_O^{\,n+1} \end{pmatrix} \\ +k_{f_{16}}\begin{pmatrix} -Y_N^{\,n}Y_{OH}^{\,n} + Y_N^{\,n}Y_{OH}^{\,n+1} \\ +Y_N^{\,n+1}Y_{OH}^{\,n} \end{pmatrix} - k_{b_{16}}\begin{pmatrix} -Y_{NO}^{\,n}Y_H^{\,n} \\ +Y_{NO}^{\,n}Y_H^{\,n+1} \end{pmatrix} + \frac{Y_{NO}^{\,n}}{\Delta t} \end{matrix}}{1/\Delta t + k_{f_{14}}Y_N^{\,n} + k_{b_{15}}Y_O^{\,n} + k_{b_{16}}Y_H^{\,n}}$$

Equation 62: Linearization of $CO_{2(g)}$ mass production.

$$Y_{CO_2}^{\,n+1} = \frac{\begin{matrix} k_{f_3}\begin{pmatrix} -Y_{CO}^{\,n}Y_O^{\,n}Y_M^{\,n} + Y_{CO}^{\,n}Y_O^{\,n}Y_M^{\,n+1} \\ +Y_{CO}^{\,n}Y_O^{\,n+1}Y_M^{\,n} + Y_{CO}^{\,n+1}Y_O^{\,n}Y_M^{\,n} \end{pmatrix} - k_{b_3}\begin{pmatrix} -Y_{CO_2}^{\,n}Y_M^{\,n} \\ +Y_{CO_2}^{\,n}Y_M^{\,n+1} \end{pmatrix} + k_{f_4}\begin{pmatrix} -Y_{CO}^{\,n}Y_{O_2}^{\,n} + Y_{CO}^{\,n}Y_{O_2}^{\,n+1} \\ +Y_{CO}^{\,n+1}Y_{O_2}^{\,n} \end{pmatrix} - k_{b_4}\begin{pmatrix} -Y_{CO_2}^{\,n}Y_O^{\,n} \\ +Y_{CO_2}^{\,n}Y_O^{\,n+1} \end{pmatrix} \\ +k_{f_5}\begin{pmatrix} -Y_{CO}^{\,n}Y_{OH}^{\,n} + Y_{CO}^{\,n}Y_{OH}^{\,n+1} \\ +Y_{CO}^{\,n+1}Y_{OH}^{\,n} \end{pmatrix} - k_{b_5}\begin{pmatrix} -Y_{CO_2}^{\,n}Y_H^{\,n} \\ +Y_{CO_2}^{\,n}Y_H^{\,n+1} \end{pmatrix} + 2k_{f_{20}}\begin{pmatrix} -2Y_H^{\,2n}Y_{CO_2}^{\,n} \\ +2Y_H^{\,n(n+1)}Y_{CO_2}^{\,n} \end{pmatrix} - 2k_{b_{20}}\begin{pmatrix} -Y_{H_2}^{\,n}Y_{CO_2}^{\,n} \\ +Y_{H_2}^{\,n+1}Y_{CO_2}^{\,n} \end{pmatrix} + \frac{Y_{CO_2}^{\,n}}{\Delta t} \end{matrix}}{1/\Delta t + k_{b_3}Y_M^{\,n} + k_{b_4}Y_O^{\,n} + k_{b_5}Y_H^{\,n} - 2k_{f_{20}}Y_H^{\,2n} + 2k_{b_{20}}Y_{H_2}^{\,n}}$$

Equation 63: Linearization of $CO_{(g)}$ mass production.

$$Y_{CO}^{\,n+1} = \frac{\begin{matrix} 2k_{f_2}\begin{pmatrix} -Y_{C_2H_2}^{\,n}Y_{O_2}^{\,n} + Y_{C_2H_2}^{\,n}Y_{O_2}^{\,n+1} \\ +Y_{C_2H_2}^{\,n+1}Y_{O_2}^{\,n} \end{pmatrix} - 2k_{b_2}\begin{pmatrix} -2Y_{CO}^{\,2n}Y_{H_2}^{\,n} \\ +Y_{CO}^{\,2n}Y_{H_2}^{\,n+1} \end{pmatrix} - k_{f_3}\begin{pmatrix} -Y_{CO}^{\,n}Y_O^{\,n}Y_M^{\,n} + Y_{CO}^{\,n}Y_O^{\,n}Y_M^{\,n+1} \\ +Y_{CO}^{\,n}Y_O^{\,n+1}Y_M^{\,n} \end{pmatrix} + k_{b_3}\begin{pmatrix} -Y_{CO_2}^{\,n}Y_M^{\,n} + Y_{CO_2}^{\,n}Y_M^{\,n+1} \\ +Y_{CO_2}^{\,n+1}Y_M^{\,n} \end{pmatrix} \\ -k_{f_4}\begin{pmatrix} -Y_{CO}^{\,n}Y_{O_2}^{\,n} \\ +Y_{CO}^{\,n}Y_{O_2}^{\,n+1} \end{pmatrix} + k_{b_4}\begin{pmatrix} -Y_{CO_2}^{\,n}Y_O^{\,n} + Y_{CO_2}^{\,n}Y_O^{\,n+1} \\ +Y_{CO_2}^{\,n+1}Y_O^{\,n} \end{pmatrix} - k_{f_5}\begin{pmatrix} -Y_{CO}^{\,n}Y_{OH}^{\,n} \\ +Y_{CO}^{\,n}Y_{OH}^{\,n+1} \end{pmatrix} + k_{b_5}\begin{pmatrix} -Y_{CO_2}^{\,n}Y_H^{\,n} + Y_{CO_2}^{\,n}Y_H^{\,n+1} \\ +Y_{CO_2}^{\,n+1}Y_H^{\,n} \end{pmatrix} + \frac{Y_{CO}^{\,n}}{\Delta t} \end{matrix}}{1/\Delta t + 4k_{b_2}Y_{CO}^{\,n}Y_{H_2}^{\,n} + k_{f_3}Y_O^{\,n}Y_M^{\,n} + k_{f_4}Y_{O_2}^{\,n} + k_{f_5}Y_{OH}^{\,n}}$$

The net reaction rates are transformed into linear form and simultaneously solved into a matrix form using Cramer's rule for all Y_i^{n+1} for i = 1..13, the computed chemical species (see Equation 51 to Equation 63, *Appendix B*).

Equation 64: Linearization of species into Matrix form.

$$A\vec{x} = \overline{D} \rightarrow \begin{bmatrix} a_{11} & a_{12} & . & . & a_{1i} \\ a_{21} & a_{22} & . & . & a_{2i} \\ . & . & . & . & . \\ . & . & . & . & . \\ a_{i1} & a_{i2} & . & . & a_{ii} \end{bmatrix} \begin{bmatrix} Y_1^{n+1} \\ Y_2^{n+1} \\ . \\ . \\ Y_{13}^{n+1} \end{bmatrix} = \overline{D}$$

$where, \quad i = 1...13 \quad (species)$

Next, the chemical sources are subsequently solved from the previous unknowns of each of the species (*i=1... 13*) mass fractions as:

Equation 65: Chemical source.

$$\dot{W}_i = MW_i \frac{Y_i^{n+1} - Y_i^n}{\Delta t}$$

Finally, the full 3-D Unsteady Navier-Stokes equation with 13 species transports, chemically reacting flows, and without body forces or external heat addition is shown in Equation 66:

Equation 66: 3D Unsteady Navier-Stokes.

$$\frac{\partial}{\partial x}\begin{pmatrix} \rho u \\ \rho u^2 + p - \tau_{xx} \\ \rho uv - \tau_{xy} \\ \rho uw - \tau_{xz} \\ \left(E_t + p\right)u - u\tau_{xx} - v\tau_{xy} - w\tau_{xz} + q_x \\ \rho uY_{O_2} - \rho DY_{O_2,x} \\ \rho uY_{O} - \rho DY_{O,x} \\ \rho uY_{H_2} - \rho DY_{H_2,x} \\ \rho uY_{H} - \rho DY_{H,x} \\ \rho uY_{OH} - \rho DY_{OH,x} \\ \rho uY_{H_2O} - \rho DY_{H_2O,x} \\ \rho uY_{N_2} - \rho DY_{N_2,x} \\ \rho uY_{C_2H_4} - \rho DY_{C_2H_4,x} \\ \rho uY_{C_2H_2} - \rho DY_{C_2H_2,x} \\ \rho uY_{N} - \rho DY_{N,x} \\ \rho uy_{NO} - \rho DY_{NO,x} \\ \rho uY_{CO_2} - \rho DY_{CO_2,x} \\ \rho uY_{CO} - \rho DY_{CO,x} \end{pmatrix} + \frac{\partial}{\partial y}\begin{pmatrix} \rho v \\ \rho vu - \tau_{yx} \\ \rho v^2 + p - \tau_{yy} \\ \rho vw - \tau_{yz} \\ \left(E_t + p\right)u - u\tau_{yx} - v\tau_{yy} - w\tau_{yz} + q_y \\ \rho uY_{O_2} - \rho DY_{O_2,y} \\ \rho uY_{O} - \rho DY_{O,y} \\ \rho uY_{H_2} - \rho DY_{H_2,y} \\ \rho uY_{H} - \rho DY_{H,y} \\ \rho uY_{OH} - \rho DY_{OH,y} \\ \rho uY_{H_2O} - \rho DY_{H_2O,y} \\ \rho uY_{N_2} - \rho DY_{N_2,y} \\ \rho uY_{C_2H_4} - \rho Dy_{C_2H_4,y} \\ \rho uY_{C_2H_2} - \rho DY_{C_2H_2,y} \\ \rho uY_{N} - \rho DY_{N,y} \\ \rho uY_{NO} - \rho DY_{NO,y} \\ \rho uY_{CO_2} - \rho DY_{CO_2,y} \\ \rho uY_{CO} - \rho DY_{CO,y} \end{pmatrix} +$$

$$\frac{\partial}{\partial z}\begin{pmatrix} \rho w \\ \rho wu - \tau_{zx} \\ \rho wu - \tau_{zy} \\ \rho w^2 + p - \tau_{zz} \\ \left(E_t + p\right)u - u\tau_{zx} - v\tau_{zy} - w\tau_{zz} + q_z \\ \rho uY_{O_2} - \rho DY_{O_2,z} \\ \rho uY_{O} - \rho DY_{O,z} \\ \rho uY_{H_2} - \rho DY_{H_2,z} \\ \rho uY_{H} - \rho DY_{H,z} \\ \rho uY_{OH} - \rho DY_{OH,z} \\ \rho uY_{H_2O} - \rho DY_{H_2O,z} \\ \rho uY_{N_2} - \rho DY_{N_2,z} \\ \rho uY_{C_2H_4} - \rho DY_{C_2H_4,z} \\ \rho uY_{C_2H_2} - \rho DY_{C_2H_2,z} \\ \rho uY_{N} - \rho Dy_{N,z} \\ \rho uY_{NO} - \rho DY_{NO,z} \\ \rho uY_{CO_2} - \rho DY_{CO_2,z} \\ \rho uY_{CO} - \rho DY_{CO,z} \end{pmatrix} + \frac{\partial}{\partial t}\begin{pmatrix} \rho \\ \rho u \\ \rho v \\ \rho w \\ E_t \\ \rho Y_{O_2} \\ \rho Y_{O} \\ \rho Y_{H_2} \\ \rho Y_{H} \\ \rho Y_{OH} \\ \rho Y_{H_2O} \\ \rho Y_{N_2} \\ \rho Y_{C_2H_4} \\ \rho Y_{C_2H_2} \\ \rho Y_{N} \\ \rho Y_{NO} \\ \rho Y_{CO_2} \\ \rho Y_{CO} \end{pmatrix} + \begin{vmatrix} 0 \\ 0 \\ 0 \\ 0 \\ 0 \\ \dot{W}_{O_2} \\ \dot{W}_{O} \\ \dot{W}_{H_2} \\ \dot{W}_{H} \\ \dot{W}_{OH} \\ \dot{W}_{H_2O} \\ \dot{W}_{N_2} \\ \dot{W}_{C_2H_4} \\ \dot{W}_{C_2H_2} \\ \dot{W}_{N} \\ \dot{W}_{NO} \\ \dot{W}_{CO_2} \\ \dot{W}_{CO} \end{vmatrix} = 0 \quad \text{and} \quad P = \rho RT \sum \frac{Y_i}{MW_i},$$

REFERENCES

1 Chase, R., and Tang, M., "A History of the NASP Program from the Formation of the Joint Program Office to the Termination of the HySTP Scramjet Performance Demonstration Program," AIAA Paper 1995-6031, April 1995.

2 Fry, Ronald S., "A Century of Ramjet Propulsion Technology Evolution," *Journal of Propulsion and Power*, Vol. 20, No. 1, January 2004.

3 Heiser, W., and Pratt, D., "Hypersonic Airbreathing Propulsion," AIAA Education Series, Washington, DC, 1994, pp. 2-27.

4 Baurle, R., Mathur, T., Gruber, M., and Jackson, K. , "A Numerical and Experimental Investigation of a Scramjet Combustor for Hypersonic Missile Applications," AIAA Paper 1998-3121, July 1998.

5 Curran, E., "Scramjet Engines: The First Forty Years," *Journal of Propulsion and Power*, Vol. 17, No. 6, November–December 2001.

6 Malo-Molina, F., Gaitonde, D., and Kutschenreuter, P., "Numerical Investigation of an Innovative Inward Turning Inlet," AIAA-2005-4871, June 2005.

7 Gaitonde, D., and Poggie, J., "Preliminary Analysis of 3-D Scramjet Flowpath with MGD Control," AIAA-2002-2134, May 2002.

8 Vadyak, J., Hoffman, J., Bishop, A., "Three-dimensional Flow Calculations Including Boundary Layer Effects for Supersonic Inlets at Angle of Attack," AIAA-1982-61, Jan 1982.

9 Vadyak, J., Smith, M., Schuster, D., "Navier-Stokes Simulations of Supersonic Fighter Intake Flowfields,"AIAA-1987-1752.

10 Dallmann, U., "Three-Dimensional Vortex Structures and Vorticity Topology," *Fluid Dynamics Research*, Vol. 3, 1988, pp. 183–189.

11 Edney, B., "Anomalous Heat Transfer and Pressure Distributions on Blunt Bodies at Hypersonic Speeds in the Presence of an Impinging Shock," Tech. Report 115. The Aeronautical Research Institute of Sweden, Stockholm, February 1968.

12 Craig, R., and Ortwerth, P., "Experimental Study of Shock Impingement on a Blunt Leading Edge with Application to Hypersonic Inlet Design," Tech. Report TR-71-10, AFAPL, October 1971.

13 Klopfer, G., and Yee, H., "Viscous Hypersonic Shock-On-Shock Interaction on Blunt Cowl Lips." AIAA-88-0233, 1988.

14 Busemann, A., “Die achsensymmetrische kegelige Ueberschallströmung,” *Luftfahrtforschung*, Vol. 19, 1942, pp.137-144.

15 Molder, S., and Szpiro, J., “Busemann Inlet for Hypersonic Speeds,” *Journal of Spacecraft and Rockets*, Vol. 3, 1966, pp.1303-1304.

16 Billig, F., Baurle, R., Tam, C., and Wornom, S., "Design and Analysis of Streamline Traced Hypersonic Inlets," AIAA 99-4974, Nov. 1999.

17 Drayna, T., Nompelis, I., and Candler, G., “Hypersonic Inward Turning Inlets: Design and Optimization,” AIAA-2006-297, Jan. 2006.

18 Tam, C., and Baurle, R., “Inviscid CFD Analysis of Streamline Traced Hypersonic Inlets at Off-Design Conditions,” AIAA-2001-0675, January 2001.

19 Jackson, K., Gruber, M., Jackson, T., and Hass, N., “HIFiRE Flight 2 Scramjet Flight Experiment Overview,” 55th JANNAF Propulsion Meeting, Boston, Massachusetts, May 2008.

20 Staiger, J., Wilkin, H., and Kutschenreuter, P., “CFD Analysis of the Hypersonic JAWS-4 Inward Turning Inlet Design,” JANNAF 31st Airbreathing Propulsion Meeting, La Jolla, CA., Dec. 2009.

21 Staiger, J., Wilkin, H., and Kutschenreuter, P., “ Experimental and Post-Test Computational Analysis of the JAWS-4 Hypersonic Inward Turning Inlet Design,” JANNAF 31st Airbreathing Propulsion Meeting, La Jolla, CA., Dec. 2009.

22 Malo-Molina, F., Gaitonde, D., and Ebrahimi, H., “Numerical Investigation of a 3-D Chemically Reacting Scramjet Engine at High Altitudes Using JP8-Air Mixtures,” AIAA Paper 2005-1435, January 2005.

23 Moss, G. P.; Smith, P. A. S.; Tavernier, D. (1995). "Glossary of Class Names of Organic Compounds and Reactive Intermediates Based on Structure (IUPAC Recommendations 1995)". *Pure and Applied Chemistry* 67: 1307–1375.

24 Atkinson R., Baulch, D., Cox, R., and Hampson, R., "Evaluated Kinetic and Photochemical Data for Atmospheric Chemistry: Supplement III, *Journal of Physical and Chemical Reference Data*, 18 (2), 1989, 881-1097.

25 Ebrahimi, H., “Validation Database for Propulsion Computational Fluid Dynamics,” *Journal of Spacecraft and Rockets*, Vol. 34, No. 5, October 1997, pp. 642-650.

26 Ebrahimi, H., “CFD Validation and Evaluation for Reacting Flow: Part III,” AIAA-95-0735, January 1995.

27 Ebrahimi, H., “CFD Validation for Scramjet Combustor and Nozzle Flows: Part I.” AIAA-93-1840, June 1993.

28 Qin, Z., Lissianski, V., Yang, H., Gardiner, W., Davis, S., and Wang, H., “Combustion Chemistry of Propane: A Case Study of Detailed Reaction Mechanism Optimization,” *Proceedings of the Combustion Institute*, Vol. 29, 2000, pp. 1663-1669.

29 Mawid, M., Private Communication, Engineering and Analysis Co., Report No. ERAC.EF.5.1997; AFRL Wright-Patterson Air Force Base.

30 Wang, H., and Laskin, A., “A Comprehensive Kinetic Model of Ethylene and Acetylene Oxidation at High Temperatures,” A Progress Report for AFOSR, 1998.

31 Wang, H., You, X., Joshi, A., Davis, S., Laskin, A., Egolfopoulos, F., and Law, C., “USC Mech Version II: High-Temperature Combustion Reaction Model of H2/CO/C1-C4 Compounds,” 2007.

32 Ebrahimi, H., "An Efficient Two-Dimensional Engineering Design Code for Scramjet Combustor, Nozzle, and Plume Analysis," AIM-91-0416; January 1991.

33 Colket, M., and Spadaccini, L., “Scramjet Fuels Autoignition Study,” *Journal of Propulsion and Power*, Vol.17, 2001, pp. 315-323.

34 Turns, S., *An Introduction to Combustion, Concepts and Applications*, The McGraw-Hill Companies, 2nd edition. 1999 p. 117.

35 Gordon, S., and McBride, B., "Computer Program for Calculation of Complex Chemical Equilibrium Compositions and Applications," NASA RP-1311, Oct. 1994.

36 Gordon, S., McBride, B., Computer Program for Calculation of Complex Chemical Equilibrium Compositions and Applications, Part II: User's Manual and Program Description," NASA RP-1311, June 1996.

37 El-Sherif, S., "Control of Emissions by Gaseous Additives in Methane-Air and Carbon Monoxide-Air Flames," *Fuel*, 79, 2000, p. 568.

38 Dixon-Lewis, G., "Mathematical Modeling and Simulation," in *Complex Chemical Reaction Systems*, edited by J. Warnatz and W. Jäger, Springer-Verlag, Berlin and Heidelberg, 1984, pp. 39-54.

39 Pope, S., *Turbulent Flows*, Cambridge University Press, Cambridge, 2000, p. 384.

40 Oefelein, J., Schefer, R., and Barlow, R., “Toward Validation of Large Eddy Simulation for Turbulent Combustion," AIAA Journal, Vol. 44, No. 3, 2006, pp. 418-433.

41 James, S., Zhu, J., and Anand, M., “Large-Eddy Simulations as a Design Tool for Gas Turbine Combustion Systems," AIAA Journal, Vol.44, No.4, 2006, pp.674-686.

42 Cazalens, M., Roux, S., Sensiau, C., and Poinsot, T., "Combustion Instability Problems Analysis for High-Pressure Jet Engine Cores," *Journal of Propulsion and Power*, Vol. 24, No.4, 2008, pp. 770-778.

43 Pope, S., *Turbulent Flows*, Cambridge University Press, Cambridge, 2000, p. 578.

44 Menon, S. and Kim, W., "Application of the Localized Dynamic Subgrid-Scale Model to Turbulent Wall-Bounded Flows," AIAA paper 97-0210.

45 Menon, S.and Patel, N., "Subgrid Modeling for Simulation of Spray Combustion in Large-Scale Combustors," AIAA Journal, Vol. 44, No. 4, April 2006.

46 Ebrahimi, H., "Validation and Evaluation of the CELMINT Code for Two-Phase Flow in Solid-propellant Rocket Motors," AIAA-95-0735, January 1996.

47 Ebrahimi, H., "Numerical Investigation of Multi-plume Rocket Phenomenology," AIAA-1997-2942, July 1997.

48 Ebrahimi, H., "An Efficient Two-dimensional Engineering Design Code for Scramjet Combustor, Nozzle, and Plume Analysis," AIAA-1991-416. January 1991.

49 Ebrahimi, H., "Numerical Simulation of Transient Jet-Interaction Phenomenology in a Supersonic Freestream," *Journal of Spacecraft and Rockets* 2000, 0022-4650, Vol. 37, No. 6, pp.713-719.

50 Malo-Molina, F., and Gaitonde, D., "Integrated Analysis of Scramjet Flowpath with Innovative Inlets," Department of Defense Proceedings of the HPCMP; June 18-21, 2007.

51 Malo-Molina, F., and Gaitonde, D., "Integrated Analysis of Scramjet Flowpath with Innovative Inlets," Department of Defense Proceedings of the HPCMP; July 14-17, 2008.

52 Malo-Molina, F., and Gaitonde, D., "Integrated Analysis of Scramjet Flowpath with Innovative Inlets," Department of Defense Proceedings of the HPCMP; June 15-19, 2009.

53 Gaitonde, D., and Shang, J., "The Structure of a Double-Fin Turbulent Interaction at Mach 4," AIAA Journal, Vol. 33, No. 12, Dec. 1995, pp. 2250–2258.

54 Gaitonde, D. , Shang, J., Zheltovodov, A., Maksimov, A., "Sidewall Interaction in an Asymmetric Simulated Scramjet Inlet Configuration," *Journal of Propulsion and Power*, Vol. 17, No. 3, May–June 2001.

55 Garrison, T., and Settles, G., "Interaction Strength and Model Geometry Effects on the Structure of Crossing-Shock/Boundary-layer Interactions," AIAA-93-0780, 1993.

56 Settles, G., and Dodson, L., "Hypersonic Shock/Boundary-Layer Interaction Database: New and Corrected Data," Technical Report, NASA Ames Research Center, Moffet Field, CA 94035-1000.

57 Gruber, M., Baurle, R., Mathur, T., and Hsu, K., "Fundamental Studies of Cavity-Based Flameholder Concepts for Supersonic Combustors," *Journal of Propulsion and Power*, Vol. 17, No. 1, January–February 2001.

58 Settles, G., Baca, B., Williams, D., and Bogdonoff, S., "A Study of Reattachment of a Free Shear Layer in Compressible Turbulent Flow," AIAA-80-1408, January 1980.

59 McDaniel, J., Fletcher, D., Hartfield, R., Jr., and Hollo, S., "Staged Transverse Injection into Mach 2 Flow Behind and Rearward Facing Step," AIAA-91-5071, December 1991.

60 Wilcox, D., "More Advanced Applications of the Multiscale Model for Turbulent Flows," AIAA-1988-220, January 1988.

61 Baurle, R., and Eklund, D., "Analysis of Dual-Mode Hydrocarbon Scramjet Operation at Mach 4-6.5," *Journal of Propulsion and Power*, Vol. 18, No. 5, 2002, pp. 990-1002.

62 Malo-Molina, F., Gaitonde, D., Ebrahimi, H., and Ruffin, S., "Numerical Simulation of a Generic High Speed Inlet/combustor with JP8 Fuel," AIAA Paper 2006-4871, June 2006.

63 Dallmann, U., "On the Formation of Three-Dimensional Vortex Flow Structures," DFVLR-IB 221-85 A13, 1985.

64 Gaitonde, D., "Three Dimensional Flow-Through Scramjet Simulation with MGD Energy-Bypass," AIAA-2003-0172, January 2003.

65 Baker, C., "The Laminar Horseshoe Vortex," *Journal of Fluid Mechanics*, Vol. 95, Part 2, 1979, pp. 347-367.

66 Jensen, J., and Braendlein, B., "Review of the Marquardt Dual Mode Mach 8 Scramjet Development," AIAA-96-3037, July 1996.

67 Steele, R., *Skin Friction Measurement Techniques for Scramjet Applications*, Report by Marquardt Co. Van Nuys Ca., ADA-231899; Sept. 89-Feb. 1990.

68 Tennekes, H., and Lumley, J., *A First Course in Turbulence*, The MIT Press, 1990, pp. 146-164.

69 Schlichting, H., *Boundary-Layer Theory*, McGrawHill series in Mechanical Engineering, 7th edition, 1979. pp. 83-110 and 225-248.

70 Bippens, H. and Turk, M., "Oil Flow Patterns of Separated Flow on a Hemisphere Cylinder at Incidence," DFVLR-FB 84-20, 1983.

71 Gaitonde, D., Shang, J., and Visbal, M., "Structure of a Double-fin Turbulent Interaction at High Speed," *AIAA Journal*, Vol. 33, No. 2, 1995, pp. 193-200.

72 Knight, D. and Degrez, G., “Shock Wave Boundary Layer Interactions in High Mach Number Flows – A Critical Survey of Current CFD Prediction Capabilities,” Technical Report AR-319, Vol. 2, AGARD, 1997.

73 Tanimizu, K., Mee, D., and Stalker, R., "Comparison of Drag Measurements of Two Axisymmetric Scramjet Models at Mach 6," 16th Australasian Fluid Mechanics Conference, December 2007.

74 Croker, B., Malo-Molina, F., Gaitonde, D., and Ebrahimi, H., “The Flowfield Structure in Generic Inward-Turning-Based Propulsion Flowpath,” AIAA-2007-5744, July 2007.

75 Ebrahimi, H., “Numerical Investigation of Jet Interaction in a Supersonic Freestream,” *Journal of Spacecraft and Rockets*, Vol. 45, No. 1, 2008, pp. 642–650.

76 Goyne, C., McDaniel J., Quagliaroli, T., Krauss, R., and Day, S., “Dual-Mode Combustion of Hydrogen in a Mach 5 Continuous-Flow Facility,” *Journal of Propulsion and Power*, Vol. 17, No. 6, 2001, pp. 1313–1318.

77 Ebrahimi, H., “Numerical Simulation of Transient Jet-Interaction Phenomenology in a Supersonic Freestream,” *Journal of Spacecraft and Rockets*, Vol. 37, No. 6, November and December 2000, pp. 713-719.

78 Gruber, M., Jackson, K., Jackson, T., and Mathur, T., “Investigations of Shock Trains in Rectangular Ducts,” JANNAF 35th Joint APS Meeting, Paper Number 4D-03, December 1998.

79 Mathur, T., Lin, K., Kennedy, P., Gruber, M., Donbar, J., Donaldson, W., Jackson, T., Smith, C., and Billig, F., “Liquid JP-7 Combustion in a Scramjet Combustor,” AIAA-2000-3581, July 2000.

80 Pitt Ford, C., and Babinsky, H., "Micro-Ramp Control for Oblique Shock Wave/Boundary Layer Interactions,” AIAA-2007-4115, June 2007.

81 Heiser, W., and Pratt, D., *Hypersonic Airbreathing Propulsion* AIAA Education Series Book, 1994.

82 Mattingly, J., and Ohain, H., *Elements of Propulsion, Gas Turbines and Rockets*, AIAA Educational Series Book, 2006, pp. 120-121.

83 Committee on Hypersonic Technology for Military Application, Air Force Studies Board. *Hypersonic Technology for Military Application*, National Academy Press; Washington, DC. 1989.

84 Tishkoff, J., Drummond, J., Edwards, T., and Nejad, A., “Future Direction of Supersonic Combustion Research: Air Force/NASA Workshop on Supersonic Combustion,” AIAA-97-1017, Jan. 1997.

85 Roudakov, A., Schikhmann,Y., Semenov, V., Novelli, P., and Fourt, O., “Flight Testing of an Axisymmetric Scramjet—Russian Recent Advances,” International Astronautical Federation, IAF Paper 93-S.4.485, Oct.1993.

86 Vinagradov, V., Kobigsky, S., and Petrov, M., "Experimental Investigation of Kerosene Fuel Combustion in Supersonic Flow," *Journal of Propulsion and Power*, Vol. 11, No. 1, 1995, pp. 130–134.

87 Ortweth, P., Mathur, A., Vinogradov, V., Grin, V., Goldfeld, M., and Starov, A., "Experimental and Numerical Investigation of Hydrogen and Ethylene Combustion in a Mach 3-5 Channel with a Single Injector," AIAA-96-3245, July 1996.

88 Owens, M., Tehranian, S., Segal, C., and Vinogradov, V., "Flame-Holding Configurations for Kerosene Combustion in a Mach 1.8 Air Flow," *Journal of Propulsion and Power*, Vol. 14, No. 4, 1998, pp. 456–461.

89 Ben-Yakar, A., Natan, B., and Gany, A., "Investigation of a Solid Fuel Scramjet Combustor," *Journal of Propulsion and Power*, Vol. 14, No. 4, 1998, pp. 447–455.

90 Roquemore, W., Shouse, D., Burns, D., Jonson, A., Cooper, C., Duncan, B., Hsu, K-Y., and Katta, V., "Trapped Vortex Combustor Concepts for Gas Turbine Engines," AIAA-2001-0483, January 2001.

91 Katta, V., and Roquemore, W., "Numerical Studies On Trapped-Vortex Concepts for Stable Combustion," *Journal of Engineering For Gas Turbines and Power*, Vol. 120, No. 12, 1998, pp. 60-68.

92 Hsu, K-Y., Goss, L., and Roquemore, W., "Characteristics of a Trapped Vortex Combustor," *Journal Of Propulsion and Power*, Vol. 14, No. 1, 1998, pp. 57-65.

93 Ben-Yakar, A., and Hanson, R., "Cavity Flame-Holders for Ignition and Flame Stabilization in Scramjets: An Overview," *Journal of Propulsion and Power*, Vol. 17, No. 4, 2001, pp. 869–877.

94 Gruber, M., Baurle, R., Mathur, T., and Hsu, K-Y., "Fundamental Studies of Cavity-Based Flame Holder Concepts for Supersonic Combustors," *Journal of Propulsion and Power*, Vol. 17, No. 1, 2001, pp. 146–153.

95 Ben-Yakar, A., and Hanson, R., "Cavity Flameholders for Ignition and Flame Stabilization in Scramjets: Review and Experimental Study," AIAA-98-3122, July 1998.

96 Baysal, O., and Stallings, R., "Computational and Experimental Investigation of Cavity Flowfields," *AIAA Journal*, Vol. 26, No. 1, 1988, pp. 6, 7.

97 Gruber, M., Donbar, J., Carter, C., and Hsu, K-Y., "Mixing and Combustion Studies Using Cavity-Based Flameholders in Supersonic Flow," ISABE-2003-1204.

98 Mathur, T., and Billig, F., "Supersonic Combustion Experiments with a Cavity-Based Fuel Injector," *Journal of Propulsion and Power*, Vol. 17, No. 6, 2001, pp. 1305-1312.

99 Berman, H., Anderson, J., and Drummond, J., "Supersonic Flow Over a Rearward Facing Step with Transverse Nonreacting Hydrogen Injection," *AIAA Journal*, 21, 1983, pp.1707– 1713.

100 Kim, K., Baek, S., Han, C., “Numerical Study on Supersonic Combustion with Cavity-based Fuel Injection," *International Journal of Heat and Mass Transfer*, Vol.47, 2004, pp.271-286.

101 Baurle, R.,Tam, C.-J., and Dasgupta, S., “Analysis of Unsteady Cavity Flows for Scramjet Applications,” AIAA Paper 2000-3617, July 2000.

102 Yu, K., Wilson, K., and Schadow, K., “Effect of Flame-Holding Cavities on Supersonic-Combustion Performance,” *Journal of Propulsion and Power*, Vol. 17, No. 6, 2001, pp. 1287–1295.

103 Reyder, Jr., R., and McDivitt, T., “Application of the CFD Code Towards Industrial Gas Fired Heater,” AIAA 2000-0456, 2000.

104 Goyne, C., McDaniel J., Quagliaroli, T., Krauss, R., and Day, S., “Dual-Mode Combustion of Hydrogen in a Mach 5 Continuous-Flow Facility,” *Journal of Propulsion and Power*, Vol. 17, No. 6, 2001, pp. 1313–1318.

105 Ebrahimi, H., “Numerical Simulation of Transient Jet-Interaction Phenomenology in a Supersonic Freestream.” *Journal of Spacecraft and Rockets*, Vol. 37, No. 6, November and December 2000.

106 Gruber, M., Jackson, K., Jackson, T., and Mathur, T., "Investigations of Shock Trains in Rectangular Ducts," JANNAF 35th Joint APS Meeting, Paper Number 4D-03, December 1998.

107 Masuya, G., Uemoto, T., Wakana, Y., Kudou, K., Murakami, A., and Komuro, T., "Performance Evaluation of Scramjet Combustors Using Kinetic Energy and Combustion Efficiencies," *Journal of Propulsion and Power*, Vol. 15, No. 3, May–June 1999.

108 Ogorodnikov, D., Vinogradov, V., Shikhman, Y., and Strokin V., "Russian Research on Experimental Hydrogen-Fueled Dual-Mode Scramjet: Conception and Preflight Tests," *Journal of Propulsion and Power*, Vol. 17, No. 5, September–October 2001.

109 Malo-Molina, F., Gaitonde, D., and Ebrahimi, H., “Scramjet Combustor Analysis Integrated to an Innovative Inward Turning Inlet.” AIAA-2008-4577, July 20–23 2008.

110 Ratner, A., Driscoll, J., Huh, H., and Bryant, R., "Combustion Efficiencies of Supersonic Flames," Journal *of Propulsion and Power*, Vol. 17, No. 2, March–April 2001.

111 Ebrahimi, H., “Recent Progress in LES/DNS Modeling and Simulation for Chemically Reacting Flows.” ASME-55351, July 2008.

112 Ebrahimi, H., “An Overview of Computational Fluid Dynamics for Application to Advanced Propulsion Systems .” AIAA-2004-2370, July 2004.